

Theo Fett & Günter Schell et al.

**CONSEQUENCES OF HYDROXYL GENERATION
BY THE SILICA/WATER REACTION**

Part II: Global and local Swelling

Part III: Damage and Young's Modulus

SCHRIFTENREIHE DES INSTITUTS
FÜR ANGEWANDTE MATERIALIEN

BAND 102

Theo Fett, Karl Günter Schell, Ethel C. Bucharsky, Gabriele Rizzi,
Susanne Wagner, Michael J. Hoffmann

**Consequences of hydroxyl generation
by the silica/water reaction**

Part II: Global and local Swelling

Part III: Damage and Young's Modulus

**Schriftenreihe
des Instituts für Angewandte Materialien
*Band 102***

Karlsruher Institut für Technologie (KIT)
Institut für Angewandte Materialien (IAM)

Eine Übersicht aller bisher in dieser Schriftenreihe erschienenen Bände
finden Sie am Ende des Buches.

Consequences of hydroxyl generation by the silica/water reaction

Part II: Global and local Swelling

Part III: Damage and Young's Modulus

by

Theo Fett

Karl Günter Schell

Ethel C. Bucharsky

Gabriele Rizzi

Susanne Wagner

Michael J. Hoffmann

Impressum



Karlsruher Institut für Technologie (KIT)
KIT Scientific Publishing
Straße am Forum 2
D-76131 Karlsruhe

KIT Scientific Publishing is a registered trademark
of Karlsruhe Institute of Technology.
Reprint using the book cover is not allowed.

www.ksp.kit.edu



*This document – excluding parts marked otherwise, the cover, pictures and graphs –
is licensed under a Creative Commons Attribution-Share Alike 4.0 International License
(CC BY-SA 4.0): <https://creativecommons.org/licenses/by-sa/4.0/deed.en>*



*The cover page is licensed under a Creative Commons
Attribution-No Derivatives 4.0 International License (CC BY-ND 4.0):
<https://creativecommons.org/licenses/by-nd/4.0/deed.en>*

Print on Demand 2022 – Gedruckt auf FSC-zertifiziertem Papier

ISSN 2192-9963

ISBN 978-3-7315-1159-5

DOI 10.5445/KSP/1000141423

PART II:

DIFFUSION AND ISOTROPIC SWELLING

Preliminary Remarks	IX
1 Basic results on diffusion and swelling	1
2 Proof of swelling via crack terminating angles	7
2.1 Terminating angle.....	7
2.2 Stress intensity factors	8
2.3 Experimental determination of shielding stress intensity factors	10
3 Effect of soaking on inert strength	15
3.1 Inert strength.....	15
3.2 Total stress intensity factor for a semi-circular surface crack	16
3.3 Toughness and inert strength.....	18
3.4 Strength of unsoaked and soaked specimens.....	20
3.5 Strength predictions	23
3.6 Analysis of nonlinear strength distributions	24
3.7 A possible reason for the bimodal strength distribution.....	25
4 Strength in silicon oil, humid air and water	31
4.1 Strength measurements on silica	31
4.2 Pop-in behaviour	34

5 Effect of swelling on dynamic strength	41
5.1 Dynamic strength.....	41
5.2 Computation of dynamic strength for edge-crack like defects	41
5.3 Strength predictions compared with experimental data.....	46
6 Swelling anisotropy	53
6.1 Motivation for anisotropic swelling.....	53
6.2 Anisotropic swelling in tension and torsion test	55
6.3 FE-Model for a single reaction event.....	60
6.4 FE-Results.....	61
7 Stress-enhanced isotropic swelling	65
7.1 Quasi-hydrostatic stress state at crack tips.....	65
7.2 Application of simple crack-tip models	66
7.3 Hydroxyl concentration under swelling stresses.....	71
8 Effects of swelling at crack tips	75
8.1 Consequences of shielding on v - K -curves.....	75
8.2 Threshold behaviour under shielding conditions	76
8.3 Swelling strains at the tip of an arrested crack	83
9 Crack-tip shielding	87
9.1 Effect of local swelling at surface cracks	87
9.2 Shielding stress intensity factors from measured water profiles.....	88

9.3	Water profiles below crack surfaces of subcritically grown cracks	91
9.4	Computation of shielding stress intensity factors	93
9.5	Crack-tip shielding and threshold behaviour	94
10	Anomalous subcritical crack growth	99
10.1	Anomalous and normal subcritical crack growth	99
10.2	Experimental crack growth results from literature	100
10.3	Expectation from reaction rate theory	101
10.4	Effect of vapour pressure	103
10.5	Effect of water solubility	103
10.6	Effect of shielding stress intensity factor	105

PART III:

DAMAGE AND YOUNG'S MODULUS

11	Damage and Young's modulus	117
11.1	Damage by hydroxyl generation	117
11.2	Experimental evidence for module reduction in silica	118
11.3	Modelling of damage by spherical pores	120
11.4	Effect of damage in thin surface layers	123
11.5	Example of application: Uniaxial stress-strain curve	128
11.6	Deviating behaviour under compressive loading	131
11.7	Global strength of a fiber	133

12 Shielding affected by damage	139
12.1 Effect of local swelling at surface cracks	139
12.2 Shielding stress intensity factors for a damaged material.....	140
12.3 Shielding stress intensity factor for asymmetric damage.....	141
12.4 Mechanical interpretation of the limit case under compression	143

APPENDIX

A1 Modifications of shielding by additional effects	149
A1.1 Deformed steady-state swelling zones	149
A1.2 Crack leaving a swelling zone	151
A1.3 Blunt crack with finite notch root radius	154
A2 Finite Element study on heart-shaped zones	163
A2.1 Zone shape	163
A2.2 Crack terminating at $\varphi=\pi$ of the heart-shaped zone.....	164
A2.3 Derivation of J-Integral for slender notches by Merkle	170
A2.4 Results for extended zones.....	173
A2.5 Crack-Opening Displacements (COD)	176
A2.6 Comparison of parameters for the two zone shapes.....	180
A3 Hydrostatic stress at crack tips	183
A3.1 Hydrostatic stress under hydroxyl damaging.....	183
A3.2 Irwin and Dugdale model.....	185

A4 Swelling stresses from crack-terminating angles.....	187
A4.1 Estimation of the magnitude of residual stresses.....	187
A4.2 Discussion of stresses	190

Preliminary Remarks

Water diffusing into silica surfaces gives rise for several effects on diffusion behaviour and mechanical properties. The most interesting observations from our point of view may be listed here.

(I) *In the absence of externally applied stresses:*

- a) Density reduction with increasing water concentration [1].
- b) Increasing concentration of molecular water at silica surfaces [2].
- c) Decrease of measured water diffusivity with time [3].
- d) Change of the shape of the water concentration with time [3].
- e) Deformation by one-side water vapour soaked specimens [4].
- f) Strength increase of water vapour soaked specimens.
- g) Increasing exponent n of the power law for subcritical crack growth with increasing soaking time.

These points were covered in Part I.

(II) *In presence of externally applied loadings:*

- a) Increasing diffusivity under externally applied tensile stresses and a decrease in compression [5].
- b) Decrease of water solubility in tension and an increase in compression [5].
- c) Increased water concentration in tension at high temperatures [6].
- d) Strongly increasing strength at high tensile stresses even under very low water vapour pressure [7].
- e) Residual deformation of thin fibers after 2-point bending tests [8].
- f) Drastically increased water concentration on crack surfaces after subcritical crack growth experiments [9].

These topics are elaborated on in Part II.

(III) *Including damage by hydroxyl generation:*

- a) Damage behavior and Young' modulus reduction
- g) Blunting of crack tip displacements in water-soaked silica [10].

Part III will deal with this topic.

For an explanation of all the findings listed under (I) there is only volume swelling by hydrogen generation an appropriate tool. Any stress relaxation mechanism as suggested in [7] will hardly be able to explain disk deformation in stress-free disks.

In order to give a transparent description, two main assumptions will be made:

- (1) For an interpretation of the increase of diffusivity and water concentration under tensile loading, a further effect may play a role. Under tensile stresses, the nanopores of the ring structure are possibly widened and diffusion and solubility may be enhanced. Such behaviour was observed in different materials and is interpreted in terms of the so-called free volume theory. This may also affect water diffusivity, generally described by the Doolittle equation [11], and solubility (see e.g. [12]). Due to the lack of results for silica, free volume effects must be ignored in the following considerations.
- (2) Water molecules are believed to diffuse through silica glass in much the same way as the noble gases. Hence, the diffusion of water molecules is also expected to show little dependence on applied stress [9]. Following this reasoning, we assume that the molecular water in the glass is located in molecular size holes in the silica glass network where the water does not contribute to the volume of the glass. Consequently, molecular water cannot contribute stress effects. Thus, the concentration of molecular water in the glass depends only on the vapour pressure in the external environment, but not on the stress in the glass.

1 Shelby, J.E., "Density of vitreous silica," *J. Non-Cryst.* **349** (2004), 331-336.
2 Oehler, A., Tomozawa, M., *J. Non-Cryst. Sol.* **347** (2004) 211-219.
3 Davis, K.M., Tomozawa, M., *J. Non-Cryst. Sol.* **185** (1995), 203-220.

- 4 S. M. Wiederhorn, F. Yi, D. LaVan, T. Fett, M.J. Hoffmann, *J. Am. Ceram. Soc.* **98**(2015), 78-87.
- 5 M. Nogami, M. Tomozawa, *Phys. and Chem. of Glasses* **25**(1984), 82-85.
- 6 A. Agarwal, M. Tomozawa, W. A. Lanford, *J. Non-Cryst.* **167**(1994), 139-148.
- 7 P.J. Lezzi, Q.R. Xiao, M. Tomozawa, T.A. Blanchet, C.R. Kurkjian, *J. of Non-Crystalline Solids* **379** (2013) 95–106.
- 8 M. Tomozawa, P.J. Lezzi, R.W. Hepburn, T. A. Blanchet, D. Cherniak, *J. Non-Cryst. Solids* **358**(2012), 2650.
- 9 M. Tomozawa, W.-T. Han and W.A. Lanford, *J. Am. Ceram. Soc.* **74** [10] (1991) 2573-2576.
- 10 Y. Bando, S. Ito, M. Tomozawa, *J. Am. Ceram. Soc.*, **67** (1984), C36 C37.
- 11 A.K. Doolittle, *J. Appl. Phys.* **22**(1951), 1471.
- 12 S. Neumann, G. Marom, *J. Mat. Sci.* **21**(1986), 26-30.

1 Basic results on diffusion and swelling

In this Introductory Section, some of the results from Part I [1.1] may be reported which will be used in the following considerations. The relationships from Part I, required in this booklet, should be briefly reproduced. Details on derivations and applications can be seen in [1.1].

Water penetrated into silica reacts with the silica network according to



with the concentration of the hydroxyl $S = [\equiv\text{SiOH}]$ and that of the molecular water $C = [\text{H}_2\text{O}]$. The equilibrium constant k of this reaction is depending on the temperature θ :

$$k = \begin{cases} S/C & \text{for } \theta < 450^\circ\text{C} \\ S^2/C & \text{for } \theta \geq 450^\circ\text{C} \end{cases} \quad (1.1.2)$$

In the range of $90^\circ\text{C} \leq \theta \leq 300^\circ\text{C}$ the equilibrium constant can be expressed by [1.2]

$$k \cong 32.3 \exp\left(\frac{-10750\text{J/mol}}{RT}\right) \quad (1.1.3)$$

where $T = \theta + 273\text{K}$ is the absolute temperature, and R the gas constant.

Due to diffusion, concentrations of molecular water, C , and hydroxyl water, S , decrease with increasing distance, z , from the glass surface. If the reaction given by eq.(1.1.1) is in *equilibrium*, the diffusion process is governed by the diffusion differential equation:

$$\frac{\partial C}{\partial t} = \frac{\partial}{\partial z} \left[D(C) \frac{\partial C}{\partial z} \right] \quad (1.1.4)$$

where D is the effective diffusivity that takes into account the chemical reaction given by eq.(1.1.1) [1.3]. The diffusivity shows an Arrhenius type of temperature dependence.

Solution of the diffusion equation requires an appropriate boundary condition, very often chosen as constant surface concentration of molecular water:

$$C(z=0, t) \equiv C(0) = C_0 = \text{constant} \quad (1.1.5)$$

For a semi-infinite body, this assumption results in the following equation as a solution of the diffusion equation, *i.e.*, eq.(1.1.4):

$$C = C_0 \operatorname{erfc} \left(\frac{z}{2\sqrt{Dt}} \right) \quad (1.1.6)$$

which is well established for liquid water as the environment [1.4].

In the case of water vapour as the environment, the behavior of water at the silica surface does not follow eq.(1.1.5). Experimental results show that the concentration of water is not a constant at the surface, but increases continuously with time, until it reaches the solubility limit of water in the silica glass [1.5, 1.6].

Experimental results for $C(z=0, t)$ are in clear contradiction with the assumption of a constant surface value for the water concentration. There is, however, an incredible agreement with the thermal analogue of thermal shock behaviour under heat transfer boundary conditions, governed by a heat transfer coefficient. This calls for a surface condition (see e.g. [1.7], Section 4.7)

$$\frac{dC}{dz} = \frac{h}{D}(C - C_0) \quad \text{at } z=0, \quad (1.1.7)$$

where again C_0 is the concentration of molecular water reached at $z=0$ for $t \rightarrow \infty$.

A swelling effect in water-containing silica at high temperatures was early reported by Shelby [1.8]. This author showed own and literature results on density reduction by water uptake at high temperature

$$\frac{\Delta\rho}{\rho_0} = -\chi C_w, \quad \rho_0 = \rho(C_w = 0) \quad (1.1.8)$$

where C_w is the weight fraction of water and χ an empirical coefficient. The observed volume swelling strain ε_v reads in terms of hydroxyl concentration S

$$\varepsilon_v = \kappa \times S \quad (1.1.9)$$

with

$$\kappa = 0.97 [0.92, 1.02] \quad (1.1.10)$$

and the numbers in brackets indicate the 95% confidence interval.

The effect of the water-silica reaction is the generation of *swelling strains*. *Swelling stresses* are a consequence of the mechanical boundary conditions. A volume element in a thick plate that undergoes swelling cannot freely expand. If the diffusion zone is small compared to the component dimensions, expansion is completely prevented in the plane of the surface and can only take place normal to the surface plane.

At a free surface, the stress state is *plane stress* and, consequently, also stresses caused by swelling are equi-biaxial ($\sigma_x=0$)

$$\sigma_{sw,y} = \sigma_{sw,z} = -\frac{\varepsilon_v E}{3(1-\nu)}, \quad \sigma_{sw,h} = -\frac{2\varepsilon_v E}{9(1-\nu)} \quad (1.1.11)$$

$\sigma_{sw,h}$ =hydrostatic stress. In (1.1.11) E is Young's modulus and ν is Poisson's ratio.

Water concentrations at silica surfaces below 500°C are available from investigations by Zouine et al. [1.4]. For these measurements the *nuclear reaction analysis* (NRA) was applied that subsumes molecular and hydroxyl water. From these measurements the water species S and C can be obtained in *molar units* by

$$C_w = C + \frac{1}{2}S = C(1 + \frac{1}{2}k) \quad (1.1.12)$$

where the quantity k is the equilibrium constant describing the ratio of $k=S/C$, Fig. 1.1.

Due to the swelling stresses, the diffusivity is a function of water concentration. The diffusivity for the case of stress-enhanced diffusion is given by the following equation [1.9]

$$D = D_0 \exp\left[\sigma_h \frac{\Delta V_w}{RT}\right] \quad (1.1.13)$$

where D_0 denotes the value of the diffusivity in the absence of a stress. T is the absolute

temperature in K ; ΔV_w is the activation volume for stress-enhanced diffusion and R is the universal gas constant.

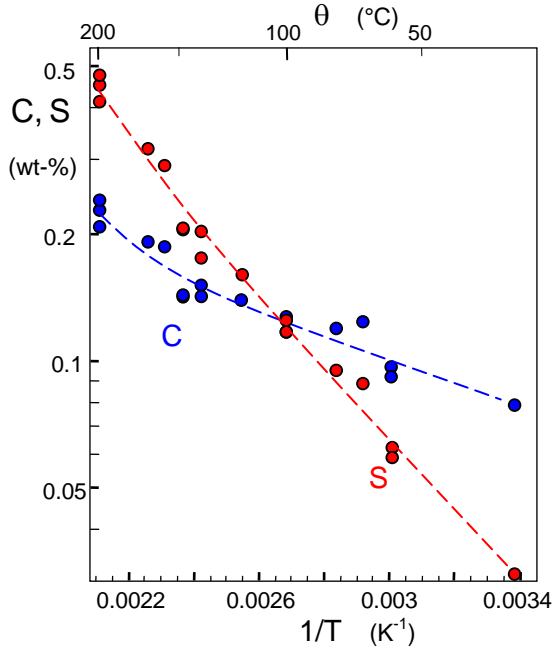


Fig. 1.1 Results on surface concentration of the molecular (blue) and hydroxyl (red) water species obtained computed from measurements by Zouine et al. [1.4].

When an externally applied stress σ_{appl} and swelling stresses σ_{sw} are present simultaneously, it is

$$D = D_0 \exp \left[(\sigma_{\text{sw},h} + \sigma_{\text{appl},h}) \frac{\Delta V_w}{RT} \right] \quad (1.1.14)$$

Also the hydroxyl concentration S resulting from the reaction (1.1.1) is stress dependent. Under uniaxial tension in z -direction it holds [1.1,1.10]

$$S = S_0 \exp \left(\frac{\sigma_{\text{appl}} \Delta V_{\text{eff}}}{RT} \right) \quad (1.1.15)$$

where ΔV_{eff} is an effective activation volume. We obtained for the case of stress-enhanced swelling [1.1, 1.10]

$$\Delta V_{\text{eff}} = 14.4 \text{ cm}^3/\text{mol} \pm 10\% \quad (1.1.16)$$

References

- 1.1 T. Fett, G. Rizzi, K.G. Schell, E.C. Bucharsky, P. Hettich, S. Wagner, M. J. Hoffmann, Consequences of hydroxyl generation by the silica/water reaction Part I: Diffusion and Swelling, KIT Scientific Publishing, Karlsruhe.
- 1.2 S. M. Wiederhorn, F. Yi, D. LaVan, T. Fett, M.J. Hoffmann, Volume Expansion caused by Water Penetration into Silica Glass, *J. Am. Ceram. Soc.* **98** (2015), 78-87.
- 1.3 Doremus, R.H., Diffusion of water in silica glass, *J. Mater. Res.*, **10** (1995), 2379-2389.
- 1.4 A. Zouine, O. Dersch, G. Walter and F. Rauch, Diffusivity and solubility of water in silica glass in the temperature range 23-200°C, *Phys. Chem. Glass: Eur. J. Glass Sci and Tech. Pt. B*, **48** [2] (2007), 85-91.
- 1.5 Davis, K.M., Tomozawa, M., Water diffusion into silica glass: structural changes in silica glass and their effect on water solubility and diffusivity, *J. Non-Cryst. Sol.* **185** (1995), 203-220.
- 1.6 M. Helmich and F. Rauch, On the mechanism of diffusion of water in silica glass, *Glastech. Ber.* **66** [8] (1993), 195-200.
- 1.7 R.H. Doremus, *Diffusion of Reactive Molecules in Solids and Melts*, Wiley, 2002, New York.
- 1.8 Shelby, J.E., Density of vitreous silica, *J. Non-Cryst.* **349** (2004), 331-336.
- 1.9 P.G. Shewman, *Diffusion in Solids*, McGraw-Hill, New York, 1963.
- 1.10 S. M. Wiederhorn, G. Rizzi, S. Wagner, M. J. Hoffmann, T. Fett, Stress-Enhanced Swelling of Silica: Effect on Strength, *J. Am. Ceram. Soc.* **99**(2016), 2956-63

2 Proof of swelling via crack terminating angles

2.1 Terminating angle

In earlier papers [2.1,2.2] we described a method for the identification of stresses in the surface region by the observation of crack-terminating angles of Vickers indentation cracks. The procedure was applied to chemically strengthened soda-lime glass [2.3] and surface layers after water soaking undergoing ion exchange [2.4,2.5].

The reaction eq.(1.1.1) results in a volume swelling [2.6] and since the free expansion in the thin layer is restricted in negative swelling stresses [2.7]. Such stresses at a free specimen surface must affect the crack front contours of cracks ending at these surfaces. This Section deals with the determination of shielding stress intensity factors from the terminating angles.

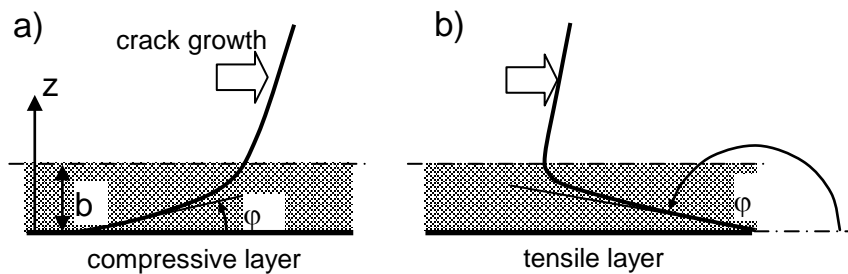


Fig. 2.1 Crack fronts terminating at the specimen surface under an angle ϕ , a) crack retard in a zone of compressive stresses, b) crack advance by tensile stresses. Arrows indicate crack growth direction.

Figure 2.1 shows a crack growing from left to right in a bar with residual stresses in thin surface layers. The crack front terminates at the free surface under an angle φ . If compressive stresses (expansive strains) occur at the surfaces, the actual crack front in a crack growth test under superimposed external load must stay behind (Fig. 2.1a). In contrast, tensile stresses caused by shrinking effects must result in an advance of the crack (Fig. 2.1b).

2.2 Stress intensity factors

The problem of a crack-front intersecting a free surface has often been studied in theoretical fracture mechanics and was also discussed in [2.1]. From curves reported in [2.8] it can be concluded that the $\frac{1}{2}$ -singularity of stresses characterizing the stress intensity factor is only possible for a crack terminating angle of

$$\varphi \cong 90^\circ - 38.8^\circ \nu \quad (2.2.1)$$

For most brittle materials with $\nu \approx 0.25$, the crack terminating angle is about $\varphi \approx 80^\circ$, i.e. deviating by 10° from the normal. For silica with $\nu = 0.17$ we have to expect: $\varphi = 83.4^\circ$, that may be abbreviated as φ_0 .

Stress intensity factors for DCDC-specimens were determined by 3-dimensional FE computations on materials with Poisson ratios in the range of $0 < \nu \leq 0.25$. In [2.1] the results were reported for $\nu = 0.25$ as fits to soda-lime glass. Similar results for the special case of silica with $\nu = 0.17$ are represented in Fig. 2.2a for crack-terminating angles of $\varphi = 45^\circ, 60^\circ, 83.4^\circ$, and 90° in form of the fracture mechanics geometric function F , defined for the DCDC-specimen by

$$F = \frac{K}{|p| \sqrt{\pi R}} \quad (2.2.2)$$

In (2.2.2) p is the pressure at the end surfaces and R is the radius of the drill hole. The FE-results are introduced as the circles. We computed stress intensity factors along the crack front for different terminating angles. For estimations on a wide range of terminating angles two theoretical limit cases were included. For $\varphi = 0$ it must hold $K(\varphi) \rightarrow \infty$ and for $\varphi = 180^\circ$: $K(\varphi) = 0$ (see e.g. Fenner and Abdul Mihsein [2.9]). The stress

intensity factors as a function of the terminating angle are given in a normalized representation in Fig. 2.2b recommended for interpolations in the region $\varphi \leq 90^\circ$.

For the applied stress intensity factor $K_{appl}(\varphi)$, the result of curve fitting reads for $\nu=0.17$ (silica)

$$\frac{K_{appl}(\varphi)}{K_{appl}(90^\circ)} \cong \frac{1}{0.00658 \varphi + 7.66 \times 10^{-13} \varphi^6} \quad (2.2.3a)$$

and for $\nu=0.225$ (soda-lime glass)

$$\frac{K_{appl}(\varphi)}{K_{appl}(90^\circ)} \cong \frac{1}{0.00606 \varphi + 8.54 \times 10^{-13} \varphi^6} \quad (2.2.3b)$$

These dependencies are shown in Fig. 2.2b as the curves together with the data points for $\nu=0.17$ as the circles.

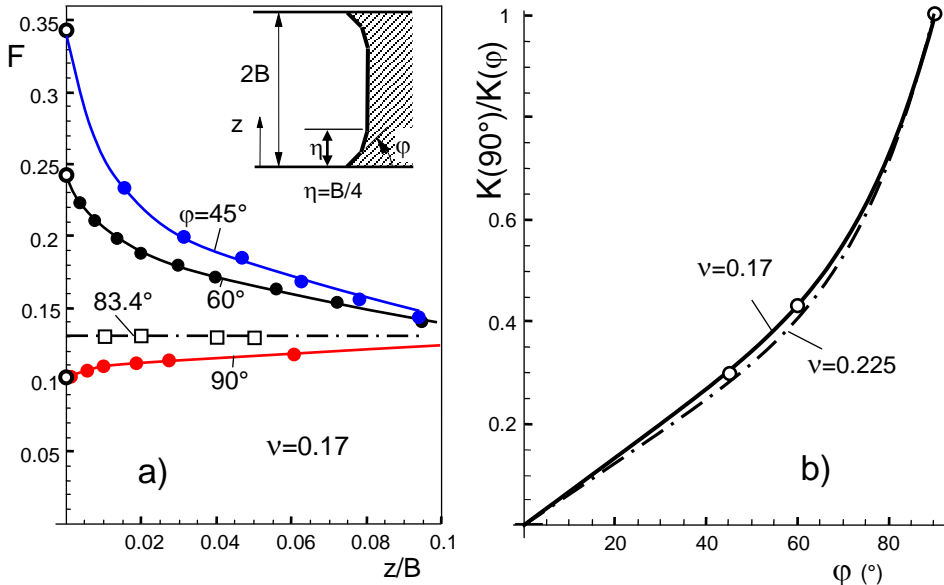


Fig. 2.2 a) Stress intensity factors in the surface region of cracks terminating under different angles φ in terms of the geometric function F according to eq.(2.2.2), b) surface stress intensity factor normalized on the value for $\varphi=90^\circ$, curves: interpolation equations (2.2.3a, 2.2.3b), circles: FE results for $\nu=0.17$.

When residual stresses are present at the surfaces at which a crack terminates, they affect the crack tip stress field by generating an additional stress intensity factor. Since for compressive stresses the crack tip is partially shielded from the externally applied stresses, it may be called “shielding” stress intensity factor, K_{sh} .

Following the superposition principle of linear-elastic fracture mechanics, the total stress intensity factor K_{tip} is the superposition of the applied one, K_{appl} , and the shielding stress intensity factor, K_{sh} .

$$K_{appl} + K_{sh} = K_{tip} \quad (2.2.4)$$

Under stable crack growth conditions, the total stress intensity factor as the sum of must equal the fracture toughness K_{Ic} . Then the terminating angle at an untoughened surface, $K_{sh}=0$, must simply fulfil $K_{tip}=K_{Ic}$. The fracture toughness of silica is at room temperature $K_{tip}=K_{Ic} \cong 0.75\text{-}0.8 \text{ MPa}\sqrt{\text{m}}$ as reported by Wiederhorn [2.10]. Under conditions of sub-critical crack growth with crack-growth rates of about 10^{-4} m/s , the stress intensity factor is roughly $K_{tip} \cong 0.57 \text{ MPa}\sqrt{\text{m}}$ [2.11] that has to be introduced on the right-hand side of eq.(2.2.4). Then it results

$$\frac{K_{appl}}{K_{tip}} = \frac{K(\varphi)}{K(\varphi_0)} \quad (2.2.5)$$

with the terminating angle φ_0 in the absence of shielding. Knowledge of terminating angles φ , φ_0 , and K_{tip} from the experiment allows the computation of K_{sh} via eqs.(2.2.4) and (2.2.5).

2.3 Experimental determination of shielding stress intensity factors

We studied crack terminating angles on DCDC-specimens [2.12] made of the silica glass EN08NB (GVB, Herzogenrath, Germany) containing 99.98% SiO_2 . DCDC-specimens were machined and annealed for 1h at 1150°C in order to remove residual stresses. Then the specimens were heat-treated in water vapour at 250°C for 92h under saturation pressure. Afterwards, fast DCDC-tests under increasing load were performed with partial

unloading for the generation of crack-arrest markings on the fracture surface. Final fracture was obtained by introducing a needle with an excessive diameter into the DCDC-hole. Figure 2.3a shows the result for a specimen without heat treatment. The terminating angle of $\varphi_0=83^\circ$, expected from eq.(2.2.1), is tentatively introduced by the straight lines showing sufficient agreement with the crack contours. A specimen tested after a 192h, 250°C vapour-treatment is given in Fig. 2.3b. This image shows clearly deviating terminating angles of only $\varphi\approx 25^\circ$ as is indicated by the straight line. In addition, we tested DCDC-specimens soaked in liquid water for 48h and 192h at 250°C.

Table 2.1 compiles the relevant test data and the experimental findings. The crack terminating angles are listed in Column 4 as the average angle. The layer thicknesses for the liquid-water soaked specimens are compiled in Column 5. The layers for the water-soaked specimens may be slightly smaller, because some dissolution of silica in water cannot be excluded. The approximation signs may indicate this. Column 6 gives the stress intensity factors for the crack extension under subcritical and spontaneous crack growth conditions.

	Test conditions	t	$\varphi(^{\circ})$	b (μm)	$K_{\text{appl},0}$ ($\text{MPa}\sqrt{\text{m}}$)	K_{appl} ($\text{MPa}\sqrt{\text{m}}$)	K_{sh} ($\text{MPa}\sqrt{\text{m}}$)
Silica	–	0	83.4	0	0.57	0.57	0
	vapour	192 h	25	17.7	“	2.94	-2.37
	liquid	48 h	41.0	≈ 8.9	“	1.77	-1.20
	liquid	192 h	29	≈ 17.7	0.8	3.44	-2.64
Soda -lime	Chem. hardened		13.5		0.75	9.16	-8.41
	water	0	107	0	0.75	0.75	0
		7 d	71	0.34		2.68	-1.93
		35 d	43	0.52		5.44	-4.69
		42 d	45	0.52		5.17	-4.42

Table 2.1 Experimental results; $K_{\text{appl},0} = K(\varphi_0)$ is the applied stress intensity factor in silica specimen without heat treatment [2.2], results on soda lime glass from measurements in [2.1].

In the case of liquid water tests for the 250°C/192h-tests, we evaluated the first crack contour as is visible after spontaneous crack propagation starting from the hole. The applied stress intensity factors K_{appl} are given in Column 7. Strongly negative shielding stress intensity factors $K_{\text{sh}} < 0$ are observed in all cases, indicating strong compressive stresses in the water diffusion layer, Column 8. In all cases, for silica as well as for soda-lime glass the materials undergo volume expansion in the water-affected surface layer. In [2.13] it is roughly shown in which way the compressive swelling stresses can be determined.

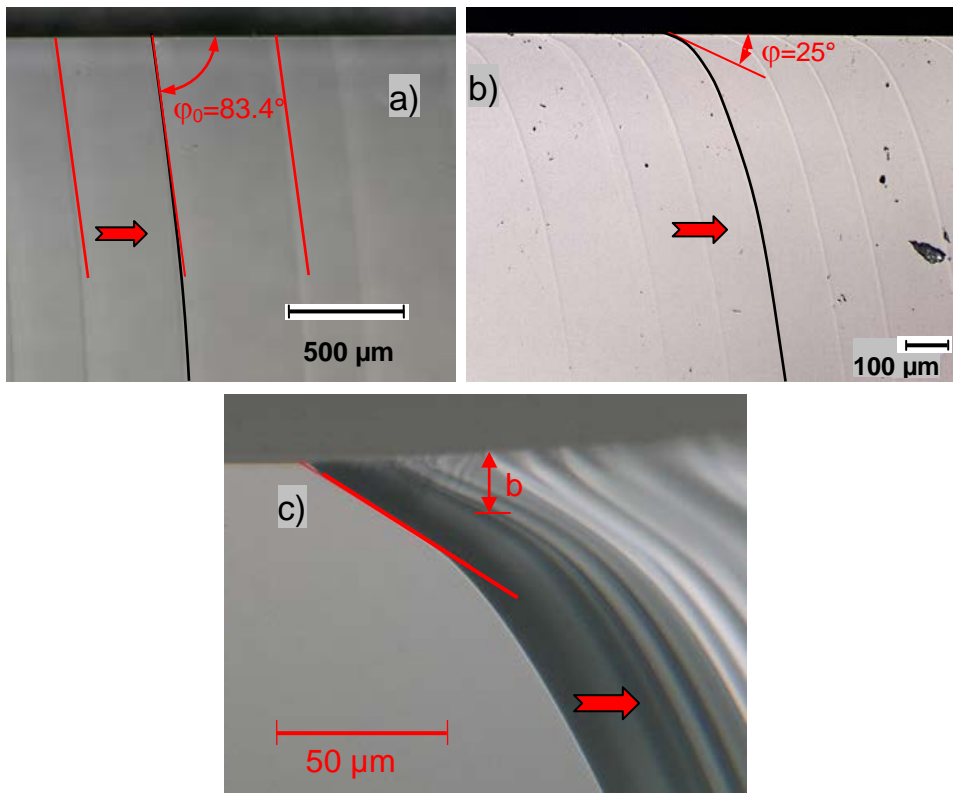


Fig. 2.3 Crack terminating angles in DCDC-specimens, a) without hot-water soaking (theoretical angles of $\varphi=83.4^\circ$ tentatively introduced as the tangents), b) after 192h, 250°C soaking in water vapour at saturation pressure, c) after 192h 250°C soaking in liquid water.; One arrest line in a) and b) stand out as black contour, crack growth direction indicated by the arrows.

References

- 2.1 K.G. Schell, S. Wagner, P. Hettich, T. Fett, G. Rizzi, M.J. Hoffmann, Identification of residual stress layers at glass surfaces via crack terminating angles, *J. Am. Ceram. Soc.* **100** (2017), 4173-4179.
- 2.2 P. Hettich, K. G. Schell, G. Rizzi, S. Wagner, T. Fett, Evaluation of crack-terminating angles in heat-treated silica DCDC-specimens, *Scientific Working Papers* **114**, 2019, ISSN: 2194-1629, Karlsruhe, KIT.
- 2.3 T. Haranoh, H. Ishikawa, N. Shinkai, M. Mizuhashi, Crack evolution in Vickers indentation for soda-lime-silica glass, *J. of Mater. Science* **17** (1982) 1493-1500.
- 2.4 W.A. Lanford, K. Davis, P. Lamarche, T. Laursen, R. Groleau, and R.H.Doremus, Hydration of Soda-Lime Glass, *J. Non-Cryst. Sol.* **33**, 249-266 (1979).
- 2.5 T. Fett, J.P. Guin, and S. M. Wiederhorn, Stresses in ion-exchange layers of soda-lime-silicate glass, *Fatigue Fract. Engng. Mater. Struct.* **28** (2005), 507-514.
- 2.6 Shelby, J.E., Density of vitreous silica, *J. Non-Cryst.* **349** (2004), 331-336
- 2.7 S. M. Wiederhorn, F. Yi, D. LaVan, T. Fett, M.J. Hoffmann, Volume Expansion caused by Water Penetration into Silica Glass, *J. Am. Ceram. Soc.* **98** (2015), 78-87.
- 2.8 Dimitrov, A., Eckensingularitäten bei räumlichen Problemen der Elastizitätstheorie: Numerische Berechnung und Anwendungen, PhD-Thesis, University of Karlsruhe, 2002.
- 2.9 Fenner, D.M., Abdul Mihsein, M.J., Crack front elastic stress state for three-dimensional crack problems, *International Journal of Fracture* **25** (1984) 121-131.
- 2.10 S.M. Wiederhorn, Fracture Surface Energy of Glass, *J. Am. Ceram. Soc.* **52** [2] 99-105 (1969).
- 2.11 S.M. Wiederhorn and L.H. Bolz, Stress Corrosion and Static Fatigue of Glass, *J. Am. Ceram. Soc.* **53**(1970) 543-548.
- 2.12 Janssen, C., Specimen for fracture mechanics studies on glass, in *Proceedings Xth International Congress on Glass*, (1974), p. 23, Kyoto, Japan.
- 2.13 P. Hettich, K. G. Schell, G. Rizzi, S. Wagner, T. Fett, Estimation of swelling stresses from crack-terminating angles, *Scientific Working Papers* **119**, 2019, ISSN: 2194-1629, Karlsruhe, KIT.

3 Effect of soaking on inert strength

3.1. Inert strength

In earlier publications [3.1-3.4], we explored the idea that water can toughen silica glass by diffusing into the glass structure from the crack tip. This process sets up a negative stress intensity factor that shields the crack tip and enhances the strength of the specimen. Because diffusion rates increase with temperature, crack tip shielding should also increase as the temperature is increased, as should the specimen strength. Using the model presented in [3.2], we explored the mechanism of crack tip shielding and showed that the calculated changes in strength resulting from water exposure at 88 °C agreed sufficiently with experimental values measured on high-silicate glass Vycor by Ito and Tomozawa [3.5], and Hirao and Tomozawa [3.6]. The effects on inert strength at this rather low soaking temperature are only about 10%. In this paper, we will address the same phenomenon, but at higher temperatures of $\theta \cong 260^\circ\text{C}$.

Strength measurements at 250°C are in principle known from literature. Li and Tomozawa [3.7] soaked silica bars for up to 4 days soaking time and tested the strengths in dynamic bending tests under subcritical crack growth conditions. To the authors' knowledge, so far no really inert strength measurements are available for water-soaked silica.

3.1.1 Water diffusion in silica

Water diffusion into the surface of silica glass has been studied experimentally by a number of investigators, and shown to depend on temperature according to

$$D_w = A_0 \exp[-Q_w / RT] \quad (3.1.1)$$

where Q_w is the activation energy, T is the absolute temperature, and R is the gas constant. As reported in reference [3.8] for silica in the temperature range 0 °C to 200 °C: $Q_w = 72.3$ kJ/mol, $\log_{10} A_0 = -8.12$ (A_0 is in m^2/s).

The diffusion distance b , an appropriate measure for the thickness of the diffusion zone (where the water concentration is roughly half of that at the surface) is given by

$$b = \sqrt{D_w t} \quad (3.1.2)$$

(t =time).

3.1.2 Volume swelling

The relation between volume swelling strain ε_v and the hydroxyl concentration S (in weight units) is given by eq.(1.1.9)

$$\varepsilon_v = \kappa \times S, \quad \kappa \cong 0.97 \quad (3.1.3)$$

The hydroxyl water S concentration can be computed from Section 4.1 in [3.9]

$$S = \frac{17}{18} \frac{0.000780 \exp(0.00868 \theta)}{\frac{1}{2} + 0.031 \exp\left(\frac{10750(\text{kJ/molK})}{RT}\right)} \quad (3.1.4)$$

A volume element near a surface that undergoes swelling cannot freely expand. If the diffusion zone is small compared to the component dimensions, expansion is completely prevented in the surface plane and can only take place normal to the surface. The swelling stress at the surface, $\sigma_{sw,0}$ is then given by eq.(1.1.11).

3.2 Total stress intensity factor for a semi-circular surface crack

As in [3.4] we begin our analysis by estimating the magnitude of the total stress intensity factor, K_{tot} , experienced by the critical crack during the strength test. The total stress

intensity factor consists of three contributions: K_{app} , which is primarily the result of the applied stresses and the geometry of the crack; K_{sh} which results from water penetration into the fresh fracture surfaces and the other surfaces of the fracture specimen. In the absence of subcritical crack growth the condition for crack extension is $K_{tot} \geq K_{Ic}$.

In order to provide a transparent analysis we restricted the possible aspect ratios of cracks to the commonly chosen semi-circular surface crack. The depth is denoted as a (Fig. 3.1) and the aspect ratio as $a/c=1$. The plane of the crack is assumed to be perpendicular to the specimen length axis.

The applied stress intensity factor given by eq.(3.2.1) and eq.(3.2.2) were derived and discussed in [3.10] for the case of straight specimen surfaces. Since the initial natural surface cracks are very small compared to the specimen thickness W , $a/W \ll 1$, it holds for the stress intensity factor at the deepest point (A)

$$K_{appl,A} = \sigma_{appl} 1.173 \sqrt{a} \quad (3.2.1)$$

and for the surface points (B)

$$K_{appl,B} = \sigma_{appl} 1.29 \sqrt{a}, \quad (3.2.2)$$

where in bending tests σ_{appl} is the outer fiber tensile stress. This solution can also be used for cylindrical specimens if the crack depth is small compared with the cylinder radius, $a/R \ll 1$. The crack is assumed to be at the midpoint of the test specimen, with one axis perpendicular to the specimen length axis and the other principal axis in the plane of the specimen surface.

As noted above, two contributions make up the shielding stress intensity factor: one coming from the diffusion zone originating from the crack faces, the second originating from the external surfaces of the specimen.

The shielding stress intensity factors at the deepest point A and the surface points B, $K_{sh,A}$ and $K_{sh,B}$, are for $b \ll R$ [3.4] and $0.15 < b/a < 1.25$

$$K_{sh,A} \cong 1.17 \sqrt{a} \sigma_{sw,0} \tanh \left(0.698 \sqrt{\frac{b}{a}} + 0.317 \frac{b}{a} \right) \quad (3.2.3)$$

$$K_{sh,B} \cong 1.29\sqrt{a}\sigma_{sw,0} \tanh\left(1.327\sqrt{\frac{b}{a}} + 0.064\frac{b}{a}\right) \quad (3.2.4)$$

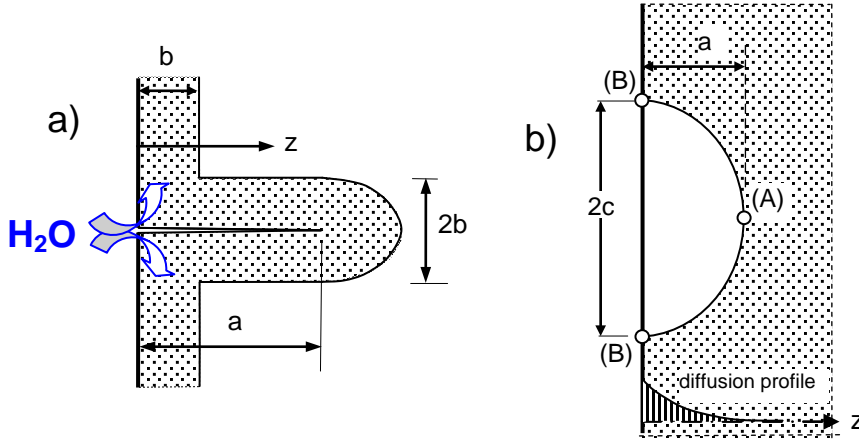


Fig. 3.1 Single failure relevant crack in a semi-infinite body exhibiting a diffusion and swelling zone, a) side view, b) top view on the crack surface.

3.3 Toughness and inert strength

3.3.1 Apparent Toughness

The total stress intensity factors including shielding are given by

$$K_{tot,A} = K_{sh,A} + K_{appl,A} \quad (3.3.1)$$

$$K_{tot,B} = K_{sh,B} + K_{appl,B} \quad (3.3.2)$$

where $K_{appl,A}$ and $K_{appl,B}$ are obtained from eq.(3.2.1) and eq.(3.2.2); $K_{sh,A}$ and $K_{sh,B}$, from eq.(3.2.3) and eq.(3.2.4). The applied stress intensity factors for inert tests have to be computed using the initial crack dimensions a_0 and c_0 .

The shielding effect is responsible for an apparent increase of the fracture toughness which is, in general, identified with the applied stress intensity factor at failure, $K_{appl,cr}$. From eqs.(3.3.1, 3.3.2) the *apparent fracture toughness*, in the following denoted as \hat{K}_{Ic} , simply results as

$$\hat{K}_{Ic} = K_{appl,cr} = K_{Ic} - K_{sh} \quad (3.3.3)$$

Since $K_{sh} < 0$, it holds $\hat{K}_{Ic} > K_{Ic}$. On the other hand it becomes clear from the fact that the inert strengths are proportional to the applied stress intensity factor, $\sigma_c \propto K_{appl,cr}$, that strength and apparent toughness increase by the same factor. In the following considerations, we therefore concentrate on the strength, exclusively. The apparent toughness for the surface points and the deepest point of a semi-circular crack is shown in Fig. 3.2a.

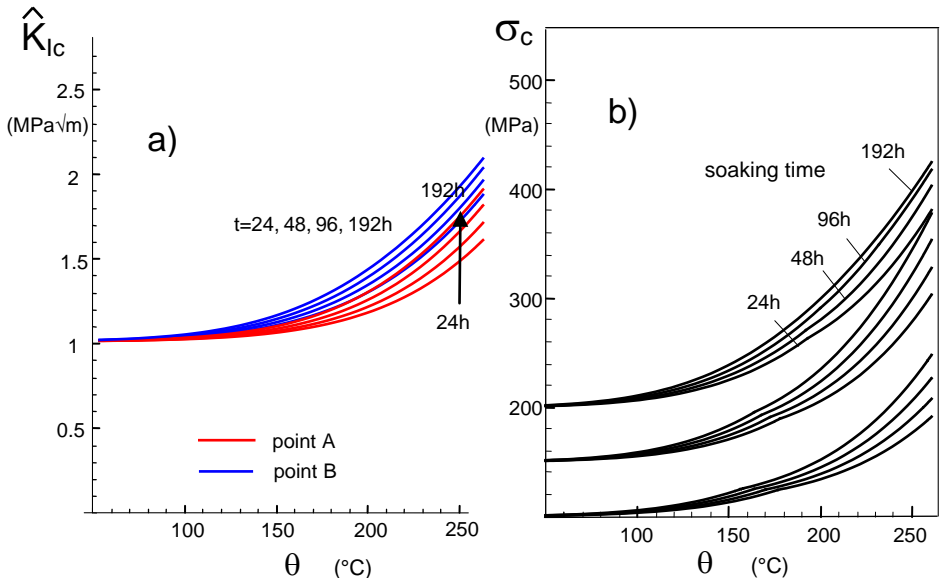


Fig. 3.2 a) Apparent fracture toughness after hot-water soaking for a semi-circular crack of 30 μ m depth, b) calculated inert strengths as a function of water-soaking temperature θ and soaking time, predicted for inert strengths of $\sigma_c = 100, 150,$ and 200 MPa for freshly abraded test specimens.

3.3.2 Inert strength

Using the temperature dependent swelling strain together with the temperature effect on the diffusivity, the inert strengths could be computed as a function of θ in the same way as outlined in [3.4]. The inert strength, σ_c , is given by the condition

$$\sigma_c = \text{Min} \left(\frac{K_{Ic} - K_{sh,A}}{1.17\sqrt{a}}, \frac{K_{Ic} - K_{sh,B}}{1.29\sqrt{a}} \right) \quad (3.3.4)$$

Strength predictions are shown in Fig. 3.2b. For this purpose initial inert strengths were assumed to be $\sigma_c=100, 150, \text{ and } 200 \text{ MPa}$.

3.4 Strength of unsoaked and soaked specimens

We studied the strength behaviour of the silica glass EN08NB (GVB, Herzogenrath) containing 99.98% SiO_2 [3.11]. Cylindrical bending bars of 45 mm length were cut from silica rods of 4 mm diameter maintaining the original surface from manufacturing. Then all specimens were annealed for 1h at 1150°C in vacuum in order to eliminate pre-existing residual surface stresses. To avoid any water contact, the series foreseen for strength measurements in an inert environment were immediately after cooling down stored in fresh silicon oil as proposed by Sglavo and Green [3.12] as an inert medium. In total, two glass deliveries were considered, denoted in the following as Batch (I) and Batch (II). The soaking conditions and surface zone parameters are given in Table 3.1.

Batch	Ref.	Time (h)	Water (°C)	Vapour (°C)	b (μm)	S (wt%)	ε_v (%)	$\sigma_{sw,0}$ (MPa)
(I)	[3.11]	192	263	-	21.7	0.85	0.82	-240
(II)	[3.13]	192	250	250	17.7	0.74	0.72	-209

Table 3.1 Soaking conditions and properties of the water layer at the surface.

Inert bending strength tests were carried out in liquid nitrogen in a 3-point testing device. The results for unsoaked specimens (open circles) are shown in Fig. 3.3a in Weibull representation. The distribution of the unsoaked specimens shows the usually expected

Weibull straight-line with a Weibull modulus of $m = 12.3$ and a characteristic strength of $\sigma_0 = 171.3$ MPa for Batch (I) both obtained by application of the Maximum Likelihood procedure [3.14]. For Batch (II) the strength distributions are shown in Fig. 3.3b. For the untreated material it was found $m = 6.6$ and $\sigma_0 = 250$ MPa. It should be noted that for Weibull-distributed initial strength values, the strength under swelling stresses cannot result in a Weibull distribution, too. The reason is due to the fact of varying apparent fracture toughness values \hat{K}_{Ic} according to eq.(3.3.3), whereas the derivation of the Weibull distribution needs a constant K_{Ic} (for details see e.g. Section 10.3 in [3.15]). The parameters derived before may be denoted as *apparent Weibull parameters*.

Even the strengths of the unsoaked specimens appear rather large. The reason for this is of course the 3-point bending loading with its reduced effective surface compared to 4-point bending tests and on the other hand the circular cross section of the specimens, that reduces the effective surface once more. The strengths could be described roughly by Weibull distributions except of Batch (I) after water soaking. Table 3.2 shows the related Weibull parameters. Since Batch (I) shows clearly deviating behaviour, the median values as the strength parameters are compiled in Table 3.3. From the strengths in the untreated state and the fracture toughness of $K_{Ic} = 0.8$ MPa \sqrt{m} [3.16], the initial crack depth a_0 can be concluded as shown in Fig. 3.4a and 3.4b.

Specimens	Batch (I)		Batch (II)	
	σ_0 (MPa)	m	σ_0 (MPa)	m
untreated	171.3	12.3	250	6.6
Water soaked	-	-	395	4.5
Vapour soaked	-	-	340	8.1

Table 3.2 Strength results, represented by the Weibull parameters.

Specimens	Batch (I)	Batch (II)
untreated	160.6 MPa	232 MPa
Water soaked	367 MPa	373 MPa
Vapour soaked	-	316 MPa

Table 3.3 Strength results, represented by the median values.

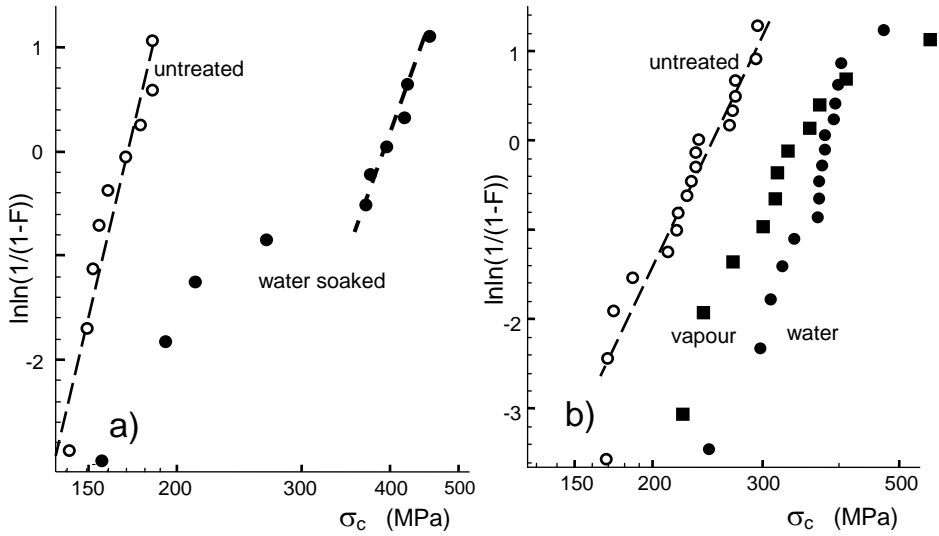


Fig. 3.3 Strength of untreated silica (open circles), liquid water treated (full circles), and vapour-treated specimens (squares), a) Batch (I), 263°C, b) Batch (II), 250°C.

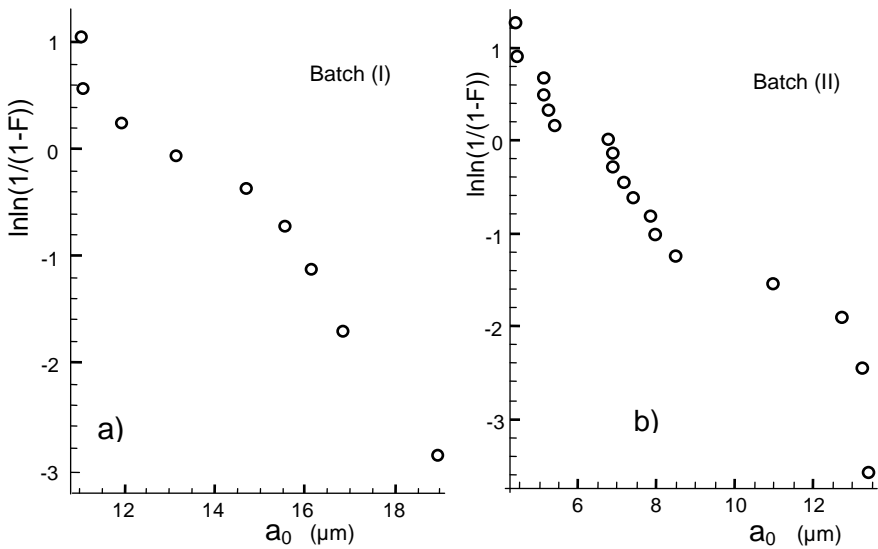


Fig. 3.4 Distributions of the initial crack depth a_0 .

3.5 Strength predictions

Measurements in liquid nitrogen showed a clear increase of the inert strength for both the water-soaked and the heat-treated specimens in saturated water vapour. The results of Fig. 3.3 are plotted once more in Fig. 3.5 together with the predictions according to eqs.(3.2.1-3.3.4).

The predictions were made on the basis of the Weibull distribution for the unsoaked specimens. First, the strength of the n^{th} specimen was computed for a total number of N specimens via

$$\sigma_n = \sigma_0 \left(\ln \frac{1}{1 - (n - 0.5) / N} \right) \quad (3.5.1)$$

For each selected specimen, the eqs.(3.2.1-3.3.4) were applied resulting in the predicted strength of soaked specimen corresponding to the same failure probability F . This procedure yields the red data in Fig. 3.5. The red arrows stand for the strength increase.

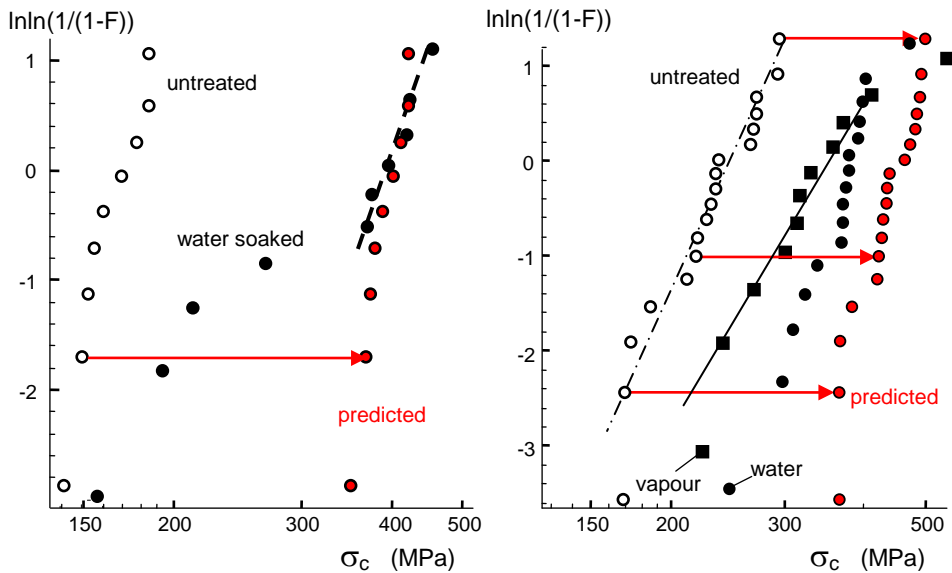


Fig. 3.5 Measured strengths (solid circles and squares) and predictions by the shielding stress intensity factor (red circles).

In the case of Batch (I), the lowest four strength data after soaking obviously differ clearly from the prediction showing typical features of a bimodal strength distribution. Due to their high strengths, the soaked specimens shattered in more than two fracture pieces (mostly 4-6 fragments). Therefore, it was not possible to carry out a fractographic study on the broken test pieces.

3.6 Analysis of nonlinear strength distributions

In the following considerations on Batch (I), it is assumed that the soaked specimens exhibit a bimodal strength distribution caused by competing of two different strength populations. Then the Weibull distributions of the strength populations “1” and “2” are given by

$$F_1 = 1 - \exp \left[- \left(\frac{\sigma_c}{\sigma_{01}} \right)^{m_1} \right] \quad (3.6.1)$$

and

$$F_2 = 1 - \exp \left[- \left(\frac{\sigma_c}{\sigma_{02}} \right)^{m_2} \right] \quad (3.6.2)$$

with the two different characteristic strengths σ_{01} and σ_{02} and the related Weibull exponents m_1 and m_2 . Superposition of these strength results in the total failure probability (for details see e.g. Section 8 in [3.15])

$$F = F_1 + F_2 - F_1 F_2 = 1 - \exp \left[- \left(\frac{\sigma_c}{\sigma_{01}} \right)^{m_1} - \left(\frac{\sigma_c}{\sigma_{02}} \right)^{m_2} \right] \quad (3.6.3)$$

The Weibull parameters obtained by curve-fitting according to eq.(3.6.3) are compiled in Table 3.4. The curve fit according to eq.(3.6.3) is introduced in Fig. 3.6 by the solid curve. The dash-dotted straight lines give the asymptotes representing the individual strength populations.

The predicted strength made by using the shielding stress intensity factor is close to the measured ones of “population 1”.

Strength population “1”		strength population “2”	
m_1	σ_{01} (MPa)	m_2	σ_{02} (MPa)
21.4	437.5 [404, 471]	2.7	394 [306, 482]

Table 3.4: Weibull parameters for the water-soaked specimens of Batch (I), 90% CI in brackets.

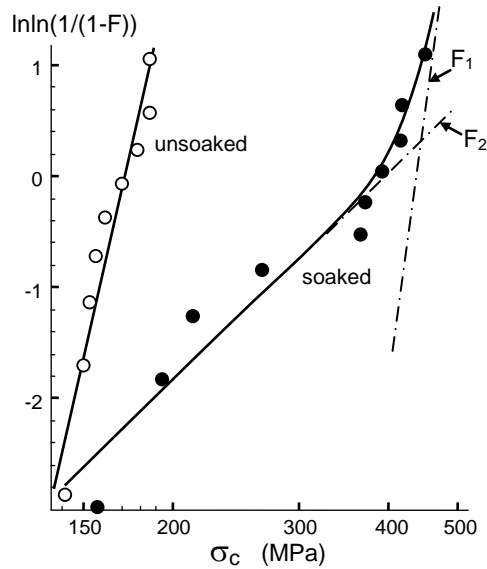


Fig. 3.6 Tessellation of the strengths for the hot water soaked specimens in two strength distributions.

3.7 A possible reason for the bimodal strength distribution

From the nearly linear shape of the strength distribution of unsoaked specimens in the Weibull plot, it can be concluded that for these results the initial cracks responsible for failure were Weibull distributed, too. The bimodal strength distribution of the soaked specimens calls for an interpretation by a bimodal distribution of the failure relevant flaws. In order to discuss the observed curve shape, let us assume coexistence of the sur-

face defects (cracks) and inner flaws (pores) as schematically illustrated in Fig. 3.7a. The blue line indicates the strengths for the surface cracks, whereas the red line gives the strengths for the inner flaws.

Under normal circumstances, the specimens will fail at the surface, because the strength is lowest there. Failure starting from internal defects is very seldom. This is possible only when the two curves intersect at a very small failure probability F .

Due to soaking, the surface is strengthened by swelling stresses. Consequently, the blue line shifts to higher strength values as indicated by the arrow in Fig. 3.7b. The defects below the surface zone of about $20\mu\text{m}$ remain unaffected and can cause failure. The measurable strength is the minimum of the shifted blue and the red line. This results in the kinked black curve as found in our measurements. Since no fractographic examination of the fracture surface was possible for the specimen fractured in liquid nitrogen, we inspected the specimens for internal flaws with a confocal microscope. Figure 3.8 shows subsurface defects that cannot be introduced by handling of the specimens. Their radii are about $5\text{-}10\mu\text{m}$. At least by this inspection technique we can confirm the existence of internal flaws competing with the surface defects on the lateral surface.

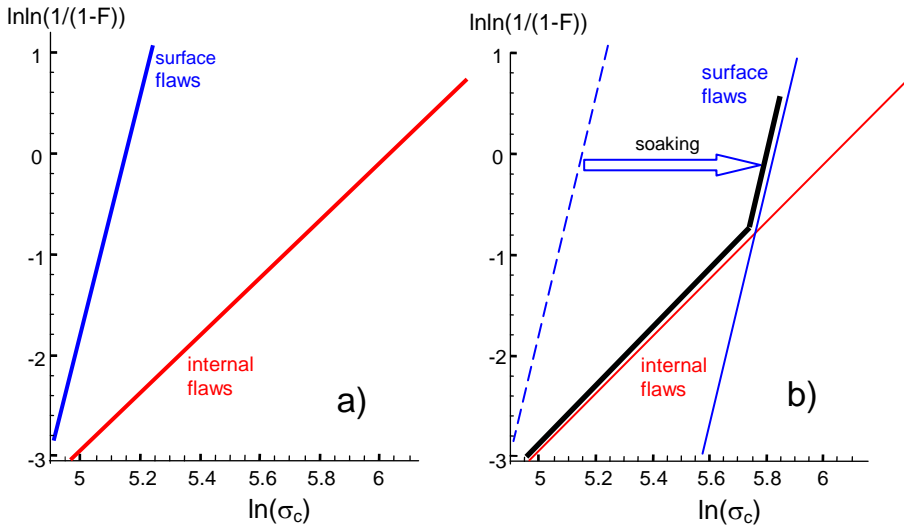


Fig. 3.7 a) Strength for failure starting at the surface flaws and at inner defects, b) shift of the surface strength by soaking resulting in a bimodal strength curve.

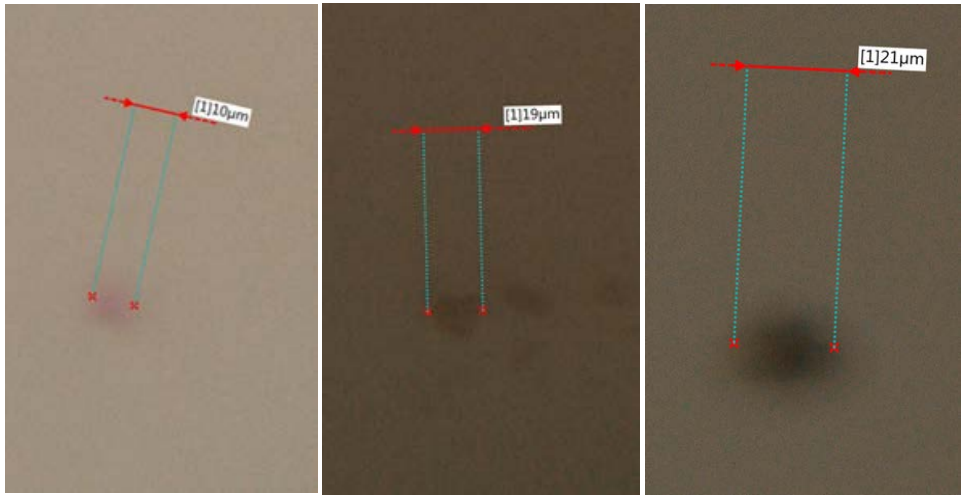


Fig. 3.8 Images of subsurface defects obtained with a confocal microscope.

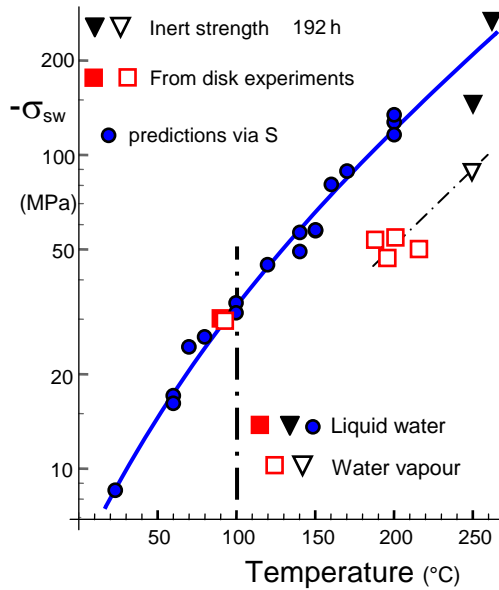


Fig. 3.9 Results of disk tests ([3.17] and Section 2 in [3.9]) and from inert strength measurement in liquid water and vapour under saturation pressure, compared with predictions based on hydroxyl concentrations in liquid water.

Finally, Fig. 3.9 shows the shielding stresses from inert bending strength measurements together with the predictions via S . The strengths for water soaked specimens are only slightly above the prediction and the strength with possibly internal failures somewhat below the predictions. The data point for the vapour-tests clearly falls below the prediction as was found already for the evaluation of crack-terminating angles in Section 2.

References

- 3.1 S.M. Wiederhorn, T. Fett, G. Rizzi, S. Fünfschilling, M.J. Hoffmann and J.-P. Guin, Effect of Water Penetration on the Strength and Toughness of Silica Glass, *J. Am. Ceram. Soc.* **94** (2011) [S1], 196-203.
- 3.2 S.M. Wiederhorn, T. Fett, G. Rizzi, M.J. Hoffmann and J.-P. Guin, The Effect of Water Penetration on Crack Growth in Silica Glass, *Engng. Fract. Mech.* **100** (2013), 3-16.
- 3.3 S.M. Wiederhorn, T. Fett, G. Rizzi, M. Hoffmann, J.-P. Guin, Water Penetration – its Effect on the Strength and Toughness of Silica Glass, *Met. Mater. Trans. A*, **44**(2013) [3], 1164 -1174.
- 3.4 T. Fett, G. Rizzi, M. Hoffmann, S. Wagner, and S.M. Wiederhorn, Effect of Water on the inert Strength of Silica Glass: Role of Water Penetration, *J. Am. Ceram. Soc.* **95**(2012) [12], 3847-3853.
- 3.5 S. Ito and M. Tomozawa, Crack Blunting of High-Silica Glass, *J. Am. Ceram. Soc.* **65**(1982) [8], 368-371.
- 3.6 K. Hirao and M. Tomozawa, Dynamic Fatigue of Treated High-Silica Glass: Explanation by Crack Tip Blunting, *J. Am. Ceram. Soc.* **70**(1987) [6], 377-82.
- 3.7 H. Li and M. Tomozawa, Mechanical strength increase of abraded silica glass by high pressure water vapor treatment, *J. Non-Cryst. Solids* **168**(1994), 287-292.
- 3.8 Zouine, A., Dersch, O., Walter, G., Rauch, F., Diffusivity and solubility of water in silica glass in the temperature range 23-200°C, *Phys. Chem. Glasses*, **48** (2007), 85-91.
- 3.9 T. Fett, G. Rizzi, K.G. Schell, E.C. Bucharsky, P. Hettich, S. Wagner, M. J. Hoffmann, Consequences of hydroxyl generation by the silica/water reaction Part I: Diffusion and Swelling, KIT Scientific Publishing, Karlsruhe.
- 3.10 J.C. Newman and I.S. Raju, An empirical stress intensity factor equation for the surface crack, *Engng. Fract. Mech.* **15**, 185-192, (1981).

- 3.11 S. Wagner, B. Hohn, D. Creek, M. J. Hoffmann, G. Rizzi, S. M. Wiederhorn, T. Fett, Inert strength measurement on hot water soaked silica, *Scientific Working Papers* **19**, 2014, ISSN: 2194-1629, Karlsruhe, KIT.
- 3.12 V.M. Sglavo and D.J. Green, Fatigue limit in fused silica, *J. Eur. Ceram. Soc.* **21** (2001) 561-567.
- 3.13 P. Hettich, S. Wagner, G. Schell, T. Fett, Inert strength measurement on silica soaked at 250°C in liquid water and water vapour, *Scientific Working Papers* **122**, 2019, ISSN: 2194-1629, Karlsruhe, KIT.
- 3.14 Lawless, J.F. (1982): *Statistical Models and Methods for Lifetime Data*, Wiley, New York.
- 3.15 Munz, D., Fett, T., *Ceramics: Mechanical Properties, Failure Behaviour, Materials Selection*, Springer-Verlag (1999).
- 3.16 S.M. Wiederhorn, Fracture Surface Energy of Glass, *J. Am. Ceram. Soc.*, **52**[2], (1969), 99-105.
- 3.17 S. M. Wiederhorn, F. Yi, D. LaVan, T. Fett, M.J. Hoffmann, Volume Expansion caused by Water Penetration into Silica Glass, *J. Am. Ceram. Soc.* **98** (2015), 78-87.

4 Strength in silicon oil, humid air and water

4.1 Strength measurements on silica

Very often strength measurements are carried out in humid environments. This may lead to subcritical crack growth effects on strength. In this Section the effect of swelling stresses on strength is discussed for subcritical crack growth conditions. An interesting effect is the occurrence of discontinuities in the load-displacement curves for strength tests performed in silicone oil as is generally assumed to be an inert environment, preventing the access of water to the crack tip [4.1].

Strengths were measured on silica glass EN08NB (GVB, Herzogenrath) containing 99.98% SiO₂. Bars 3×4×45 mm³ were cut out of a plate 350×350×4 mm³ and surface machined by grinding with a grinding wheel, D91-C75. To eliminate residual surface stresses introduced by grinding, we annealed our specimens in vacuum for 1h at 1150°C. The series for strength measurements in an inert environment was immediately stored in fresh silicon oil as an inert medium after cooling to room temperature, following the procedure of Sglavo and Green [4.2]. In our tests, we used the original silicon oil (Wacker AK 100, Wacker-Chemie AG, München), without an additional drying procedure. Each test series was carried out with fresh oil.

Four-point bending strength tests with the normal rectangular bending bars were made in silicone oil, as recommended by Sglavo and Green [4.2]. These investigators dried silica glass rods at 120°C for 2h before being completely immersed and fractured in a silicone oil bath. This procedure was considered in [4.2] to be an inert environment, preventing the access of water to the crack tip.

In all the tests the loading rate was 50N/s (42 MPa/s) resulting in test durations of 2-3 seconds. The average strength of 15 tests, resulted in $\sigma_c=103.5$ MPa (SD 9.2 MPa). Under the assumption of half-penny shaped initial cracks, the average depth a_0 of the

introduced crack during grinding, can be calculated from K_{Ic} and the measured strength, σ_c .

$$a_0 = \left(\frac{K_{Ic}}{\sigma_c Y} \right)^2 \quad (4.1.1)$$

By using $Y \cong 1.3$ and $K_{Ic} = 0.8 \text{ MPa}\sqrt{\text{m}}$ we obtain $a_0 = 35 \text{ }\mu\text{m}$.

Two series of specimens were then soaked for 24h in liquid water at 250°C in an autoclave. Drying the specimens in vacuum removed surface moisture. After 2 days of drying at 60°C in vacuum, the average strength in silicon oil was found to be $\sigma_c = 119.7 \text{ MPa}$ (SD 9.9 MPa).

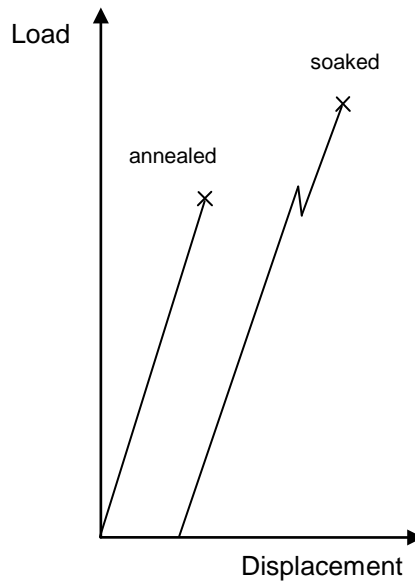


Fig. 4.1 Load displacement plots in silicon oil. The water-soaked specimens showed a load pop-in that was missing in the tests on unsoaked bars.

The load-displacement curves obtained in the strength tests in silicon oil were completely different from those obtained from the specimens that were not exposed to saturated steam at 250°C . Only the unexposed annealed specimens showed the usual straight displacement versus load behaviour until failure. All specimens exposed to water at

250 °C showed pop-ins as schematically indicated in Fig. 4.1, accompanied by clearly audible cracking noise. The fracture surface of one such test specimen is shown in Fig. 4.2a and Fig. 4.2b. Figure 4.2b represents the fracture origin. At this magnification, the initial crack of depth $a \approx 31 \mu\text{m}$ is clearly visible. The same holds for the increased crack after the load pop in.

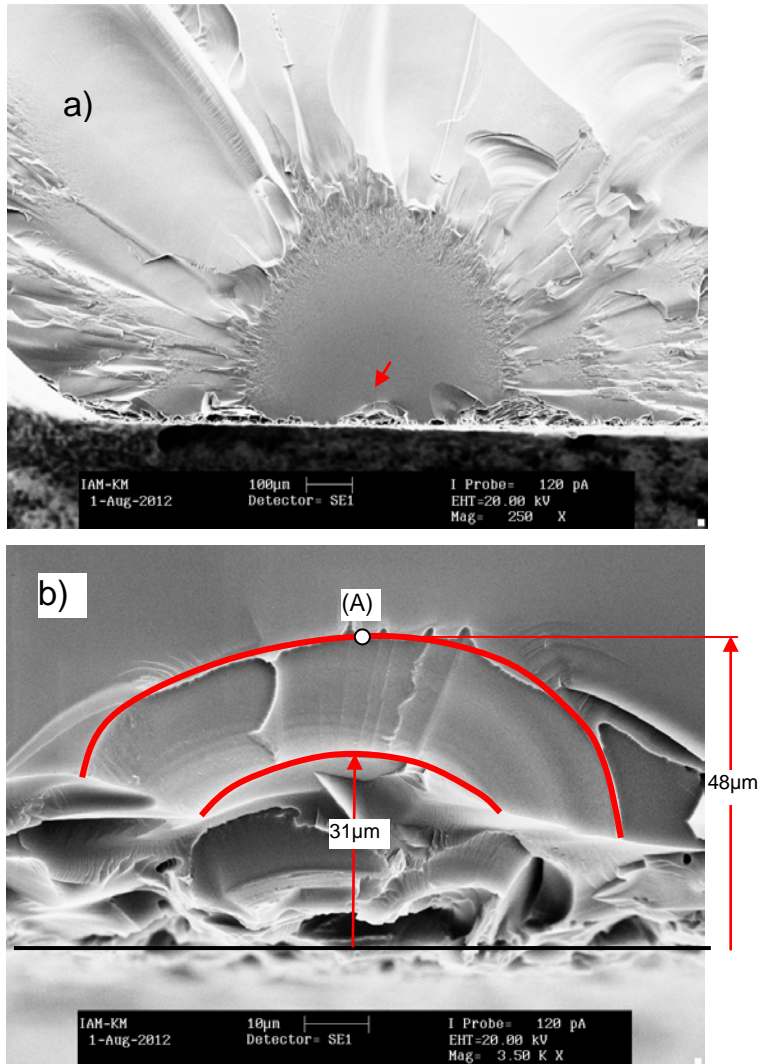


Fig. 4.2 Fracture surface of a water-soaked specimen measured in silicon oil, a) overall view, b) identification of the initial crack size $a_0 \approx 31 \mu\text{m}$ and the extended crack after the pop-in ($a = 48 \mu\text{m}$).

The arrest contour gives a new depth of 48 μm from which later final fracture starts. The crack ends at the surface are not visible, therefore the evaluation is limited here to the deepest points of the cracks, represented by semi-circular surface cracks, $a/c=1$.

The stress intensity factors related to the failure stress can be computed via FE-results of Newman and Raju [4.3]. Since the initial natural surface cracks are very small compared to the specimen thickness W , $a/W \ll 1$, the solution holds for the stress intensity factor at the deepest point (A) of the semi-circle:

$$K_{\text{appl},A} = \sigma_{\text{appl}} 1.173\sqrt{a} \quad (4.1.2)$$

From the strength of $\sigma_f = 119.7 \text{ MPa}$ and the outer crack contour $a_c = 48 \mu\text{m}$ at which catastrophic failure starts, we obtain $K_{\text{appl},A} = 0.97 \text{ MPa}\sqrt{\text{m}}$, that is slightly above the fracture toughness of $K_{\text{Ic}} = 0.8 \text{ MPa}\sqrt{\text{m}}$ [4.4]. This results in a shielding term at the deepest point of the critical crack of $K_{\text{sh}} = 0.97 - 0.8 = -0.17 \text{ MPa}\sqrt{\text{m}}$.

The applied stress intensity factor at which the crack extended from its original depth of $a_0 \cong 31 \mu\text{m}$ occurred at about 80-85% of the strength, i.e. at the stress where the load pop-in was observed. This results in an applied stress intensity factor of $K_{\text{appl},A} \approx 0.61\text{-}0.63 \text{ MPa}\sqrt{\text{m}}$ that is clearly below K_{Ic} . Consequently, crack extension from a_0 to a_c must be caused by subcritical crack growth. The fracture behaviour, Fig. 4.2b, will be addressed below in the discussion Section 4.2.

4.2 Pop-in behaviour

4.2.1 Subcritical crack growth in silicon oil tests

Measurements in silicon oil resulted in real inert strengths only in the case of the annealed un-soaked specimens. In strength tests on soaked specimens, also carried out in silicon oil, we found clear evidence for the occurrence of subcritical crack growth, even though the environment had prevented any water supply.

Now let us look for a water source in the absence of any supply from the environment. Water that diffused into silica during the water soaking procedure reacts with the silica network according to eq.(1.1.1). For 250 °C, the ratio S/C is about 2.7. From Fig. 4.4a in

[4.5] we get by a slight temperature extrapolation to 250°C a *total water* concentration at the surface of $C_w \approx 0.7$ wt-percent. Consequently, the surface concentration is $C \approx 0.3$ wt-% of *molecular* H_2O . This shows that molecular water, necessary for bond splitting during subcritical crack growth is in the soaked specimens always available ahead a crack tip. The distribution of molecular water after 24h soaking at 250°C is illustrated in Fig. 4.3. Under these soaking conditions it results from eqs.(3.1.1) and (3.1.2): $b = 6.3 \mu\text{m}$ shown in Fig. 4.3 by the dashed contour. The C -profile along the x -axis as the prospective crack plane is concluded from FE-results in [4.6]. The content of molecular water is negligible for $x > 3b$.

For strength tests in water, the cracks grow also strongly accelerated due to the effect of escaping from the initial swelling zone (Section A1 in [4.5]). However, in contrast to the silicon oil tests, there is now no crack arrest possible since water is always available to the advancing crack tip. Consequently, in these tests accelerated cracking is directly followed by final fracture without any further increase of loading necessary. The pop-in is therefore missing.

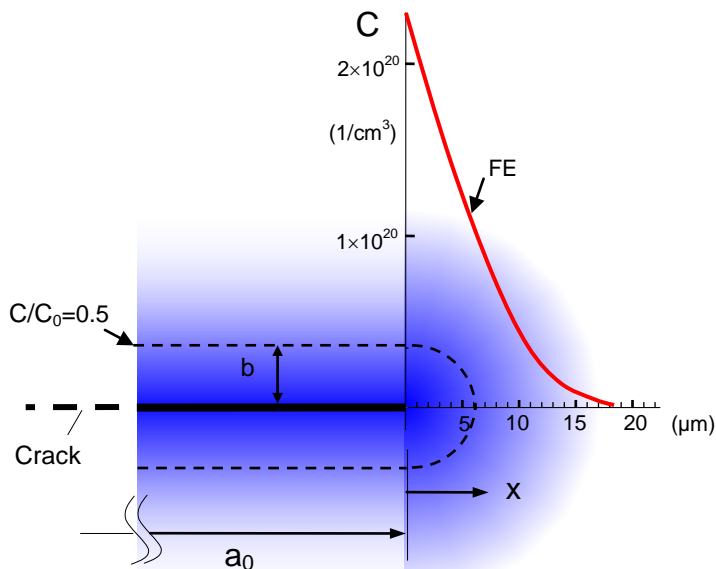


Fig. 4.3 Distribution of molecular water in the surrounding of a crack tip after 24h water soaking at 250°C .

4.2.2 Interpretation of crack extension accompanied by load pop-ins

A side-view of the semi-circular surface crack is shown in Fig. 4.4a. From all surfaces which are in contact with water vapour during high-temperature soaking, water diffuses into silica. This holds also for crack surfaces. For reasons of transparency in the computation of the shielding stress intensity factor these contours are approximated by a zone of constant thickness b ending in a half-circle.

If the crack grows under increasing load by an amount of Δa , it will escape from the initial swelling zone, as illustrated by the dashed crack extension. The related shielding stress intensity factor is schematically plotted in Fig. 4.4b as a function of crack propagation Δa . When $\Delta a=b$ is reached and the crack tip leaves the swelling zone, the shielding stress intensity factor strongly decreases as was shown in [4.7] for ion-exchange layers in soda-lime glass. Superposition of the applied stress intensity factor $K_{\text{appl}} \propto \sqrt{a}$ (dashed curve in Fig. 4.4c) and the shielding stress intensity factor K_{sh} results in the total stress intensity factor $K_{\text{total}}=K_{\text{tip}}$ as given by eq.(3.3.1).

The development of K_{tip} with increasing crack length, $a_0+\Delta a$, and increasing load is schematically shown in Fig. 4.4c by the solid curve. Under increasing load the first positive total stress intensity factor, $K_{\text{min}}=-K_{\text{sh}}$, is reached at $\Delta a=0$ for the curve indicated by $\sigma_{f,\text{min}}$ which is the minimum possible strength in a dynamic strength tests

$$\sigma_{f,\text{min}} = \frac{-K_{\text{sh}}}{1.17\sqrt{a_0}} \quad (4.2.1)$$

From the shape of the $K_{\text{tip}}-\Delta a$ -curve, it is evident that a crack extension by subcritical crack growth must accelerate rapidly in the region where K_{tip} increases rapidly, namely at $\Delta a \geq b$.

On the other hand, we have to take into consideration the fact that simultaneously with the loss of shielding also the available water for subcritical crack growth disappears after a crack extension of about $\Delta a \approx b$. This results in an abruptly arresting crack so far $K_{\text{tip}} < K_{\text{Ic}}$. Final cracking can occur only after a sufficient increase of the loading. This trivially must result in the observed load-displacement curve of Fig. 4.1.

4.2.3 Interpretation of the shielding stress intensity factor

The shielding stress intensity factor at the deepest point of a semi-circular surface crack soaked from the side surface and the crack surfaces, Fig. 4.4a, is given by [4.8]

$$K_{sh,A} \cong -1.17\sqrt{a} \frac{\varepsilon_v E}{3(1-\nu)} \tanh\left(0.698\sqrt{\frac{b}{a}} + 0.317\frac{b}{a}\right) \quad (4.2.2)$$

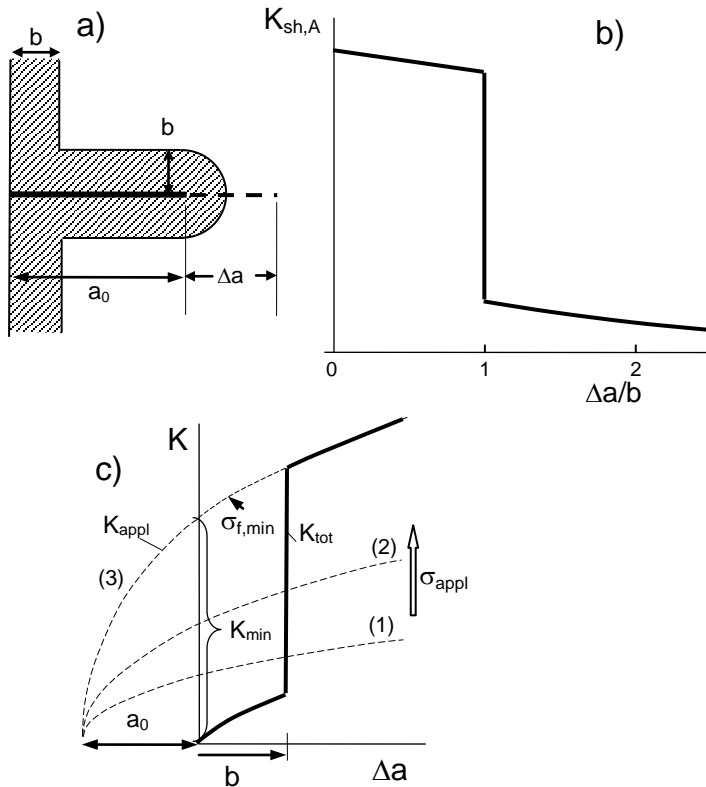


Fig. 4.4 a) Crack propagating out of the initial swelling zone, b) shielding stress intensity factor during crack escape, c) increase of the total stress intensity factor K_{tot} during crack growth for three applied loads (schematic). Below the applied stress $\sigma_{appl} = \sigma_{f,min}$ defining a lower limit for measurable strengths, no subcritical crack growth is possible because of $K_{tot} < 0$.

For the crack with depth of $a = 48 \mu\text{m}$ and a volume strain at 250°C of $\varepsilon_v = 0.722\%$ given by eq.(3.1.4), it results from (4.2.2) with $E = 72 \text{ GPa}$ and $\nu = 0.17$:

$$K_{sh} = -0.48 \text{ MPa}\sqrt{\text{m}} \quad (4.2.3)$$

From the experiment we found a shielding term at the deepest point of the critical crack of only $K_{sh} \cong -0.17 \text{ MPa}\sqrt{\text{m}}$, i.e. 36% of the expected result, eq.(4.2.3). The reason is rather trivial. Equation (4.2.2) holds for a crack of depth a_0 that is fully surrounded by the swelling zone as is schematically shown in Fig. 4.4a.

Two contributions make up the shielding stress intensity factor. One is coming from the diffusion zone originating from the crack faces, $K_{sh,1}$, the second originating from the external surfaces of the specimen, $K_{sh,2}$.

For a transparent interpretation, let us apply the K -separation according to [4.8]. The total shielding stress intensity factor is the sum

$$K_{sh} = K_{sh,1} + K_{sh,2} \quad (4.2.4)$$

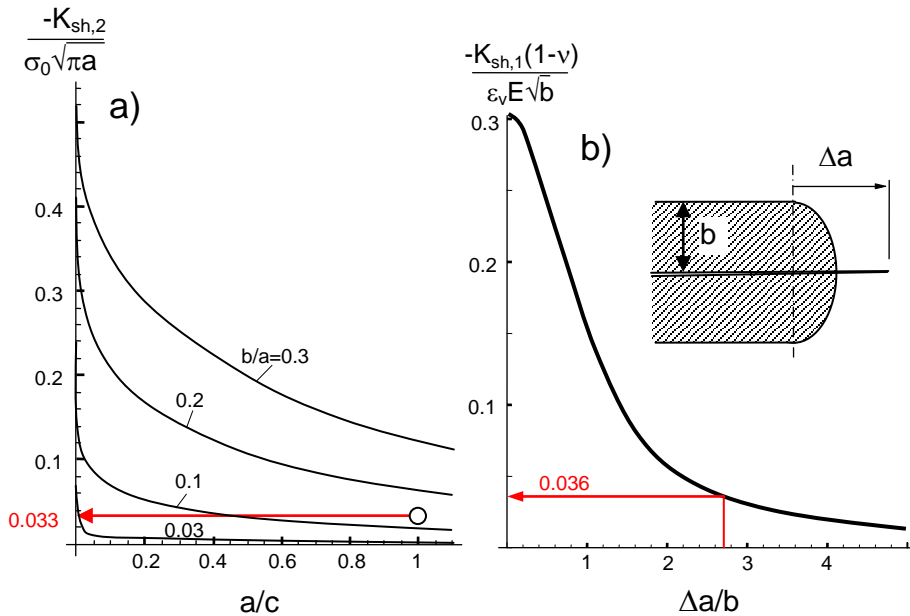


Fig. 4.5 a) Influence of aspect ratio a/c and relative depth of the swelling zone b/a on the shielding stress intensity factors K_{sh} at the deepest point of a semi-elliptical surface crack [4.8], b) shielding stress intensity factor $K_{sh,1}$ for a crack growing out of the initial swelling zone, [4.9].

The stress intensity factor by the side surface is shown in Fig. 4.5a as a function of b/a and the crack aspect ratio a/c ($2c$ =width of the crack). In our case results for $a/c=1$ and $b/a=6.3\mu\text{m}/48\mu\text{m}=0.13$ (circle in Fig. 4.5a) with $\sigma_{\text{sw}}=-210$ MPa:

$$K_{\text{sh},2} = -0.0844 \text{ MPa}\sqrt{\text{m}}.$$

When the crack can grow subcritically by an amount of Δa , it will escape from the initial swelling zone, as illustrated in Fig. 4.5b. The stress intensity factor $K_{\text{sh},1}$ for the swelling zone developing from the crack faces, is shown in Fig. 4.5b as given in [4.9], Fig. I5.6.

The shielding stress intensity factor $K_{\text{sh},1}$ for an extension of $\Delta a=48\mu\text{m}-31\mu\text{m}=17\mu\text{m}$ and $\Delta a/b=2.7$ decreases (red arrow in Fig. 4.5b) to a normalized stress intensity factor of 0.036. Consequently, it results

$$K_{\text{sh},1} = -0.036 \frac{\varepsilon_v E}{1-\nu} \sqrt{b} = -0.0566 \text{ MPa}\sqrt{\text{m}} \quad (4.2.5)$$

The total shielding term after $17\mu\text{m}$ crack extension results from eq.(4.2.4) as

$$K_{\text{sh}} = -0.0566 \text{ MPa}\sqrt{\text{m}} - 0.0844 \text{ MPa}\sqrt{\text{m}} = -0.141 \text{ MPa}\sqrt{\text{m}}$$

This is about 83% of the experimental value of $-0.17 \text{ MPa}\sqrt{\text{m}}$.

References:

-
- 4.1 H. Li and M. Tomozawa, Mechanical strength increase of abraded silica glass by high pressure water vapor treatment, *J. Non-Cryst. Solids* **168**(1994), 287-292.
 - 4.2 V.M. Sglavo and D.J. Green, Fatigue limit in fused silica, *J. Eur. Ceram. Soc.* **21** (2001) 561-567.
 - 4.3 J.C. Newman and I.S. Raju, An empirical stress intensity factor equation for the surface crack, *Engng. Fract. Mech.* **15**, 185-192, (1981).
 - 4.4 S.M. Wiederhorn, Fracture surface energy of glass, *J. Am. Ceram. Soc.* **52** (1969), 99-105.

- 4.5 T. Fett, G. Rizzi, K.G. Schell, E.C. Bucharsky, P. Hettich, S. Wagner, M. J. Hoffmann, S.M. Wiederhorn, Consequences of hydroxyl generation by the silica/water reaction Part I: Diffusion and Swelling, KIT Scientific Publishing, Karlsruhe.
- 4.6 S.M. Wiederhorn, T. Fett, G. Rizzi, M. Hoffmann, J.-P. Guin, Water Penetration – its Effect on the Strength and Toughness of Silica Glass, *Met. Mater. Trans. A*, **44**(2013) [3], 1164 -1174.
- 4.7 Fett, T., Guin, J.P., Wiederhorn, S.M., Interpretation of effects at the static fatigue limit of soda-lime-silicate glass, *Engng. Fract. Mech.* **72**(2005), 2774-279.
- 4.8 T. Fett, G. Rizzi, M. Hoffmann, S. Wagner, and S.M. Wiederhorn, Effect of Water on the inert Strength of Silica Glass: Role of Water Penetration, *J. Am. Ceram. Soc.* **95**(2012) [12], 3847-3853.
- 4.9 T. Fett, New contributions to R-curves and bridging stresses – Applications of weight functions, IAM 3, KIT Scientific Publishing, 2012, Karlsruhe.

5 Effect of swelling on dynamic strength

5.1 Dynamic strength

In Section 3 we considered the effect of volume swelling by hydroxyl generation on the *inert strength* of hot-water soaked silica. The strength behaviour was discussed on the basis of the total water concentrations from Zouine *et al.* [5.1] and Wiederhorn *et al.* [5.2]. The hydroxyl concentration at silica surfaces is time dependent as can be seen from the studies by Davis and Tomozawa [5.3] and Oehler and Tomozawa [5.4].

Very often strength measurements are carried out in humid environments. This leads to subcritical crack growth effects on strength. In this Section, the effect of swelling stresses on strength is discussed for subcritical crack growth conditions according to [5.5]. Special attention will be drawn on the evaluation of the power law exponent n for subcritical crack growth as had very early been developed for glass by Charles [5.6].

For strength tests carried out in humid environment at various loading rates, so-called dynamic strength tests, one can show theoretically that the swelling effect caused by the reaction of water with silica must result in apparently increased crack-growth exponents.

5.2 Computation of dynamic strength for edge-crack like defects

5.2.1 Surface defects modeled by edge cracks

The most transparent description of crack-growth problems can be given by using a solution for one-dimensional edge cracks. Under an applied remote stress σ_{app} the related applied stress intensity factor is

$$K_{appl} = 1.122\sqrt{\pi a} \sigma_{appl} \quad (5.2.1)$$

The shielding stress intensity factor for an edge crack of depth a is derived in Section A1.5 in [5.7] based on results in [5.8]

$$K_{sh} \cong 1.122\sqrt{\pi a} \sigma_{sw,0} \tanh^{3/2} \left(\left[0.385\sqrt{\frac{b}{a}} + 0.832\frac{b}{a} \right]^{2/3} \right) \quad (5.2.2)$$

with the thickness of the swelling zone b given by eq.(3.1.2) and the swelling stress $\sigma_{sw,0}$ at the surface. The crack-tip stress intensity factor results by superposition of the applied and shielding stress intensity factors:

$$K_{tip} = K_{appl} + K_{sh}, \text{ where } K_{sh} < 0 \quad (5.2.3)$$

5.2.2 Cracks fully embedded in the swelling zone

If the crack is *fully embedded* in the swelling stress zone, *i.e.*, if $a \ll b$, it results from eqs.(5.2.1 – 5.2.3):

$$K_{tip} = 1.122(\sigma_{appl} + \sigma_{sw,0})\sqrt{\pi a}. \quad (5.2.4)$$

Let us describe the subcritical crack growth rate, v , by a power law relation

$$v = \frac{da}{dt} = AK_{tip}^n = A(K_{appl} + K_{sh})^n \quad (5.2.5)$$

In the absence of swelling, $\sigma_{sw,0} = 0$ and $K_{sh} = 0$, the following well-known equation holds (see e.g. [5.9]):

$$\sigma_{f,0}^{n+1} = B\sigma_{c,0}^{n-2} \dot{\sigma}(n+1), \quad B = \frac{2K_{Ic}^{2-n}}{1.122^2 \pi A(n-2)}. \quad (5.2.6)$$

where $\sigma_{c,0}$ is the inert strength, the strength in the absence of subcritical crack growth. In presence of swelling stress $\sigma_{sw,0}$, we obtain the following equations:

$$(\sigma_f + \sigma_{sw,0})^{n+1} = B\sigma_c^{n-2} \dot{\sigma}(n+1) \quad (5.2.7)$$

$$\sigma_f = \underbrace{(B\sigma_c^{n-2}(n+1))^{1/(n+1)} \dot{\sigma}^{1/(n+1)}}_{\sigma_{f,0}} - \sigma_{sw,0} \quad (5.2.8)$$

$$\Rightarrow \sigma_f = \sigma_{f,0} - \sigma_{sw,0} \quad (5.2.8a)$$

The *inert strength* is in soaked specimens

$$\sigma_c = \frac{K_{lc} - K_{sh}}{1.122\sqrt{\pi a_0}} \quad (5.2.9)$$

and in un-soaked specimens it holds

$$\sigma_{c,0} = \frac{K_{lc}}{1.122\sqrt{\pi a_0}} \quad (5.2.10)$$

where a_0 is the initial crack depth. It follows that the swelling stress is simply given as

$$\sigma_{sw,0} = \sigma_{c,0} - \sigma_c \quad (5.2.11)$$

Two conclusions can be drawn from eq.(5.2.8a) and eq.(5.2.11):

Strength increase

Since the inert strength after soaking exceeds that without soaking, an increase of strength in humid environment results equal to the increase of the inert strength

$$\sigma_f - \sigma_{f,0} = \sigma_c - \sigma_{c,0} \quad (5.2.8b)$$

Apparent power-law exponent n'

Whereas for the un-soaked material the exponent in the power-law relation, n , can simply be obtained from the slope of the $\sigma_f = f(\dot{\sigma})$ plot, this is no longer possible for the water-soaked material as can be easily shown. Let us consider eq.(5.2.8) in the form

$$\sigma_f = \lambda \dot{\sigma}^{1/(n+1)} + \sigma_c - \sigma_{c,0} \quad (5.2.8c)$$

with the abbreviation

$$\lambda = (B\sigma_c^{n-2}(n+1))^{1/(n+1)} \quad (5.2.12)$$

A straight-line evaluation of eq.(5.2.8c) must result in an apparent crack exponent n' defined by

$$\sigma_f = -\sigma_{sw,0} + \lambda \dot{\sigma}^{1/(n+1)} \Rightarrow \sigma_f \propto \dot{\sigma}^{1/(n'+1)} \quad (5.2.13)$$

or in logarithmic representation

$$\frac{1}{n'+1} = \frac{d(\log \sigma_f)}{d(\log \dot{\sigma})} = \frac{d[\log(\lambda \dot{\sigma}^{1/(n+1)} - \sigma_{sw,0})]}{d(\log \dot{\sigma})} \quad (5.2.14)$$

By using logarithmic derivations, $d(\log x) = (1/x) dx$, we obtain the following equation:

$$n' = n + (n+1) \frac{\sigma_c - \sigma_{c,0}}{\sigma_{f,0}} \quad (5.2.15)$$

$$n' \approx n + (n+1) \frac{\sigma_f - \sigma_{f,0}}{\sigma_{f,0}}$$

Since $\sigma_{sw,0} < 0$ it follows that $n' > n$. Thus, the apparently increased n' -value is an artifact of the logarithmic representation of a shift of a straight line by a constant value of $-\sigma_{sw,0}$.

5.2.3 Crack partially embedded in the swelling zone

The treatment for crack sizes competing with the swelling zone size is rather complicated and nontransparent, since it requires numerical computations. One reason for this complication is the fact that the swelling stresses are now no longer constant but decrease from a maximum value at the surface continuously with increasing distance from the surface, roughly given as

$$\sigma_{sw} \cong \sigma_{sw,0} \operatorname{erfc} \left[\frac{z}{2b} \right] \quad (5.2.16)$$

As a consequence of the large n -value for silica ($n > 30$), eq.(5.2.5) makes clear that the largest stress increments $d\sigma_{\text{appl}}$ per crack length increment da occur at the initial crack depth $a \approx a_0$. This follows from $d\sigma_{\text{appl}} = \dot{\sigma} dt$, and $da = AK^n dt$ via $d\sigma_{\text{appl}}/da \propto 1/K^n$. The geometric function can be assumed to be constant: $F(b/a) \cong F(b/a_0)$. In the presence of swelling, we obtain then the following equations:

$$[\sigma_f + F\left(\frac{b}{a_0}\right)\sigma_{sw,0}]^{n+1} = \lambda^{n+1}\dot{\sigma} \quad (5.2.17)$$

$$\Rightarrow \sigma_f = \lambda\dot{\sigma}^{1/(n+1)} - F\left(\frac{b}{a_0}\right)\sigma_{sw,0} \quad (5.2.18)$$

The geometric function for an edge crack occurring in (5.2.2) was determined by FE-computations as

$$F(b/a) \cong \tanh^{3/2} \left(\left[0.385\sqrt{\frac{b}{a}} + 0.832\frac{b}{a} \right]^{2/3} \right) \quad (5.2.19)$$

Again a straight-line evaluation of eq.(5.2.18) results in an apparent crack exponent n' defined by

$$\sigma_f = -F\left(\frac{b}{a_0}\right)\sigma_{sw,0} + \lambda\dot{\sigma}^{1/(n+1)} \Rightarrow \sigma_f \propto \dot{\sigma}^{1/(n'+1)} \quad (5.2.20)$$

or equivalently

$$\frac{1}{n'+1} = \frac{d(\log\sigma_f)}{d(\log\dot{\sigma})} = \frac{d[\log(\lambda\dot{\sigma}^{1/(n+1)} - F\left(\frac{b}{a_0}\right)\sigma_{sw,0})]}{d(\log\dot{\sigma})} \quad (5.2.21)$$

Again using logarithmic derivations, we obtain the following equation:

$$n' = n + (n+1) \frac{-F\left(\frac{b}{a_0}\right)\sigma_{sw,0}}{\sigma_{f,0}} = n + (n+1) \frac{\sigma_f - \sigma_{f,0}}{\sigma_{f,0}} \quad (5.2.22)$$

5.2.4 Semi-circular and semi-elliptical surface cracks as defects

The derivation of strength expressions for other crack shapes is identical as has been outlined for edge cracks. The geometric function $F(b/a_0)$ has of course to be replaced by those for the special type of crack. For the semi-circular crack it holds at the deepest point (A) and the surface points (B):

$$K_{sh,A,B} \cong \sqrt{a} \sigma_{sw,0} F_{A,B}\left(\frac{b}{a_0}\right) \quad (5.2.23)$$

$$F_A\left(\frac{b}{a_0}\right) = 1.17 \tanh\left(0.698\sqrt{\frac{b}{a_0}} + 0.317\frac{b}{a_0}\right) \quad (5.2.24)$$

$$F_B\left(\frac{b}{a_0}\right) = 1.29 \tanh\left(1.327\sqrt{\frac{b}{a_0}} + 0.064\frac{b}{a_0}\right) \quad (5.2.25)$$

This solution for $K_{A,B}$ was given in [5.10] and has been used in Section 3.2. Since the stress intensity factors at the deepest point and the surface points are different it is impossible that the crack will maintain its shape during extension. The equilibrium shape will become a semi-ellipse with an aspect ratio of $a/c \neq 1$ (c =half crack width).

5.3 Strength predictions compared with experimental data

As an example of application eqs.(5.2.19-5.2.22), a result from literature may be discussed. Li and Tomozawa [5.11] investigated the effect of soaking time on the dynamic fatigue behavior of silica glass for soaking at 250 °C in saturated water vapour. All their strength measurements were performed at room temperature, in air at a relative humidity of 15 % to 30 %. The material tested was a grade of industrial silica, TO8, by Heraeus-Amersil Inc. The strength data after different soaking times are re-plotted in Fig 5.1a. The dynamic strength measurements are shown in Fig. 5.1b in form of normalized strength increments as functions of exposure time t (squares in Fig. 5.1b). The curve is tentatively introduced as a guideline to the squares representing a soaking-time dependency of $t^{1/4}$ since $K_{sh} \propto \sqrt{b} \propto t^{1/4}$.

A further interesting result found by Li and Tomozawa [5.11] was the observation that the crack growth exponent of the v - K_{Ic} curve increased with exposure time. The circles in Fig. 5.1c show the reported exponents as a function of the strength increase for a stress rate of $d\sigma_{appl}/dt = 10$ MPa/s. The perpendicular bars represent the standard deviations. The straight line represents the predictions by eqs.(5.2.19-5.2.22). For comparison, we have to take into account the large data scatter in Fig. 5.1c, and, consequently, a large uncertainty of the experimental n' -values. For a comparison of measured and computed n -values in Fig. 5.1, we determined the confidence intervals of the values $1/(n'+1)$ from Fig. 5.1a.

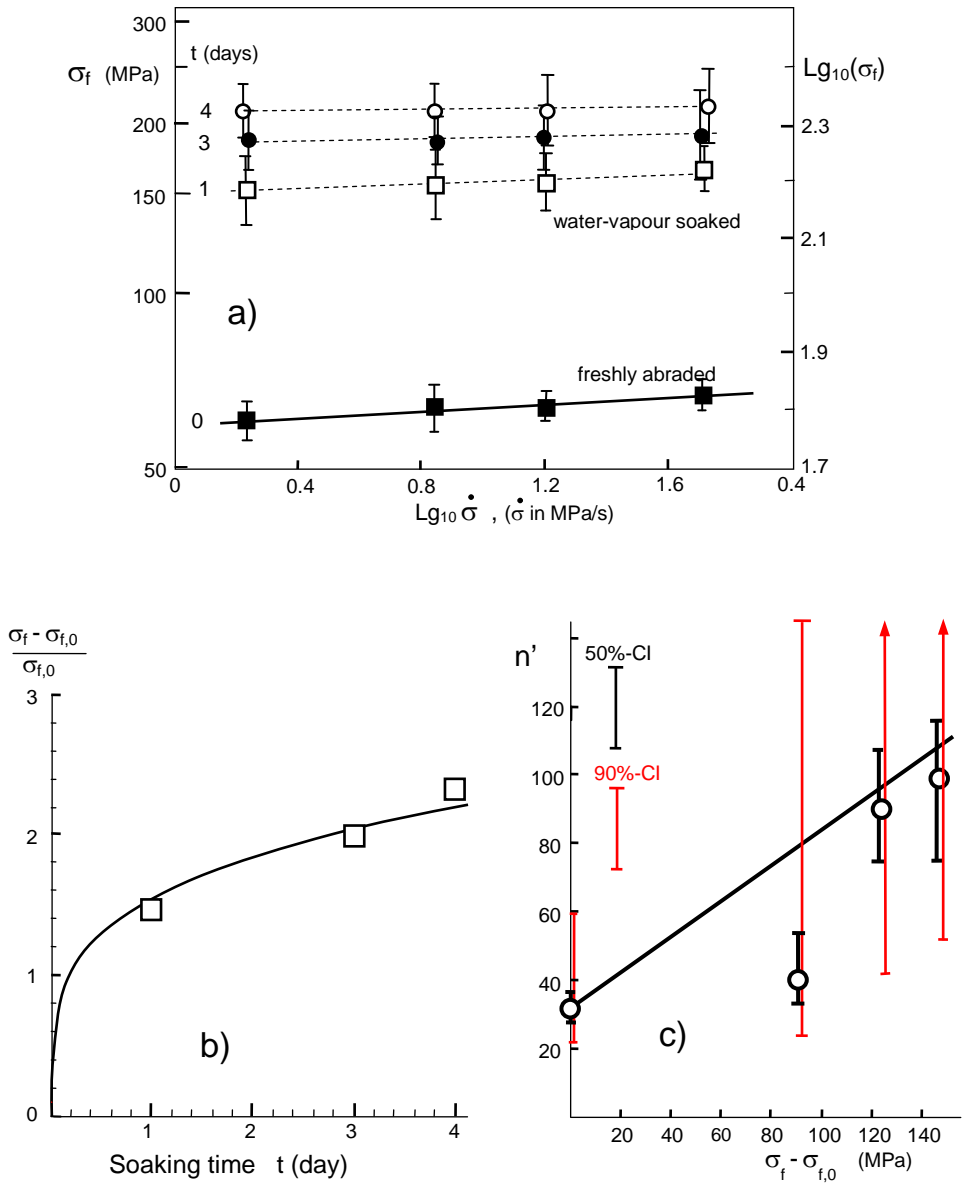


Fig. 5.1 a) Dynamic bending strength tests by Li and Tomozawa [5.11] (for clarity the symbols and scatter bars show slightly displaced abscissa values), b) normalized increase of dynamic strength versus heat-treatment time at 250°C; Squares: results from [5.11], curve: tentatively introduced guide line to the squares representing a dependency $\propto \sqrt{b \propto t^{1/4}}$, c) n' -values reported in [5.11] (circles), straight line: eq.(5.2.22), b) and c) at $d\sigma_{\text{appl}}/dt = 10$ MPa/s.

From the limits of these intervals we computed the related limits for n' . Whereas the intervals for $1/(n'+1)$ are symmetric, those for n become strongly non-symmetric. The 50%- and 90%-confidence intervals (CI) are compiled in Table 5.1. These intervals are also plotted in Fig. 5.1c. Li and Tomozawa [5.11] reported for soaking times of 0 and 4 days the same interval as we found for 50% confidence levels. Confidence levels of 50% are not very often used for data assessment. For this purpose, mostly 90% or 95% levels are applied.

Time	σ_f (MPa)	$\sigma_f - \sigma_{f,0}$ (MPa)	n'	50% CI	90% CI
0 d	59.7	0	32.7	[29.7, 37.9]	[21.8, 63.7]
1 d	149.3	89.6	40.4	[33.4, 50.9]	[23.06, 147]
3 d	183.4	123.7	80.4	[64.2, 107]	[42.1, >1000]
4 d	207.0	147.3	91	[75.1, 116]	[51.4, 380]

Table 5.1 Evaluation of the strength data from Fig. 5.1a with confidence intervals for crack-growth exponents.

On the basis of the 90%-CI, we conclude from Fig. 5.1c that the theoretical prediction and the experimental results by Li and Tomozawa [5.11] are in agreement, i.e. the crack growth exponent increases as expected from eq.(5.2.22). Since the geometric function is $F(b/a) \leq 1$, the swelling stress at the surface must be $|\sigma_{sw}| \geq 147.3$ MPa. Figure 5.2 shows the predictions introduced into Fig. 5.1c. This representation states that the predicted straight-lines according to eqs.(5.2.20) and (5.2.22) are in good agreement with the measurements. This can be seen especially for the strengths after 1 day soaking because in this case the standard deviations were given in [5.11].

An equivalent representation of the agreement between experiment and prediction is given in Fig. 5.3 where the measured strengths are plotted again with a linear ordinate scaling. The black curve represents the power-law equation (5.2.5) with $n=32.7$. In a linear plot this curve is of course no longer a straight line. The small curvature is hardly visible. The red curves are identical with the black one but shifted by constant stress values $\Delta\sigma_f$ (indicated by the arrow in Fig. 5.3). From this plot, it can be concluded that the shifted curves agree with the measurements within the natural data scatter (standard deviation bars given for 3 days soaking exclusively). This fact again confirms the dependency (5.2.18)

$$\Rightarrow \sigma_f = \sigma_{f,0} + const.$$

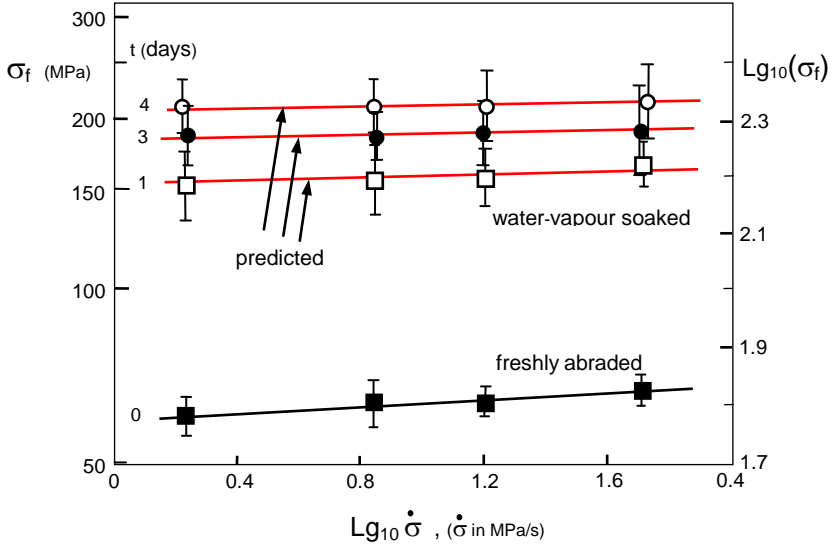


Fig. 5.2 Predicted straight lines (red) according to eqs.(5.2.20) and (5.2.22) introduced by the red lines.

The derivations in this section were performed for the power-law description by eq.(5.2.5) because of its simple mathematical handling. From chemical reaction theory (see e.g. [5.12]) it follows for the $v(K)$ -relation (see also Section 10.3)

$$v(K) = v_0 \exp[B K] \quad (5.3.1)$$

with material parameters v_0 and B . A first estimation of the parameters for eq.(5.3.1) can be obtained analytically when a crack-growth law is given as a power law relation and the exponent is large

$$v(K) = A K^n \quad (5.3.2)$$

From (5.3.1) we get the derivative

$$\frac{d \ln v}{dK} = B \Rightarrow \frac{d \ln v}{\underbrace{\frac{1}{K} dK}_{d(\ln K)}} \frac{1}{K} = b \quad (5.3.3)$$

$$\frac{d \ln v}{d \ln K} = BK \tag{5.3.4}$$

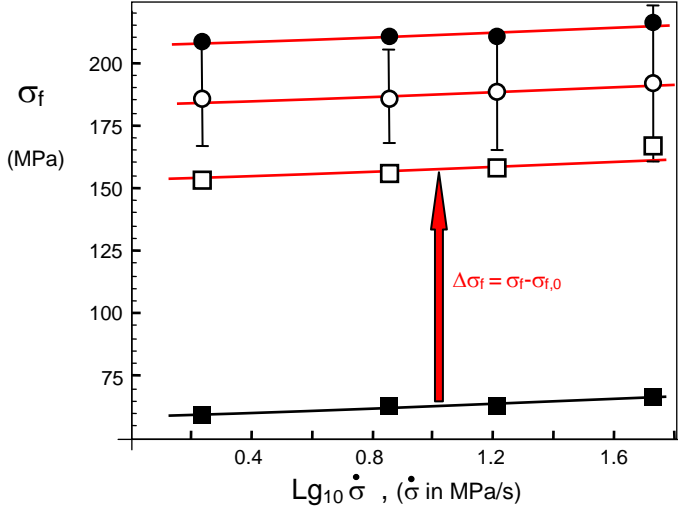


Fig. 5.3 Data of Fig. 5.2 represented with linear ordinate scaling (note that curves are no longer exactly straight). Red curves agree with the black one shifted by a constant stress $\Delta\sigma_f$.

On the other hand we obtain from eq.(5.3.2)

$$\frac{d \ln v}{d \ln K} = n \tag{5.3.5}$$

i.e. $BK \cong n \tag{5.3.6}$

and

$$v_0 \cong A K^n \exp[-BK] \tag{5.3.7}$$

When evaluating experimental results, a mean value of K on the v - K curve has to be used. As a consequence of (5.3.6) the effective slope n' is equivalent to a coefficient B'

$$B' K = n' \tag{5.3.8}$$

Summary on strength results: The present section dealt with the influence of swelling and shielding in silica caused by the reaction between SiO_2 and water.

We considered the effect of swelling stresses on the crack-growth exponent of the power-law for subcritical crack growth. It could be shown that the apparent exponent n' of a power law description according to

$$v \propto K_{app}^n$$

must decrease with increasing swelling. This theoretical consequence of swelling in silica is in rather good agreement with experiments from literature.

References

-
- 5.1 Zouine, A., Dersch, O., Walter, G., Rauch, F., Diffusivity and solubility of water in silica glass in the temperature range 23-200°C, *Phys. Chem. Glasses*, **48** (2007), 85-91.
- 5.2 S. M. Wiederhorn, F. Yi, D. LaVan, T. Fett, M.J. Hoffmann, Volume Expansion caused by Water Penetration into Silica Glass, *J. Am. Ceram. Soc.* **98** (2015), 78-87.
- 5.3 Davis, K.M., Tomozawa, M., Water diffusion into silica glass: structural changes in silica glass and their effect on water solubility and diffusivity, *J. Non-Cryst. Sol.* **185** (1995), 203-220.
- 5.4 Oehler, A., Tomozawa, M., Water diffusion into silica glass at a low temperature under high water vapor pressure, *J. Non-Cryst. Sol.* **347**(2004) 211-219.
- 5.5 G. Schell, T. Fett, Crack growth exponent n for water-vapour soaked silica, *Scientific Working Papers* **74**, 2017, ISSN: 2194-1629, Karlsruhe, KIT.
- 5.6 R. J. Charles, Dynamic fatigue of glass, *Journal of Appl. Phys.* **29**(1958), 1657-1661.
- 5.7 T. Fett, G. Rizzi, K.G. Schell, E.C. Bucharsky, P. Hettich, S. Wagner, M. J. Hoffmann, , Consequences of hydroxyl generation by the silica/water reaction Part I: Diffusion and Swelling, KIT Scientific Publishing, Karlsruhe.
- 5.8 Fett, T., Failure due to semi-elliptical surface cracks under arbitrary stress distributions, *Fatigue and Fracture of Engineering Materials and Structures*, **23**(2000), 347-53
- 5.9 Munz, D., Fett, T., *Ceramics: Mechanical Properties, Failure Behaviour, Materials Selection*, Springer-Verlag (1999).

5.10 T. Fett, G. Rizzi, M. Hoffmann, S. Wagner, and S.M. Wiederhorn, Effect of Water on the inert Strength of Silica Glass: Role of Water Penetration, *J. Am. Ceram. Soc.* **95**(2012) [12], 3847-3853.

5.11 H. Li and M. Tomozawa, Mechanical strength increase of abraded silica glass by high pressure water vapor treatment, *J. Non-Cryst. Solids* **168**(1994), 287-292.

5.12 S.M. Wiederhorn and L.H. Bolz, Stress Corrosion and Static Fatigue of Glass, *J. Am. Ceram. Soc.* **53**[1810] 543-548 (1970).

6 Swelling anisotropy

6.1 Motivation for anisotropic swelling

Strongly different stress states can result in the same hydrostatic stress term σ_h . An example for this fact is illustrated in Fig. 6.1 where in all cases the hydrostatic stress disappears completely, $\sigma_h=0$. This is trivial when all stress components disappear, Fig. 6.1a.

In the case of Fig. 6.1b, where the transversal stresses are half of the longitudinal stress with inverse sign, it is again $\sigma_h=0$ according to $\sigma_h=(\sigma_x+\sigma_y+\sigma_z)/3$. The same holds for torsion loading, $\sigma_y=-\sigma_z$, Fig. 6.1b'.

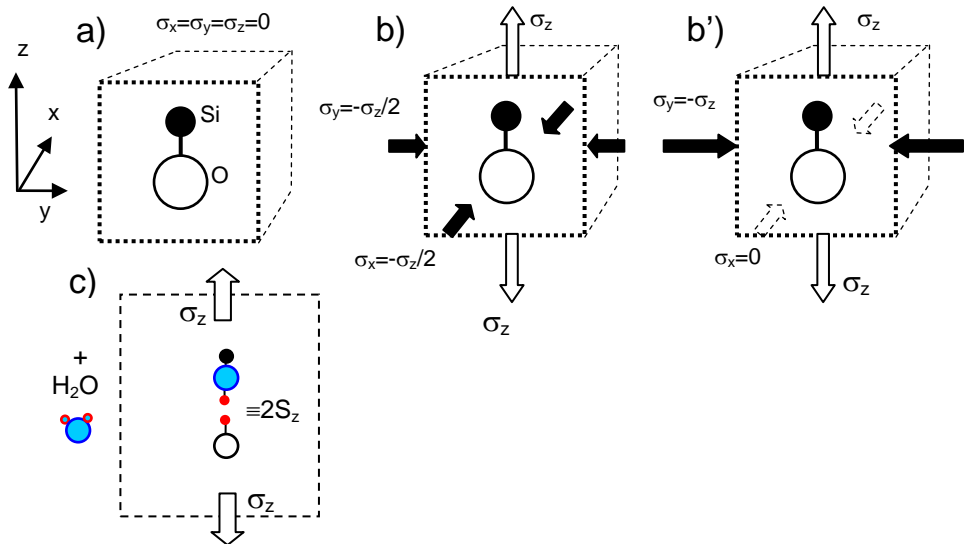


Fig. 6.1 Three stress states acting on a Si-O-bond exhibiting the same disappearing hydrostatic stress $\sigma_h=0$: a) isotropic swelling is expected, for b), b') swelling in z-direction should dominate as illustrated by c), case b') describes torsion loading, c) water molecule reacting with a stressed bond oriented in z-direction, producing two hydroxyls, $2S_z$.

It is hardly imaginable that the high tensile stresses in bond direction should have no effect on bond fracture. It has to be expected that the reaction in tensile direction should produce swelling even for the hydrostatic stress state $\sigma_h=0$.

Figure 6.2 shows the load-displacement curves for bond breaking by reaction (1.1.1). Perpendicular to the loading direction the necessary energy for splitting the bond is U and must be delivered by thermal fluctuations.

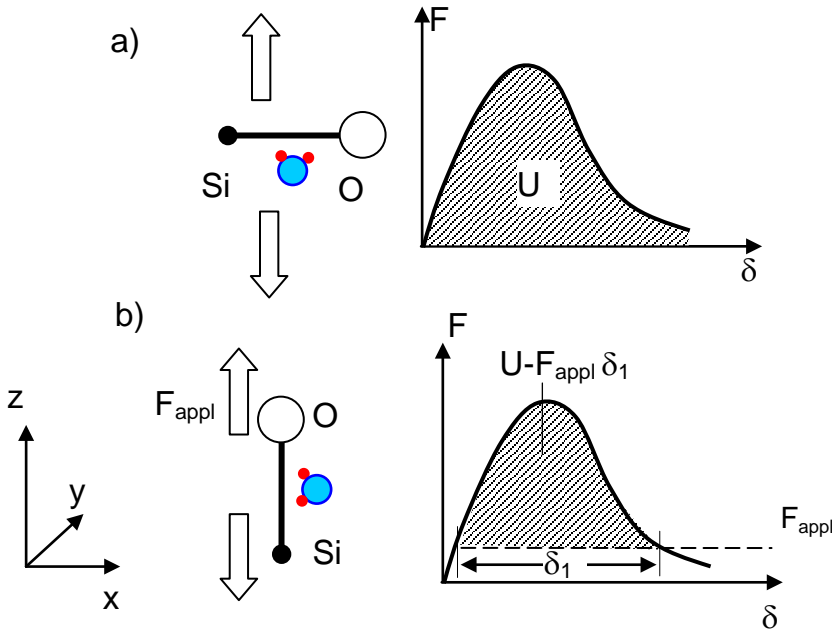


Fig. 6.2 Energy conditions for bond breaking.

The portion N_x (subscript x means the bonds oriented in x -direction in which no stress acts) of opened bonds results from the Boltzmann equation as

$$N_x \propto \exp\left(-\frac{U}{RT}\right) \quad (6.1.1)$$

The same equation holds for the y -direction

$$N_y \propto \exp\left(-\frac{U}{RT}\right) \quad (6.1.2)$$

The potential barrier U belongs to the case when no stresses are present or when the bond is perpendicular to the stress, Fig. 6.2a. Under action of a force F in bond-direction, Fig. 6.2b, the potential barrier is reduced to $U-F\delta_1$. Consequently, the occurrence of opened bonds in z -direction is increased

$$N_z \propto \exp\left(-\frac{U - \sigma_z V}{RT}\right) \quad (6.1.3)$$

where V is an activation volume. In the following considerations, it will be shown that the strongest anisotropy effect has to be expected for the torsion loading case.

6.2 Anisotropic swelling in tension and torsion test

6.2.1 Uniaxial loading

The case of uni-axial loading was outlined in detail in [6.1] and Sections 6 and 7 of [6.2]. In the following considerations, we will handle also the torsion test by superimposing uniaxial stresses in y - and z -directions as illustrated in Fig.6.3.

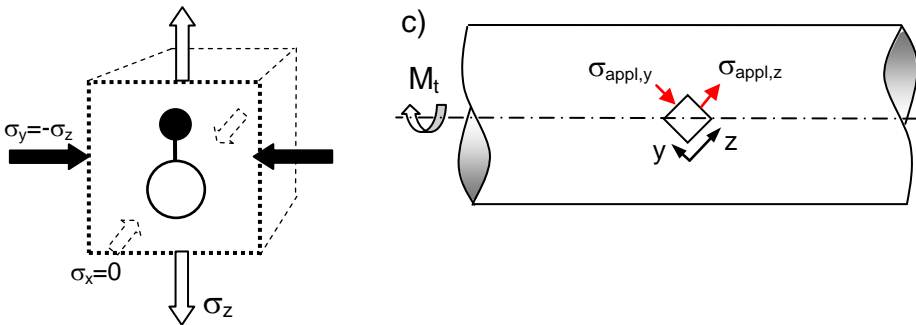


Fig. 6.3 Loading cases: a) uniaxial tension, b) uniaxial compression, c) cylinder under a torsion moment M_t .

The hydroxyl concentration S is under purely uniaxial stress according to eqs.(1.1.15, 1.1.16)

$$S = S_0 \exp\left(\frac{\sigma_{appl}\Delta V_{eff}}{RT}\right) \quad (6.2.1)$$

where ΔV_{eff} is an effective activation volume of

$$\Delta V_{eff} = 14.4 \text{ cm}^3/\text{mol} \pm 10\% \quad (6.2.2)$$

and S_0 the initial hydroxyl concentration in the absence of load.

For small arguments of the exponential function, eq.(6.2.1) can be linearized by first order expansion

$$S = S_0 \exp\left(\frac{\sigma_{appl}\Delta V_{eff}}{RT}\right) = S_0 \left(1 + \frac{\sigma_{appl}\Delta V_{eff}}{RT}\right) \quad (6.2.3)$$

The increase of the hydroxyl concentration by the stress, $\Delta S = S - S_0$, is simply

$$\Delta S = S_0 \frac{\sigma_{appl}\Delta V_{eff}}{RT} \quad (6.2.4)$$

Taking into account the proportionality between S and the volume swelling strain ε_v according to eq.(1.1.9)

$$\varepsilon_v = \kappa \times S, \quad \kappa = 0.97 \quad (6.2.5)$$

eq.(6.2.4) yields for the stress-affected increase $\Delta\varepsilon_v = \varepsilon_v - \varepsilon_{v0} = \kappa\Delta S$

$$\Delta\varepsilon_v = \varepsilon_{v0} \frac{\sigma_{appl}\Delta V_{eff}}{RT} \quad (6.2.6)$$

The individual swelling strain components were found to be interrelated by [5.1]

$$\varepsilon_{sw,x}^{(z)} = \varepsilon_{sw,y}^{(z)} = -0.24\varepsilon_{sw,z}^{(z)} \quad (6.2.7)$$

where the upper index (z) stands for “loading in z -direction”. Equation (6.2.7) gives rise for the definition of a “Poisson’s ratio ν_{sw} ” for swelling strains

$$V_{sw} = -\frac{\varepsilon_{sw,y}^{(z)}}{\varepsilon_{sw,z}^{(z)}} \quad (6.2.8)$$

Its value would result in $v_{sw}=0.24$. Finally, the stress-affected part of volume swelling is obtained as

$$\Delta\varepsilon_v = \varepsilon_{sw,x}^{(z)} + \varepsilon_{sw,y}^{(z)} + \varepsilon_{sw,z}^{(z)} = 0.52\varepsilon_{sw,z}^{(z)} \quad (6.2.9)$$

so that from eqs.(6.2.6) and (6.2.9):

$$\varepsilon_{sw,z}^{(z)} = 1.92\varepsilon_{v0} \frac{\sigma_{appl}\Delta V_{eff}}{RT} \quad (6.2.10)$$

6.2.2 Torsion loading

The results for the uniaxial loading case may be used to describe more complicated loading by superposition. Under torsion loading, the maximum and minimum principle stresses appear in a coordinate system turned by 45° with respect to the length axis. In this system, Fig. 6.3, the “applied” stresses are

$$\sigma_{appl,y} = -\sigma_{appl,z}, \quad \sigma_{appl,x} = 0 \quad (6.2.11)$$

In order to show the principal effect of torsion stresses on the swelling strains and hydroxyl concentration, let us assume a volume element without restrictions on the boundaries, so that swelling strains can freely expand or contract without generation of swelling stresses. In the absence of load, this volume element may contain an initial hydroxyl concentration S_0 .

For the applied stress in z -direction, the swelling strains are given by eq.(6.2.7). Under the compressive stress in y -direction, the subscripts have to be changed

$$\varepsilon_{sw,z}^{(y)} = \varepsilon_{sw,x}^{(y)} = -V_{sw}\varepsilon_{sw,y}^{(y)} = V_{sw}\varepsilon_{sw,z}^{(z)} \quad (6.2.12)$$

The *total swelling strains* from (6.2.7) and (6.2.12) then read by superposition:

$$\varepsilon_{sw,z} = \varepsilon_{sw,z}^{(y)} + \varepsilon_{sw,z}^{(z)} = (1 + V_{sw})\varepsilon_{sw,z}^{(z)} \quad (6.2.13)$$

$$\varepsilon_{sw,y} = \varepsilon_{sw,y}^{(y)} + \varepsilon_{sw,y}^{(z)} = -(1 + \nu_{sw})\varepsilon_{sw,z}^{(z)} \quad (6.2.14)$$

$$\varepsilon_{sw,x} = \varepsilon_{sw,x}^{(y)} + \varepsilon_{sw,x}^{(z)} = 0 \quad (6.2.15)$$

The total change of volume swelling $\Delta\varepsilon_v$ is simply

$$\Delta\varepsilon_v = \varepsilon_{sw,x} + \varepsilon_{sw,y} + \varepsilon_{sw,z} = 0 \quad (6.2.16)$$

As an important consequence, we have to conclude that under torsion loading, no volume increase occurs. From eq.(6.2.5) we have to conclude furthermore that no increase of the hydroxyl concentration can occur, i.e. $\Delta S=0 \Rightarrow S=S_0=\text{const.}$

The *elastic strains* result from Hooke's law

$$\varepsilon_z = \frac{1}{E}\sigma_z - \frac{\nu}{E}\sigma_y \Rightarrow \varepsilon_z = \frac{1+\nu}{E}\sigma_{appl} \quad (6.2.17)$$

$$\varepsilon_y = \frac{1}{E}\sigma_y - \frac{\nu}{E}\sigma_z \Rightarrow \varepsilon_y = -\frac{1+\nu}{E}\sigma_{appl} \quad (6.2.18)$$

$$\varepsilon_x = 0 \quad (6.2.19)$$

The *total strains* as the sums of elastic and swelling contributions read

$$\varepsilon_{z,total} = \varepsilon_z + \varepsilon_{sw,z} \quad (6.2.20)$$

$$\varepsilon_{y,total} = \varepsilon_y + \varepsilon_{sw,y} \quad (6.2.21)$$

$$\varepsilon_{x,total} = 0 \quad (6.2.22)$$

A small volume element ΔV is considered, that contributes to the torsion moment or the drilling angle. The share to the applied moment may be denoted as $\Delta M_{t,appl}$, the contribution by swelling as $\Delta M_{t,sw}$. Since the swelling strains have the same signs as the elastic strains, the deformations in a torsion test on a cylindrical specimen under constant load must increase by swelling. In the first case, the torsion angle, increases by an amount $\Delta\varphi_{t,sw}$

$$\frac{\Delta\varphi_{t,sw}}{\Delta\varphi_{t,appl}} = \frac{\varepsilon_{sw,z}}{\varepsilon_z} = \frac{(1+\nu_{sw})}{(1+\nu)} \frac{1.92\varepsilon_{v0}}{RT} E \Delta V_{eff} \quad (6.2.23)$$

Inversely, the stresses must decrease due to swelling, if the cylindrical specimen is loaded under displacement conditions where the drilling angle, φ_t , is kept constant. For the latter case, the ratio of the torsion moment by swelling, ΔM_{sw} , and due to the applied moment, ΔM_{appl} , are simply related by

$$\frac{\Delta M_{t,sw}}{\Delta M_{t,appl}} = - \frac{\Delta\varphi_{t,sw}}{\varphi_t} \quad (6.2.24)$$

6.2.3 Expectations for torsion tests

It is self-evident that only the water-affected zones directly under the surface can contribute to the change of the torsion moment or twist angle, i.e. water must be present at the considered location. The water diffusion layer b increases with time t according to eq.(3.1.2).

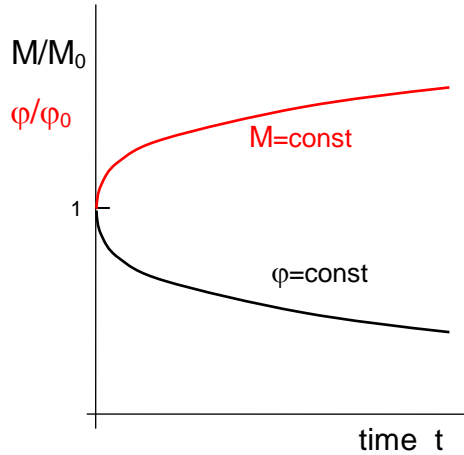


Fig. 6.4 Time dependence of twist angle (red curve) in a constant moment test and time dependent moment for twist angle kept constant (black curve).

The main expectations are:

1. the remaining S after the test must be the same as the value S_0 before the test
2. in a test under constant twist angle (black curve in Fig. 6.4), the swelling stresses in the surface layer must decrease, resulting in a reduced torsion moment $M=M_0-\Delta M$ with $\Delta M \propto \varepsilon_{sw,z} \times b \propto \sqrt{t}$
3. in a constant moment test (red curve in Fig. 6.4), the reduced moment ΔM must be compensated, i.e. an additional twist angle $\Delta\varphi \propto \sqrt{t}$ must appear, so that the instantaneously applied angle φ_0 is increased to $\varphi_0+\Delta\varphi$.
4. After unloading a remaining twist angle $\Delta\varphi$ should be observable.

6.3 FE-Model for a single reaction event

Due to the reaction (1.1.1), a SiO-bond may fracture in the absence of externally applied stresses. The coordinate system is oriented so that the z -axis agrees with the direction in which the repulsive forces between the silanols act (Fig. 6.5a). The related “nano-pore” defined by the dashed circle in Fig. 6.5a was modelled as a sphere of radius R in an “infinite body” [6.3].

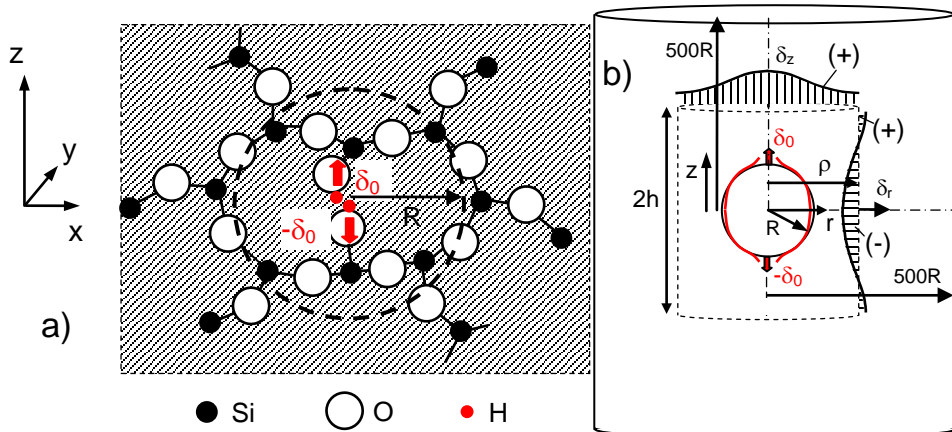


Fig. 6.5 a) Bond breaking by water/silica reaction; the two hydroxyls yield an expansive displacement δ_0 in z -direction; the volume element in which the reaction occurred is represented by the dashed circle, b) Finite Element model of a “nano pore” loaded by axial displacement δ_0 .

In a FE-study, we realized the “infinite body” by a cylinder of radius $500 R$ and half height $500 R$, Fig. 6.5b. For the computations, we used ABAQUS Version 6.9 on a mesh of 1246 elements and 3880 nodes. Due to symmetry, only a 4th of the total body had to be modelled. As the only material parameter of relevance we used the Poisson ratio of $\nu=0.17$. Expansion of the pore is prescribed by a displacement δ_0 in z -direction.

6.4 FE-Results

Figure 6.6 represents the displacement distribution for a cylinder contour with $h=\rho=16 R$, so that the distance from the pore is sufficiently large. On the other hand, the contour is small compared with the modelled body. Saint-Venant’s theorem ensures that no boundary effects and details of the pore shape can affect the results noticeably. The displacements are normalized on the maximum displacements present on the symmetry lines.

The volume changes in axial and radial directions, ΔV_z and ΔV_r , are given by

$$\Delta V_z = 2\pi \int_0^\rho \delta_z(r) r dr \quad , \quad \Delta V_r = 2\pi \rho \int_0^{h=\rho} \delta_r(z) dz \quad (6.4.1)$$

Since the cylinder volume is

$$V_0 = \rho^2 \pi h \stackrel{\rho=h}{=} \rho^3 \pi \quad (6.4.2)$$

the increase of the volume swelling strain results in

$$\Delta \mathcal{E}_v = \frac{\Delta V_z + \Delta V_r}{\rho^3 \pi} \quad (6.4.3)$$

Finally, the anisotropy ratio $\bar{\mathcal{E}}_{sw,z} / \Delta \mathcal{E}_v$ is obtained by:

$$\frac{\bar{\mathcal{E}}_{sw,z}}{\Delta \mathcal{E}_v} = \frac{\Delta V_z}{\Delta V_z + \Delta V_r} \quad (6.4.4)$$

For the cylinder contour of $\rho = h = 16 R$, the evaluation of eq.(6.4.4) results in

$$\frac{\bar{\varepsilon}_{sw,z}}{\Delta\varepsilon_v} = 2.06 \quad (6.4.5)$$

Having in mind that the volume strain is

$$\Delta\varepsilon_v = \bar{\varepsilon}_{sw,x} + \bar{\varepsilon}_{sw,y} + \bar{\varepsilon}_{sw,z} = \bar{\varepsilon}_{sw,z} + 2\bar{\varepsilon}_{sw,r} \quad (6.4.6)$$

a ‘‘Poisson’s ratio $\bar{\nu}$ ’’ for swelling strains can be defined via

$$\bar{\nu} = -\frac{\bar{\varepsilon}_{sw,r}}{\bar{\varepsilon}_z} \quad (6.4.7)$$

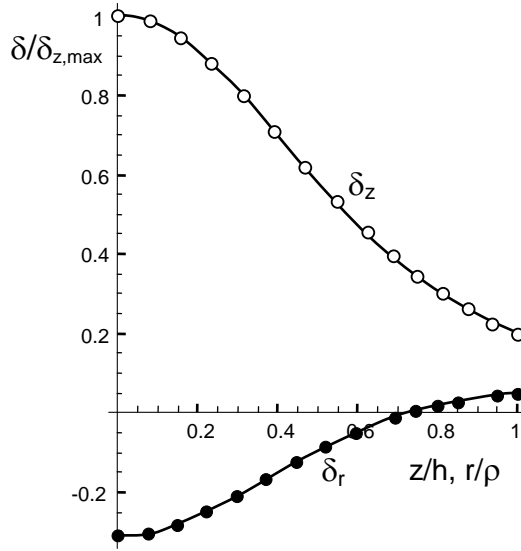


Fig. 6.6 Displacement distributions δ_z and δ_r at the cylinder contour in a distance of $h=16R$.

From eqs.(6.4.5) to (6.4.7) we obtain

$$\frac{\bar{\varepsilon}_{sw,z}}{\Delta\varepsilon_v} = \frac{\bar{\varepsilon}_{sw,z}}{\bar{\varepsilon}_{sw,z} + 2\bar{\varepsilon}_{sw,r}} = \frac{1}{1 + 2\frac{\bar{\varepsilon}_{sw,r}}{\bar{\varepsilon}_{sw,z}}} = \frac{1}{1 - 2\bar{\nu}} = 2.06 \Rightarrow \bar{\nu} = 0.257 \quad (6.4.8)$$

resulting in a Poisson’s ratio as is usual for ceramics.

The transverse swelling strains are

$$\frac{\bar{\varepsilon}_{sw,r}}{\Delta\varepsilon_v} = \frac{\bar{\varepsilon}_{sw,x}}{\Delta\varepsilon_v} = \frac{\bar{\varepsilon}_{sw,y}}{\Delta\varepsilon_v} = -0.53 \quad (6.4.9)$$

It has to be emphasized here once more, that the results from FE were obtained under the assumption that all stress-enhanced swelling strains are oriented in direction of the load. This is of course an upper limit case.

Influence of the chosen geometry: In order to show the effect of the *finite* body that had to be modelled for the FE-computations, we computed the average strains on cylinder contours, $\bar{\varepsilon}$, in different distance from the pore. Figure 6.7 shows the ratios $\bar{\varepsilon}_z / \Delta\varepsilon_v$ and $\bar{\varepsilon}_r / \bar{\varepsilon}_z$.

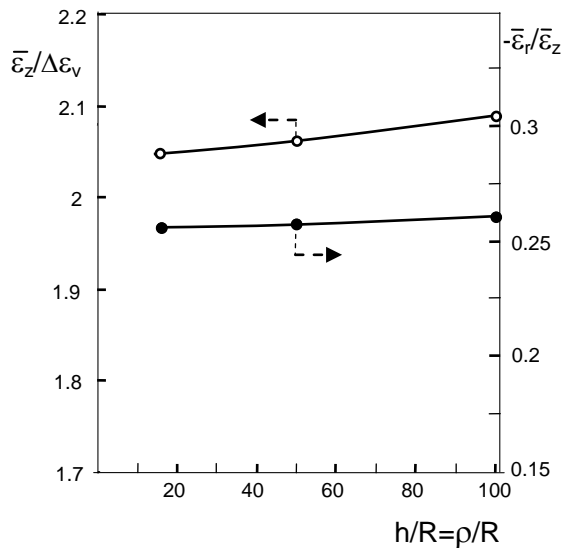


Fig. 6.7 Strain ratios $\bar{\varepsilon}_z / \Delta\varepsilon_v$ and $-\bar{\varepsilon}_r / \bar{\varepsilon}_z$ vs. h/R or ρ/R .

It can be seen that the results are rather independent of the chosen cylinder contour. For $\bar{\varepsilon}_z / \Delta\varepsilon_v$ the maximum variation within the range of $16R \leq h, \rho \leq 100R$ is less than 2%. This weak dependency clearly indicates that the theorem of Saint-Venant is sufficiently fulfilled, i.e. that

$$R \ll h, \quad \rho \ll 500R$$

When this condition holds, the validity of Saint-Venant's theorem suggests that special details of the pore-shape cannot have a noticeable influence on $\bar{\varepsilon}_z / \Delta\varepsilon_v$ and $\bar{\varepsilon}_r / \bar{\varepsilon}_z$.

References

- 6.1 S. M. Wiederhorn, G. Rizzi, S. Wagner, M. J. Hoffmann, T. Fett, Stress-Enhanced Swelling of Silica: Effect on Strength, *J. Am. Ceram. Soc.* **99**(2016), 2956-63.
- 6.2 T. Fett, G. Rizzi, K.G. Schell, E.C. Bucharsky, P. Hettich, S. Wagner, M. J. Hoffmann, Consequences of hydroxyl generation by the silica/water reaction Part I: Diffusion and Swelling, KIT Scientific Publishing, Karlsruhe.
- 6.3 G. Rizzi, T. Fett, FE-study on maximum swelling anisotropy in silica, *Scientific Working Papers* **40**, 2015, ISSN: 2194-1629, Karlsruhe, KIT.

7 Stress-enhanced isotropic swelling

7.1 Quasi-hydrostatic stress state at crack tips

In gases and liquids, the loading is always hydrostatic. In a solid the situation is more complicated, since the individual stress components σ_x , σ_y , σ_z are in general independent of each other and are not necessarily equal. Especially in uniaxial tension or compression, the hydrostatic stress deviates clearly from the tensile stress. In contrast to this, the stress state ahead of crack tips is more hydrostatic since the tensile stress in the prospective plane and the tensile stress normal on this plane are identical, $\sigma_x = \sigma_y$, and the tensile stress σ_z is very close to the tip: $\sigma_z = \nu(\sigma_x + \sigma_y)$.

In the case of purely hydrostatic loading $\sigma_x = \sigma_y = \sigma_z$, swelling must be isotropic since no direction is preferred. In this Section the behaviour of cracks is considered and therefore isotropic swelling behaviour with identical swelling strains $\epsilon_{sw,x} = \epsilon_{sw,y} = \epsilon_{sw,z}$ may be assumed.

In order to allow a most transparent analysis, we assume in the following considerations the applicability of:

1. *Isotropic swelling* behavior, $\epsilon_{sw,x} = \epsilon_{sw,y} = \epsilon_{sw,z}$, independent of the stress direction.
2. Replacement of the pressure p by the negative *hydrostatic stress* term σ_h .

Whereas in *uniaxial tension* the ratio of the hydrostatic stress to the maximum stress (the stress σ_y normal to the crack plane) is only

$$\sigma_h / \sigma_y = \frac{1}{3} \quad (7.1.1)$$

it holds along a prospective crack plane

$$\frac{\sigma_h}{\sigma_y} = \frac{2}{3}(1 + \nu) \stackrel{\nu=0.17}{=} 0.78 \quad (7.1.2)$$

This value is much closer to the purely hydrostatic stress state described by $\sigma_h/\sigma_y=1$ and should therefore be applied to crack problems. This possibility of a captivatingly transparent description will be chosen here accepting the probability of underestimation of swelling effects. In experiments in which uniaxial stresses rather than hydrostatic ones are applied during the reaction, this assumption was re-examined in Section 6 to account for the possibility that local swelling is not isotropic [7.1].

In the following Section, the experiment by Tomozawa et al. [7.2] will be discussed under the simplified assumptions mentioned before.

7.2 Application of simple crack-tip models

7.2.1 Sharp crack approach

Different crack-tip models are commonly used in fracture mechanics for the description of stresses ahead of a crack. Linear-elastic fracture mechanics as a continuum mechanics theory assumes the existence of a mathematically sharp crack. In this case, the stresses near the crack tip become singular, $\sigma \rightarrow \infty$ for a crack-tip distance of $r \rightarrow 0$.

The stresses in the crack plane ahead the crack tip, caused by the *total* stress intensity factor K_{ip} , are

$$\sigma_x = \sigma_y, \quad \sigma_z = 2\nu\sigma_y \quad (7.2.1)$$

with

$$\sigma_y = \frac{K_{ip}}{\sqrt{2\pi r}} \quad (7.2.2)$$

Generally, it is assumed that crack extension under inert conditions occurs, when the normal component σ_y equals the ideal strength σ_0 . When K_{Ic} is the fracture toughness, it then simply holds

$$\sigma_y = \sigma_0 \frac{K_{ip}}{K_{Ic}} \quad (7.2.3)$$

The fracture toughness of silica is $K_{Ic} = 0.75\text{-}0.8 \text{ MPa}\sqrt{\text{m}}$ [7.3] and the theoretical strength is about [7.4]

$$\sigma_0 = \frac{E}{\pi} \cong 23 \text{ GPa} \quad (7.2.4)$$

as is in agreement with strengths up to 25GPa measured by Brambilla and Payne [7.5] on extremely thin silica fibers of about 60 nm radius.

The highest tensile strengths for thicker silica glass fibers in ultra high vacuum at room temperature are about $\sigma_c \cong 12.6 \text{ GPa}$ [7.6]. Strengths for optical fibers are lower than the theoretical strength, σ_0 , due to the unavoidable presence of surface defects in these fibers [7.7].

The critical distance r_{cr} at which the normal stress component σ_z for $K=K_{Ic}$ equals the theoretical strength, is according to (7.2.2)

$$r_{cr} = \frac{1}{2\pi} \left(\frac{K_{Ic}}{\sigma_0} \right)^2 = 0.19 \text{ nm} \quad (7.2.5)$$

This value is smaller than the “microstructure” given by the SiO_2 ring diameter. This makes clear that failure within such small dimensions cannot be described by a mathematically sharp crack. Consequently, the K -description via continuum mechanics must fail, when the tip distance competes with the microstructure of the material.

7.2.2 Slender notch approach

In a micro-structurally motivated approach, the crack tip region (Fig. 7.1a) is considered as a slender notch with root radius ρ in the order of the average radius of the SiO_2 rings, Fig. 7.1b. This description may be applied in the following considerations. For such a notch, Wiederhorn et al. [7.8] suggest a crack-tip radius of $\rho = 0.5 \text{ nm}$.

Stresses at slender notches were given by Creager and Paris [7.9]. The stress component normal to the crack plane (the tangential stress $\sigma_t = \sigma_y$) is in distance ξ from the notch root

$$\sigma_y = \frac{2K}{\sqrt{\pi(\rho + 2\xi)}} \frac{\rho + \xi}{\rho + 2\xi} \quad (7.2.6)$$

The other stress components are

$$\sigma_x = \frac{2K}{\sqrt{\pi(\rho + 2\xi)}} \frac{\xi}{\rho + 2\xi} \quad (7.2.7)$$

$$\sigma_z = \frac{2\nu K}{\sqrt{\pi(\rho + 2\xi)}} \quad (7.2.8)$$

Consequently, the hydrostatic stress term from the applied stresses results as

$$\sigma_{appl,h} = \frac{2(1+\nu)K}{3\sqrt{\pi(\rho + 2\xi)}} \quad (7.2.9)$$

The location at which failure occurs can be computed by application of the ‘‘Theory of Critical Distances’’ (TCD) as was developed by Taylor [7.10,7.11]. In a ‘‘non-local approach’’, the TCD postulates that failure occurs when a distance dependent effective stress σ_{eff} exceeds the tensile strength σ_0 .

The effective stress is in this approach the stress value σ_y in a distance of $\xi=L/2$ from the notch root, where the length L is given by

$$L = \frac{1}{\pi} \left(\frac{K_{Ic}}{\sigma_0} \right)^2 (\equiv 2r_c) \quad (7.2.10)$$

i.e. twice of the critical crack-tip distance in the continuum mechanics description by eq.(7.2.5). Introducing (7.2.10) and (7.2.4) into (7.2.6) and setting $\xi=L/2$ results in

$$\rho = \frac{(1+\sqrt{5})}{2\pi\sigma_0^2} K_{Ic}^2 = 0.62\text{nm} \quad (7.2.11)$$

This says that in the light of the TCD-approach the guess by Wiederhorn et al. [7.8] is a very good estimate. Their value of $\rho=0.5$ nm would be exact for a theoretical strength of $\sigma_0=25.6$ GPa.

The hydrostatic stress at $K=K_{Ic}$ is

$$\sigma_{appl,h} = (\sqrt{5}-1) \frac{(1+\nu)}{3} \sigma_0 \quad (7.2.12)$$

For a test under subcritical crack growth conditions, the necessary stress intensity factor is smaller than fracture toughness K_{Ic} . From the average crack rate of $v \approx 10^{-7}$ m/s (estimation in [7.12]) and crack-growth curves in water by Wiederhorn and Bolz [7.13], the stress intensity factor results to be $K_{appl} \approx 0.48$ MPa \sqrt{m} .

The total stress intensity factor is the sum of the applied, K_{appl} , and shielding term K_{sh}

$$K = K_{appl} + K_{sh}, \quad K_{sh} < 0 \quad (7.2.13)$$

The shielding stress intensity factor was estimated in [7.12] to be $K_{sh} = -0.1$ MPa \sqrt{m} at $v \approx 10^{-7}$ m/s. Then the total stress intensity factor would be $K \approx 0.38$ MPa \sqrt{m} .

For the reduced stress intensity factor during subcritical crack growth, $K < K_{Ic}$, eq.(7.2.12) reads

$$\sigma_{appl,h} = (\sqrt{5} - 1) \frac{(1 + \nu)}{3} \frac{K}{K_{Ic}} \sigma_0 \quad (7.2.14)$$

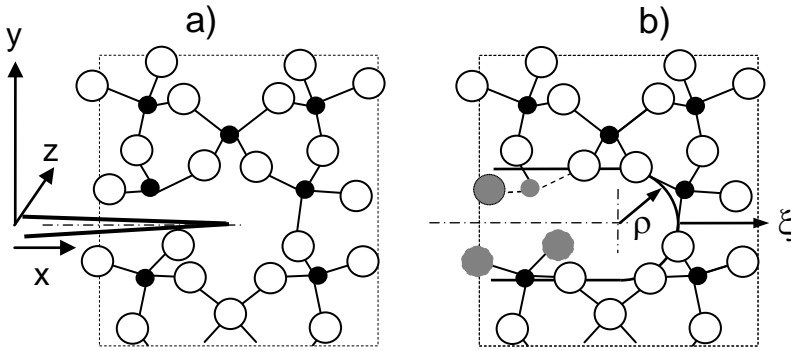


Fig. 7.1 a) Crack in silica terminating in a nano-pore, b) equivalent slender notch with a finite notch root radius ρ , grey molecules are mechanically inactive.

Swelling stresses under isotropic swelling conditions at slender notches were determined in [7.14] by using the FE-method. Results for the hydrostatic stress term under plane strain conditions are shown in Fig. 7.2 by the circles. It can be concluded from this representation that the hydrostatic swelling stress normalized on the volume strain hardly changes over the swelling zone.

Outside the swelling zone, the hydrostatic stress term disappears practically. In addition, the effect of the swelling zone height b is small. The square indicates the theoretically known value for an infinitely thin surface layer, given by

$$\sigma_{sw,h} \cong -\frac{2}{9} \frac{E \varepsilon_v}{1-\nu} = -\eta S \tag{7.2.15}$$

with the coefficient

$$\eta \cong \frac{2}{9} \frac{0.97 E}{1-\nu} \cong 18.7 \text{ GPa} \tag{7.2.16}$$

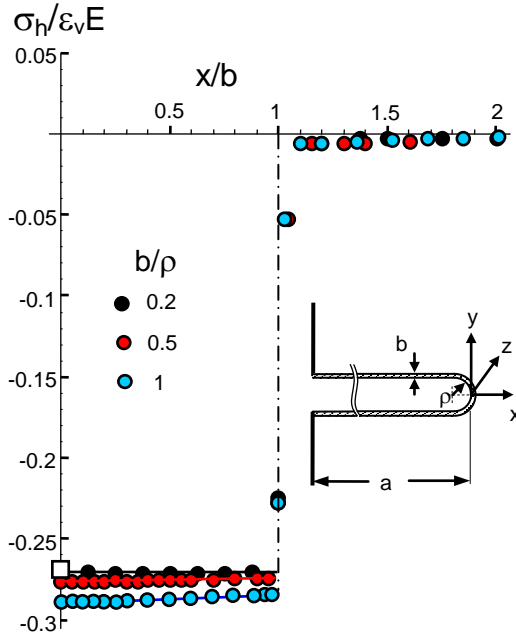


Fig. 7.2 Hydrostatic swelling stresses, normalized on the volume expansion strain for 3 different relative zone heights b/ρ .

The hydroxyl swelling stress at the surface ($x \rightarrow 0$) can be approximately expressed as

$$\sigma_h \left(\frac{b}{\rho} \right) = -\frac{2 \varepsilon_v E}{9(1-\nu)} \left(1 + 0.078 \frac{b}{\rho} \right) \tag{7.2.17}$$

The other individual swelling stress components in the directions of a rectangular coordinate system are given in Section A1.3.

7.3 Hydroxyl concentration under swelling stresses

Since now the hydroxyl concentrations S , S_0 are known from Sections 5 to 8 in [7.15] and applied hydrostatic stress $\sigma_{\text{appl},h}$ from 7.2.2, we can estimate the molar volume.

In presence of externally applied and internal swelling stresses, σ_{appl} and σ_{sw} , the total stresses are given as their sum

$$\sigma = \sigma_{\text{appl}} + \sigma_{\text{sw}}, \quad \sigma_h = \sigma_{\text{appl},h} + \sigma_{\text{sw},h} \quad (7.3.1)$$

This leads to

$$S = S_0 \exp\left(\frac{(\sigma_{\text{appl},h} + \sigma_{\text{sw},h})\bar{V}_s}{RT}\right) \quad (7.3.2)$$

The hydrostatic swelling stress is proportional to the hydroxyl concentration

$$\sigma_{\text{sw},h} = -\eta S \quad (7.3.3)$$

with a coefficient of proportionality η , depending on the stress state of loading. Consequently:

$$S = S_0 \exp\left(\frac{(\sigma_{\text{appl},h} - \eta S)V_{\text{eff}}}{RT}\right) \quad (7.3.4)$$

This is an implicit equation with respect to S that occurs on the left side as well as in the exponent. Its explicit form is

$$S = \frac{RT}{\eta\bar{V}_s} \text{PLog}\left[\frac{\eta S_0 \bar{V}_s}{RT} \exp\left(\frac{\sigma_{\text{appl},h} \bar{V}_s}{RT}\right)\right] \quad (7.3.5a)$$

where PLog stands for the *product-logarithm function* (see e.g. [7.16]). Since this function may not be available on all computer systems, the inverse representation can be used resulting equivalently in

$$\sigma_{appl,h} = \eta S + \frac{RT}{V_s} \ln\left(\frac{S}{S_0}\right) \quad (7.3.5b)$$

In terms of the hydrostatic swelling stress, eq.(7.2.15), we analogously obtain

$$\sigma_{sw,h} = -\frac{RT}{V_s} \text{PLog}\left[-\frac{\sigma_{sw,h,0}\bar{V}_s}{RT} \exp\left(\frac{\sigma_{appl,h}\bar{V}_s}{RT}\right)\right] \quad (7.3.6)$$

where $\sigma_{sw,h,0}$ is the swelling stress for $S=S_0$. Having in mind that the stress state ahead of a crack is not exactly a hydrostatic one and swelling cannot be completely isotropic it would be better to call the result an effective volume $\bar{V}_s \rightarrow \Delta V^{\text{eff}}$. On the other hand, it has to be expected that ΔV^{eff} may depend on the chosen crack-tip model, too.

The effective volume can be determined from the measurement of hydroxyl concentration as

$$\Delta V^{\text{eff}} = \frac{RT}{\sigma_{appl,h} - \eta S} \ln\left(\frac{S}{S_0}\right) \quad (7.3.7)$$

Unfortunately, the authors of [7.2] didn't provide correct stress intensity factors for their tests (details in the Appendix of [7.17]). The resulting ΔV^{eff} is plotted in Fig. 7.3a versus the theoretical strength for $K_{\text{appl}} \cong 0.48 \text{ MPa}\sqrt{\text{m}}$ according to [7.13] and constant shielding stress intensity factors of $K_{\text{sh}}=0$ to $-0.3 \text{ MPa}\sqrt{\text{m}}$.

Figure 7.3b shows V_{eff} for 3 applied stress intensity factors K_{appl} for which the stress intensity factors K_{ip} were computed by use of eq.(10.6.6). For the most probable value of theoretical strength, $\sigma_0 = 23 \text{ GPa}$, large values of the effective volume ΔV^{eff} have to be expected for the low-temperature region $<450^\circ\text{C}$.

At temperatures $T > 500^\circ\text{C}$, the water/silica reaction is of the order 2



At temperatures $T < 450^\circ\text{C}$, hydroxyls are immobile. Only those hydroxyls can react in the reverse reaction step, which are directly neighboring. Consequently, the reaction is of first order. When $[2S]=[2 \text{ SiOH}]$ is the concentration of the immovable hydroxyl, the reaction equation reads now



The activation volumes related to the two completely different reactions may now be quite different.

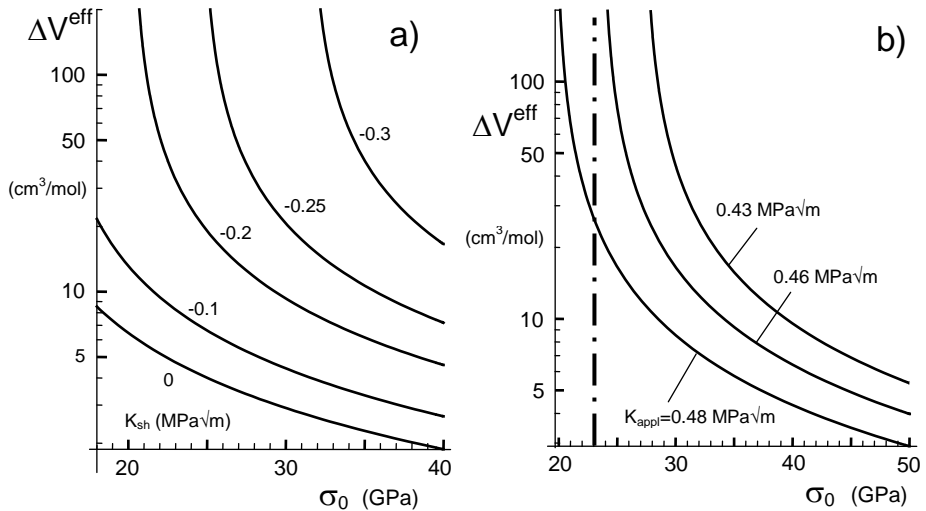


Fig. 7.3 Effective volume ΔV^{eff} derived for the slender notch crack-tip model as a function of the ideal or theoretical strength σ_0 of $\sigma_0=23$ GPa; a) for constant shielding stress intensity factors at $K_{\text{app}}=0.48$ $\text{MPa}\sqrt{\text{m}}$, b) for constant applied stress intensity factors according to eq.(10.6.6).

References

- 7.1 R.B de Boer, On the thermodynamics of pressure solution – interaction between chemical and mechanical forces, *Geochimica et Cosmochimica Acta*, **41**(1977), 249-256
- 7.2 M. Tomozawa, W.-T. Han and W.A. Lanford, Water Entry into Silica Glass during Slow Crack Growth, *J. Am. Ceram. Soc.* **74** [10] (1991), 2573-2576.
- 7.3 S.M. Wiederhorn, Fracture surface energy of glass, *J. Am. Ceram. Soc.* **52**(1969), 99-105.
- 7.4 Silva, E. C. C. M.; Tong, L.; Yip, S.; Van Vliet, K. J. *Small* **2006**, *2*, 239–243.

- 7.5 G. Brambilla, D.N. Payne, The ultimate strength of glass silica nanowires, *Nano Letters*, **9**(2009), 831-835.
- 7.6 C.R. Kurkjian, P.K. Gupta, R.K. Brow, and N. Lower, The intrinsic strength and fatigue of oxide glasses, *J. Noncrystal. Solids*, **316**(2003), 114-124.
- 7.7 W. Weibull, A Statistical Theory of the Strength of Materials, *Ingenjersvetenskap-sakad. Handl.* **151**(1939), 1-45.
- 7.8 S.M. Wiederhorn, E.R. Fuller, Jr. and R. Thomson, Micromechanisms of crack growth in ceramics and glasses in corrosive environments, *Metal Science*, **14**(1980), 450-8.
- 7.9 Creager, M., Paris, P.C., Elastic field equations for blunt cracks with reference to stress corrosion cracking, *Int. J. Fract.* **3**(1967), 247-252.
- 7.10 D. Taylor, Predicting the fracture strength of ceramic materials using the Theory of critical distances, *Engineering Fracture Mechanics*, **71**(2004), 2407.
- 7.11 D. Taylor, *The Theory of Critical Distances: A New Perspective in Fracture Mechanics*. Elsevier, Oxford, UK (2007).
- 7.12 S. M. Wiederhorn, T. Fett, G. Rizzi, M. J. Hoffmann, J.-P. Guin, The Effect of Water Penetration on Crack Growth in Silica Glass, *Engng. Fract. Mech.* **100**(2013), 3-16
- 7.13 Wiederhorn, S.M. and Bolz, L.H., Stress Corrosion and Static Fatigue of Glass, *J. Am. Ceram. Soc.* **53**[10] (1970) 543-549.
- 7.14 G. Rizzi, G. Schell, T. Fett, Swelling stresses ahead of slender notches, *Scientific Working Papers* **52**, 2016, KIT Scientific Publishing, Karlsruhe.
- 7.15 T. Fett, G. Rizzi, K.G. Schell, E.C. Bucharsky, P. Hettich, S. Wagner, M. J. Hoffmann, Consequences of hydroxyl generation by the silica/water reaction Part I: Diffusion and Swelling, *KIT Scientific Publishing, Karlsruhe*.
- 7.16 R. Corless, G. Gonnet, D. Hare, D. Jeffrey and D. Knuth, "On the Lambert W Function," *Advances in Computational Mathematics*, **5**(1996), 329-359.
- 7.17 G. Schell, G. Rizzi, T. Fett, Hydroxyl concentrations on crack surfaces from measurements by Tomozawa, Han and Lanford, *Scientific Working Papers* **82**, 2018, ISSN: 2194-1629, Karlsruhe, KIT.

8 Effects of swelling at crack tips

8.1 Consequences of shielding on ν - K -curves

The shielding stress intensity factor, K_{sh} , caused by an expanding zone with a constant volume strain over the zone size was given by McMeeking and Evans [8.1]. The shielding term for variable hydroxyl concentrations was described in [8.2] and will be extended to variable Young's modulus in Sections 11.6.1 and 12.2. Generally it holds

$$K_{sh} = \int_0^{\infty} (S \times E) h(\omega') d\omega' \quad (8.1.1)$$

with the Green's function

$$h = -\frac{1}{2}\psi \frac{\kappa}{1-\nu} \frac{1}{\sqrt{\omega'}} \quad (8.1.2)$$

and $\psi \approx 0.22$ [8.1]. The effect of the shielding stress intensity factor on the ν - K -curves was outlined in [8.2] for constant modulus E . Equations (8.1.1) and (8.1.2) result in the same relation as given in [8.1] with an effective coefficient ψ_{eff}

$$K_{sh} = -\psi_{eff} \frac{\varepsilon_v E}{1-\nu} \sqrt{\omega'} \quad (8.1.3)$$

From theoretical considerations by Wiederhorn [8.3], the subcritical crack growth law is of the form

$$\nu = \nu_0 \exp(bK_{tip} / RT) \stackrel{def}{=} \nu_0 \exp(BK_{tip}) \quad (8.1.4)$$

defining $B=b/RT$. Equation (8.1.4) would suggest for small stress intensity factors that a subcritical crack growth rate of ν_0 would occur in the absence of any loading. The model of single bond rupture by Michalske and Freiman [8.4] gives rise for the back reaction. Instead of (8.1.4) it was suggested in literature (see also [8.5]) to use

$$\nu = 2\nu_0 \sinh(bK_{tip} / RT) \quad (8.1.5)$$

The effective stress intensity factor acting at the crack tip, K_{tip} , represents the singular stress field at the crack tip. From the principle of superposition, K_{tip} is given by

$$K_{tip} = K_{appl} + K_{sh} \quad (8.1.6)$$

where K_{appl} is the externally applied stress intensity factor and K_{sh} is the stress intensity factor due to shielding.

The effect of a shielding stress intensity factor on the ν - K -curve of silica is a shift of the ν - K_{tip} -curve to the left (to lower stress intensity factors) as has been shown in [8.2] on the basis of the ν - K_{appl} -curve from Double Cantilever Beam (DCB)-measurements by Wiederhorn and Bolz [8.6].

8.2 Threshold behaviour under shielding conditions

8.2.1 Approximation by rate-independent shielding stress intensity factor

In the case of silica, swelling causes a negative shielding stress intensity factor. This fact gives rise for a threshold of the ν - K_{appl} -curve as was shown in [8.7]. This can be simply concluded from eq.(8.1.5). In order to give a transparent description of the general consequences of shielding first a constant shielding stress intensity factor is assumed. For this purpose a shielding stress intensity factor of $K_{sh} = -\frac{1}{4} K_{Ic}$ was chosen (note that $-K_{sh}$ is a *positive* number). In Fig. 8.1 the dash-dotted curve represents the ν - K_{tip} dependency as the subcritical crack growth curve of the material in the absence of shielding, $K_{sh}/K_{Ic}=0$. Compared to this curve, the shielding-affected blue curve for $K_{sh} = -\frac{1}{4} K_{Ic}$ is shifted to the right. A threshold value at $\frac{1}{4} K_{Ic}$ is visible.

From the data of Fig. 2.8b in [8.8] it can be concluded that not exclusively swelling of glasses can be expected. Whereas the Al-glass and the Ca-containing glass of Fig. 2.8b should show negative shielding stress intensity factors due to volume expansion similar to silica, the volume shrinking of the B₂O₃-glass and the K-containing glass must result in positive shielding stress intensity factors, where now the notation “shielding” does loss

its original sense. The related v - K_{appl} -curve for $K_{\text{sh}}=1/4 K_{\text{Ic}}$ (red) shows a finite subcritical crack growth rate that does not disappear at $K_{\text{appl}}=0$, no surprising result in the light of shrinking.

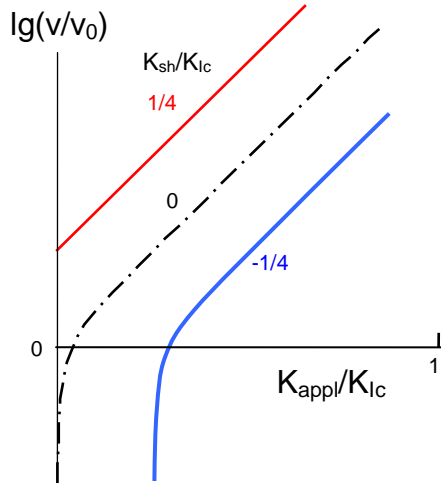


Fig. 8.1 Effect of constant shielding on the v - K curves for negative, disappearing, and positive shielding stress intensity factors.

8.2.2 Change of the swelling zone shape during crack growth

Muraoka and Abe [8.9] carried out static tensile tests on silica fibers with small semi-elliptical surface cracks. By microscopic inspection, the crack sizes were determined and via time measurements, the crack growth rates were computed. In Fig. 8.2a, the crack growth rates are plotted versus K_{appl} (circles and black curve) after correction of the stress intensity factor solution from $v=0.3$ to $v=0.17$ [8.10]. The blue line represents results by Wiederhorn and Bolz [8.6] and is introduced as a reference curve. In terms of the applied stress intensity factor, K_{appl} , this curve can be expressed in the range of $3 \times 10^{-11} \text{ m/s} < v < 10^{-5} \text{ m/s}$ by

$$v = v_0 \exp(B^* K_{\text{appl}}) \quad (8.2.1)$$

with the parameters $v_0 = 4.5 \cdot 10^{-27} \text{ m/s}$, $B^* = 91.2 / \text{MPa}\sqrt{\text{m}}$ for room temperature.

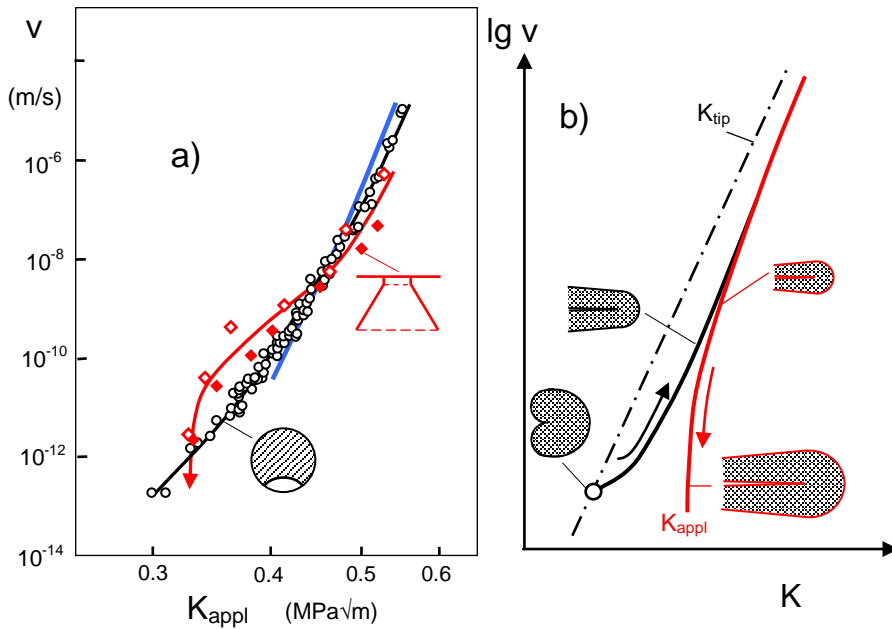


Fig. 8.2 a) ν - K -curve of subcritical crack growth for silica obtained from static lifetime tests by Muraoka and Abe [8.9] (circles and black curve), blue line: results by Wiederhorn and Bolz [8.6], red data and line: re-evaluated data by Sglavo and Green on cone cracks [8.11], b) Development of the swelling zone and the applied stress intensity factor for tests with constant load (schematic).

Figure 8.2a shows ν - K -data on cone cracks by Sglavo and Green [8.11] as the red squares. The absolute values of original stress intensity factors indirectly obtained from fracture toughness K_{Ic} were corrected by a Finite Element solution including partial crack closure and crack-face friction as derived in [8.12]. In this case, a threshold stress intensity factor at about $0.35 \text{ MPa}\sqrt{\text{m}}$ is visible. From Fig. 8.2a it can be concluded that the measurable crack-growth curves $\nu(K_{\text{appl}})$ are not a material property but are also influenced by the testing procedure. When a crack starts growing in a test under static load, the initial zone shape is first heart-shaped. Such a zone does not show a shielding stress intensity factor as has been early stated by McMeeking and Evans [8.1]. Consequently, the ν - K_{appl} -curve must start on the curve for $K_{\text{sh}}=0$, i.e. $\psi=0$, indicated in the schematic Fig. 8.2b by the circle. With increasing crack length, the shielding zone develops in length direction [8.1] resulting in an increasing coefficient ψ until the saturation value of about $\psi=0.22$ is reached. Then any further crack growth goes along the red curve, which may show the result from a crack-growth test under monotonously decreasing stress

intensity factor as is for instance feasible in tests on cone cracks introduced by a Vickers indentation. Such a crack shows a crack extension Δa that is large compared to the height ω of the swelling zone, $\Delta a > 5\omega$, so that the shielding zone is fully developed. As has been shown by McMeeking and Evans [8.1] the shielding coefficient is not a constant but needs a crack extension of at about $\Delta a \geq 5\omega$ before $\psi = 0.22$ is sufficiently reached.

8.2.3 Threshold stress intensity factor

Figure 8.3 shows $v(K_{\text{appl}})$ -results for silica in water at room temperature by Sglavo et al. [8.13] (solid circles) together with the results by Wiederhorn and Bolz [8.6] (dash-dotted line). The threshold value for subcritical crack-growth was obtained in [8.13] as $K_{\text{th}} = 0.31\text{--}0.32 \text{ MPa}\sqrt{\text{m}}$. The open circles represent the measurements of subcritical crack growth at 700°C in lab air of relative humidity 40-60% by Aaldenberg and Lezzi [8.14].

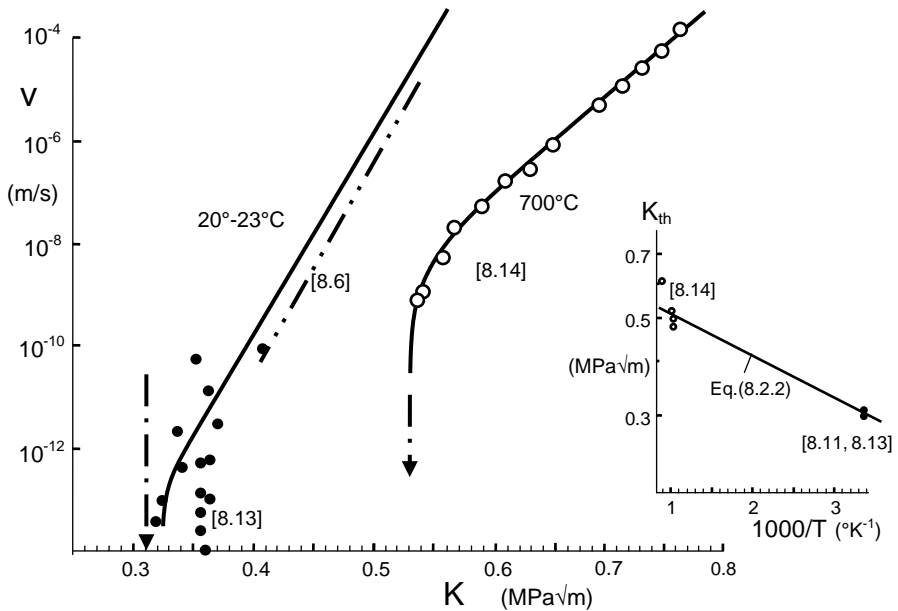


Fig. 8.3 Subcritical crack growth data at room temperature obtained from the ISF-procedure by Sglavo and Green [8.11, 8.13] (solid circles), dash-dotted line: Wiederhorn and Bolz [8.6], measurements by Aaldenberg and Lezzi [8.14] at 700°C in lab air (open circles). Inset: Threshold vs. temperature.

Fitting these results by equations (8.1.5) and (8.1.6) with $K_{sh} = -K_{th}$ results in:

$$\text{For } 20^{\circ}\text{C: } v_0 = 2.5 \times 10^{-14} \text{ m/s, } B = 90 \text{ (MPa}\sqrt{\text{m}})^{-1}, K_{th} = 0.32 \text{ MPa}\sqrt{\text{m}},$$

$$\text{and } 700^{\circ}\text{C: } v_0 = 2 \times 10^{-9} \text{ m/s, } B = 46.8 \text{ (MPa}\sqrt{\text{m}})^{-1}, K_{th} = 0.53 \text{ MPa}\sqrt{\text{m}}.$$

The related fitting curves are introduced in Fig. 8.3. Ignoring the different humidity in [8.11] and [8.14], the threshold stress intensity factor as a function of temperature θ (plotted in the inset in Fig. 8.3) may be described by an Arrhenius dependency

$$K_{th} \cong K_{th,0} \exp\left[\frac{-Q}{RT}\right] \quad (8.2.2)$$

with the parameters $K_{th,0} = 0.638 \text{ MPa}\sqrt{\text{m}}$ and $Q = 1.83 \text{ kJ/mol}$.

8.2.4 Variable shielding

Deviations from the assumption of a constant shielding stress intensity factor K_{sh} have to be expected. The steepness of the v - K_{appl} curve is influenced by two opposite effects. An increase of K_{appl} causes an increase of the shielding-stress intensity factor due to increased S -concentration. On the other hand, the increase in the crack velocity v greatly shortens the time available for diffusion in the crack tip region and reduces the size of the shielding zone. It remains unclear which influence dominates.

1) According to the derivation by Wiederhorn, the stress intensity factor K is the physically active total stress intensity factor K_{tip} governing the singular crack-tip stress field. In a $\lg(v)$ - K_{tip} -plot this must result in a straight line:

$$\log(v/v_0) = a_1 + b_1 K_{tip} \quad (8.2.3)$$

2) As the subcritical crack growth curve for silica in liquid water at 25°C (Wiederhorn and Bolz [8.6]) shows, the crack velocity as a function of the applied stress intensity factor is also very straight over a large region of crack rates, Fig. 8.4a. This can be expressed as

$$\log(v/v_0) = a_2 + b_2 K_{appl} \quad (8.2.4)$$

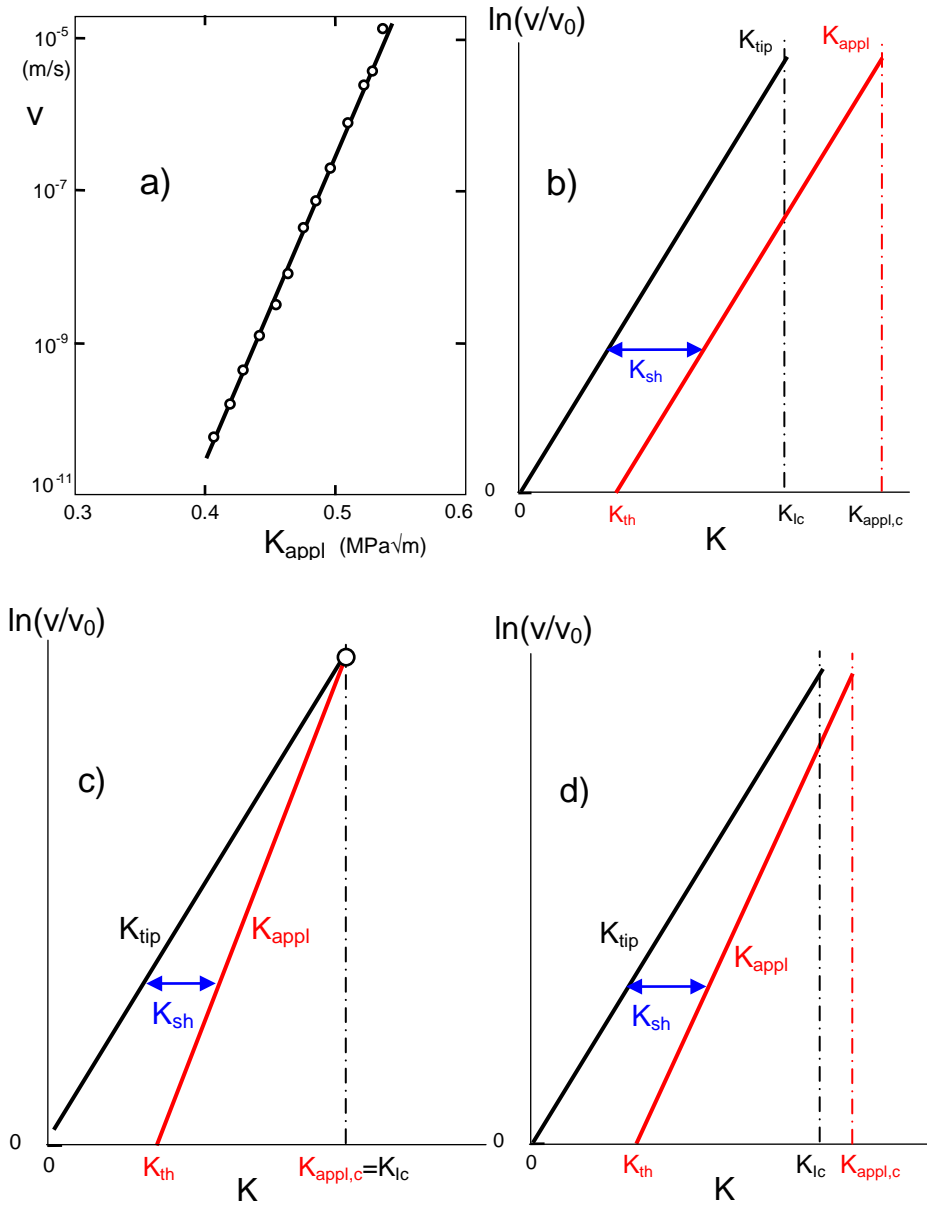


Fig. 8.4 a) v - K_{app} curve of silica in liquid water by Wiederhorn and Bolz [8.6] at a temperature of 25°C, b) comparison of v - K_{tip} and v - K_{appl} -curves for a constant shielding stress intensity factor, $K_{sh}(K_{Ic})=const.$, c) comparison of v - K_{tip} and v - K_{appl} -curves for variable $K_{sh}(K_{Ic})=0$, d) most general case.

Equation (8.1.6) requires that even the shielding stress intensity factor must fulfil a similar relation, namely,

$$\log(V/V_0) = a_3 + b_3 K_{sh} \quad (8.2.5)$$

If K_{sh} depends on v , there must exist an intersection of the straight lines according to (8.2.3) and (8.2.4). Figure 8.4b shows the case of a constant shielding stress intensity factor

$$K_{sh} = f(v) = -K_{th} \quad (8.2.6)$$

When K_{tip} reaches fracture toughness K_{Ic} , the crack extension becomes very fast. Velocities in the order of sound velocity occur. Consequently, diffusion effects of surface water into the crack-tip region will disappear as well as the related shielding term, i.e. $K_{sh}(K_{Ic}) \rightarrow 0$.

This limit situation is indicated by the circle in Fig. 8.4c. In this special case, the shielding stress intensity factor holds in terms of K_{tip}

$$K_{sh} \approx - \left(1 - \frac{K_{tip}}{K_{Ic}} \right) K_{th} \quad (8.2.7)$$

In terms of K_{appl}

$$K_{sh} \approx - \frac{K_{Ic} - K_{appl}}{K_{Ic} - K_{th}} K_{th} \quad (8.2.8)$$

and

$$K_{tip} \approx \frac{K_{appl} - K_{th}}{K_{Ic} - K_{th}} K_{Ic} \quad (8.2.9)$$

as illustrated in Fig. 8.4c. The most general case is illustrated in Fig. 8.4d. In this case, the apparent fracture toughness is in the range

$$K_{Ic} \leq K_{appl,c} \leq K_{Ic} + K_{th} \quad (8.2.10)$$

8.3 Swelling strains at the tip of an arrested crack

8.3.1 AFM results on surface overlapping

Atomic force microscope (AFM) measurements on fracture surfaces from [8.15] were used to estimate the swelling strains [8.7]. From Fig. 8.5a one can see that there is extra material (the dark grey area) at the tip of an arrested crack held in water of room temperature at $K_I = 0.25 \text{ MPa}\cdot\text{m}^{1/2}$ for 80 days. This material was not there before the crack was formed in the glass.

Not any crack growth was observed during the long holding time. For causing crack growth, the stress intensity factor had to be increased above $K = 0.37\text{-}0.4 \text{ MPa}\sqrt{\text{m}}$. If the crack were just loaded and unloaded, the crack profile would be relatively flat and to experimental precision, the two fracture surfaces would overlap perfectly.

The excess material ahead of the actual crack tip can be interpreted as a water diffusion zone where swelling by the volumetric strain ε_v took place. After complete cracking of the specimen, each half of this region can expand normally to the new crack face. This results in a volume expansion and in an overlapping of the surface profiles. Figure 8.5b gives a few measurements of the overlapping displacements with a maximum value of about 6 nm. Our very first evaluation of the displacement results was performed based on the few equidistant displacements (squares introduced in Fig. 8.5b).

Comparing these few displacements with finite element results provided an average volume swelling strain of $\varepsilon_v = 13.8\%$ [8.2, 8.7]. The related average hydroxyl concentration is

$$S = \frac{\varepsilon_v}{0.97} = 14.2 \text{ wt\%} \quad (8.3.1)$$

and the average of Young's modulus results from Section 11 as

$$E = 5900 \text{ MPa} \quad (8.3.2)$$

This is a strong reduction to only $\approx 8\%$ compared with the undamaged modulus of $E_0 = 72000 \text{ MPa}$.

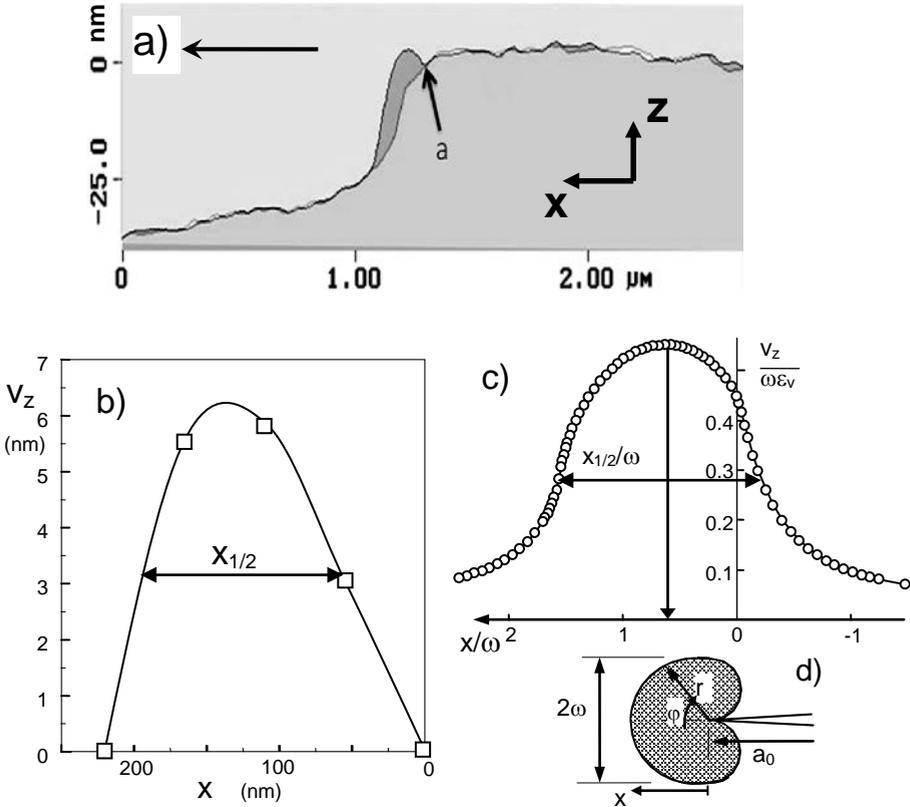


Fig. 8.5 Determination of glass expansion due to water penetration of a crack tip: a) AFM scan of a crack tip that was held under load in water at room temperature, $K_{\text{appl}} = 0.254 \text{ MPa}\cdot\text{m}^{1/2}$ for 80 days, b) profile of the swelling region on the fracture surface, c) Finite Element analysis of a heart-shaped swelling zone [8.7].

8.3.2 Influence of reduced Young's modulus due to damage

In our opinion the swelling visible from the AFM measurements is caused by stress-enhanced generation of silanol groups in the water-silica reaction, eq.(1.1.1) with the equilibrium of the reaction under tensile stress shifted to the right. The increased hydroxyl content results in the observed volume. In order to check the influence of a probably *reduced Young's modulus* in the swelling zone on the displacements, the displacements were additionally computed for the case that in the swelling zone the modulus is reduced

to 10% of that outside the swelling zone. Figure 8.6 shows a comparison of the related displacements. For reasons of clearness the results are slightly shifted in height direction. Differences between the two profiles are negligible. This makes clear that the evaluation of the swelling strains is not affected by damage accompanied by module reduction.

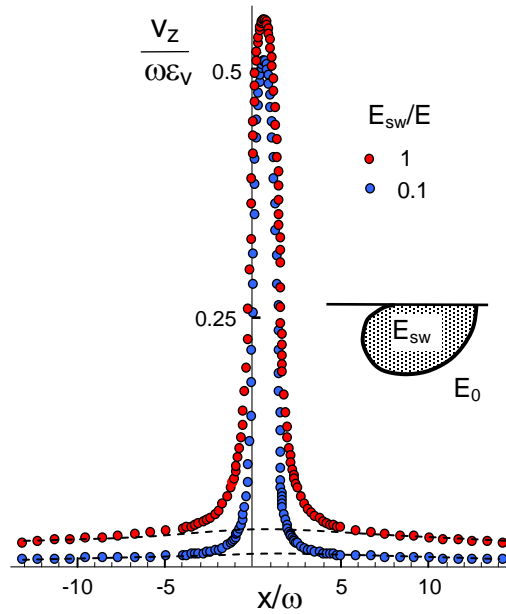


Fig. 8.6 Comparison of the displacements v_z for a strongly reduced Young's modulus in the swelling zone (blue symbols) with the results for constant modulus (data points shifted slightly in height direction for better visibility).

References

- 8.1 McMeeking, R.M., Evans, A.G. Mechanics of transformation-toughening in brittle materials, *J. Am. Ceram. Soc.* **65**(1982), 242–246.
- 8.2 S.M. Wiederhorn, T. Fett, G. Rizzi, M.J. Hoffmann and J.-P. Guin, The Effect of Water Penetration on Crack Growth in Silica Glass, *Engng. Fract. Mech.* **100** (2013), 3–16.

- 8.3 Wiederhorn, S.M., A Chemical Interpretation of Static Fatigue, J. Am. Ceram. Soc. **55**(1972), 81-85.
- 8.4 T.A. Michalske, W. Freiman, A molecular mechanism for stress corrosion in vitreous silica, J. Am. Ceram. Soc. **66**[4] (1983), 284-288.
- 8.5 Fuller, E.R., Thomson, R.M., Lattice theories of fracture, in: Fracture Mechanics of Ceramics Vol. IV (1978), Plenum Press, New York, 507–548.
- 8.6 Wiederhorn, S.M. and Bolz, L.H., Stress Corrosion and Static Fatigue of Glass, J. Am. Ceram. Soc. **53**[10] (1970), 543-548.
- 8.7 S. M. Wiederhorn, T. Fett, G. Rizzi, S. Fünfschilling, M.J. Hoffmann, J.-P. Guin, Effect of Water Penetration on the Strength and Toughness of Silica Glass, J. Am. Ceram. Soc. **94** [S1] (2011), S196-S203.
- 8.8 T. Fett, G. Rizzi, K.G. Schell, E.C. Bucharsky, P. Hettich, S. Wagner, M. J. Hoffmann, , Consequences of hydroxyl generation by the silica/water reaction Part I: Diffusion and Swelling, KIT Scientific Publishing, Karlsruhe.
- 8.9 M. Muraoka and H. Abé, Subcritical Crack Growth in silica Optical Fibers in a Wide Range of Crack Velocities, J. Am. Ceram. Soc. **79**(1996), 51-57.
- 8.10 Rizzi, G., Fett, T., Finite Element study on semi-elliptical surface cracks in a cylinder, Scientific Working Papers **41**, 2016, ISSN: 2194-1629, Karlsruhe, KIT.
- 8.11 V.M. Sglavo and D.J. Green, Fatigue limit in fused silica, J. Eur. Ceram. Soc. **21** (2001) 561-567.
- 8.12 G. Rizzi, T. Fett, Finite Element study on a Vickers cone crack, Scientific Working Papers **4**, 2013, ISSN: 2194-1629, Karlsruhe, KIT.
- 8.13 V. Sglavo, T. Fett, K.G. Schell, M. J. Hoffmann, S. M. Wiederhorn, ν - K -data for silica from interrupted lifetime measurements, Scientific Working Papers **137**, 2020, ISSN: 2194-1629, Karlsruhe, KIT.
- 8.14 J. S. Aaldenberg, P. J. Lezzi, Measurement of the silica glass fatigue limit, J. Am. Ceram. Soc., **103** (2020), 3097-3103.
- 8.15 J.-P. Guin and S.M. Wiederhorn, Investigation of the Subcritical Crack Growth Process in Glass by Atomic Force Microscopy, Ceram. Trans. **199** (2007), 13-21.

9. Crack-tip shielding

9.1 Effect of local swelling at surface cracks

The stresses ahead a crack tip are according to eq. (7.1.2) nearly hydrostatic. Consequently, we obtain with the hydroxyl concentration S_0 for $\sigma_h=0$

$$S = S_0 \exp\left(\frac{\sigma_h \Delta V}{RT}\right) \quad (9.1.1)$$

where R is the universal gas constant, T the temperature in °K, and ΔV is the reaction volume. This relation implies that in the high crack-tip stress field nearly all water C_w is present in form of hydroxyl S . As could be deduced from density measurements, the hydroxyl generation results in a volume expansion ε_v according to eq.(1.1.9).

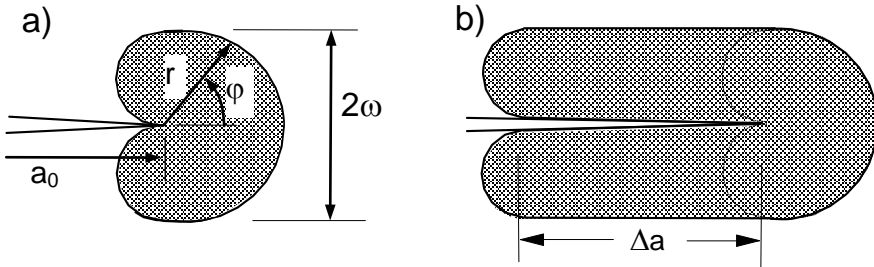


Fig. 9.1 a) Swelling zone at the tip of an arrested crack under mechanical loading, caused by stress-enhanced diffusion, b) zone for a crack grown by Δa .

For a sharp crack, the singular hydrostatic near-tip stresses are given as

$$\sigma_h = \frac{2}{3}(1 + \nu) \frac{K}{\sqrt{2\pi r}} \cos(\varphi/2) \quad (9.1.2)$$

where r and φ are the polar coordinates with the origin at the crack tip, Fig. 9.1a. As a consequence of eq.(9.1.1), very high hydroxyl concentrations and swelling strains must

occur in the crack-tip region. This allows the assumption that near a crack tip the water is present predominantly in the form of hydroxyl water.

9.2 Shielding stress intensity factors from measured water profiles

9.2.1 Shielding zone at a crack tip

Due to restrictions in free expansion, the swelling strains ε_v result in swelling stresses which give rise for the “shielding” stress intensity factor $K_{sh} < 0$. At first loading, the swelling zone at the crack tip $r(\sigma_h, \varphi)$ is heart-shaped as illustrated in Fig. 9.1a.

The height of the contour for constant hydrostatic stress σ_h is due to eq.(9.1.2)

$$\omega = \frac{(1 + \nu)^2}{4\sqrt{3}\pi} \left(\frac{K_I}{\sigma_h} \right)^2 \quad (9.2.1)$$

The shielding stress intensity factor caused by a swelling zone of height ω is [9.1]

$$K_{sh} = -\psi \frac{\varepsilon_v E}{1 - \nu} \sqrt{\omega} \quad (9.2.2)$$

where E is Young’s modulus and ν Poisson’s ratio. The zone of an arrested crack (not grown before loading) is heart-shaped, Fig. 9.1a, resulting in the coefficient $\psi=0$. When a crack has grown at least for $\Delta a \cong 5\omega$, Fig. 9.1b, a value of $\psi=0.22$ is reached as was shown by McMeeking and Evans [9.1] and confirmed in [9.2]. The coefficient ψ was computed in [9.1] also for different shapes at the zone end as illustrated in Fig. 9.2a, (A)-(C). Figure 9.2b shows the related coefficients ψ for the general representation by eq.(9.2.2) as the solid circles. We interpolate these data by an interpolating curve through the data points that can be expressed simply, see Appendix A1, by

$$\psi \cong 0.37 \left(1 - \frac{1}{2} \tanh \left(\frac{7}{9} \frac{r_0}{\omega} \right) \right) \quad (9.2.3)$$

As an application of this relation, the coefficient ψ may be estimated for a deviating zone shape. Computations of swelling zones are mostly carried out for diffusion in a motion-

less coordinate system with a fixed crack tip, i.e. for an *arrested* crack. Whereas for a *growing* crack the transversal diffusion normal to the crack plane is hardly affected by the moving crack tip, the diffusion and the crack propagation compete in crack direction [9.3, 9.4]. In [9.5] it was found for crack rates $v > 10^{-12}$ m/s under the assumption that the diffusion normal to the crack-plane direction is not affected by the crack rate ($v_{\perp} = 0$)

$$\frac{3}{4} \frac{8}{\sqrt{27}} < \frac{r_0}{\omega} < \frac{8}{\sqrt{27}} \tag{9.2.4}$$

For $r_0/\omega = 0.8 \times 8/\sqrt{27} \approx 1.23$, it results from eqs.(9.2.2, 9.2.3) a coefficient $\psi \approx 0.23$, introduced in Fig. 9.2b as the open circle.

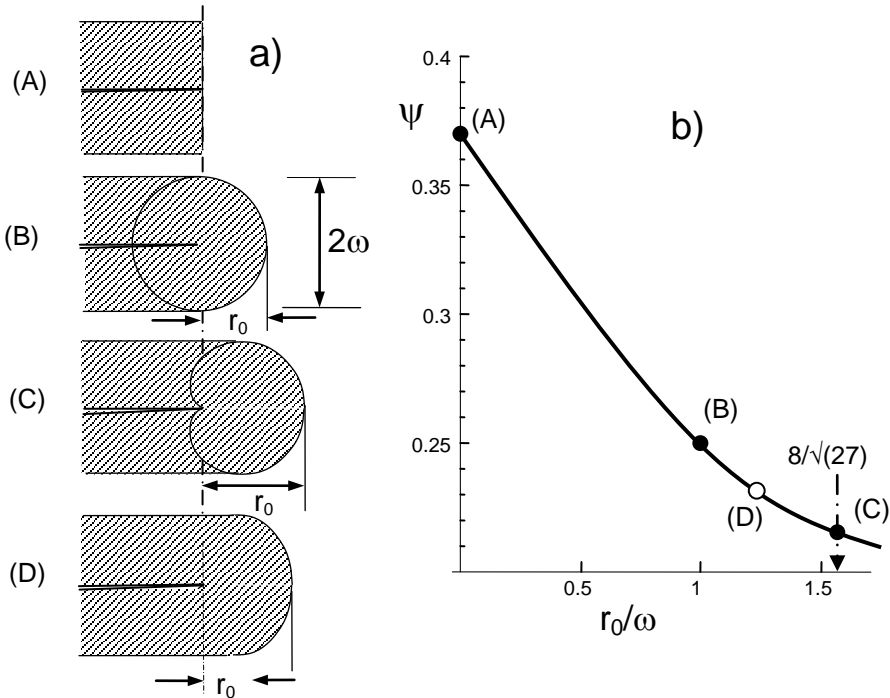


Fig. 9.2 Cracks grown for $\Delta z > 5\omega$, a) swelling zones with different shape at the zone end, b) shielding stress intensity factors by eq.(9. 2.2) (circles) and interpolating curve according to eq.(9.2.3) for the zone ends given in a), open circle represents the case of a growing crack with competing rates of crack rate and diffusion, case (D).

9.2.2 Shielding stress intensity factor for varying hydroxyl concentration

In Section 9.2.1 we considered zones with constant swelling volume ε_v . In the general case, we have to expect hydroxyl concentrations and swelling strains that decrease with distance from the crack. A Green's function procedure for such cases had been developed in [9.6]. Equation (9.2.2) holds for the case of a step-shaped constant strain $\varepsilon=\varepsilon_0$ inside and $\varepsilon=0$ outside the swelling zone. For the more general case, we have to subdivide the zone in parts of thickness $d\omega'$ at a distance, ω' , from the crack plane (Fig. 9.3).

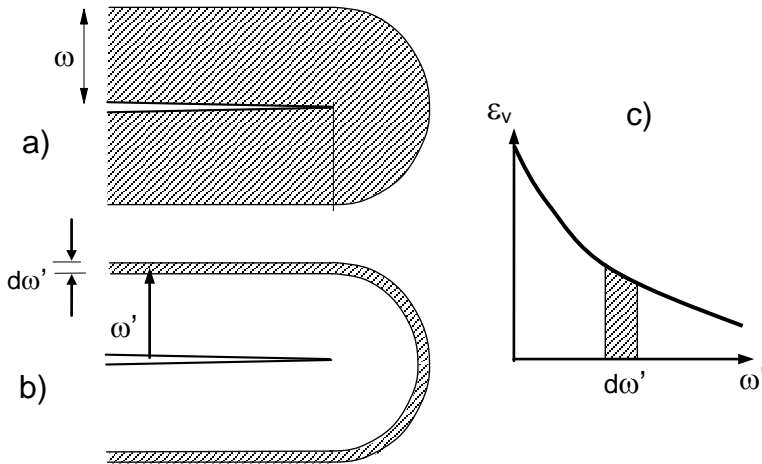


Fig. 9.3 a) Zone with constant S and ε_v , b) differential layer of thickness $d\omega'$, c) continuously varying swelling strain.

The stress intensity factor caused by this zone of strain $\varepsilon_v(\omega')$ results from (9.2.2) as

$$d(K_{sh}) = -\frac{1}{2} 0.22 \frac{\varepsilon_v E}{1-\nu} \frac{1}{\sqrt{\omega'}} d\omega' \quad (9.2.5)$$

Now the stress intensity factor for the varying ε_v results from

$$K_{sh} = \int_0^{\infty} \varepsilon_v h(\omega') d\omega' \quad (9.2.6)$$

with the Green's- or "weight function" h

$$h \stackrel{\text{def}}{=} -0.11 \frac{E}{1-\nu} \frac{1}{\sqrt{\omega'}} \quad (9.2.7)$$

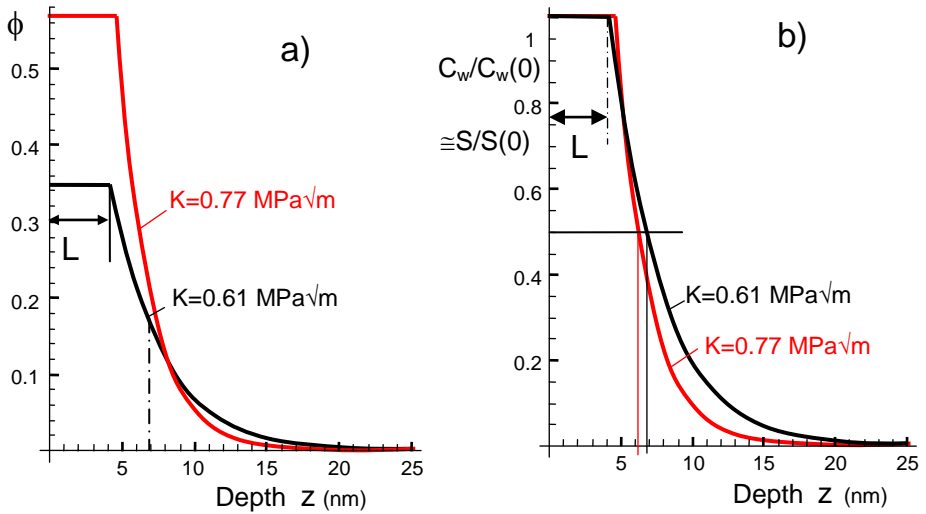


Fig. 9.4 Water profiles measured by Lechenault et al. [9.7] on DCDC specimens fractured in heavy water, a) water profiles expressed by the neutron reflectivity ϕ , b) normalized on the concentration at the surface.

9.3 Water profiles below crack faces of subcritically grown cracks

9.3.1 Results by Lechenault et al. [9.7]

Subcritical crack growth tests were carried out on DCDC specimens of silica by Lechenault et al. [9.7]. The water entrance into the fracture surfaces formed by the passage of the crack exposed to deuterium oxide D_2O was evaluated with a neutron reflection technique to measure the penetration of the deuterium oxide into the silica glass. The authors found a satisfactory fit to the reflection data by assuming that the water concentration was constant at the surface up to a distance of L , followed by an exponential de-

crease in concentration for distances greater than L . Consequently, Lechenault et al. [9.7] fitted their results by the expression

$$C_w / C_w(0) = \begin{cases} 1 & \text{for } z \leq L \\ \exp[-(z-L)/\eta] & \text{for } z > L \end{cases} \quad (9.3.1)$$

and found the parameters $L=4.3$ nm, $\eta=3.5$ nm for a region of low crack rates ($v \approx 10^{-8}$ m/s) at $K=0.61$ MPa·m^{1/2} and $L=4.6$ nm, $\eta=2.3$ nm for higher crack rates ($v \approx 4 \times 10^{-6}$ m/s) at $K=0.77$ MPa·m^{1/2}. These water profiles are illustrated in Fig. 9.4.

9.3.2 Result by Tomozawa et al. [9.8]

The concentration of water below the crack surfaces was measured by Tomozawa et al. [9.8] using the nuclear reaction analysis (NRA). The profile of the hydrogen concentration is shown in Fig. 9.5a. In order to allow an approximate extrapolation of measured data to the surface, we fitted the data c_H by a complementary error function

$$c_H = c_{H,0} \operatorname{erfc} \left[\frac{z}{2b} \right] + \underbrace{0.005 \times 10^{22} / \text{cm}^3}_{\text{Background}} \quad (9.3.2)$$

taking into account the background level of $0.005 \times 10^{22} / \text{cm}^3$. The coefficient $c_{H,0}$ is the surface concentration.

The red bar in Fig. 9.5a indicates the 90%-CI of the surface concentration. The depth b at which the concentration decreased to $\cong 50\%$ of the surface value in Fig. 9.5a is about 5 nm. By fitting (9.3.2) to the measurements, the best set of parameters was found in [9.9] to be

$$c_{H,0} = 1.30 [1.055, 1.55] 10^{22} / \text{cm}^3, \quad b = 4.95 [3.28, 6.61] \text{ nm (90\% CI)}.$$

with the mean squares sum of $11.65 (10^{22} / \text{cm}^3)^2$. The maximum hydroxyl concentration at $z=0$, $S(0)$, could be computed in [9.9] with the result

$$S(0) = 16.5 [14.4, 18.4] \text{ (wt\%)} \quad (9.3.3)$$

For a second description of the water distribution let us be guided by the results of Lechenault et al. [9.7]. We fitted the measurements by Tomozawa et al. [9.8] also via eq.(9.3.1) with the parameters

$$c_{H,0}=1.12 \cdot 10^{22}/\text{cm}^3, L=3.0 \text{ nm}, \eta=2.96 \text{ nm}$$

and a mean squares sum of $11.78 \times (10^{22}/\text{cm}^3)^2$. This result is shown in Fig. 9.5b. Having in mind the rather strong scatter of the surface values, the two representations in Figs. 9.5a and 9.5b are equal.

9.4 Computation of shielding stress intensity factors

9.4.1 Evaluation for undamaged material

Subtracting the background level and introducing eq.(9.3.2) into eq.(9.2.6) or (8.1.1), and assuming at the tip $S/S_0 \cong c_H/c_{H0}$, yields

$$K_{sh} = \int_0^{\infty} \kappa S(\omega') h(\omega') d\omega' = -\psi \sqrt{2/\pi} \frac{\kappa S(0)E}{1-\nu} \sqrt{b} \Gamma\left(\frac{3}{4}\right) \quad (9.4.1)$$

with the Euler Gamma function Γ that for the argument $3/4$ reads $\Gamma(3/4)=1.2254$, so that we can finally write with $\sqrt{2/\pi}\Gamma(3/4) = 0.9777 \cong 1$

$$K_{sh} \cong -\psi \frac{\kappa S(0)E}{1-\nu} \sqrt{b} \quad (9.4.2)$$

Comparing eqs.(9.2.2) and (9.4.2) allows to identify approximately: $b \cong \omega$. For the representation of the water profile by eq.(9.3.1), the evaluation of eq.(9.2.6) yields

$$K_{sh} = \int_0^{\infty} \kappa S(\omega') h(\omega') d\omega' = -\psi \frac{\kappa S(0)E}{1-\nu} \left(\sqrt{L} + \frac{1}{2} \sqrt{\pi\eta} \exp\left(\sqrt{\frac{L}{\eta}}\right) \operatorname{erfc}\left(\sqrt{\frac{L}{\eta}}\right) \right) \quad (9.4.3)$$

From the surface concentration in Fig. 9.5a, given by eq.(9.3.3), the shielding stress intensity factor results as

$$K_{sh} \cong -0.21 \text{ MPa}\sqrt{\text{m}} \quad (9.4.4)$$

For the description by eq.(9.3.1) we obtain:

$$K_{sh} \cong -0.20 \text{ MPa}\sqrt{\text{m}} \tag{9.4.5}$$

where $\cong 73\%$ of the total value come from the constant part of the water profile.

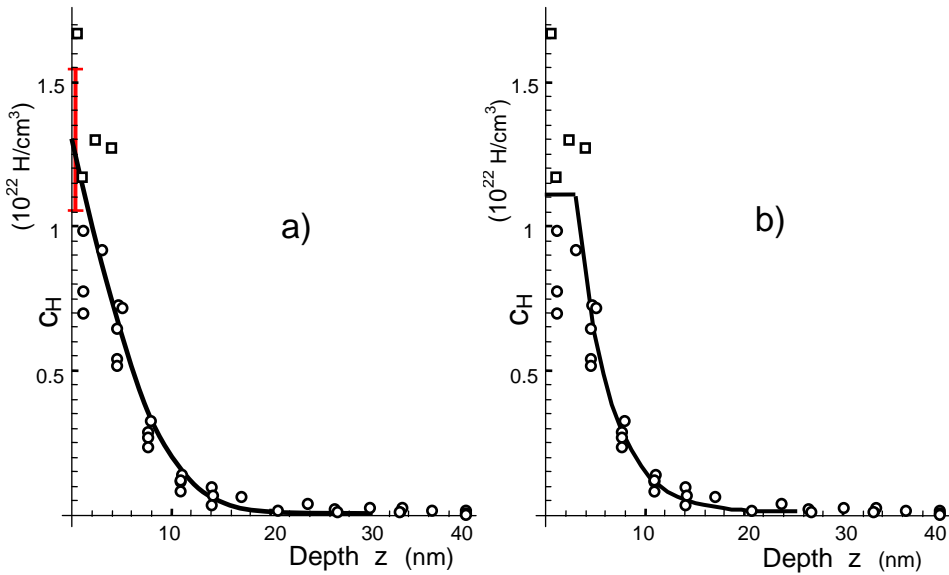


Fig. 9.5 Hydrogen concentration in the surface region of a growing crack via NRA-measurements by Tomozawa et al. [9.8], a) representation by eq.(9.3.2), b) expressed via eq.(9.3.1).

9.5 Crack-tip shielding and threshold behaviour

When a grown crack has been unloaded and is again loaded, the crack tip will only see loading by a stress intensity factor if $K_{appl} > K_{sh}$. Consequently, the shielding stress intensity factor causes a threshold value for the subcritical crack growth as is schematically illustrated in Fig 9.6b. The stress intensity at which K_{total} and crack growth rate disappear in a crack-growth test under monotonously decreasing loading may be denoted as $K_{appl}(K_{tip}=0) = K_0$ or K_{th} where “th” stands for “threshold”. Then it holds for a crack-arrest test under decreasing load

$$K_{total} = K_{appl} + K_{sh} = 0 \quad (9.5.1a)$$

or

$$K_0 = K_{th} = -K_{sh} \quad (9.5.1b)$$

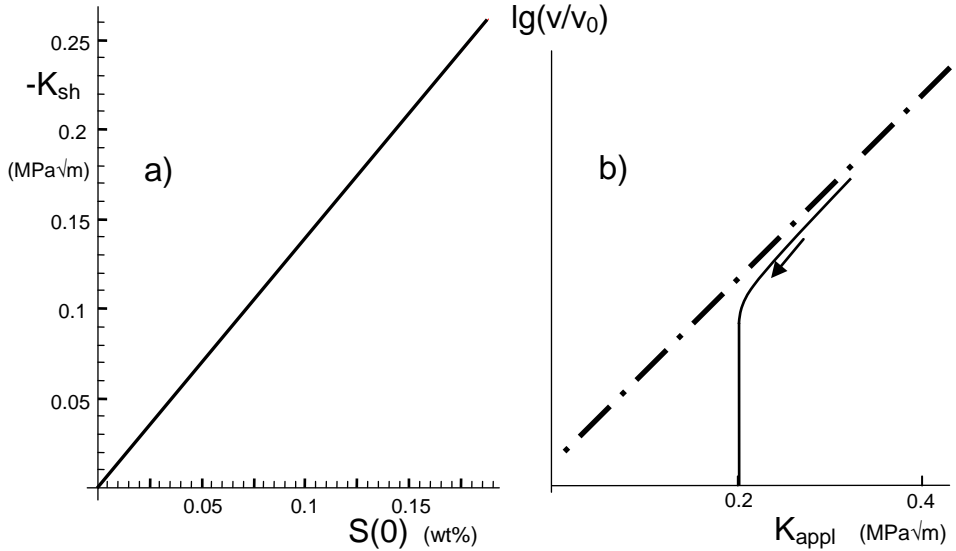


Fig. 9.6 a) Shielding stress intensity factors for the unloading case of $K_{total} = K_{appl} + K_{sh} < 0$, b) expected threshold values of the v - K_{appl} curve, schematic.

It should be emphasized that this threshold behaviour can only occur if the cracks have already grown subcritically (Fig. 9.1b). Cracks that are loaded for the first time can grow immediately, since the shielding zone has a heart-shaped contour (Fig. 9.1a) for which $K_{sh}=0$, [9.1]. The shielding stress intensity K_{sh} is plotted in Fig. 9.1 for a zone of height ω according to McMeeking and Evans [9.1]. These data can be simply described by Evans and Faber [9.10] as

$$\frac{K_{sh}}{K_{\infty}} = \frac{2}{\pi} \arctan(\Delta a / \omega) \quad (9.5.2)$$

The applied stress intensity factor for a constant applied load depends on the crack extension Δa via

$$\frac{K_{appl}}{K_{appl,0}} = \sqrt{1 + \frac{\Delta a}{a_0}} = \sqrt{1 + \frac{\Delta a / \omega}{a_0 / \omega}} \tag{9.5.3}$$

where $K_{appl,0}$ stands for $K_{appl,\Delta a=0}$.

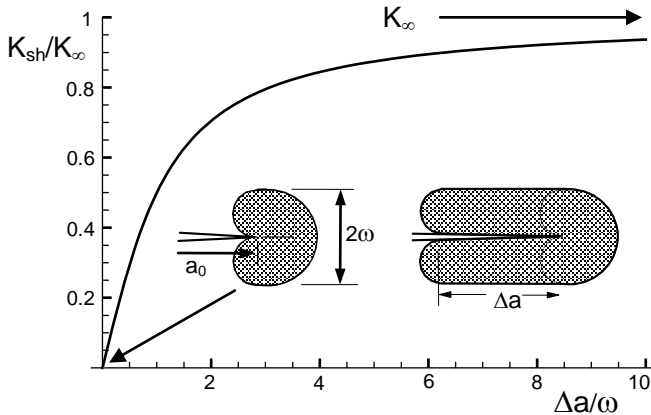


Fig. 9.7 Shielding stress intensity factor K_{sh} normalized on its saturation value K_{∞} , reached for $\Delta a/\omega \rightarrow \infty$ obtained by McMeeking and Evans [9.1].

For a crack growing at $K_{total} > 0$, the applied stress intensity factor increases and the shielding stress intensity factor becomes stronger negative. The total stress intensity factor must first increase and then decrease. After a minimum, the total stress intensity factor rises again.

The arrest condition is illustrated in Figs. 9.8a and 9.8b for short cracks of different initial lengths a_0/ω and varying saturation values K_{∞} of the shielding stress intensity factor. The shielding stress intensity factor can depend in principle on the externally applied load and the actual crack rate. For reasons of transparency we assume in Figs. 9.8a and 9.8b constant values for ω and K_{∞} . Crack arrest occurs in those cases for which the curves intersect the line $K_{total}=0$, indicated by the open circles. The dashed extensions are hypothetical total stress intensity factors which make no physical sense since stress singularities at a crack tip are only present for $K_{total} > 0$. From Fig. 9.8b it becomes obvious that subcritical crack growth for small cracks can take place below that threshold stress intensity factor that occurs in the case of cracks under decreasing loading (here $K_0=0.2 \text{ MPa}\sqrt{\text{m}}$).

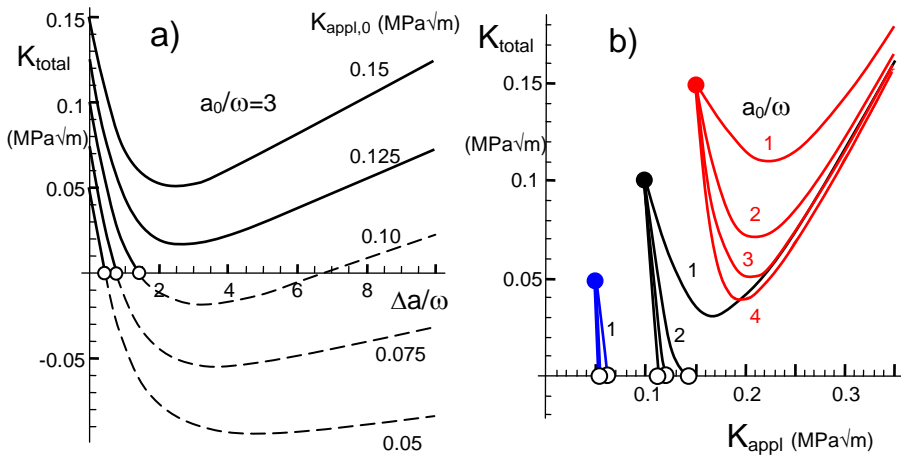


Fig. 9.8 Total stress intensity factor for $K_0 = -0.2 \text{ MPa}\sqrt{\text{m}}$, open circles: arrest condition $K_{total}=0$; a) K_{total} vs. Δa for $a_0=3\omega$, b) K_{total} vs. K_{appl} for different initial crack lengths a_0 and $K_0=0.2 \text{ MPa}\sqrt{\text{m}}$.

References

- 9.1 McMeeking, R.M., Evans, A.G., Mechanics of Transformation-Toughening in Brittle Materials, *J. Am. Ceram. Soc.* **65**(1982), 242-246.
- 9.2 G. Rizzi, T. Fett, Defects at silica surfaces and crack-tip shielding- A Finite Element Study, *Scientific Working Papers* **33**, 2015, ISSN: 2194-1629, Karlsruhe, KIT.
- 9.3 Zhao, T., Nehorai, A., Detection and localization of a moving biochemical source in a semi-infinite medium, Report, Electrical and Computer Engineering Dept. Univ. of Illinois, Chicago, USA.
- 9.4 Babich, V.M., On asymptotic solutions of the problems of moving sources of diffusion and oscillations, UDC 534.231.1, 517.226, 1991, pp. 3067-3071, Plenum Publishing Corp.
- 9.5 T. Fett, New contributions to R-curves and bridging stresses – Applications of weight functions, IAM 3, KIT Scientific Publishing, 2012, Karlsruhe.
- 9.6 S. M. Wiederhorn, T. Fett, G. Rizzi, M. J. Hoffmann, J.-P. Guin, The Effect of Water Penetration on Crack Growth in Silica Glass, *Engng. Fract. Mech.* **100**(2013), 3-16.

9.7 F. Lechenault, D.L. Rountree, F. Cousin, J.-P Bouchaud, L. Ponson and E. Bouchaud, Evidence of Deep Water Penetration in Silica during Stress Corrosion Fracture, *Phys. Rev. Let.* **106**(2011), 165504.

9.8 M. Tomozawa, W.-T. Han and W.A. Lanford, Water Entry into Silica Glass during Slow Crack Growth, *J. Am. Ceram. Soc.* **74** [10] (1991) 2573-2576.

9.9 G. Schell, G. Rizzi, T. Fett, Hydroxyl concentrations on crack surfaces from measurements by Tomozawa, Han and Lanford, *Scientific Working Papers* **82**, 2018, ISSN: 2194-1629, Karlsruhe, KIT.

9.10 Evans, A.G., Faber, K.T., Crack-growth resistance of microcracking brittle materials, *J. Am. Ceram. Soc.* **67**(1984), 255-260.

10 Anomalous subcritical crack growth

10.1 Anomalous and normal subcritical crack growth

Similar to other glasses, silica also shows the effect of subcritical crack growth. The fundamental effect, namely bond break processes, requires very high stresses. They are available in the singular stress field of cracks at crack-tip distances in the order of a few molecule diameters. Crack growth in silica glass has been well described by fracture mechanics techniques representing the mechanical load by the stress intensity factor.

Subcritical crack propagation of silica is usually presented in form of $v(K)$ -curves where v is the crack-growth rate and K the externally applied stress intensity factor. Results are reported as a function of relative humidity and temperature in [10.1-10.4]. For silica, the astonishing effect of decreasing crack-growth rate v at an increased temperature was observed for constant partial water pressure in the humid environment. This surprising result observed in v - K experiments by Suratwala and Steele [10.5] is called *anomalous subcritical crack growth* behavior. A comparison for different glasses is given in Fig. 10.1.

Whereas for silica the crack velocity decreases with temperature, it increases for all other glasses [10.5]. This conclusion is of course somewhat problematic since curves (1) and (2) are not for silicate glass and curves (3-6) obtained in vacuum cannot describe any influence that water might have. In addition, it is mentioned in [10.2] that silica in the vacuum tests failed not before toughness was reached. This implies a very steep v - K -curve and consequently subcritical crack growth at a value of $K=0.8 K_{Ic}$ could simply not be reached.

Suratwala and Steele [10.5] assume that the negative temperature dependence will stem from a change in the slow crack growth resistance of the glass upon exposure to temperature and stress. In the following considerations we will try to explain the effect by a simpler reason. In [10.6] we discussed the apparently incompatible temperature trends qualitatively.

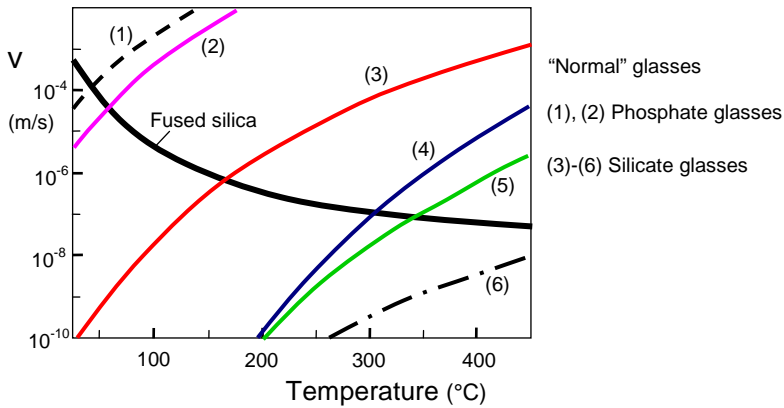


Fig. 10.1 Subcritical crack growth rate vs. temperature for different glasses at an individual stress intensity factor of $K=0.8 K_{Ic}$. Curves (1, 2, and silica): Measurements in N_2 at 2700 Pa partial water vapour pressure. Curves (3-6): measurements in vacuum [10.2]. Curves (1, 2): Phosphate glasses [10.7, 10.8]. Details can be found in [10.5].

10.2 Experimental crack growth results from literature

In order to discuss anomalous crack growth, two basic results from literature are compiled. In Fig. 10.2a v - K -curves for constant vapour pressure of $p=2100$ - 2200 Pa are plotted [10.5]. There is a clear *decrease* of crack velocity with increasing temperature visible and is the reason for the notation “anomalous subcritical crack growth”. Measurements on silica in liquid water were published by Wiederhorn and Bolz [10.1] as shown in Fig. 10.2b for the temperature region $2^\circ C \leq T \leq 90^\circ C$. From this figure it is evident that the crack-growth rates increase with increasing temperature. At first glance, this seems to be in contrast to the results of Suratwala and Steele [10.5].

In this Section it will be shown that the main difference between these contrary results is the fact of strongly different water vapour pressure in the two tests. Whereas in the tests of Fig. 10.2a the pressure was kept constant at 2.1-2.2 kPa, the saturation pressure varies in the water tests of Fig. 10.2b strongly, namely by a factor of >100 (0.6 kPa at $2^\circ C$ and 70 kPa at $90^\circ C$).

Consequently, the water concentrations at the crack tips are clearly different. This will be outlined in the following theoretical considerations.

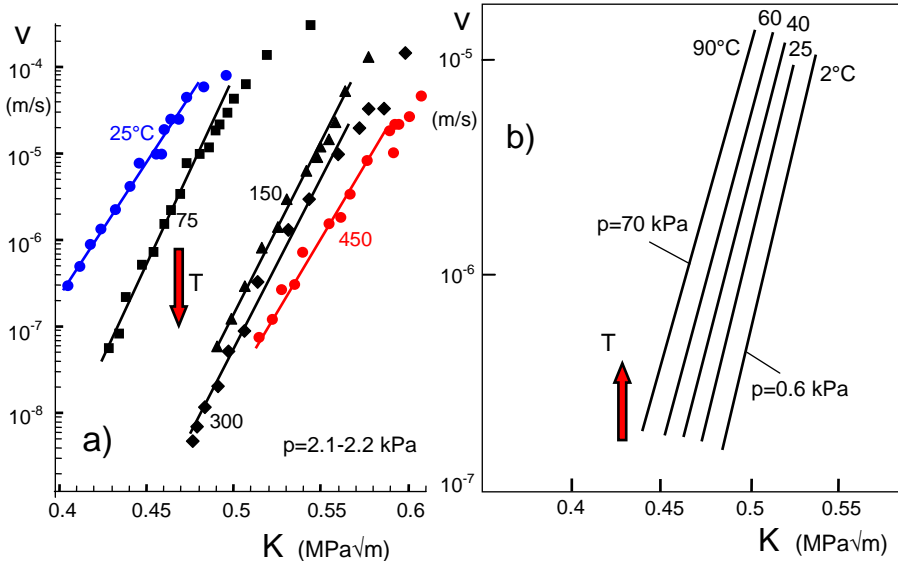


Fig. 10.2 a) v - K -curves for constant vapour pressure of $p=2.1-2.2$ kPa by Suratwala and Steele [10.7], b) v - K -curves in liquid water by Wiederhorn and Bolz [10.1].

10.3 Expectation from reaction rate theory

In [10.9] Wiederhorn et al. suggest for the subcritical crack growth rate v as a function of stress intensity factor K , and temperature

$$v = A_1 C k_r(T) \exp\left[\frac{-Q + bK}{RT}\right] \quad (10.3.1)$$

where again C is the concentration of molecular water [H₂O], T the temperature in °K, R the gas constant, Q the activation energy and A_1 and b are proportionality constants. In eq.(10.3.1) the quantity $k_r(T)$ is the rate coefficient for the single-step reaction showing the temperature dependency

$$k_r(T) \propto T \exp\left[\frac{-\Delta G}{RT}\right] \quad (10.3.2)$$

(ΔG =free energy of activation). From eqs.(10.3.1) and (10.3.2) we get with $Q_1=Q+\Delta G$

$$v = A_2 CT \exp\left[\frac{-Q_1 + bK}{RT}\right] \tag{10.3.3}$$

Under a water vapour pressure p , and the solubility for molecular water at $p=1$ kPa, C_{1kPa} , the water concentration reads

$$C = p C_{1kPa} \tag{10.3.4}$$

and equation (10.3.3) results in

$$v = A_2 p C_{1kPa} T \exp\left[\frac{-Q_1 + bK}{RT}\right] \tag{10.3.3a}$$

When evaluating the temperature dependence, it should be noted that both pressure and solubility also vary with temperature. These influencing factors will be considered in the following Sections.

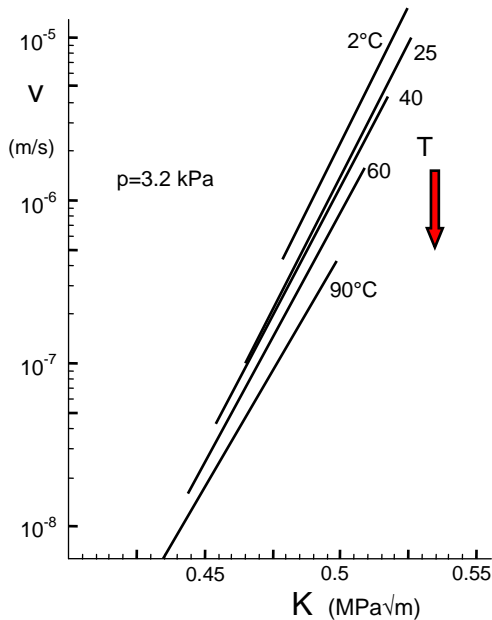


Fig. 10.3 v - K -curves in liquid water by Wiederhorn and Bolz [10.1], transformed to a common saturation pressure of 3.2 kPa (saturation pressure at 25°C) according to eq.(10.3.3a).

10.4 Effect of vapour pressure

The crack-growth rates from Fig. 10.2b are transformed by eq.(10.3.3a) to a constant vapour pressure of $p=3.2$ kPa (saturation pressure at 25°C), Fig. 10.3, exhibiting clearly the same temperature trend as found by Suratwala and Steele [10.5]. It should be noted that in the plot only the ordinate has been reduced to constant pressure and the abscissa values remain unaffected. From this plot one could claim that even in liquid water anomalous subcritical crack growth is present.

10.5 Effect of water solubility

Since the v - K -curves should depend on the water concentrations at glass surfaces, results of water concentrations are shown in Fig. 10.4 as a function of temperature. These data represent the concentrations of the molecular and hydroxyl water species derived in Section 4 of [10.10] on the basis of measurements by Zouine et al. [10.11] under saturation pressure. According to eqs. (4.1.3) and (4.1.4a) in [10.10] it results for the molecular water C in *mass units*

$$C = \frac{C_w}{1 + \frac{1}{2}k}, \quad (10.5.1)$$

and for the hydroxyl concentration S

$$S = \frac{17}{18} \frac{C_w}{\left(\frac{1}{2} + \frac{1}{k}\right)} \quad (10.5.2)$$

(C_w = total water concentration, k = equilibrium constant). Figure 10.4 shows the concentrations of the two water species $S \propto p$ and $C \propto p$ normalized on the water vapour pressure of $p=1$ kPa. The straight lines can be expressed by

$$\Rightarrow C_{1\text{kPa}} \cong \exp\left[-22.79 + \frac{35.84\text{kJ/mol}}{RT}\right] \quad (10.5.3)$$

$$S_{1\text{kPa}} \cong \exp\left[-19.41 + \frac{25.09\text{kJ/mol}}{RT}\right] \quad (10.5.4)$$

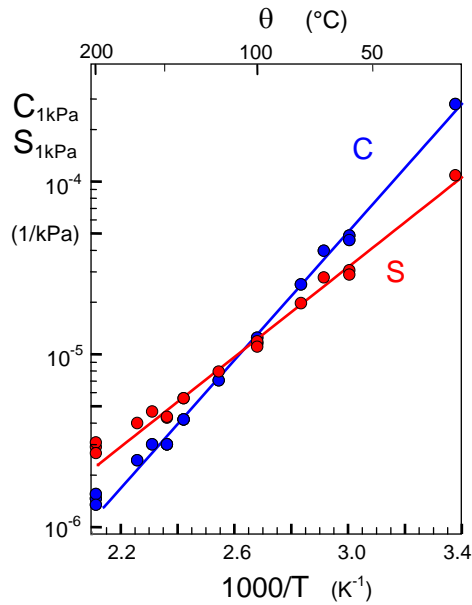


Fig. 10.4 Solubility of water species at silica surfaces under saturation pressure derived from data by Zouine et al. [10.11], water concentrations normalized on the saturation pressure.

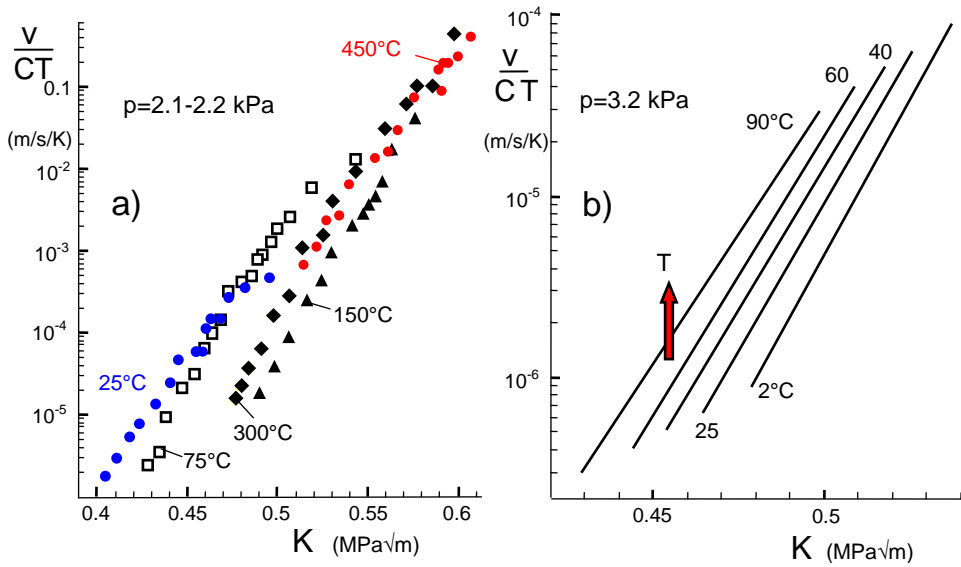


Fig. 10.5 Crack-growth rates normalized on the molecular water concentration and temperature T , a) data from Fig. 10.2a, b) data from Fig. 10.2b.

The crack velocities of Fig. 10.2 are plotted in Fig. 10.5 in the normalized representation as $v/(C \times T)$ vs. applied K for the partial water vapour pressure of $p=3.2$ kPa (i.e. the saturation pressure at 25°C). It can be seen that the temperature tendency of Fig. 4b is now again as normal crack-growth behaviour. This makes clear that even for constant vapour pressure the anomalous crack-growth behaviour is at least partially caused by the reduced surface water concentration with increasing temperature.

10.6 Effect of shielding stress intensity factor

10.6.1 Constant shielding

In our opinion, at least a part of the observed trend is caused by crack-tip shielding. In the preceding considerations we implicitly identified the externally applied stress intensity factor K_{appl} with the K -value acting at the crack tip, K_{tip} . It was early outlined in [10.12, 10.13] that a shielding stress intensity factor must develop as a consequence of volume increase by the hydroxyl generation (for references see e.g. [10.14]).

Computations by McMeeking and Evans [10.15] result in a shielding stress intensity factor for a grown crack which is surrounded by a zone of thickness ω undergoing a volume strain ε_v

$$K_{sh} = -\psi \frac{\varepsilon_v E}{1-\nu} \sqrt{\omega} \quad (10.6.1)$$

with $\psi=0.22$ [10.15]. E is Young's modulus and ν Poisson's ratio. In case of glass, ω is the thickness of the water diffusion zone around the crack tip.

It has been shown in [10.16] that water-induced swelling at crack tips generates an intrinsic stress intensity factor $K_{sh} < 0$ that shields a crack from an externally applied loading K_{appl} so that the stress intensity factor K_{tip} at the crack tip is reduced. The effective stress intensity factor acting at the crack tip, K_{tip} , represents the singular stress field at the tip. From the principle of superposition, K_{tip} is given by

$$K_{\text{tip}} = K_{\text{appl}} + K_{sh}, \quad K_{sh} < 0 \quad (10.6.2)$$

i.e. $K_{\text{tip}} < K_{\text{appl}}$.

The effect of the shielding stress intensity factor on the ν - K -curves was outlined in [10.16]. As shown by eq.(1.1.9), the volume strain ε_v is related to the hydroxyl concentration S by the proportionality $\varepsilon \propto S$. Consequently, it holds

$$K_{sh} = -\nu \frac{\kappa S E}{1-\nu} \sqrt{\omega} \quad (10.6.3)$$

again with $\kappa \approx 0.97$. The hydroxyl concentration S in the crack-tip stress field is thermally activated as eq.(1.1.3) implies. Since also the diffusivity is thermally activated, the water diffusion zone, $\omega = f(\sqrt{D}t)$, increases with temperature due to the increase of the diffusivity. When in a subcritical crack growth test the shielding stress intensity factor equals $-K_{appl}$, the total stress intensity factor K_{tip} disappears followed by abruptly decreasing crack rates, i.e. the threshold values K_{th} of the ν - K curve is reached. This is equivalent to

$$K_{th} = -K_{sh} \quad (10.6.4)$$

Threshold values for silica were evaluated by Sglavo et al. [10.17] on the basis of literature results, [10.18,10.19]. The threshold stress intensity factor as a function of temperature at ≈ 2 kPa partial water pressure was described by an Arrhenius temperature dependency

$$K_{th} \cong K_{th,0} \exp\left[\frac{-q}{RT}\right] \quad (10.6.5)$$

$K_{th,0} = 0.638 \text{ MPa}\sqrt{\text{m}}$, $q = 1.83 \text{ kJ/mol}$. The value $K_{th,0}$ in eq.(10.6.5) depends on the water partial pressure, for which unfortunately no measurements are currently available. For this reason, the procedure described here is not suitable for real predictions, but may be suitable for qualitative interpretations. Equations (10.6.4) and (10.6.5) make it possible to calculate the shielding stress intensity factor K_{sh} and via eq.(10.6.2) the total stress intensity factor K_{tip} acting at the crack tip. This value is responsible for the crack-tip stresses and subcritical crack growth rates.

Finally, Fig. 10.6 gives the curves of Fig. 10.5 vs. the difference $K_{appl} - K_{th}$. Under the assumption that $K_{sh} \neq f(K_{appl})$, the curves in Fig. 10.6 agree with the ν - K_{tip} curves. The diagrams of Fig. 10.6 show that, for the same water concentration, plotting against the stress intensity factor K_{tip} (actually prevailing at the crack tip) leads to normal subcritical crack growth in both cases, namely increasing crack rates with increasing temperature.

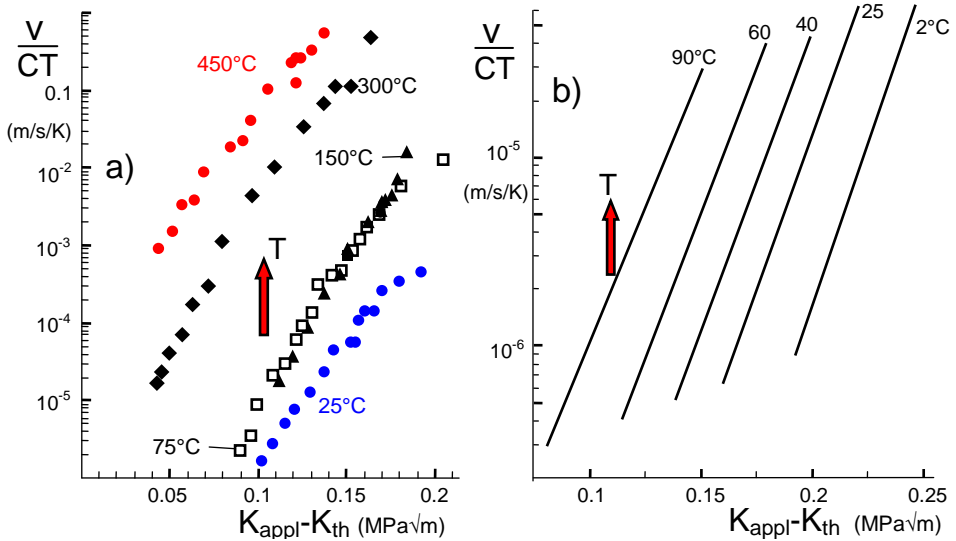


Fig. 10.6 Crack-growth rates from Figs.10.5a and 10.5b plotted vs. stress intensity factor $K_{\text{appl}} - K_{\text{th}}$.

10.6.2 Variable shielding

Deviations from the assumption of a constant shielding stress intensity factor K_{sh} have to be expected. With increasing crack-growth rates the time for the water entrance via diffusion decreases and, consequently, the zone height ω in eq.(10.6.3) becomes smaller. This yields in decreasing shielding stress intensity factor K_{sh} with increasing v or increasing load. A computation of $K_{\text{sh}}(K_{\text{appl}}, T)$ was performed in [10.6] resulting in rather complicated equations and should not be duplicated here.

An approximate method may be suggested to estimate K_{sh} or, equivalently, K_{tip} as a function of K_{appl} . For this purpose, let us use the results of Section 8.2 for the case that shielding K_{sh} disappears at fracture toughness, Fig. 8.4c. This situation is shown in Fig. 10.7. The total or tip-stress intensity factor $K_{\text{total}} = K_{\text{tip}}$ holds according to eq.(8.2.9)

$$K_{\text{tip}} = \frac{K_{\text{appl}} - K_{\text{th}}}{K_{\text{Ic}} - K_{\text{th}}} K_{\text{Ic}} \quad (10.6.6)$$

Figure 10.8 represents the v - K_{tip} results for the data in Figs. 10.5a and 10.5b. Even from these plots normal subcritical crack growth can be stated. With increasing temperature

the crack growth rates for identical water concentrations at the glass surfaces increase, too. This holds for tests in liquid water as well as tests in humid air.

Finally, Fig. 10.9a shows the stress intensity factor K_{tip} necessary for reaching a constant normalized crack velocity v/CT . There seems to exist a discontinuity in Fig. 10.9a between 75°C and 150°C. Figure 10.9b shows the applied stress intensity factor necessary to reach a crack velocity of $v=10^{-7}$ m/s at a partial water vapour pressure of $p_{H_2O}=2100-2200$ as a function of temperature. In both representations, there seems a change of the crack-growth behaviour visible at about 140°C. A possible reason might be capillary condensation at crack tips. A zone of liquid water can be identified at a crack tip at low temperatures in humid air as had been shown by Ciccotti et al. [10.20], Grimaldi et al. [10.21], and Pallares et al [10.22]. At the high temperatures this is no longer possible. So one would expect a discontinuity between tests in “water” and tests in humid air.

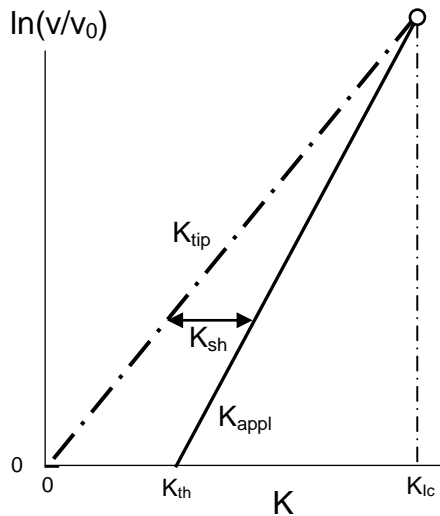


Fig. 10.7 Suggestion for the estimation of the v - K_{tip} curve.

For the slopes of the v - K -curves one would expect from the theoretical analysis by Wiederhorn et al. [10.9] according to eq.(10.3.1)

$$\log v \propto BK_{tip}, \quad B = \frac{b}{RT} \tag{10.6.7}$$

i.e. a decrease of B with increasing reciprocal absolute temperature T . From the subcritical crack growth rates of Fig. 10.8 the slopes, B , were determined. Additionally the parameter B for a representation by $\log(\dot{v}) \propto B K_{\text{appl}}$ is introduced for the data by Wiederhorn and Bolz [10.1]. The result is illustrated in Fig. 10.10a where the parameter B from eq.(10.6.7) is plotted. The squares show the results obtained from the data in [10.5] and the circles from data in [10.1].

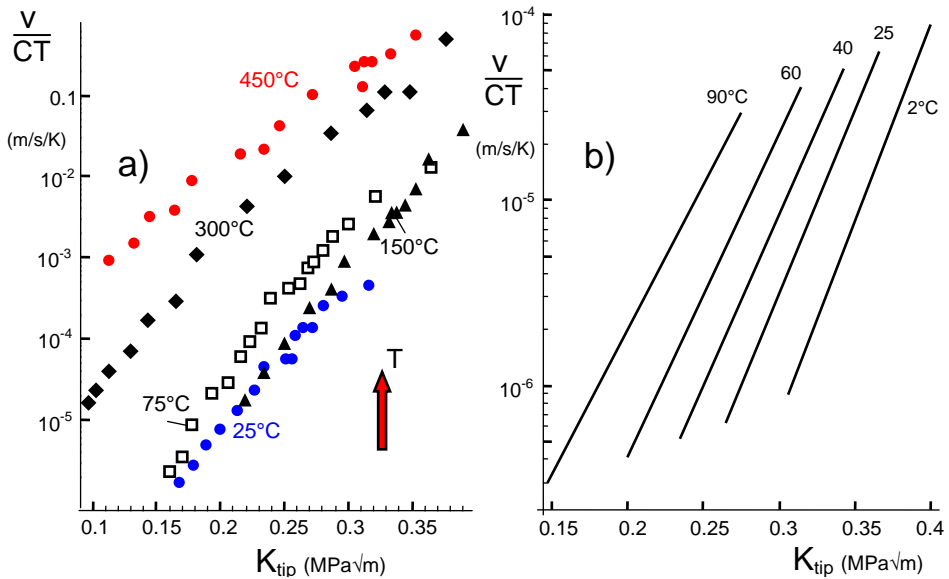


Fig. 10.8 Crack-growth rates from Figs. 10.5a and 10.5b plotted vs. total stress intensity factor K_{tip} .

The values of B increase with decreasing temperature. This applies to all results with the exception of the data by Suratwala and Steele [10.5] for temperatures below 150°C, see also the jump in Fig. 10.9a. Below this temperature, the effect seems to be slightly reversed. In Fig. 10.10b the parameter b defined in eq.(10.3.1) is shown. The parameter b is for the representation via K_{tip} a constant. This holds for the data from [10.1] and the data above $\approx 100^\circ\text{C}$ from [10.5] but decreases for lower temperatures as is included in Fig. 10.10b as the dashed line. The representation by eq.(10.6.7) yields (Standard Deviations in brackets)

$$b = 0.112[0.0017](\text{m}^{5/2}/\text{mol}) \quad \text{for [10.1]} \quad (10.6.8a)$$

$$b = 0.158[0.0073](\text{m}^{5/2}/\text{mol}) \quad \text{for } [10.5] \text{ and } \geq 150^\circ\text{C} \quad (10.6.8b)$$

For a representation by $\log(\dot{\nu}) \propto B K_{\text{appl}}$, Wiederhorn and Bolz [10.1] suggested $b=0.216 \text{ m}^{5/2}/\text{mol}$, introduced in Fig. 10.10b as the dash-dotted line.

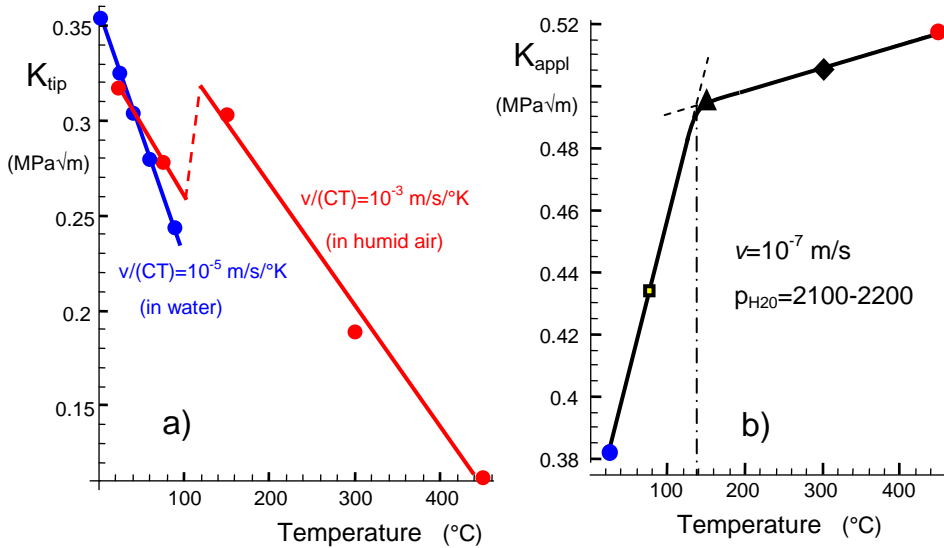


Fig. 10.9 a) Stress intensity factors K_{tip} for constant normalized subcritical crack growth rates $\dot{\nu}/(CT)$ as a function of temperature, red: results in humid air by Suratwala and Steele [10.5], blue: results in liquid water by Wiederhorn and Bolz [10.1], b) applied stress intensity factors necessary for a crack-growth rate of $\dot{\nu} = 10^{-7} \text{ m/s}$ at $p = 2100\text{--}2200 \text{ Pa}$ pressure.

10.6.3 Expectations for other glasses

In the previous considerations, only silica was considered. Here, we will look on other glasses, too. Density measurements on several glass compositions were reported by Scholze [23]. The materials were: (B) B_2O_3 -glass, (K) $\text{K}_2\text{O-SiO}_2$ -glass (20-80 mol-%), (Ca) $\text{Na}_2\text{O-CaO-SiO}_2$ -glass (16-10-74 mol-%), (Al) $\text{Li}_2\text{O-Al}_2\text{O}_3\text{-SiO}_2$ -glass (20-5-75 mol-%), and (Si) silica.

The related volume strains ε_v of all the glasses according to Section 2 in [10.10] are plotted in Fig. 10.11. Whereas the B_2O_3 -glass shows strong *volume shrinking* due to water

uptake, silica shows clear *volume expansion*. The effects on the other glasses are rather small. Materials Ca and Al also swell. K shrinks slightly.

In contrast to the crack-tip shielding for silica, it has to be expected that the B_2O_3 -glass B should exhibit an increase of total stress intensity factors. Slight shielding effects may occur in the soda-lime glass as well as in the Al-glass.

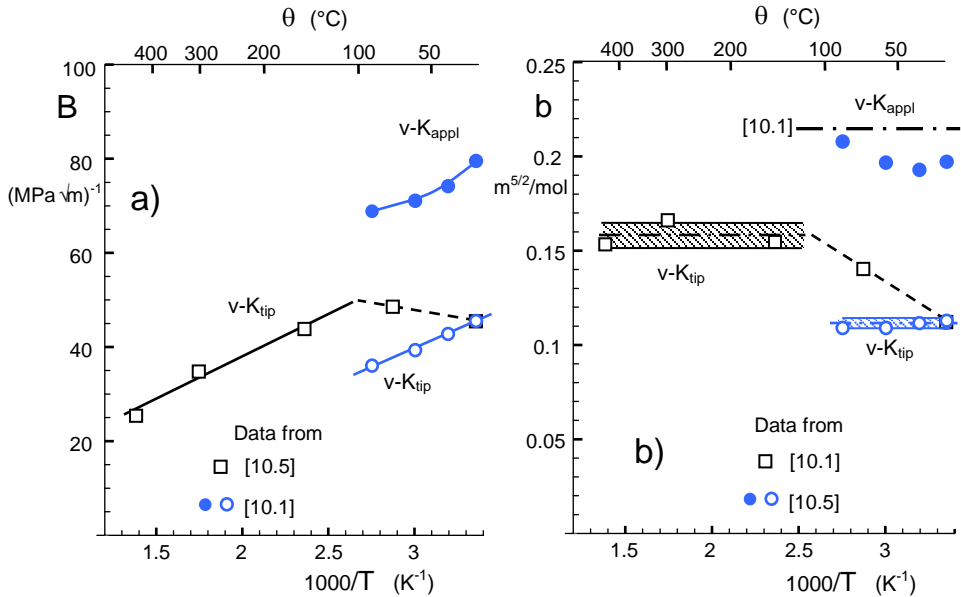


Fig. 10.10 a) Slopes B of subcritical crack growth curves $v(K_{tip})$ as a function of temperature, b) parameter $b = B \times RT$, hatched area: scatter ranges of ± 1 Standard Deviation, dash-dotted line: suggestion by Wiederhorn and Bolz [10.1].

Conclusions: We studied subcritical crack growth results measured by Suratwala and Steele [10.5] in water vapour and by Wiederhorn and Bolz [10.1] measured in liquid water under saturation pressure. From the results shown before, the *anomalous* subcritical crack growth in the experiments by Suratwala and Steele [10.5] is a consequence of the decreasing surface water solubility with increasing temperature and the plotting against the applied stress intensity factor K_{appl} instead of the physically acting value K_{tip} that governs the singular stress field at crack tips. With other words: Subcritical crack growth

in silica is *normal* since for constant water concentration at crack tips the crack-growth rate at constant, K_{tip} , increases with increasing temperature.

It is also noteworthy that if the temperature dependence of the saturation pressure is eliminated exclusively in the tests in liquid water [10.1], anomalous crack growth behaviour would appear (Fig. 10.3).

This suggests that the representation of v - K -curves for constant pressure instead of constant water concentration in the glass and by plotting the crack-growth rates vs. the applied stress intensity factor (instead of the physically relevant crack-tip stress intensity factor, K_{tip}) is responsible for the anomalous behaviour of silica.

Finally, it can be shown that the parameter b in eq.(10.3.1) is a constant if the crack-tip stress intensity factor K_{tip} is used for K .

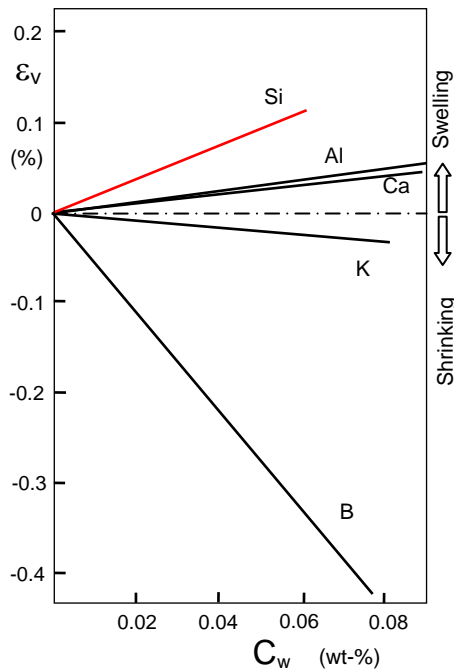


Fig. 10.11 Volume strains for several glasses from [10.10]. B: B_2O_3 -glass, K: K_2O - SiO_2 -glass (20-80 mol-%), Ca: Na_2O - CaO - SiO_2 -glass (16-10-74 mol-%), Al: Li_2O - Al_2O_3 - SiO_2 -glass (20-5-75 mol-%), Si: Silica

References

- 10.1 S.M. Wiederhorn and L.H. Bolz, Stress Corrosion and Static Fatigue of Glass, *J. Am. Ceram. Soc.* **53**[1810] 543-548 (1970).
- 10.2 S.M. Wiederhorn, H. Johnson, A.M. Diness and A.H. Heuer, Fracture of Glass in Vacuum, *J. Am. Ceram. Soc.* **57** [188] 336-341 (1974).
- 10.3 S. Sakaguchi and Y. Hibino, Fatigue in low-strength silica optical fibres, *J. Mater. Sci.* **19** 3416-3420 (1984).
- 10.4 M. Muraoka and H. Abé, Subcritical Crack Growth in silica Optical Fibers in a Wide Range of Crack Velocities, *J. Am. Ceram. Soc.* **79**[181] 51-57 (1996).
- 10.5 T.I. Suratwala and R.A. Steele, Anomalous temperature dependence of sub-critical crack growth in silica glass, *J. Non-Crystalline Sol.* **316** 174-182 (2003).
- 10.6 T. Fett, K.G. Schell, E.C. Bucharsky, M.J. Hoffmann, Anomalous subcritical crack growth in silica, *Glass Physics and Chemistry*, **47**(2021), 581-589.
- 10.7 T.I. Suratwala, R.A. Steele, G.D. Wilke, J. Campbell, *J. Non-Crystalline Sol.* **263/264** (2000), 213.
- 10.8 S. Crichton, M. Tomozawa, J. Hayden, T. Suratwala, J. Campbell, *J. Am. Ceram. Soc.* **82** (1999), 3097.
- 10.9 S.M. Wiederhorn, E.R. Fuller, R. Thomson, Micromechanisms of crack growth in ceramics and glasses in corrosive environments, *Metal Science*, Aug-Sept (1980), 450-458.
- 10.10 T. Fett, G. Rizzi, K.G. Schell, E.C. Bucharsky, P. Hettich, S. Wagner, M. J. Hoffmann, Consequences of hydroxyl generation by the silica/water reaction Part I: Diffusion and Swelling, KIT Scientific Publishing, Karlsruhe.
- 10.11 A. Zouine, O. Dersch, G. Walter and F. Rauch, Diffusivity and solubility of water in silica glass in the temperature range 23-200°C, *Phys. Chem. Glass: Eur. J. Glass Sci and Tech. Pt. B*, **48** [2] (2007), 85-91.
- 10.12 S. M. Wiederhorn, T. Fett, G. Rizzi, S. Fünfschilling, M.J. Hoffmann, J.-P. Guin, Effect of Water Penetration on the Strength and Toughness of Silica Glass, *J. Am. Ceram. Soc.* **94** [S1] (2011), 196-S203.
- 10.13 S.M. Wiederhorn, T. Fett, G. Rizzi, M. Hoffmann, J.-P. Guin, Water Penetration – its Effect on the Strength and Toughness of Silica Glass, *Met. Mater. Trans. A*, **44**(2013) [3], 1164 -1174.

- 10.14 Shelby, J.E., Density of vitreous silica, *J. Non-Cryst.* **349** (2004), 331-336.
- 10.15 McMeeking, R.M., Evans, A.G. Mechanics of transformation-toughening in brittle materials, *J. Am. Ceram. Soc.* **65**(1982), 242–246.
- 10.16 Wiederhorn, S.M., Fett, T., Rizzi, G., Hoffmann, M.J., Guin, J.-P., The Effect of Water Penetration on Crack Growth in Silica Glass, *Engng. Fract. Mech.*, **100** (2013), 3–16.
- 10.17 V. Sglavo, T. Fett, K.G. Schell, M.J. Hoffmann, S.M. Wiederhorn, v - K -data for silica from interrupted lifetime measurements, **144**, 2020, ISSN: 2194-1629, Karlsruhe, KIT.
- 10.18 V.M. Sglavo and D.J. Green, Fatigue limit in fused silica, *J. Eur. Ceram. Soc.* **21** (2001) 561-567.
- 10.19 J. S. Aaldenberg, P. J. Lezzi, Measurement of the silica glass fatigue limit, *J. Am. Ceram. Soc.*, **103**(2020), 3097-103.
- 10.20 M. Ciccotti, M. George, V. Ranieri, L. Wondraczek, and C. Marliere, Dynamic Condensation of Water at Crack Tips in Fused Silica Glass, *J. Non Cryst. Solids*, **354** [2–9] 564–8 (2008).
- 10.21 A. Grimaldi, M. George, G. Pallares, C. Marniere, M. Ciccotti, The crack tip: A nanolab for studying confined liquids, *Phys. Rev. Letters*, **100**, 165505 (2008).
- 10.22 G. Pallares, A. Grimaldi, M. George, L. Ponson, M. Ciccotti, Quantitative analysis of crack closure driven by Laplace pressure in silica glass, *J. Am. Ceram. Soc.* **94**(2011), 2613-2618.
- 23 Scholze, H., Glas, Springer Verlag, Berlin, 1988.

Consequences of hydroxyl generation by the silica/water reaction

Part III: Damage and Young's Modulus

11 Damage and Young's modulus

11.1 Damage by hydroxyl generation

When a hydroxyl has been formed, the initial silica ring is broken and the mechanical cohesion is weakened as is illustrated in Fig. 11.1. Such “defects” in the glass structure can be treated by using the damage variable D of continuum damage mechanics (Kachanov [11.1], Lemaitre [11.2]). This parameter is proportional to the density of micro-defects.

According to the postulate of strain equivalence by Lemaitre [11.3], the effective elastic modulus, E_D , decreases with increasing damage

$$E_D = E_0(1 - D) \quad (11.1.1)$$

where E_0 is the modulus of virgin glass. The damage variable D can be determined from module measurements via eq.(11.1.1). The occurrence of this effect is in principle known from measurements on NaO-SiO₂ glass by Ito and Tomozawa [11.4]. To the authors' knowledge, so far no comparable uni-axial measurements on fused silica are available. Therefore, we temporarily consider the damage D as a certain function of the hydroxyl concentration:

$$D = f(S) \quad (11.1.2)$$

Apart from the equi-triaxial loading case with $\sigma_x = \sigma_y = \sigma_z$ (including the case of disappearing stresses), the elastic modulus must become a tensor with components depending on the degree of loading multiaxiality.

Since this possibility would make the further treatment very difficult [11.3] and non-transparent, we assume in the following considerations that the damage remains isotropic and is considered to be of scalar nature. This is equivalent to the assumption of randomly orientated defects. Then also E remains isotropic. We assume that the defects in SiO₂, caused by hydroxyl generation, might behave like normal nano-pores.

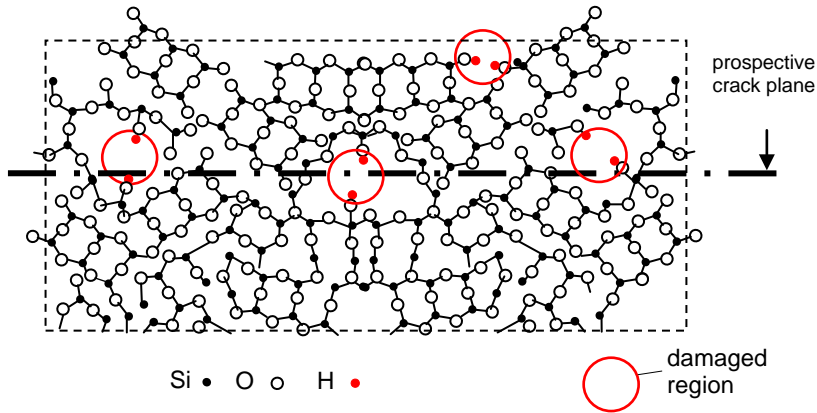


Fig. 11.1 Volume element of silica showing damage by bond breaking due to the water/silica reaction, third dimension ignored.

11.2 Experimental evidence for modulus reduction in silica

In literature, there is experimental evidence for modulus decrease with increasing hydroxyl content. This can be seen from measurements of sound velocity as a function of water content. Measurements on longitudinal sound velocities in silica specimens with different water content were reported by Fraser [11.5] and Le Parc et al. [11.6]. Individual least-squares fits were made resulting for the data set by Fraser [11.5]

$$v \cong 5974(1 - 4.185S) \quad \text{in (m/s)} \quad (11.2.1)$$

and the set by LeParc et al. [11.6]

$$v \cong 5959(1 - 5.34S) \quad \text{in (m/s)} \quad (11.2.2)$$

When we normalize the results of the two test series on their individual values for $S=0$, we get the representation in Fig. 11.2a. A common straight-line fit of these data yields

$$\frac{v}{v_0} = 1 - BS \quad (11.2.3)$$

with the parameter

$$B=5.04 [4.23, 5.85]$$

(90%-Confidence Intervals, CI, in brackets). The dependency of eq.(11.2.3) is introduced in Fig. 11.2a as the straight line. The longitudinal sound velocity depends on Young's modulus E and density ρ via $v \propto \sqrt{E/\rho}$.

Whereas the densities for the measurements by Fraser are compiled in [11.5], we used for the results by LeParc et al [11.6] S according to the measurements by Shelby [11.7] (see also Section 2.1 in [11.8]):

$$\frac{E_D}{E_0} = \rho / \rho_0 \times (v/v_0)^2 = 1 - \lambda S \quad (11.2.4)$$

with $\lambda=10.6$ [8.7, 12.5]. It has to be noted that this value holds for isotropic damage since the natural OH-content doesn't show any preference for a special direction. The Young's modulus resulting from the data by Fraser [11.5] is shown in Fig. 11.2b.

Figure 11.2b represents in addition stiffness coefficients C_{11} by the triangles as were reported by Kushibiki et al. [11.9].

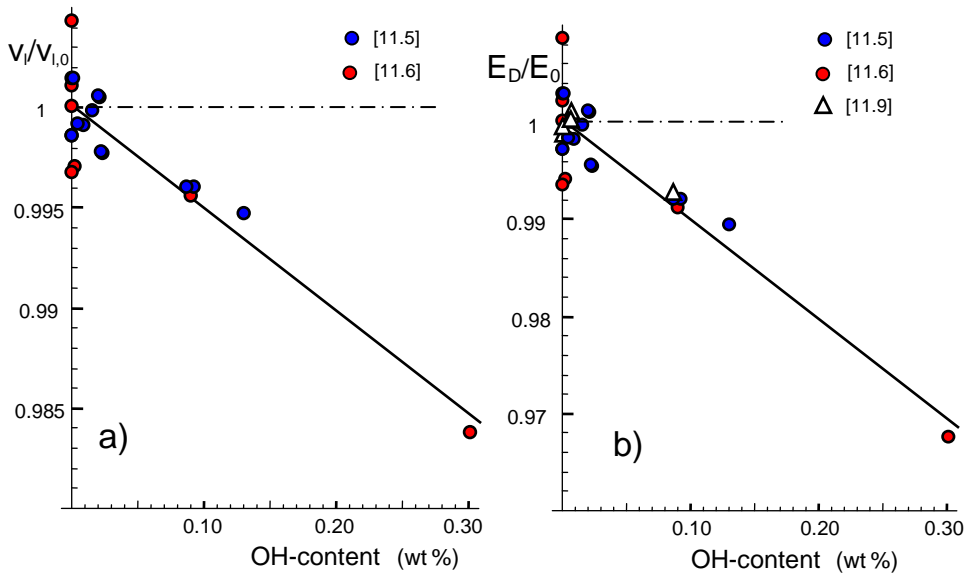


Fig. 11.2 a) Longitudinal sound velocity in silica with different OH-content (blue circles: results by Fraser [11.5], red circles: results by LeParc et al. [11.6]), b) Young's modulus for the data of Fig. 11.2a together with stiffness results by Kushibiki et al. [11.9] as the triangles.

11.3 Modelling of damage by spherical pores

Analytical computations on the reduction of Young's modulus with porosity were carried out by Wang [11.10] for spherical pores of equal size and constant spacing. Unfortunately, the results were given as tabulated data. They were the basis of a number of fitting relations, mostly using exponential functions, which trivially must fail for large porosities since they could not represent the requirement of $E=0$ for a finite critical porosity. An overview can be obtained in [11.11, 11.12].

To overcome such problems, we fitted the analytical data by Wang [11.10] according to

$$\frac{E_D}{E_0} = \exp \left[-A_1 P - \frac{A_2}{(P_{\max} - P)^{1/8}} P^2 \right] \quad (11.3.1)$$

with $P_{\max}=0.4764$ from [11.10] and the free fitting parameters A_1 and A_2 resulting as

$$A_1 = 3.580 [3.565, 3.595], \quad A_2 = 3.747 [3.699, 3.795]$$

with very narrow 90% confidence intervals indicating the good agreement with the numerical data. Figure 11.3a shows good agreement between eq.(11.3.1) and the numerical data entered by the circles. The dashed line indicates the initial slope that for small porosities reads

$$\frac{E_D}{E_0} \cong 1 - A_1 P \quad (11.3.2)$$

and intersects the abscissa at a characteristic porosity P_c of

$$P_c = 1/A_1 = 0.278 P_{\max} \quad (11.3.3)$$

In order to give a better resolution for the agreement at low modules, Fig. 11.3b represents the same results in logarithmic ordinate scaling. For our purpose we rewrite eq.(11.3.1) by normalizing the porosities on the maximum value P_{\max} and then replace P by S

$$\frac{E_D}{E_0} = \exp \left[-B_1 (S/S_{\max}) - \frac{B_2}{(1 - S/S_{\max})^{1/8}} \left(\frac{S}{S_{\max}} \right)^2 \right] \quad (11.3.4)$$

with parameters $B_1=1.667$, $B_2=0.933$. From eq.(11.2.4) and the initial slope of eq.(11.3.4) we obtain via $B_1/S_{\max}=\lambda$ the maximum value of hydroxyl concentration

$$S_{\max} = \frac{B_1}{\lambda} = 0.157 [0.133, 0.192] \quad (11.3.5)$$

A simpler pore model was proposed by Phani and Niyogi [11.13] with the result of

$$\frac{E_D}{E_0} = (1 - aP)^n \quad (11.3.6)$$

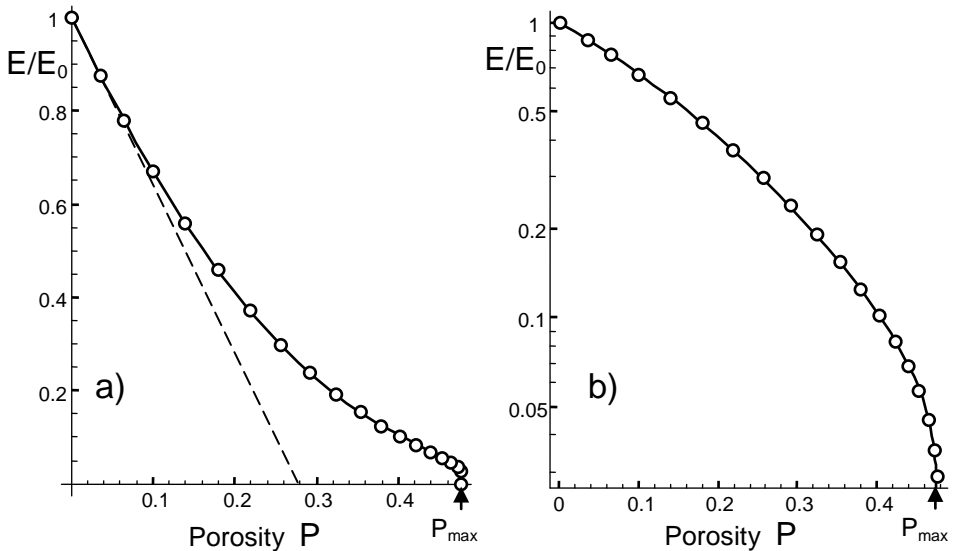
This type of equation applied to the hydroxyl damage gives good agreement with the Wang solution over a large range of hydroxyl concentrations for the parameter set

$$n=2, a=\lambda/2 \cong 5.3 \quad (11.3.7)$$

The modulus ratio can be described by

$$\frac{E_D}{E_0} = (1 - S/S_{\max})^2 \quad (11.3.8)$$

The related dependency is shown in Fig. 11.3c by the red curve that gives disappearing of Young's modulus at $S_{\max}=0.188 [0.16, 0.23]$.



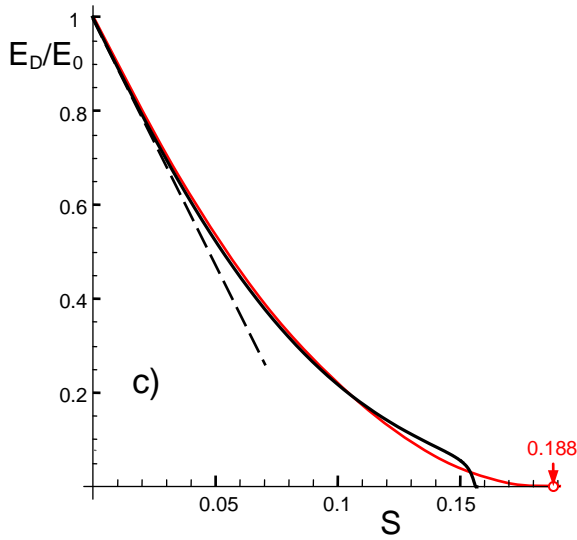


Fig. 11.3 a) Effect of porosity on Young's modulus for spherical pores; analytical results from Wang [11.10] (circles) compared with suggested fitting relation eq.(11.3.1) (curve); b) logarithmic ordinate scaling, c) Young's modulus as a function of hydroxyl concentration.

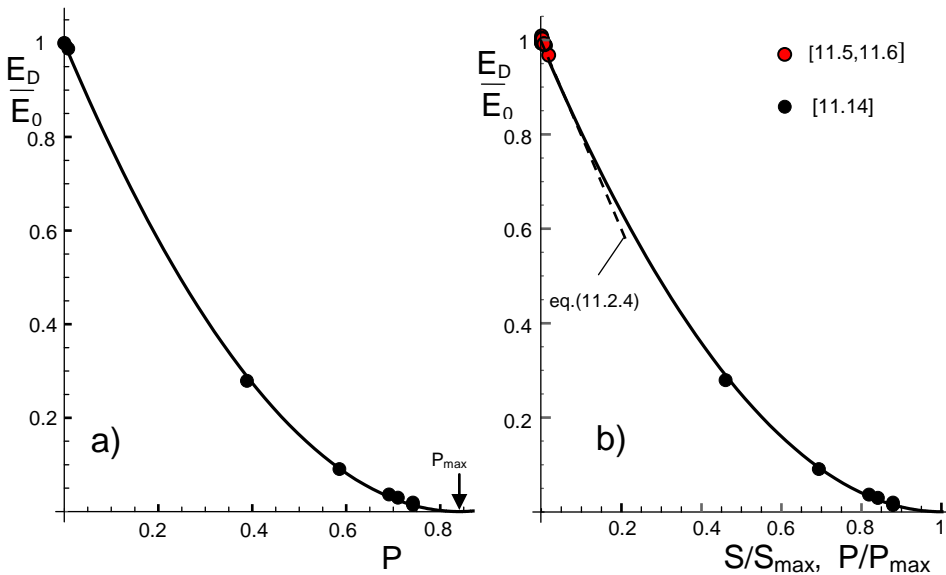


Fig. 11.4 a) Results of porosity on Young's modulus for silica by Adachi and Sakka [11.14], curve: best fit according to eq.(11.3.6), b) comparison with results from longitudinal sound velocity in silica for different OH-content (red circles: results by LeParc et al. [11.6] and Fraser [11.5]).

The fact that eq.(11.3.6) is an appropriate description for silica glass in the region of low moduli $E_D E_0 \rightarrow 0$, as can be seen from measurements by Adachi and Sakka [11.14], plotted by the circles in Fig. 11.4a. By fitting the data, we obtain the best representation for the parameter set:

$$n=2, a=1.19 \quad (11.3.9)$$

introduced in Fig. 11.4a by the circles. Figure 11.4b shows all measurements from Figs. 11.2 and 11.4a in a normalized representation. The dashed line illustrates a linear extension of the small-concentration data.

11.4 Effect of damage in thin surface layers

11.4.1 Global stress

If the damage is concentrated on thin surface layers of a thickness d that is small to the undamaged bulk thickness W , $d \ll W$, the strain in the damaged surface layer must equal the strain in the bulk:

$$\varepsilon = \frac{\sigma_D}{E_D} = \frac{\sigma_0}{E_0} \quad (11.4.1)$$

The reduced average stress in the damaged surface, σ_D , is therefore according to eq.(11.1.1)

$$\sigma_D = \sigma_0(1 - D) \quad (11.4.2)$$

(σ_0 = stress in the undamaged bulk).

External loading in z -direction will increase the distance between atoms of the ring structure, resulting in the strain ε_z in loading direction. Failure of the material is reached, when the strain reaches a critical value ε_c . The damage in the material affects also the load-bearing capacity of any area element since it reduces its net cross section and, consequently, the strength of the damaged material σ_f . If $\sigma_{f,0}$ denotes the strength in the absence of damage, the strength of the damaged material is

$$\sigma_{f,D} = \sigma_{f,0}(1 - D) \quad (11.4.3)$$

The strength of water-damaged silica fibres is strain-controlled for $d \ll W$. This means that the strain at failure ε_c is the same in the surface layer and the bulk. This condition yields

$$\varepsilon_c = \frac{\sigma_{f,D}}{E_D} = \frac{\sigma_{f,0}(1-D)}{E_0(1-D)} = \frac{\sigma_{f,0}}{E_0} \quad (11.4.4)$$

Equation (11.4.4) tells us that the damage problem can be handled simply by using bulk material parameters ($E_0, \sigma_{f,0}$) since the damage by broken bonds cancels out in (11.4.4). For some more details on fiber strength, see Section 11.7.

11.4.2 Effect on crack resistance and stress intensity factors

The damage of the initial ring structure of silica, Fig. 11.1, must also affect the resistance against crack propagation. The crack growth resistance G_c represents the energy necessary to split all bonds that are broken when the crack has passed the considered volume element. Application of the damage variable yields for the crack growth resistance of the damaged material, $G_{c,D}$,

$$G_{c,D} = G_{c,0}(1-D) \quad (11.4.5)$$

($G_{c,0}$ =crack resistance for the undamaged material, $D=0$) or in terms of stress intensity factors

$$K_{c,D} = \sqrt{E G_{c,D}} = K_{Ic}(1-D) \quad (11.4.6)$$

where $K_{c,D}$ is the reduced toughness of the damaged material and K_{Ic} the fracture toughness measured in fracture mechanics tests on the undamaged material.

In the special case of a crack *fully embedded* in a material of reduced but constant modulus, E_D , the problem simplifies strongly. The applied stress intensity factor is generally given by

$$K_{appl} = \sigma_{appl} F \sqrt{\pi a} \quad (11.4.7)$$

(F =Fracture mechanics geometric function, a =crack length, Fig. 11.5).

Using the actual stress from eq.(11.4.2), K_{appl} reads for the crack fully embedded in the damaged zone

$$K_{\text{appl},D} = \underbrace{\sigma_{\text{appl},0} F \sqrt{\pi a}}_{K_{\text{appl},0}} (1-D) = K_{\text{appl},0} (1-D) \quad (11.4.8)$$

where $K_{\text{appl},0}$ stands for the applied stress intensity factor formally computed with stresses σ_0 as present in the bulk material

$$K_{\text{appl},0} = \sigma_0 F \sqrt{\pi a} \quad (11.4.9)$$

From (11.4.6), (11.4.8) and (11.4.9) it results equivalently to eq.(11.4.4)

$$\frac{K_{\text{appl},D}}{K_{c,D}} = \frac{K_{\text{appl},0} (1-D)}{K_{Ic} (1-D)} = \frac{K_{\text{appl},0}}{K_{Ic}} \quad (11.4.10)$$

Also in terms of stress intensity factors, surface cracks fully embedded in the surface layer can be handled simply by using bulk material parameters (K_{appl} , K_{Ic}) instead of the unknown parameters in the layer.

11.4.3 Effect on pre-existing dimples

By removing the plastic protective coating on fibers with an acid, defects will be generated that can be described as hemispherical pits [11.15]. Depending on their geometry, such defects can reduce the surface strength clearly.

At the deepest point of a pit surrounded by the hydroxyl-damaged material under tensile stress σ_D , the stress is increased by the stress-concentration factor β , so that the maximum stress at the deepest point (A), Fig. 11.5, is

$$\sigma_{\text{max},D} = \beta \sigma_D \quad (11.4.11a)$$

For a half-sphere it is for instance $\beta \approx 2$. Before the hydroxyl-damaged layer was generated, it did hold equivalently for the undamaged material under stress σ_0

$$\sigma_{\text{max},0} = \beta \sigma_0 \quad (11.4.11b)$$

From (11.4.11a) and (11.4.11b) we have to conclude that in the case of failure the strengths in presence and absence of hydroxyl damage are reduced both by the common factor $1/\beta$. When the strengths in presence of the pit are denoted by $\sigma_{f,pit,D}$ and $\sigma_{f,pit,0}$, it holds

$$\sigma_{f,pit,0} = \frac{1}{\beta} \sigma_{f,0} \quad (11.4.12a)$$

$$\sigma_{f,pit,D} = \frac{1}{\beta} \sigma_{f,D} \quad (11.4.12b)$$

Apart from the fact that the strengths are reduced, it can be seen from the combined eqs.(11.4.12a) and (11.4.12b)

$$\frac{\sigma_{f,pit,D}}{\sigma_{f,D}} = \frac{\sigma_{f,pit,0}}{\sigma_{f,0}} \quad (11.4.13)$$

with the consequence that also in this case the hydroxyl damage has no influence on strength.

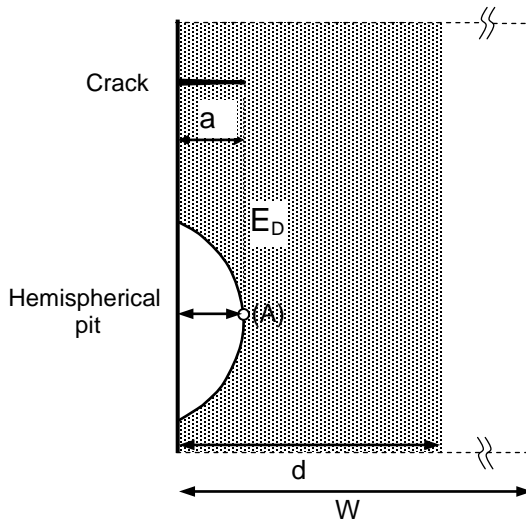


Fig. 11.5 Cross-section through a crack and a partially embedded hemispherical pit in a hydroxyl-damaged surface layer of thickness $d \ll W$ ($W =$ radius of the fiber) and $a \ll d$.

11.4.4 Effect of swelling stresses

If the volume swelling occurs in a constrained manner, such as at the glass surface, then the swelling causes a build-up of compressive stresses in the surface region, which can strengthen the glass significantly as has been outlined in [11.16].

The compressive swelling stresses in axial and circumferential directions, y , z , respectively, are generally proportional to the product of volume swelling strain ε_v and Young's modulus E

$$\sigma_{sw,y}, \sigma_{sw,z} \propto \varepsilon_v E \quad (11.4.14)$$

For the most simple case of *isotropic* swelling, the factor of proportionality is for instance $1/(3(1-\nu))$, where ν is Poisson's ratio.

The related volume swelling strain, $\varepsilon_v > 0$, can be expressed according to eq.(1.1.9) by

$$\varepsilon_v = \kappa \times S \quad (11.4.15)$$

with the coefficient $\kappa \approx 0.97$.

When for example $\sigma_{sw,z,0}$ denotes the axial swelling stress in the undamaged material, it holds as a consequence of eq.(11.1.1) that the swelling stress in the hydroxyl-damaged surface is

$$\sigma_{sw,z,D} = \sigma_{sw,z,0}(1-D) \quad (11.4.16)$$

As an example, this dependency may be applied to the *crack-like surface defects*.

The so-called shielding stress intensity factor $K_{sh} < 0$ that shields the crack tip partially from the applied load is in the damaged material

$$K_{sh,D} = \sigma_{sw,z,D} F \sqrt{\pi a} = \sigma_{sw,z,0} F \sqrt{\pi a} (1-D) = K_{sh,0}(1-D) \quad (11.4.17)$$

where $K_{sh,0}$ stands for the shielding stress intensity factor in the undamaged material.

In presence of crack-tip shielding, failure occurs, when the total stress intensity factor K_{tip} reaches fracture toughness. In the damaged material the principle of superposition results in

$$K_{tip,D} = K_{appl,D} + K_{sh,D} = K_{lc,D} \quad , \quad K_{sh,D} < 0 \quad (11.4.18)$$

Using eqs.(11.4.6), (11.4.8) and (11.4.17) gives the same result in terms of the stress intensity factors in the undamaged material

$$K_{tip,D} = (K_{appl,0} + K_{sh,0})(1 - D) = K_{lc,0}(1 - D) \quad (11.4.19)$$

The equal sign on the right of (11.4.19) makes clear, that the shielding effect can be described by stress intensity factors in the undamaged material.

For the case of the surface additionally damaged by *pit-like surface defects*, the tensile stress σ_D , has to be replaced by the total stress $\sigma_D + \sigma_{sw,z,D}$ resulting, equivalently to eq.(11.4.19), in

$$\sigma_{max,D} = \beta(\sigma_D + \sigma_{sw,z,D}) = \beta(\sigma_0 + \sigma_{sw,z,0})(1 - D) = \sigma_{f,0}(1 - D) \quad (11.4.20)$$

Again from the equal sign on the right, it becomes obvious that treatment with damaged quantities gives the same results as are obtained when hydroxyl damage is completely ignored.

11.5 Example of application: Uniaxial stress-strain curve

11.5.1 Swelling excluded

As has been outlined in [11.17], the hydroxyl concentration is stress-dependent. In order to allow a transparent derivation, swelling stresses may be neglected first. The hydroxyl concentration as a function of stress can be written

$$S = S_0 \exp \left[\sigma \frac{\Delta V_{eff}}{RT} \right] \quad (11.5.1)$$

At temperatures $>500^\circ\text{C}$, the parameter ΔV_{eff} reads for uniaxial loading [11.17]

$$\Delta V_{eff} = 14.4 \text{ cm}^3/\text{mol} \quad (11.5.2)$$

The total strain ϵ under the applied stress is

$$\varepsilon = \frac{\sigma_{appl}}{E_D(S)} \quad (11.5.3)$$

where for $E_D(S)$ the equations (11.3.4) or (11.3.8) have to be introduced. The maximum stress, asymptotically reached for $\varepsilon \rightarrow \infty$, is

$$\sigma_{\max} = -\frac{RT}{\Delta V_{eff}} \text{Log} \left[\frac{S_0}{S_{\max}} \right] \quad (11.5.4)$$

In Fig. 11.6 the σ - ε -curves are shown for 650°C (355 Torr water vapour pressure) and for 500°C with parameters S_0 (6 Torr pressure) taken from [11.17]. The dashed lines indicate the two asymptotes for $\varepsilon \rightarrow 0$ and $\varepsilon \rightarrow \infty$ of the solid curves.

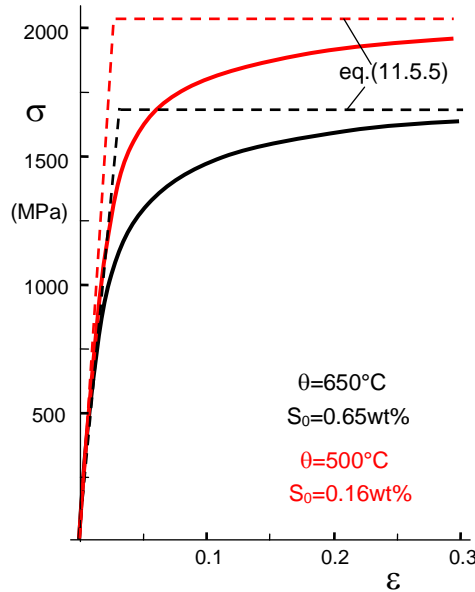


Fig. 11.6 Stress-strain curves for 650°C, 355 Torr and 500°C 6 Torr, hydroxyl concentrations S_0 from [11.17]; Approximate description of the stress-strain curves by eq.(11.5.5) (dashed lines).

For simpler mechanics computations, the stress-strain curves can be approximated by the two asymptotes (dashed lines in Fig. 11.6) where the rising part represents Young's modulus and the horizontal line the saturation stress given by eq.(11.5.4), i.e. a uniaxial "yield stress" $\sigma_Y = \sigma_{\max}$. Then it holds

$$\sigma = \begin{cases} E_0 \varepsilon & \text{for } \varepsilon < \frac{\sigma_{\max}}{E_0} \\ \sigma_Y & \text{for } \varepsilon \geq \frac{\sigma_{\max}}{E_0} \end{cases} \quad (11.5.5)$$

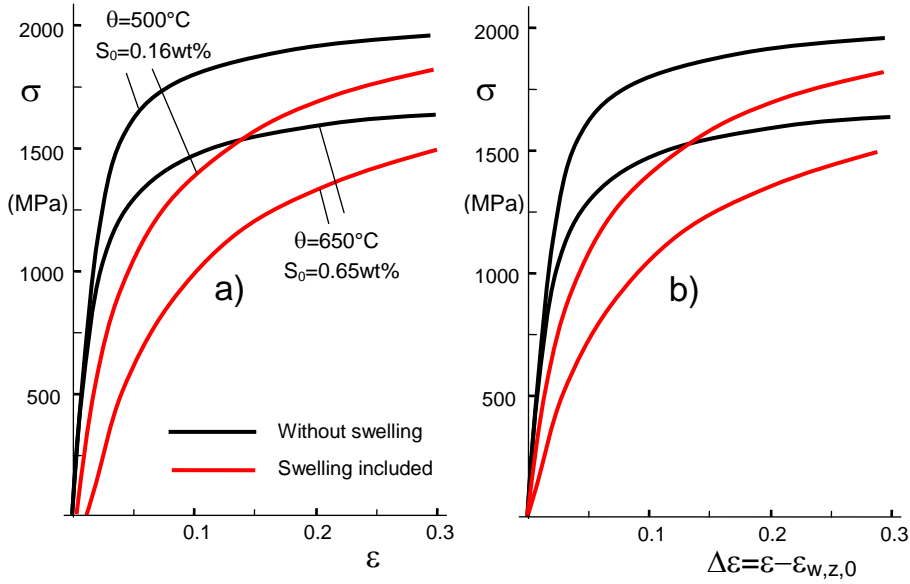


Fig. 11.7 Stress-strain curves, curve for 650°C and 500°C, black: without swelling, red: swelling included, a) total strain as the abscissa, b) strain by external loading as abscissa.

11.5.2 Swelling included

When swelling strains are taken into consideration, eq.(11.5.3) has to be replaced by

$$\varepsilon = \frac{\sigma}{E_D(S)} + \varepsilon_{sw,z} \quad (11.5.6)$$

where $\varepsilon_{sw,z}$ is the swelling strain in axial direction. According to [11.17], the eq.(11.5.1) yields

$$\varepsilon_{sw,z} = \alpha \kappa S = \alpha \kappa S_0 \exp\left[\sigma_{appl} \frac{\Delta V_{eff}}{RT}\right] \quad (11.5.7)$$

with $\kappa=0.97$, $\alpha=1.92$ [11.17]. The stress-strain curve obtained via eqs. (11.5.6) and (11.5.7) is shown in Fig. 11.7a as the red curves together with the curves by eq.(11.5.3) as the black ones. The offset of the red curves comes from the fact that even in the absence of stresses a swelling strain occurs that is caused by the initial hydroxyl concentration S_0 . When $\varepsilon_{sw,z,0}$ is the swelling strain caused by the initial concentration S_0 , the strain increase under load is $\Delta\varepsilon=\varepsilon-\varepsilon_{sw,z,0}$. This is shown in Fig. 11.7b.

11.6 Deviating behaviour under compressive loading

In the previous considerations, we applied the model of pore-like defects. This model describes symmetrical material response under tension and compression loading. For special cases of applications, the description by crack-like defects may be of advantage. This model allows introducing non-symmetry of deformation in tension and compression. Due to the fact that the crack surfaces cannot interpenetrate each other under compressive normal stress, the reduction of Young's modulus is less strong than in tension, represented by

$$E = \begin{cases} E_0 (1 - D) & \text{for } \sigma \geq 0 \\ E_0 (1 - hD) & \text{for } \sigma < 0 \end{cases} \quad (11.6.1)$$

with the crack closure parameter $0 \leq h \leq 1$, often found to be $h=0.2$ [11.18].

11.6.1 Shielding-stress intensity factor for damaged material

A consequences of damage by hydroxyl generation is the reduction of Young's modulus E . When E_D is the modulus in the damaged state and E_0 the value for undamaged silica, we could derive the relation [11.19, 11.20] (see Section 11.3)

$$\frac{E_D}{E_0} = (1 - \frac{1}{2} \lambda S)^2 = (1 - S / S_{\max})^2 \quad (11.6.2)$$

with $\lambda=10.6$ [8.7, 12.5] (90%-CI in brackets). The hydroxyl concentration at which the Young's modulus disappears is $S_{\max}=2/\lambda=0.188$ [0.16, 0.23].

Including the varying modulus in the computation of the shielding stress intensity factor requires a modification of the equations in Section 9.2.2. Now the stress intensity factor results from

$$K_{sh} = \frac{1}{S(0)E_0} \int_0^{\infty} (S \times E) \left(\frac{\partial K_{sh}}{\partial \omega'} \right) d\omega' \quad (11.6.3)$$

The concentration profiles by Lechenault et al. [11.21], Fig. 9.4, clearly show the characteristic shape with a plateau as would be expected from the Irwin and Dugdale crack-tip zone models for “plastic flow” behaviour.

11.6.2 Shielding stress intensity factor for asymmetric damage

In the case of disappearing total stress intensity factor at the crack tip, $K_{total} = K_{appl} + K_{tip} \leq 0$, all volume elements in the water-affected zone are under compression due to volume swelling by hydroxyl generation [11.22]. In the previous considerations, we applied the model of pore-like defects. This model describes symmetrical material response under tension and compression loading. The Young's modulus in compression is not necessarily identical in tension and compression.

Figure 11.8b again shows the shielding stress intensity factor for the hydroxyl concentration according to eq.(11.6.3) for different values of the non-symmetry coefficient or crack closure parameter $0 \leq h \leq 1$. The asymmetry gives reason to define an upper limit for the shielding stress intensity factor. The zone in front of the crack tip is under tension for a load of $K_{tip} > 0$, Fig. 11.8a. The crack flanks, on the other hand, are stress-free with regard to the applied load and are under pressure due to the swelling stresses. In this region the lower expression in (11.6.1) holds. As the limit approximation, the reduced modulus in the zone ahead of the tip is assumed to be free of any stress ($E_b \rightarrow 0$) and the crack-face region is assumed to exhibit the initial modulus, i.e. $h \rightarrow 0$. This approximation is described by using the value $\psi = 0.37$ according to McMeeking and Evans [11.23]. Finally, Fig. 11.8b represents results from [11.19] for an erfc-shaped hydroxyl distribution with a surface value $S(0)$ and a parameter b of 4.95 nm (solid curves), according to

$$S = S(0) \operatorname{erfc} \left[\frac{z}{2b} \right] \quad (11.6.4)$$

The dashed line in Fig. 11.8b shows the upper limit solution for the same S -distribution addressed before.

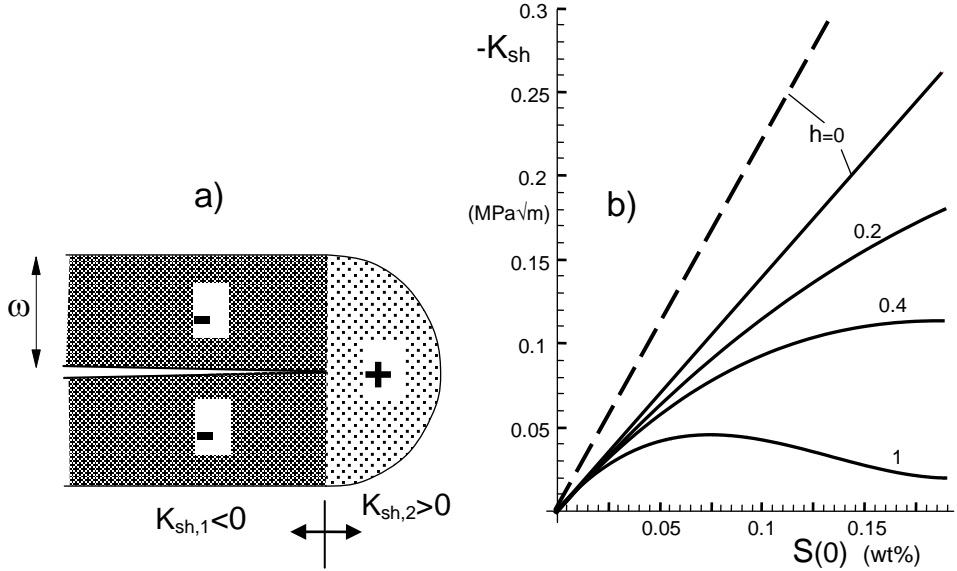


Fig. 11.8 a) Negative and positive contributions to the total shielding stress intensity factor, b) shielding stress intensity factors for an erfc-shaped hydroxyl distribution, eq.(11.6.4), as a function of the surface concentration $S(0)$. Solid curves: from [11.21], dashed curve: via eq.(9.2.2) with $\psi=0.37$, $E=E_0$.

11.7 Global strength of a fiber

The hydroxyl-damage in the glass also affects the load-bearing capacity of any area element, since it reduces its net cross-section, A_D

$$A_D = A_0(1-D) \quad (11.7.1)$$

where A_0 denotes the total geometrical cross section subsuming damaged and undamaged regions.

When again $\sigma_{f,0}$ denotes the strength in the absence of hydroxyl damage, and $\sigma_{f,D}$ the strength in the hydroxyl-damaged state, the strength results as given in eq.(11.4.3).

Let us now consider the strength of silica fibers. First, the water distribution may be replaced by $C=C_0=\text{const.}$ over the thickness b and $C=0$ in the bulk indicated in the inset of Fig. 11.9. The total cross section area A of the fiber with radius R is

$$A = R^2 \pi \quad (11.7.2a)$$

that of the inner circle of radius $R-b$

$$A_{\text{inn}} = (R-b)^2 \pi \quad (11.7.2b)$$

and the ring-shaped area is

$$A_b = R^2 \pi - (R-b)^2 \pi = (2R-b)\pi b \quad (11.7.2c)$$

Failure in the *undamaged fiber* occurs at the surface, when the stress reaches the strength $\sigma_{f,0}$. The force P_0 at failure is then

$$P_0 = \sigma_{f,0} R^2 \pi \quad (11.7.3)$$

When the surface is damaged by an amount of D , the strength in the layer b decreases to $\sigma_{f,D}$ according to eq.(11.4.3). Since the Young's modulus decreases in the same way, eq.(11.1.1), it is clear that the critical strain ϵ_c remains unaffected as is visible from eq.(11.4.4).

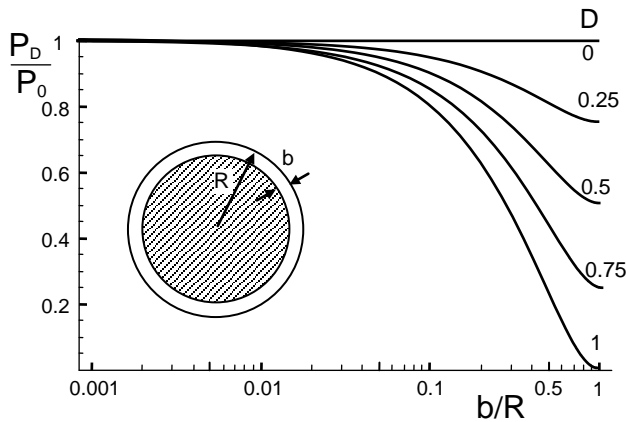


Fig. 11.9 Failure load of a fiber for differently damaged surface regions as a function of layer thickness b .

The Bernoulli Theorem tells us that plane cross sections must remain plane. It implies that the strain in the damaged and undamaged parts of the fiber must be the same.

This again implies that at failure $\sigma=\sigma_{f,0}$ is in the *inner* area A_{inn} and $\sigma=\sigma_{f,D}=\sigma_{f,0}(1-D)$ in the surface layer. The total load P_D of the damaged fiber at failure is the sum of the load in the inner (undamaged) area and the load in the damaged *ring-shaped* zone, i.e.

$$P_D = \sigma_{f,0}(R-b)^2 \pi + \sigma_{f,0}(1-D)(2R-b)b \pi \quad (11.7.4)$$

The reduction of the fracture load follows from eqs.(11.7.3) and (11.7.4)

$$\frac{P_D}{P_0} = \frac{(R-b)^2 + (1-D)b(2R-b)}{R^2} = 1 - \frac{2bD}{R} + \frac{b^2D}{R^2} \quad (11.7.5)$$

and is plotted in Fig. 11.9 for several damage values D as a function of the layer thickness. It becomes clear, that for small ratios of $b/R < 0.02$, the strength (computed from the load P_D) is hardly affected.

In the special case of thin layers, $b \ll R$, it results approximately

$$\frac{P_D}{P_0} \cong 1 - \frac{2b}{R} D \quad (11.7.6)$$

Figuratively speaking, it can be said that even in the absence of any load-carrying contribution from the stresses in the surface layer, $D=1$, the strength of the entire fiber is hardly affected.

References

-
- 11.1 L.M. Kachanov, Time of the rupture process under creep conditions, TVZ Akad Nauk S.S.R. Otd Tech. Nauk **8**(1958)
- 11.2 J. Lemaitre, Evaluation of dissipation and damage in metals, Proc. I.C.M. 1, Kyoto Japan (1971).
- 11.3 J. Lemaitre, How to use damage mechanics, Nuclear Engng. Design **80**(1984), 233-245.

- 11.4 S. Ito and M. Tomozawa, *J. de Phys.* C9 (1982), 68.
- 11.5 D.B. Fraser, Factors Influencing the Acoustic Properties of Vitreous Silica, Citation: *Journal of Applied Physics* 39(1968), 5868-5878.
- 11.6 R Le Parc, C Levelut, J Pelous, V Martinez, B Champagnon, Influence of fictive temperature and composition of silica glass on anomalous elastic behavior *J. Phys.: Condens. Matter* **18**(2006), 7507-27.
- 11.7 Shelby, J.E., Density of vitreous silica, *J. Non-Cryst.* **349** (2004), 331-336.
- 11.8 T. Fett, G. Rizzi, K.G. Schell, E.C. Bucharsky, P. Hettich, S. Wagner, M. J. Hoffmann, Consequences of hydroxyl generation by the silica/water reaction Part I: Diffusion and Swelling, KIT Scientific Publishing, Karlsruhe.
- 11.9 J. Kushibiki, M. Arakawa, Y. Yohashi, K. Suzuki, T. Maruyama, A super-precise CTE evaluation method for ultra-low-expansion-glasses using the LFB ultrasonic material characterization system, *Jap. J. of Appl. Phys.* **44**(2005), 4374-4380.
- 11.10 J.C. Wang, Young's modulus of porous materials, *J. Mater. Sci.* **19**(1984), 801-808.
- 11.11 K.K. Phani, S.K., Niyogi, Elastic-modulus–porosity relationship for Si₃N₄, *J. Mater. Sci. Letters* **6**(1987), 511–515
- 11.12 K.K. Phani, S.K. Niyogi, A.K. De, Porosity dependence of fracture mechanical properties of reaction sintered Si₃N₄, *J. Mater. Sci. Letters* **7**(1988), 1253–1256.
- 11.13 K.K. Phani, S.K. Niyogi, A.K. De, Young's modulus of porous brittle solids, *J. Mater. Sci.* **22**(1987), 257–263.
- 11.14 Adachi, T, Sakka, S., Dependence of the elastic moduli of porous silica gel prepared by the sol-gel method on heat-treatment, *J. Mater. Sci.* **25**(1990), 4732-37.
- 11.15 D. Inniss, Q. Zhong, C.R. Kurkjian, Chemically corroded pristine silica fibers: Blunt or sharp flaws?, *J. Am. Ceram. Soc.* **76**(1993), 3173-77.
- 11.16 S.M. Wiederhorn, T. Fett, G. Rizzi, M. Hoffmann, J.-P. Guin, Water Penetration – its Effect on the Strength and Toughness of Silica Glass, *Met. Mater. Trans. A*, **44** [3], 1164 -1174 (2013).
- 11.17 S. M. Wiederhorn, G. Rizzi, S. Wagner, M. J. Hoffmann, and T. Fett, Stress-Enhanced Swelling of Silica: Effect on Strength, *J. Am. Ceram. Soc.* **99**(2016), 2956-63.
- 11.18 J. Lemaitre, J.P. Sermage, One damage law for different mechanisms, *Comp. Mech.*, **20**(1997), 84-88.

- 11.19 T. Fett, G. Schell, C. Bucharsky, Hydroxyl Damage in Silica: Full-range description including large damages **126**, 2019, ISSN: 2194-1629, Karlsruhe, KIT.
- 11.20 K.G. Schell, T. Fett, C. Bucharsky, M.J. Hoffmann, S.M. Wiederhorn, Damage by Hydroxyl Generation in Silica, *Glass Physics and Chemistry*, **46**(2020), 424-428.
- 11.21 F. Lechenault, D.L. Rountree, F. Cousin, J.-P. Bouchaud, L. Ponsion and E. Bouchaud, "Evidence of Deep Water Penetration in Silica during Stress Corrosion Fracture," *Phys. Rev. Let.* **106**(2011), 165504.
- 11.22 S. M. Wiederhorn, T. Fett, G. Rizzi, M. J. Hoffmann, J.-P. Guin, The Effect of Water Penetration on Crack Growth in Silica Glass, *Engng. Fract. Mech.* **100**(2013), 3-16.
- 11.23 McMeeking, R.M., Evans, A.G., Mechanics of Transformation-Toughening in Brittle Materials, *J. Am. Ceram. Soc.* **65**(1982), 242-246.

12 Shielding affected by damage

12.1 Effect of local swelling at surface cracks

The reaction of water and silica in the surface diffusion zone, eq. (1.1.1), affects the fracture mechanics stress intensity factor K at the tips of cracks. As a consequence of the high near-tip stresses, very high hydroxyl concentrations must occur in the crack-tip region. This allows the assumption that near a crack tip the water is present predominantly in the form of hydroxyl water.

Due to restrictions in free expansion, the swelling strains ε_v result in swelling stresses which give rise for the “shielding” stress intensity factor $K_{sh} < 0$. At first loading, the swelling zone at the crack tip $r(\sigma_h, \varphi)$ is heart-shaped as illustrated in Fig. 12.1a.

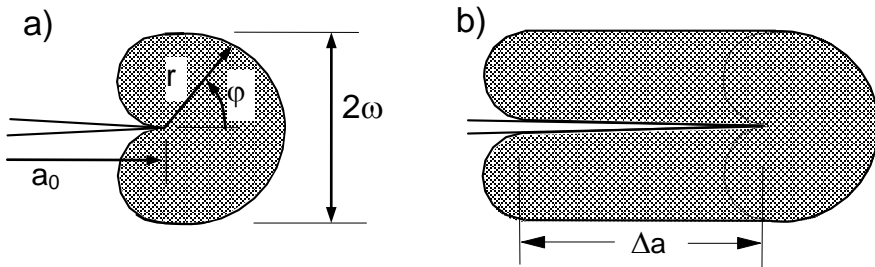


Fig. 12.1 a) Swelling zone at the tip of an arrested crack under mechanical loading, caused by stress-enhanced diffusion, b) zone for a crack grown by Δa .

The shielding stress intensity factor caused by a swelling zone of height ω is [12.1, 12.2]

$$K_{sh} = -\nu \frac{\varepsilon_v E}{1 - \nu} \sqrt{\omega} \quad (12.1.1)$$

where E is Young's modulus and ν Poisson's ratio.

12.2 Shielding stress intensity factors for a damaged material

A consequence of damage by hydroxyl generation is the reduction of Young's modulus E . When E_D is the modulus in the damaged state and E_0 the value for undamaged silica, we could derive the relation (11.3.8), [12.2]

$$\frac{E_D}{E_0} = (1 - S / S_{\max})^2 \quad (12.2.1)$$

with $S_{\max} = 0.188 [0.16, 0.23]$.

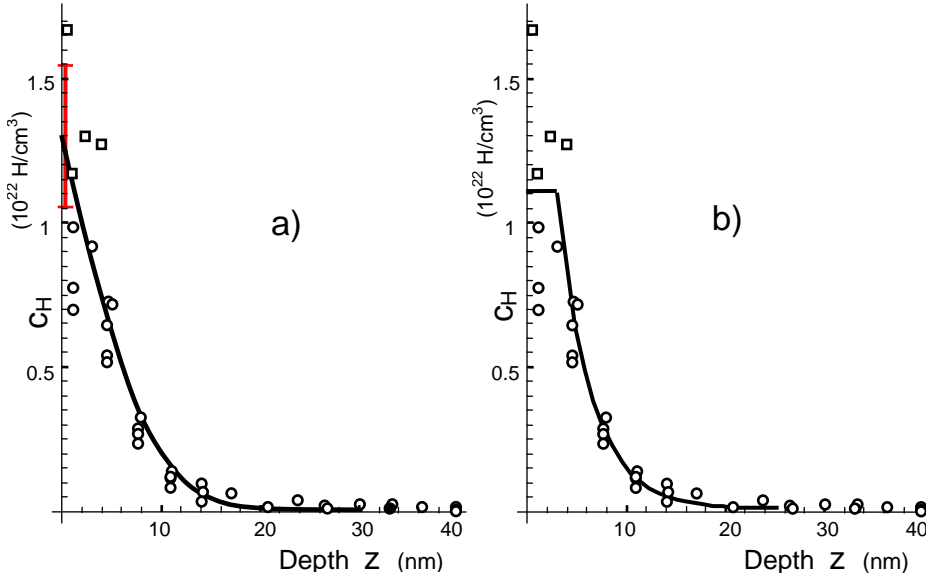


Fig. 12.2 a) Water profile on DCDC specimen on the faces of a growing crack fractured in liquid water by Tomozawa et al. [12.3].

Including the varying modulus into the computation of the shielding stress intensity factor requires a modification of eq.(9.2.6). Now the stress intensity factor results from

$$K_{sh} = \frac{1}{S(0)E_0} \int_0^{\infty} (S \times E) \left(\frac{\partial K_{sh}}{\partial \omega} \right)_{\omega=\omega'} d\omega' \quad (12.2.2)$$

In order to explain the evaluation of eq.(12.2.2), again the measurements by Tomozawa et al. [12.3], plotted already in Fig. 9.5, may be used here again, Fig. 12.2.

12.3 Shielding stress intensity factor for asymmetric damage

In the case of disappearing total stress intensity factor at the crack tip, $K_{\text{total}} = K_{\text{appl}} + K_{\text{tip}} \leq 0$, all volume elements in the water-affected zone are under compression due to volume swelling by hydroxyl generation [12.4]. In the previous considerations, we applied the model of pore-like defects. This model describes symmetrical material response under tension and compression loading. The Young's modulus in compression is not necessarily identical in tension and compression, see Section 11.6.

Figure 12.3b again shows the shielding stress intensity factor for the hydroxyl concentration according to eqs.(12.2.1) and (11.6.1) for different values of the non-symmetry coefficient or crack closure parameter $0 \leq h \leq 1$.

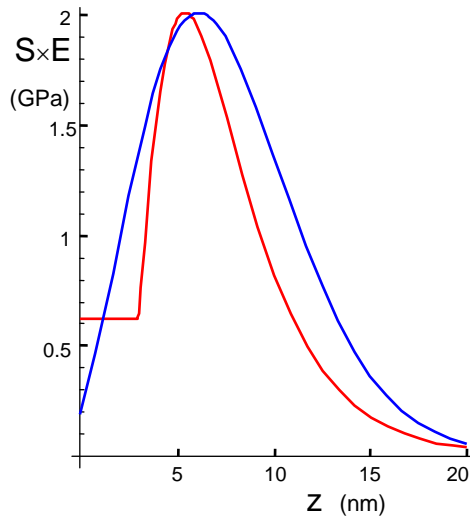


Fig. 12.3 Distribution of the product $S \times E$ relevant for eq.(11.2.2), computation for $h=1$ in eq.(11.6.1), b) for the representations by Fig. 12.2a (blue curve) and Fig. 12.2b (red curve).

The product $S \times E$ that governs the shielding stress intensity factor according to eq.(12.2.2) is shown in Fig. 12.3. The blue curve shows the result for the representation by Fig.12.2a and the red curve by Fig. 12.2b. The region at a depth of $\approx 5-6$ nm has the strongest influence on shielding.

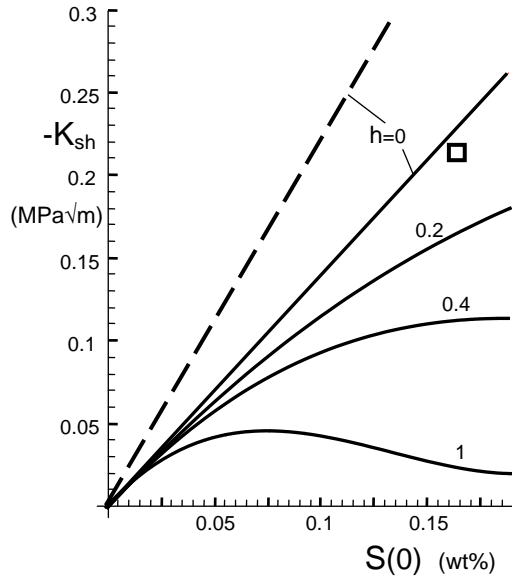


Fig. 12.4 Shielding stress intensity factors for an erfc-shaped hydroxyl distribution, as a function of the surface concentration $S(0)$ from Fig. 11.8b. Square: Result for $S(0)=16.5\%$ and $h \approx 0.05$.

Figure 12.4 again represents the results of Fig. 11.8b for an erfc-shaped hydroxyl distribution with a surface value $S(0)$ and a parameter b of 4.95 nm (solid curves).

An effective value of h can be estimated from the experimental result of $S(0)=16.5\%$, a crack-growth rate of $v \approx 10^{-9} \text{m/s}$, and a related applied stress intensity factor $K_{app} \approx 0.43 \text{MPa}\sqrt{\text{m}}$ (see Fig. 8.4a). According to eq.(8.2.8), we obtain for $K_{Ic} = 0.75 \text{MPa}\sqrt{\text{m}}$ and $K_{th} = 0.3 \text{MPa}\sqrt{\text{m}}$ [12.5]: $K_{sh} = -0.213 \text{MPa}\sqrt{\text{m}}$ as introduced as the square in Fig. 12.4. This value is equivalent to an asymmetry parameter of

$$h \approx 0.05 \tag{12.3.1}$$

12.4 Mechanical interpretation of the limit case under compression

The question remains how to explain such an asymmetry in the modulus of elasticity. A possible interpretation of the asymmetry coefficient h is illustrated in Figure 12.5a, where a water molecule may attack a load-carrying bond of the silica net structure.

A SiO_2 -ring of the silica network may be described by a spherical (nano)-void in a continuous material. This allows a fracture mechanics treatment by an FE-study. According to the finite crack-tip curvature for cracks, the radius of such a void has to be expected in the order of $\rho = 0.5 \text{ nm}$ [12.6], Fig. 12.5a.

Under a remote tensile load in z -direction, σ_∞ , the red Si-O-bond may be cracked by reaction with molecular water (blue/red). In the tensile case the opened bond cannot transfer any significant tensile forces, Fig. 12.5b. Consequently, it would be $h \rightarrow 1$ in eq.(11.6.1).

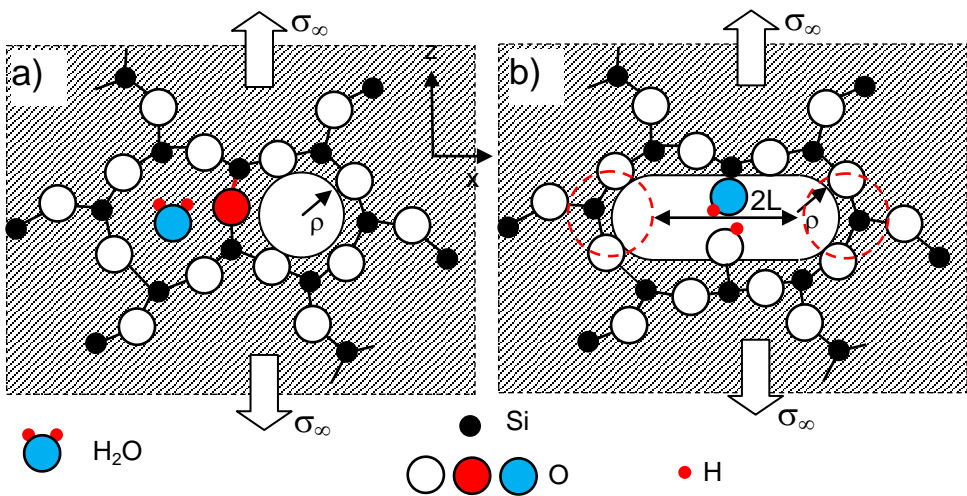


Fig. 12.5 a) Bond breaking under uni-axial tension by reaction with molecular water (attacked Si-O-bond in red).
 in red).

Due to the initially load-carrying but now fractured bond, the stress concentrations increase at the ends of the now tablet-shaped void as indicated by the red circles. Due to

the exponential increase of the hydroxyl concentration with stress, newly reacting water molecules will predominantly react at these locations.

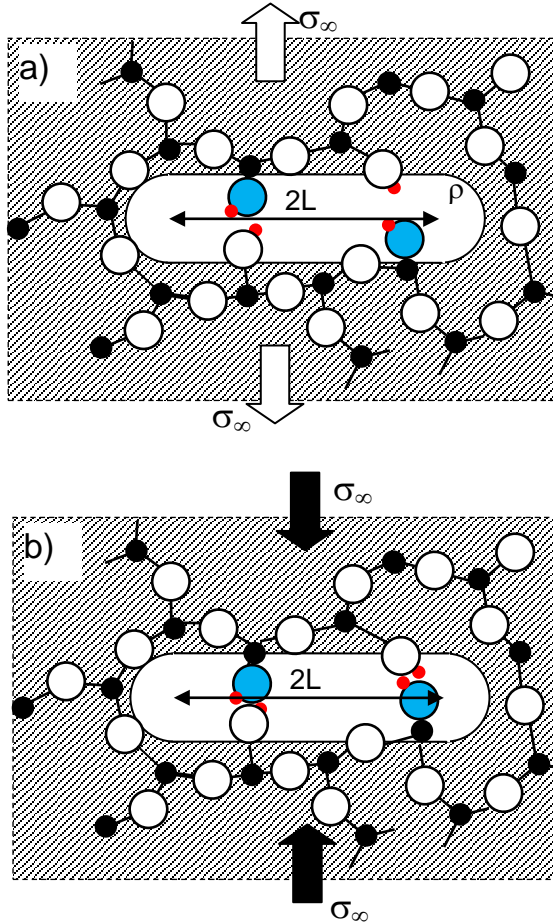


Fig. 12.6 a) Additionally cracked bond at a location of high stress concentration, b) limit case of a wedge-like contact of the hydroxyls under compression.

References

- 12.1 McMeeking, R.M., Evans, A.G., Mechanics of Transformation-Toughening in Brittle Materials, *J. Am. Ceram. Soc.* **65**(1982), 242-246.
- 12.2 T. Fett, G. Schell, C. Bucharsky, Hydroxyl Damage in Silica: Full-range description including large damages **126**, 2019, ISSN: 2194-1629, Karlsruhe, KIT.
- 12.3 M. Tomozawa, W.-T. Han and W.A. Lanford, Water Entry into Silica Glass during Slow Crack Growth, *J. Am. Ceram. Soc.* **74** [10] (1991) 2573-2576.
- 12.4 S. M. Wiederhorn, T. Fett, G. Rizzi, M. J. Hoffmann, J.-P. Guin, The Effect of Water Penetration on Crack Growth in Silica Glass, *Engng. Fract. Mech.* **100**(2013), 3-16.
- 12.5 V. Sglavo, T. Fett, K.G. Schell, M. J. Hoffmann, S. M. Wiederhorn, ν - K -data for silica from interrupted lifetime measurements 137, 2020, ISSN: 2194-1629, Karlsruhe, KIT.
- 12.6 S.M. Wiederhorn, E.R. Fuller, Jr. and R. Thomson, Micromechanisms of crack growth in ceramics and glasses in corrosive environments, *Metal Science*, **14**(1980), 450-8.

APPENDIX

A1 Modifications of shielding by additional effects

A1.1 Deformed steady-state swelling zones

The computations of the swelling zones are mostly carried out for diffusion in a motionless coordinate system with a fixed crack tip, i.e. for an *arrested* crack. Whereas for a *growing* crack the transversal diffusion normal to the crack plane is hardly affected by the moving crack tip, the diffusion and the crack propagation compete in crack direction [A1.1, A1.2]. The consequence for strongly stress enhanced diffusion zones with cordial shape is a reduced ratio of the zone size in length direction r_0 to the zone height ω (Fig. A1.1a), which for an arrested crack is [A1.3]

$$\frac{r_0(0)}{\omega(0)} = \frac{8}{\sqrt{27}} \quad (\text{A1.1.1})$$

In this relation $r_0(0)$, $\omega(0)$ stands for $r_0(v=0)$ and $\omega(v=0)$, respectively.

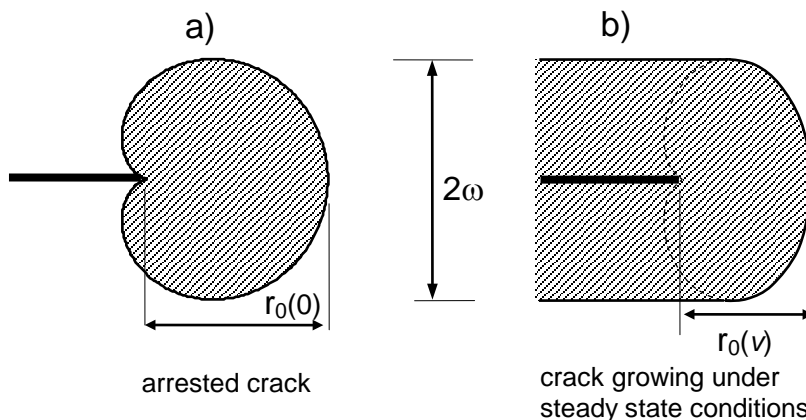


Fig. A1.1 a) Swelling zone ahead the tip of an arrested crack, b) zone with reduced length $r_0(v)$ for a crack growing at a constant crack-growth rate v (schematic).

For the stress intensity factor of the deformed zones one can use some single results from literature. Depending on the subcritical crack growth rate, a growing crack can show a crack-tip diffusion zone with a reduced value of r_0/ω as studied in [A1.4]. Such a zone is illustrated in Fig. A1.1b. The stress intensity factors for three different ratios of r_0/ω are available from [A1.3]. These cases are illustrated in Fig. A1.2a. Figure A1.2b shows the related coefficients ψ for the general representation

$$K_{sh} = -\psi \frac{\varepsilon_0 E}{1-\nu} \sqrt{\omega} \tag{A1.1.2}$$

by the circles. The interpolating curve through the data points in Fig. A1.2b. Figure A1.2 can be expressed simply by

$$\psi \cong 0.37 \left(1 - \frac{1}{2} \tanh \left(\frac{7}{9} \frac{r_0}{\omega} \right) \right) \tag{A1.1.3}$$

This interpolation relation enables the computation of stress intensity factors for deformed diffusion zones.

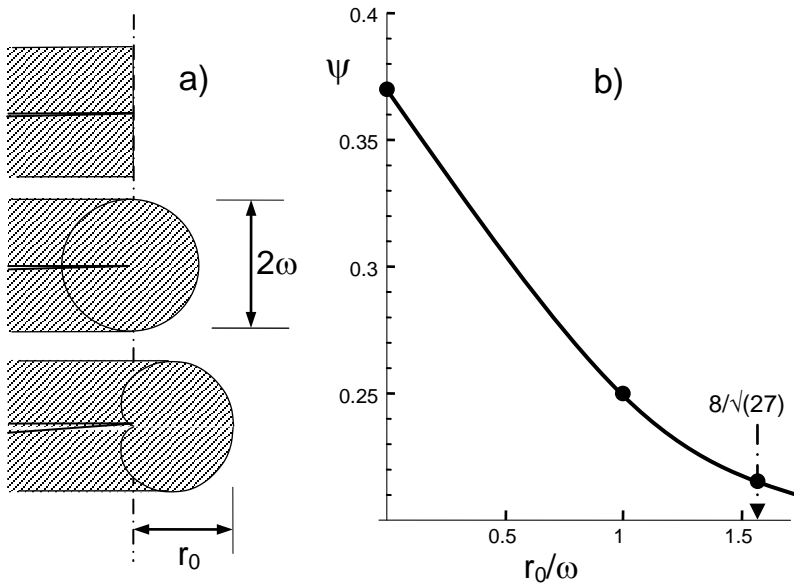


Fig. A1.2 a) Swelling zones with different shape at the zone end, b) shielding stress intensity factors by eq.(A1.1.2) for the zones given in a), expressed by the coefficient ψ .

A1.2 Crack leaving a swelling zone

At higher temperatures and after long time, also unloaded cracks may develop a swelling zone of thickness b by water diffusion into the crack faces, Fig. A1.3a. In this case, the zone end is modeled by a semicircle. If the swelling strain is constant in the swelling zone, $\varepsilon_v = \varepsilon_0 = \text{const.}$, and $\varepsilon_v = 0$ outside the zone, the shielding stress intensity factor is

$$K_{sh} = -\psi \frac{\varepsilon_0 E}{1-\nu} \sqrt{b} \quad (\text{A1.2.1})$$

with the coefficient ψ depending on the zone shape in the crack-tip region. If such a crack grows by an amount of Δa , it will escape from the initial swelling zone, as illustrated in Fig. A1.3a-Fig. A1.3d for different zone ends. The shielding stress intensity factors for two limit cases of the zone shape near the crack tip are plotted in Fig. A1.3e. For the circular zone end (Fig. A1.3b), the shielding stress intensity factor is given by the squares. A straight zone end with $r_0/b=0$ yields the dash-dotted curve. The two dependencies can be described by eq.(A1.2.1) where now ψ is a function of $\Delta a/b$. In order to minimize the uncertainty in the true shape of the zone ends it was recommended in [A1.5] to use for computations $r_0/b = 0.5$ with coefficient $\psi = 0.3$.

The stress intensity factor solution for the case $r_0/b=1/2$ (Fig. A1.3d) can be obtained by linear interpolation of the two limit cases resulting in the dashed curve of Fig. A1.3e. The coefficient ψ may be approximated by

$$\psi \cong \begin{cases} 0.305 + \frac{1}{12} \Delta a/b & \text{for } \Delta a/b \leq \frac{1}{2} \\ 0.34 \exp[-2\sqrt{\Delta a/b - \frac{1}{2}}] & \Delta a/b > \frac{1}{2} \end{cases} \quad (\text{A1.2.2})$$

It should be mentioned that the curves in Fig. A1.3e change abruptly caused by the assumption of a sharp layer boundary. For an arbitrarily varying strain distribution, the weight function or Green's function method from [A1.6] can be used. The stress intensity factor caused by a swelling layer of thickness db' in the surface distance $z=b'$ (a) undergoing the strain $\varepsilon(b')$ results as

$$d(K_{sh}) = K_{sh}(b'+db') - K_{sh}(b') \quad (\text{A1.2.3})$$

This gives rise for a Green's- or "weight function" h defined as

$$h = \frac{d(K_{sh})}{db'} \quad (A1.2.4)$$

For any swelling distribution $\varepsilon(z)=\varepsilon(b')$, the related shielding stress intensity factor is then obtained by summing over all the zone increments db' multiplied with the local swelling strain

$$K_{sh} = \frac{1}{\varepsilon_0} \int_0^\infty \varepsilon(b') h(b') db', \quad \varepsilon_0 = \varepsilon(b'=0) \quad (A1.2.5)$$

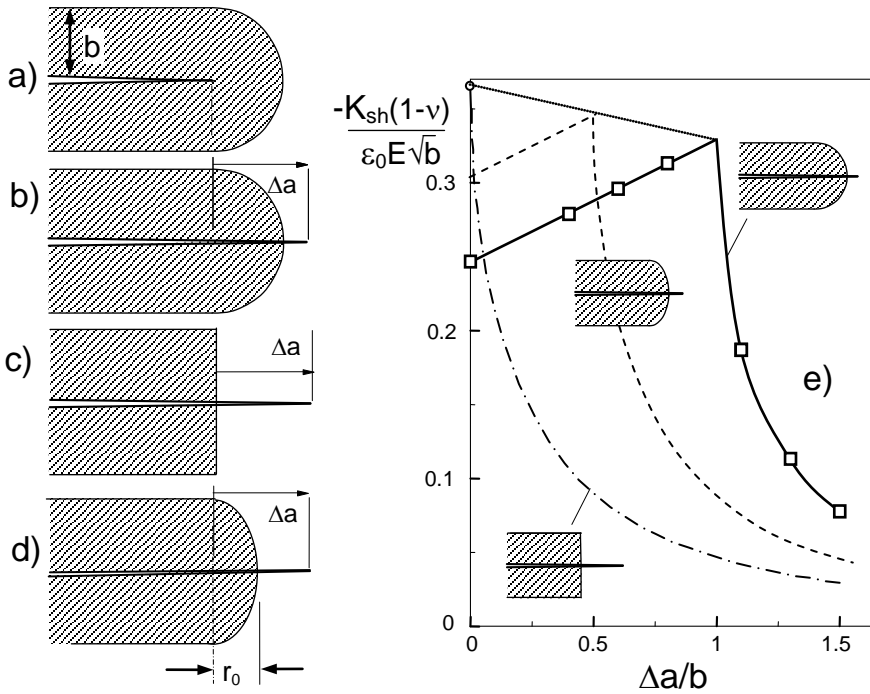


Fig. A1.3 a) Crack with a thick circular swelling layer of constant swelling strain, b) crack after additional extension Δa for a circular zone, c) for a rectangular zone, d) for a zone with $r_0/b=1/2$, e) variation of the shielding stress intensity factor for a crack growing in and outside the initial layer according to [A1.3] (dash-dotted curve) and [A1.5] (squares); dashed curve: interpolated from the continuous and dash-dotted curves for $r_0/b=1/2$.

In the absence of stress-enhanced diffusion, the swelling profiles are represented by the complementary error function. The volumetric strain at the location $z=b'$ is in this case

$$\varepsilon = \varepsilon_0 \operatorname{erfc}\left(\frac{b'}{2\sqrt{D_0 t}}\right) \quad (\text{A1.2.6})$$

where ε_0 is the strain at the free surface, D_0 the diffusion coefficient and t the time after the first water contact.

Equation (A1.2.5) has been evaluated for the case of $r_0/b=1/2$. The resulting shielding stress intensity factors related to the erfc-shaped swelling profiles are shown in Fig. A1.4b. The numerical result for $r_0/b=1/2$ can be approximated by equation (A1.2.1) with

$$\psi \approx \frac{0.305}{1 + \left(\frac{\Delta a}{b}\right)^2} \quad (\text{A1.2.7})$$

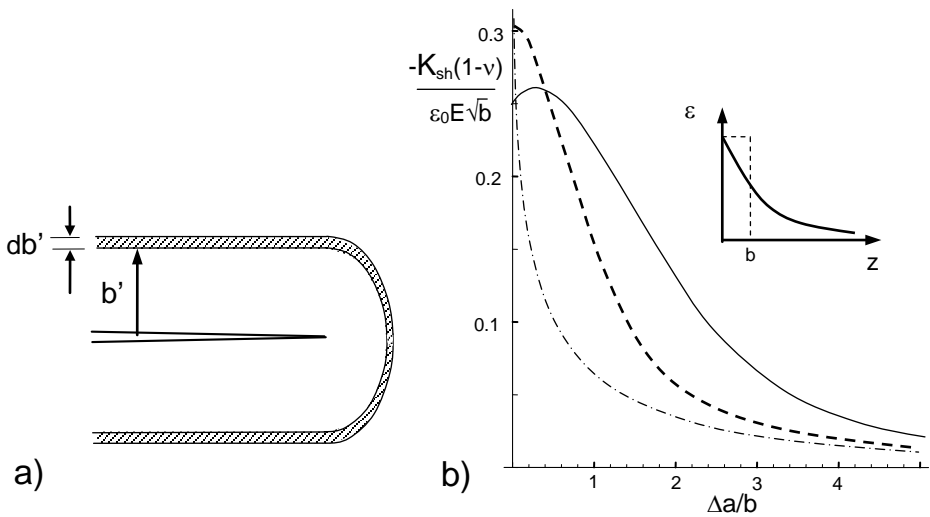


Fig. A1.4 a) Green's function as the shielding stress intensity factor of a thin swelling layer of thickness b' , b) stress intensity factors according to the dashed curve in (d) for an erfc-shaped strain distribution (insert); curves according to Fig. A1.3e.

A1.3 Blunt crack with finite notch root radius

Two crack-tip models are commonly used in fracture mechanics for the description of stresses ahead of a crack. Whereas continuum mechanics assumes the existence of a mathematically sharp crack, in a micro-structurally motivated approach the slender notch with a finite radius at the crack end is considered. Stresses at a sharp crack tip are described by the crack-tip stress intensity factor K_{ip} . They become singular if the tip is approached, $\sigma \rightarrow \infty$ for $r \rightarrow 0$. However, the K -description via continuum mechanics must fail for very short distances, when the tip distance competes with the microstructure of the material. In the micro-structurally motivated approach, the crack tip region can be considered as a slender notch with root radius ρ in the order of the average radius of the SiO₂ rings. Wiederhorn et al. [A1.7] suggest a crack-tip radius $\rho = 0.5$ nm for the silica network.

Whereas shielding stress intensity factors are well known for sharp cracks [A1.6], there is a lack in multiaxiality behaviour of swelling stresses for the slender notch model. The individual swelling stress components and also the hydrostatic stress terms are necessary for computations on stress-enhanced equilibrium of the silica/water reaction. In contrast to *internal swelling*, the stress components by *externally applied* loading are known from Creager and Paris [A1.8].

A1.3.1 Finite element model

Finite Element computations in order to determine swelling stresses for the slender notch model as a function of the distance from the notch root and differently high swelling zones were carried out in [A1.9]. A single crack embedded in a swelling zone of height h and constant volume swelling is shown in Fig. A1.5. The crack length, a , is small compared to the specimen dimensions, realizing the edge-cracked semi-infinite body. On the other hand, the crack length is at least a factor of 10 larger than the notch radius ρ so that a “slender” notch is sufficiently guaranteed. Zones of different heights were modelled in a finite element (FE) study. Solid continuum elements (8-node bi-quadratic) were chosen and the computations were carried out with ABAQUS Version 6.8. The volume strain was replaced by the equivalent thermal problem by heating the swelling zone by ΔT keeping $T=0$ in the rest of the structure. This results in the strain

$$\varepsilon_v = 3\alpha\Delta T \tag{A1.3.1}$$

(α =thermal expansion coefficient) with isotropic expansion in x -, y -, and z -directions

$$\varepsilon_v = \varepsilon_x + \varepsilon_y + \varepsilon_z \tag{A1.3.2}$$

Requirements for the z -coordinate were chosen as “plane strain” as is fulfilled at crack tips.

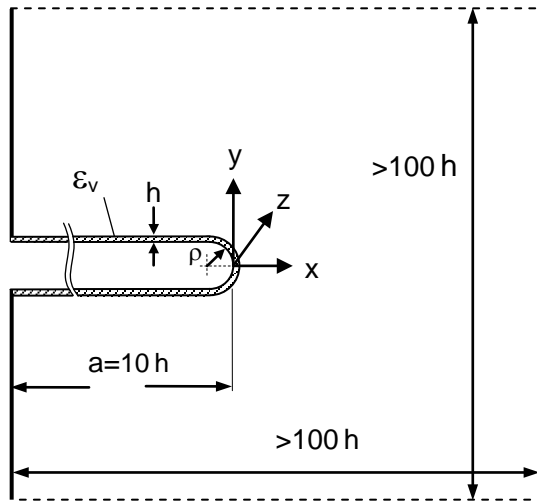


Fig. A1.5 Slender notch at a surface with swelling zone of thickness h .

A1.3.2 Results

Swelling stresses in x -, y -, and z -directions are plotted in Figs. A1.6a-d for zone heights of $h/\rho=0.2, 0.5$ and 1.0 . The black data represent the hydrostatic stress, defined by

$$\sigma_h = \frac{1}{3}(\sigma_x + \sigma_y + \sigma_z) \tag{A1.3.3}$$

Whereas all stresses are compressive within the swelling zone, they roughly disappear outside for the z -direction and for the hydrostatic stress. The x -component remains in compression and the y -component becomes tension as a consequence of the equilibrium condition.

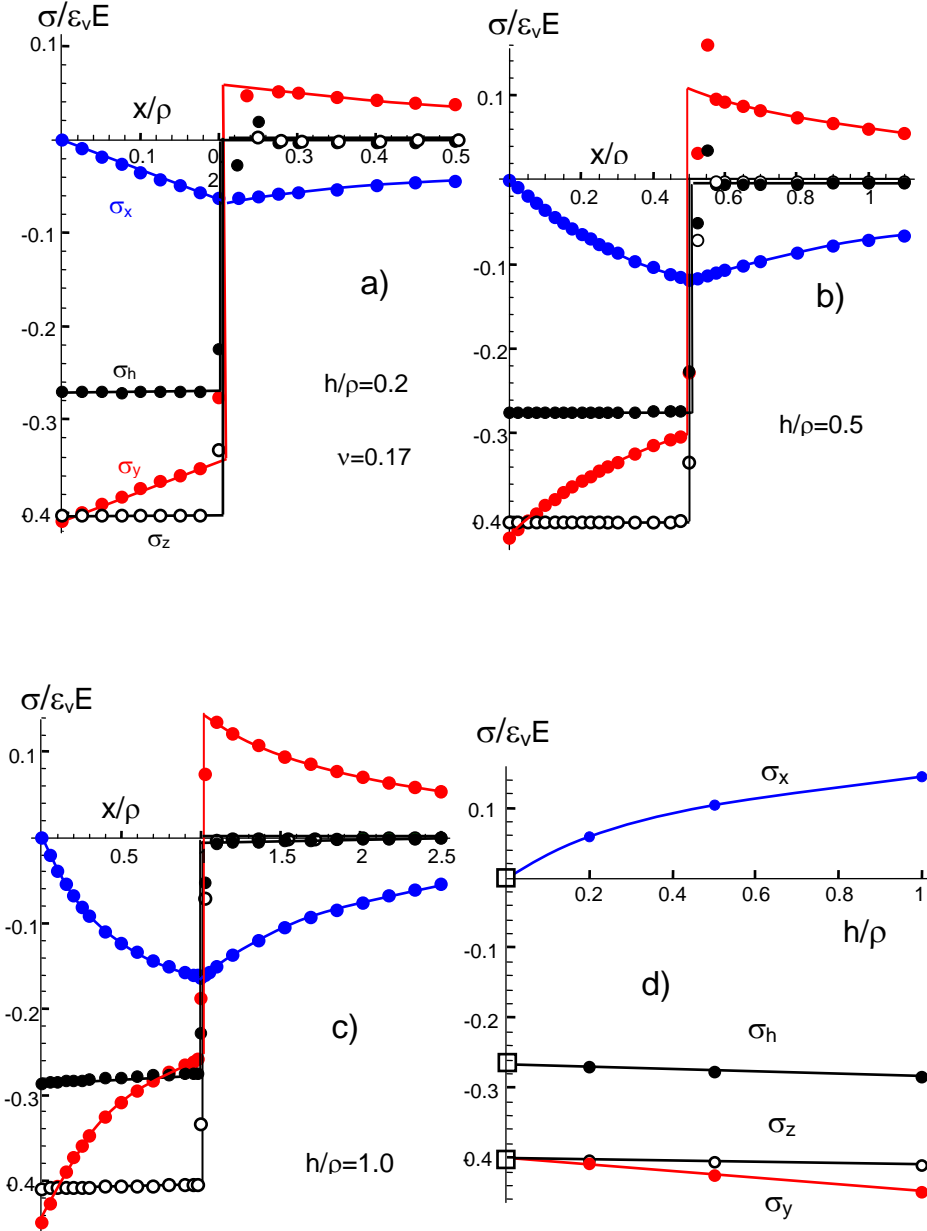


Fig. A1.6 a)-c) Swelling stresses, normalized on the volume expansion strain for 3 different zone heights h , d) Effect of zone height h on swelling stresses at the notch root, $x=0$.

The surface stresses ($x \rightarrow 0$) are represented in Fig. A1.6d as a function of the relative height h/ρ of the swelling zone. The squares indicate theoretically known values for an infinitely thin surface layer: At a free surface, the stress state is plane stress and, consequently, also stresses caused by swelling are equi-biaxial ($\sigma_x=0$)

$$\sigma_y = \sigma_z = -\frac{\varepsilon_v E}{3(1-\nu)} \quad (\text{A1.3.4})$$

where E is Young's modulus and ν is Poisson's ratio. For silica it is $\nu=0.17$, consequently: $\sigma/\varepsilon_v E = -0.4016$ for the y - and z -directions. The hydrostatic stress reads

$$\sigma_h = \frac{1}{3}(\sigma_y + \sigma_z) = -\frac{2\varepsilon_v E}{9(1-\nu)} \quad (\text{A1.3.5})$$

i.e. $\sigma_h/(\varepsilon_v E) = 0.2677$.

In order to characterize the "multiaxiality" of the swelling stresses, we plot in Fig. A1.7a the hydrostatic stress normalized on the z -component. This parameter is $2/3 \approx 0.67$ for thin swelling layers and decreases slightly for σ_h/σ_y and increases for σ_h/σ_z . The variation over the swelling zones is negligible as can be concluded from Fig. A1.7b.

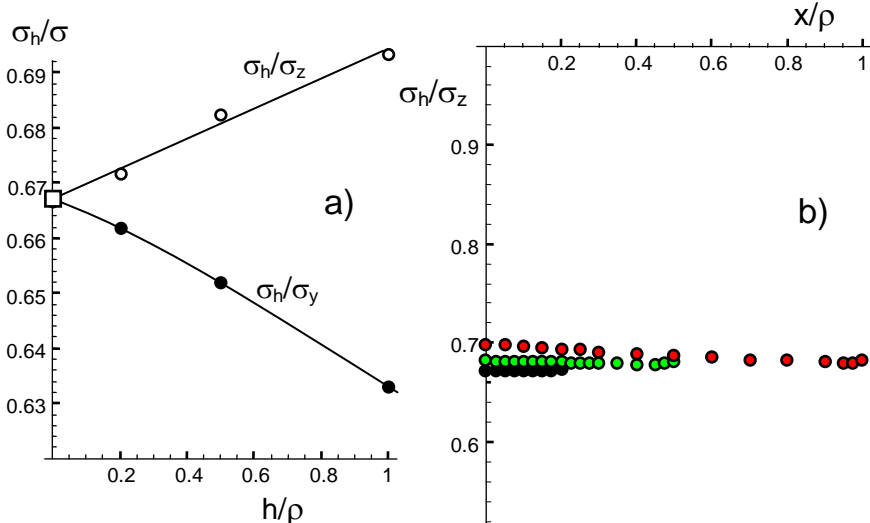


Fig. A1.7 a) Effect of zone height h on multi-axiality at the notch root, $x=0$, b) variation of the multi-axiality ratio σ_h/σ_z over the swelling zones.

A1.3.3 Effect of finite notch length

From Fig. A1.6a-d it is visible that the hydrostatic swelling stress shows a small variation over the swelling zone. For an understanding of this small effect, we increased for $b/\rho=1$ the notch length to $a/\rho=30$. Figure A1.8a shows the effect for σ_h . In this plot the data for $a/\rho=10$ are represented by the black symbols, those for $a/\rho=30$ by the red ones. It is obvious that the variation over the region $0 \leq x \leq b$ clearly decreases. In Fig. A1.8b the effect on the normal swelling stress σ_y is shown. Here, the variation remains unaffected over the zone size. Only the absolute stress values $\sigma/\varepsilon_v E$ shift slightly.

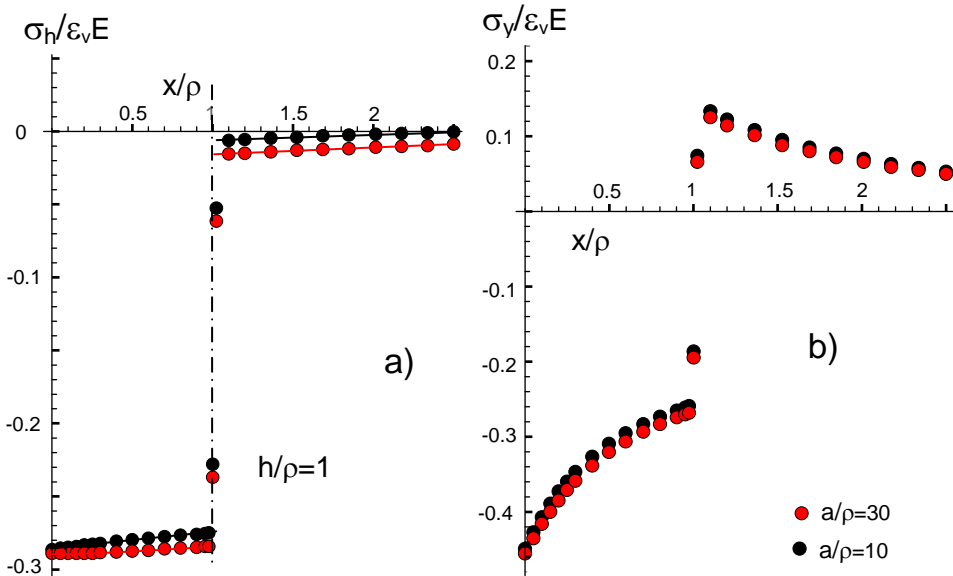


Fig. A1.8 Effect of the notch length on the hydrostatic and the normal swelling stress.

A1.3.4 Including shielding stress intensity factors

Stresses at slender notches were given by Creager and Paris [A1.8]. The stress component normal to the crack plane (the stress σ_y) is in distance x from the notch root

$$\sigma_y = \frac{2K}{\sqrt{\pi(\rho + 2x)}} \frac{\rho + x}{\rho + 2x} \quad (\text{A1.3.6})$$

The other stress components are

$$\sigma_x = \frac{2K}{\sqrt{\pi(\rho + 2x)}} \frac{x}{\rho + 2x} \quad (\text{A1.3.7})$$

$$\sigma_z = \frac{2\nu K}{\sqrt{\pi(\rho + 2x)}} \quad (\text{A1.3.8})$$

Consequently, the hydrostatic stress term from the applied stresses results as

$$\sigma_{appl,h} = \frac{2(1+\nu)K}{3\sqrt{\pi(\rho + 2x)}} \quad (\text{A1.3.9})$$

Equations (A1.3.6-A1.3.9) are valid for applied stress intensity factors K_{appl} , shielding stress intensity factors K_{sh} , and total stress intensity factor K_{tip} , which are defined as

$$K_{tip} = K_{appl} + K_h \quad (\text{A1.3.10})$$

The shielding stress intensity factor for an edge crack of finite length a , embedded in a swelling zone of height b , was already computed via FE in [A1.10]. The results can be expressed by the relation

$$K_{sh}(b/a) \cong K_{sh}(0) \exp\left[-1.18 \frac{b}{a}\right] \quad (\text{A1.3.11})$$

with

$$K_{sh}(0) = -\psi(0) \frac{\varepsilon_v E}{1-\nu} \sqrt{b} \quad (\text{A1.3.12})$$

and different zone shape [A1.3]

$$\psi(0) = \begin{cases} 0.22 & \text{for heart shape} \\ 0.25 & \text{for semi circle} \end{cases} \quad (\text{A1.3.13})$$

Now we can use this solution for the computation of the shielding stress intensity factor in eqs.(A1.3.6-A1.3.9), resulting in swelling stresses contributed by K_{sh} . The resulting stresses are then subtracted from the results in Fig. A1.6d. The difference is the contribution by local swelling exclusively, i.e. for $K_{sh}=0$.

Two different procedures are now possible for the computation of swelling stresses:

- Fitting the dependencies of Fig. A1.9 and adding the swelling stresses caused by the shielding stress intensity factor.
- Use of the data in Fig. A1.6d directly because these values include already the shielding effect.

Since the resolved data of Fig. A1.9 vary clearly stronger with the distance x from the notch root it is recommended to use results of Fig. A1.6d. For the hydrostatic stress term, it is suggested for $0 < x \leq b$:

$$\sigma_h\left(\frac{x}{\rho}, \frac{b}{\rho}\right) = -\frac{2 \varepsilon_v E}{9(1-\nu)} \left(1 + 0.078 \frac{b}{\rho}\right) \quad (\text{A1.3.14})$$

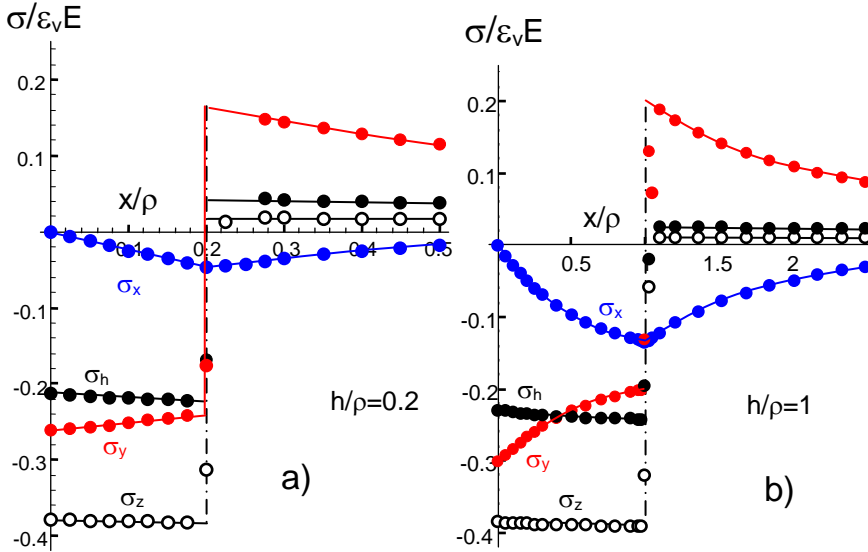


Fig. A1.9 Swelling stresses for a disappearing shielding stress intensity factor, $K_{sh}=0$.

References

- A1.1 Zhao, T., Nehorai, A., Detection and localization of a moving biochemical source in a semi-infinite medium, Report, Electrical and Computer Engineering Dept. Univ. of Illinois, Chicago, USA.
- A1.2 Babich, V.M., On asymptotic solutions of the problems of moving sources of diffusion and oscillations, UDC 534.231.1, 517.226, 1991, pp. 3067-3071, Plenum Publishing Corp.
- A1.3 McMeeking, R.M., Evans, A.G., Mechanics of Transformation-Toughening in Brittle Materials, *J. Am. Ceram. Soc.* **65**(1982), 242-246.
- A1.4 T. Fett, New contributions to R-curves and bridging stresses – Applications of weight functions, IAM 3, KIT Scientific Publishing, 2012, Karlsruhe.
- A1.5 Fett, T., Guin, J.P., Wiederhorn, S.M., Interpretation of effects at the static fatigue limit of soda-lime-silicate glass, *Engng. Fract. Mech.* **72**(2005), 2774-279.
- A1.6 Wiederhorn, S.M., Fett, T., Rizzi, G., Hoffmann, M.J., Guin, J.-P., The Effect of Water Penetration on Crack Growth in Silica Glass, *Engng. Fract. Mech.* **100**(2013), 3-16.
- A1.7 S.M. Wiederhorn, E.R. Fuller, Jr. and R. Thomson, Micromechanisms of crack growth in ceramics and glasses in corrosive environments, *Metal Science*, **14**(1980), 450-8.
- A1.8 Creager, M., Paris, P.C., Elastic field equations for blunt cracks with reference to stress corrosion cracking, *Int. J. Fract.* **3**(1967), 247-252.
- A1.9 G. Rizzi, G. Schell, T. Fett, Swelling stresses ahead of slender notches, **52**, 2016, ISSN: 2194-1629, Karlsruhe, KIT.
- A1.10 G. Rizzi, T. Fett, Defects at Silica Surfaces - A Finite Element Study, *Scientific Working Papers* **33**, 2015, KIT Scientific Publishing, Karlsruhe.

A2 Finite Element study on heart-shaped zones

A2.1 Zone shape

The singular hydrostatic near-tip stresses are given as

$$\sigma_h = \frac{2}{3}(1+\nu) \frac{K}{\sqrt{2\pi r}} \cos(\varphi/2) \quad (\text{A2.1.1})$$

where r and φ are the polar coordinates with the origin at the crack tip, see Fig. A2.1a. Equations (9.1.1) and (A2.1.1) imply that in the high crack-tip stress field nearly all water is present in form of hydroxyl S .

The shape $r(\varphi)$ of the zone contour for constant σ_h in plane strain results from eq.(A2.1.1) as

$$r = \frac{8}{3\sqrt{3}} \omega \cos^2(\theta/2) \quad (\text{A2.1.2})$$

with the height ω of the zone for a prescribed hydrostatic stress

$$\omega = \frac{(1+\nu)^2}{4\sqrt{3}\pi} \left(\frac{K_I}{\sigma_h} \right)^2 \quad (\text{A2.1.3})$$

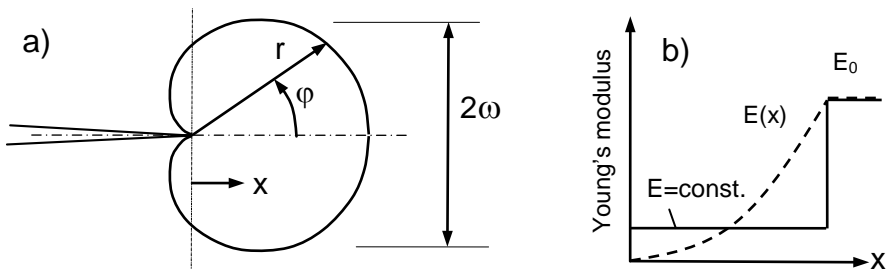


Fig. A2.1 a) Contour for a constant hydrostatic stress ahead of a loaded crack, b) variation of Young's modulus in a frontal zone $E(x)$ (dashed curve), replaced by an average (effective) modulus E .

The contour of constant hydrostatic stress according to eqs.(A2.1.2, A2.1.3) is shown in Fig. A2.1a as the heart-shaped curve. This contour also describes the damage zone in front of the tip of a crack that has not yet grown by subcritical or stable crack growth. The hydroxyl generation by the reaction (1.1.1) causes damage since the originally intact silica ring structure is cracked by the water attack. One of the consequences of such damage is the reduction of Young's modulus E (see Section 11).

As Fig. A2.1a shows, the tip of the crack is not embedded in the heart-shaped zone but terminates at $r=0$. This point in principle belongs to both the frontal zone and the undamaged surrounding material. A description by eq.(11.3.8) leads to a variable module distribution $E(x)$, which is replaced here by an average constant value for reasons of simplicity, Fig. A2.1b. The module E_0 prevails outside the crack-tip zone. Another reason for the decrease in the elasticity module in the "frontal process zone" is microcracking in polycrystalline ceramics as was studied by Evans and Faber [A2.1].

A2.2 Crack terminating at $\varphi=\pi$ of the heart-shaped zone

A2.2.1 Constant modulus over the zone size

First we studied the case that a constant modulus is prescribed over the whole zone. In the heart-shaped zone the Young's modulus is $E \leq E_0$ and outside the zone E_0 . FE calculations were performed with ABAQUS 6.9. In order to obtain normalized stress intensity factors K' according to (A2.2.2a), $\omega=1$, $\sigma_{\text{appl}}=1$, and $E_0=1$ were chosen. Table A2.1 shows the J-integrals according to Rice [A2.2] and the stress intensity factors obtained from the first contours for the lowest Young's modulus of $E=0.01 E_0$. Apart from the first contour, the results are almost constant. Due to symmetry, no mode-II stress intensity factor could appear. The average mode-I stress intensity factor over contour 2-8 is 1.974 and the Standard Deviation 0.00125 (0.06%). The interrelation between crack opening displacement v and stress intensity factor K_I is for the near-tip field along the symmetry line (here: $-x=r < \omega$) in plain strain with $E=E_0/(1-\nu^2)$

$$K_I = \sqrt{\frac{\pi}{8}} v \frac{E'}{\sqrt{r}} \quad (\text{A2.2.1})$$

Normalized displacements v' represented in Fig. A2.2 are defined as

$$v' = v \frac{E_0}{\sigma_{app} \omega (1 - \nu^2)} \quad (\text{A2.2.1a})$$

The stress intensity factors obtained from the least-squares fit of the displacements in Fig. A2.2 are compiled in Table A2.2, Column 3. In this context, it has to be noted that crack opening *displacements* COD are defined as the distance from the symmetry line to one of the surfaces. Unfortunately, the (total) crack opening, i.e. the distance between the crack flanks, is sometimes also referred to as COD.

Contour	J	K_I	K_{II}
1	370.3	1.953	0
2	378.0	1.973	0
3	378.0	1.973	0
4	378.1	1.973	0
5	378.6	1.975	0
6	379.2	1.976	0
7	379.6	1.977	0
8	378.8	1.975	0

Table A2.1 J-integral and stress intensity factors for the first contours ($E=0.01$, $E_0=1$, $\nu=0.17$, $\omega=1$) in normalized form.

An independent procedure for the stress intensity factor determination is the evaluation of the near-tip stresses ahead of the crack tip, i.e. the stresses along the prospective crack propagation plane. For the normal component on this plane it holds for the first terms

$$\sigma_{yy} = \frac{K}{\sqrt{2\pi x}} + A\sqrt{x} \quad (\text{A2.2.2})$$

A regression analysis of the data in Fig. A2.3 provides the stress intensity factors. The results obtained from the data fit of Fig. A2.3 are compiled in Table A2.2, Column 4 in the dimensionless form of

$$K' = \frac{K}{\sigma_{appl} \sqrt{\omega}} \tag{A2.2.2a}$$

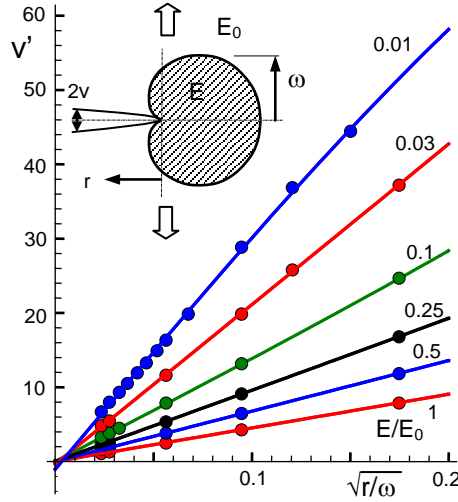


Fig. A2.2 FE-results of near-tip CODs fitted according to eq.(A2.2.1).

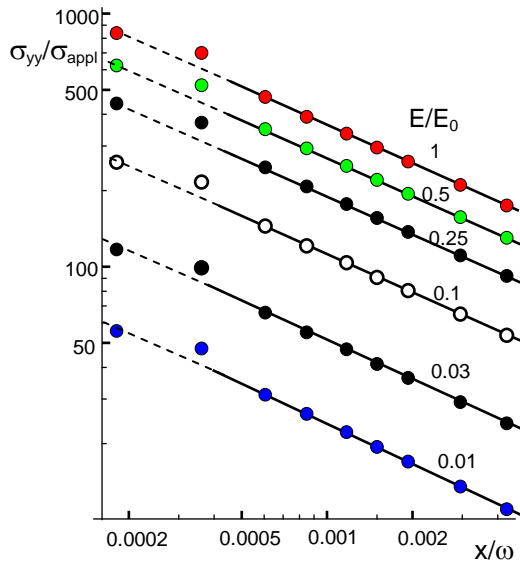


Fig. A2.3 Normalized stress $\sigma_{yy} / \sigma_{appl}$ along the prospective crack propagation line ($\varphi=0$), lines: fitting curves according to eq.(A2.2.2), yielding the stress intensity factor for the data points in the range of $0.0005 < x/\omega < 0.004$.

A2.2.2 Step-shaped modulus distribution

So far only cases with a constant modulus were studied, Fig. A2.4a. An additional FE-evaluation was made for the case of a variable modulus in the zone ahead the tip. As Fig. A2.4b shows, the modulus was varied in 4 steps. In the inner zone of Fig. A2.4b, the modulus E was $E=0.25 E_0$, then $E=0.57 E_0$, $E=0.72 E_0$, and outside $E=E_0$. The result from the J-Integral was (for $E_0=1$, $\nu=0.17$, $\sigma_{\text{appl}}=1$ and $\omega=1$): $K^*=14.83$, hardly different from the case of constant modulus $E=0.25 E_0$. Also this value is introduced in the second Column of Table A2.2.

E/E_0	K^* , eq.(A2.2.2a)		
	via J	via COD	via σ_{yy}
1	29.21	29.11	28.78
0.5	21.82	21.81	21.58
0.25	15.43	15.40	15.21
0.25/0.57/0.72/1.	14.83	-	-
0.1	9.039	8.871	8.892
0.03	4.141	4.153	4.065
0.01	1.974	1.997	1.943

Table A2.2 Normalized stress intensity factors K^* from J-Integral, COD, and near-tip stress σ_{yy} in the form of eq.(A2.2.2a).

The K -values for the single zones of Fig. A2.4a, compiled in Table A2.2, are plotted in Fig. A2.5a by the symbols (for the geometric data see the insert). In this plot the stress intensity factors were normalized on the J-based K value at $E/E_0=1$. The red triangle corresponds to the varying Young's modulus shown in Fig. A2.4b. Figure A2.5b represents the ratio of the data for COD- and σ_{yy} -based stress intensity factors normalized on the stress intensity factors from the J-Integral. The hatched area indicates the region of data scatter with an average value and "scatter" of about

$$K(E)/K_J(E) \approx 0.993 \pm 0.015$$

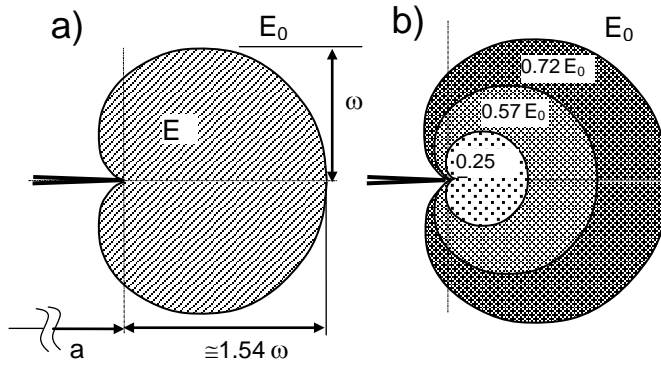


Fig. A2.4 a) Crack-tip zone with a Young's modulus E deviating from the bulk modulus E_0 , $E < E_0$, b) stepwise decreasing modulus in zones of height $1/3$, $2/3$, and $3/3\omega$.

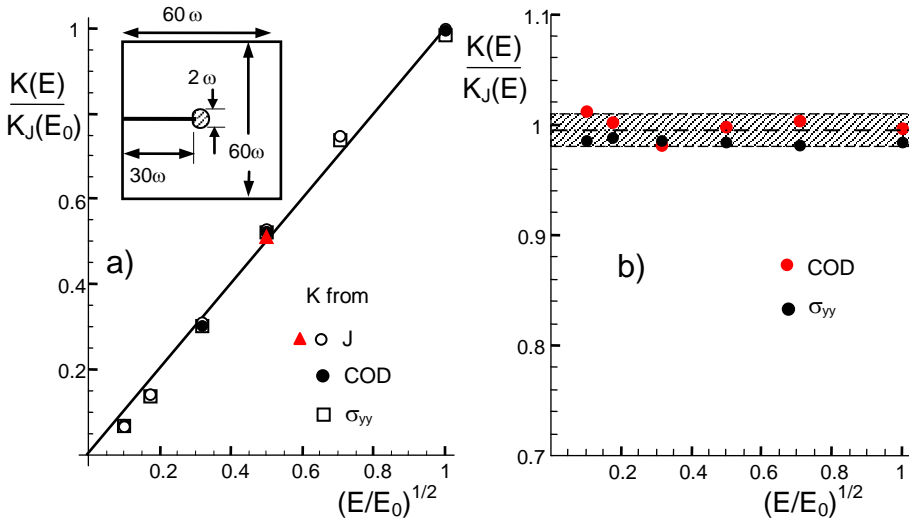


Fig. A2.5 a) Stress intensity factors from J-Integral, COD, and near-tip stress σ_{yy} , (K -values normalized on the result from J-Integral for $E/E_0=1$), red triangle for step-shaped E -distribution, b) comparison of K from COD and σ_{yy} with the individual results from J-Integral

A2.2.3 Conclusions from the FE-analysis

From the results of Fig. A2.5 it becomes evident that

- the stress intensity factors are roughly independent of the computation method,
- the stress intensity factor is only affected by the modulus closest to the crack tip,

- the straight-line behaviour of Fig. A2.5a suggests the representation by

$$K \cong K_{\text{appl}} \sqrt{\frac{E}{E_0}} \quad (\text{A2.2.3})$$

The FE-results confirm eq.(A2.2.3) as had to be expected from the theoretical analysis by Merkle [A2.3] on slender notches embedded in the reduced modulus at the notch-root.

From the agreement between the theoretical solution by Merkle [A2.3] and the FE-results for $0.1 \leq E/E_0 \leq 1$, it can be concluded that our crack-zone modelling and the accuracy of our FE-mesh is sufficient at least for this range. For the lowest value of $E/E_0 \leq 0.01$, the FE-program indicated convergence problems. With regard to the data accuracy it should be noted that the theoretical analysis was carried out for an infinite body ($\omega/a, \omega/H, \omega/W \rightarrow \infty$), while the FE calculation was carried out on a finite one.

For conditions comparable with “small-scale yielding” in elastic-plastic fracture mechanics, i.e. $\omega \ll (a, W-a)$, the effect of the zone with reduced E on K_{appl} becomes a “null-effect” [A2.2]. Then it holds

$$K_{\text{appl}} = \sigma_0 F(a/W, H/W) \sqrt{\pi a} \quad (\text{A2.2.4})$$

with the geometric function $F(a/W, H/W)$ and the remote normal tractions σ_0 at the plate ends.

We used in our study a ratio of $\omega/a=1/30$ and expected that the zone would be sufficiently small to fulfill geometry conditions for small-scale yielding. Despite this relatively small zone, influences from this zone can still be seen in Fig. A2.5a. This may at least partially be caused by the influence of an effective zone length $a_{\text{eff}}=a+\lambda\omega$, $\lambda \geq 0$ with $\lambda=0$ for the case of homogeneous material.

In the case of $\lambda > 0$, eq.(A2.2.4) reads

$$K_{\text{appl}} = \sigma_0 F(a_{\text{eff}}/W, H/W) \sqrt{\pi a_{\text{eff}}} \quad (\text{A2.2.5})$$

The stress intensity factors for $E/E_0=0.25$ and $\omega/a=0, 1/30$, and $1/90$ are plotted in Fig. A2.6. A clear trend with ω/a is visible, showing an increase of the stress intensity factor with increasing relative zone sizes.

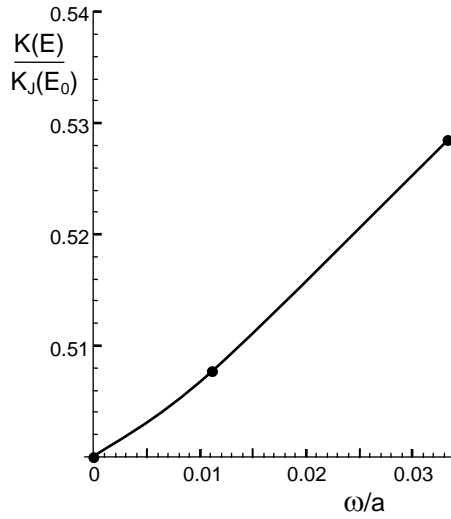


Fig. A2.6 Stress intensity factor from J-Integral for ($E/E_0=0.25$).

A2.3 Derivation of J-Integral for slender notches by Merkle

Merkle [A2.3] showed that the relation (A2.2.3) is exact in the case of a slender notch ending in a region of Young's modulus E different from the bulk material E_0 . In his analytical derivation he assumes a half-infinite crack in an infinite body loaded by remote tension in y -direction resulting in the applied stress intensity factor K_{appl} . Our FE-computations were carried out on a finite rectangular plate (inset in Fig. A2.5a).

The stress intensity factors were evaluated via the J-integral defined by

$$J = \int_{\Gamma} W dy - \mathbf{T} \frac{\partial u}{\partial x} ds \quad (\text{A2.3.1})$$

where W is the strain energy density, Γ the path around the crack tip, \mathbf{T} the tractions on the path, u the displacement in y -direction, and ds a length increment of Γ .

For reasons of simplicity we used the usual path along the surfaces represented in Fig. A2.7 with the line segments (1)-(8). Along the contours (3), (5) and (7) no tractions act and on (4) and (6) constant tensile stresses are prescribed.

The J-integral along the surface segment (1) is

$$J_1 = \int_{\Gamma_1} W dy \tag{A2.3.2}$$

In order to simplify the path-integration, the slender notch was approximated by a narrow elliptic notch with parabolic end shape (Fig. A2.8).

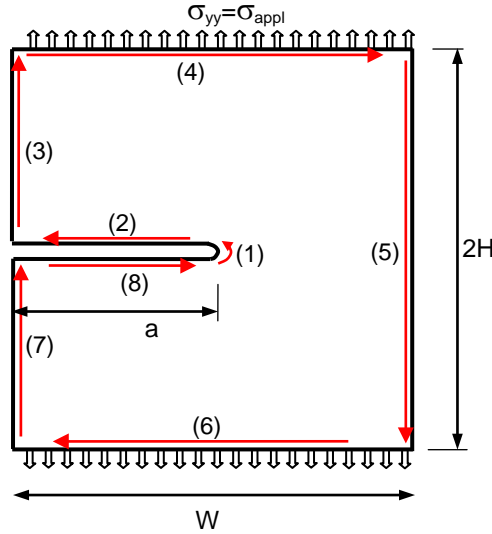


Fig. A2.7 Integration path for J-evaluation (red arrows)

An arbitrary point on the curved surface of Fig. A2.8c is described by the geometrical interrelations

$$y = r \sin \varphi, \quad r = \frac{\rho}{1 + \cos \varphi} \Rightarrow dy = \frac{\rho d\varphi}{1 + \cos \varphi} \tag{A2.3.3}$$

First it has to be noted that in the J-Integral only the modulus at the surface, E_s , enters and the variation with the distance from the surface doesn't play any role. In a subcritically grown crack the reduced value E_s is constant along the whole notch surface.

Merkle [A2.3] showed that the elastic strain energy along the crack surfaces (1, 2, 8) is

$$W = \frac{\sigma_r^2}{2E'_s} = \frac{K^2 \cos^2(\varphi/2)}{E'_s \pi r} \tag{A2.3.4}$$

with the tangential stresses σ_t . From the geometrical relations in eq.(A2.3.3) it follows after a simple mathematical manipulation

$$W = \frac{K^2}{E'_s} \frac{(1 + \cos \varphi)^2}{2\pi \rho} \quad (\text{A2.3.5})$$

Consequently, the J-integral along path parts (1, 2, 8) reads

$$J_1 = \frac{K^2}{E'_s} \frac{1}{2\pi} \int_{-\pi}^{\pi} (1 + \cos \varphi) d\varphi \Rightarrow J_1 = \frac{K^2}{E'_s} \quad (\text{A2.3.6})$$

This of course holds for large zones, $\omega \gg \rho$ to $\omega \gg \rho$, for which $\varphi \rightarrow \pi$ can be sufficiently fulfilled. Since the results of eq.(A2.3.6) and (A2.3.7) no longer depend on the notch radius, they should also apply to the sharp crack by taking $\rho \rightarrow 0$. The remote (or “applied”) stress σ_{appl} at lines (4) and (6) cause the applied stress intensity factor K_{appl} and the related “applied J-integral”

$$J_{4,6} = \frac{K_{appl}^2}{E'_0} \quad (\text{A2.3.7})$$

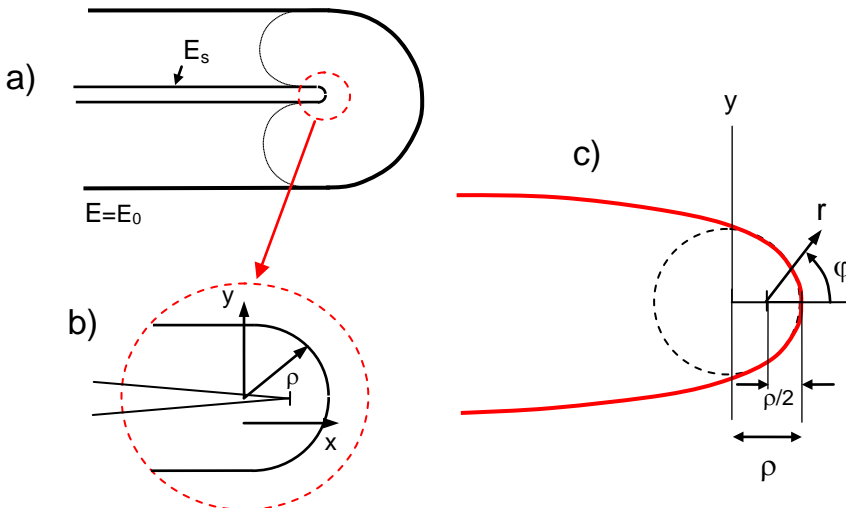


Fig. A2.8 a) Contour at the tip of a subcritically grown crack, b) detail of a), c) crack surface approximated by an elliptical notch showing the same curvature radius ρ , schematic.

The J-integral along a closed path must disappear as shown by Rice [A2.2], i.e.

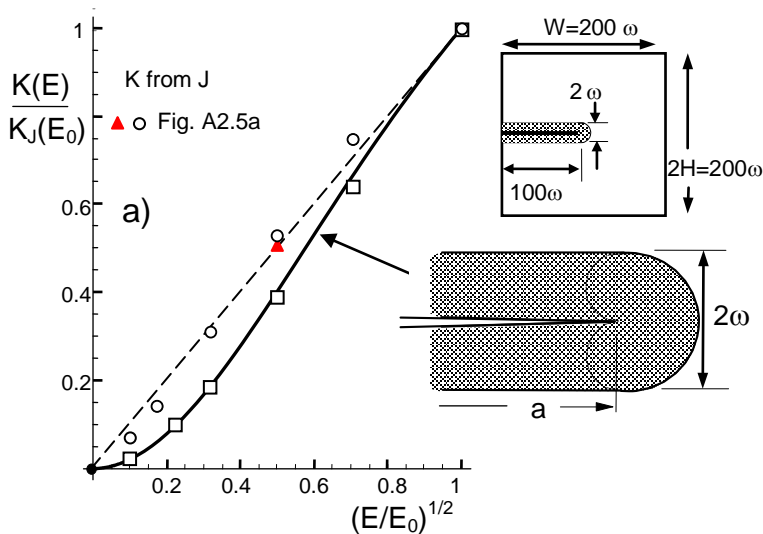
$$J_{4,6} = J_1 \Rightarrow \frac{K_{appl}^2}{E'_0} = \frac{K^2}{E'_s} \Rightarrow K = K_{appl} \sqrt{\frac{E}{E_0}} \tag{A2.3.8}$$

It should be mentioned, that the derivation by Merkle [A2.3] deals with the case of a zone of different Young's modulus ahead of a crack tip with finite notch root radius $\rho > 0$.

When the radius ρ becomes smaller in the limit-case consideration, the geometry of Figs. A2.8b and A2.8c remains self-similar and not necessarily represents the sharp crack.

A2.4 Results for extended zones

While in Section A2.2 only zones in front of the crack tip were considered, in this Section, we additionally compile results for zones extending over the entire crack length. In this case, the crack tip is fully embedded in the zone of reduced module. The plate dimensions and the crack length were increased by a factor of about 3 in order to reduce any influence of ω/a furthermore. This is shown in the plots of Fig. A2.9.



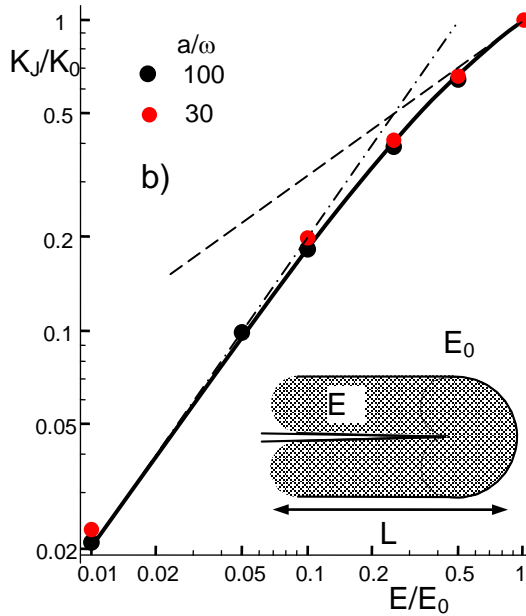


Fig. A2.9 a) Stress intensity factors from J-Integral, K_J (normalized on the value K_0 obtained for $E=E_0$) for embedded crack tips (squares) compared with the K_J -results of Fig. A2.5a (plotted by circles and triangle), solid curve: Approximation via eq.(A2.4.1), b) Stress intensity factors from J-Integral, dashed line: asymptote with slope=1/2, dash-dotted line: asymptote with slope=1.

The stress intensity factors exclusively on the basis of the J-Integral are given in Fig. A2.9a. The squares for $E/E_0 \leq 0.25$ were fitted by

$$\frac{K(E)}{K(E_0)} \cong \frac{2E}{E + E_0} \quad (\text{A2.4.1})$$

This expression is introduced by the solid curve.

We also evaluated COD-results as done in Section A2.2 and obtained the near-tip profiles given in Fig. A2.10. Stress intensity factors K_{COD} were computed from the Irwin-parabola

$$v = \sqrt{\frac{8}{\pi}} \frac{K_{\text{COD}}}{E/(1-\nu^2)} \sqrt{r} \quad (\text{A2.4.2})$$

where ν is the opening displacement and ν Poisson's ratio (0.17 for silica). The displacements in the crack wake are given for the two geometries $\omega/a=30$ and 100. In both cases $a/W=a/H=0.5$ was kept constant. The plot v vs. \sqrt{r} showed very straight lines.

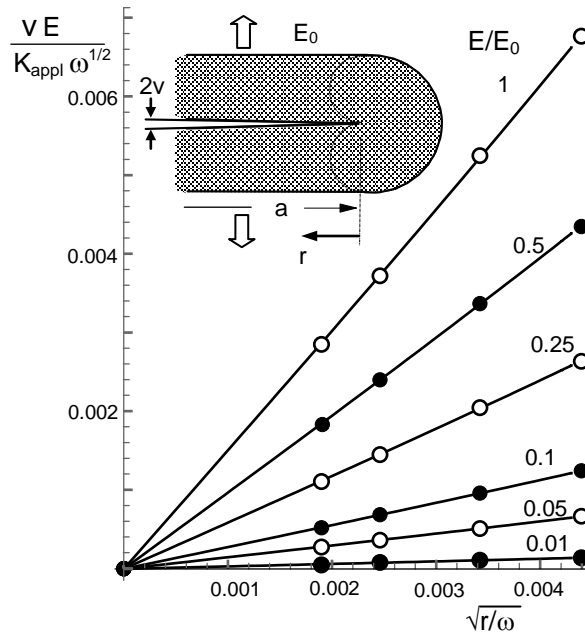


Fig. A2.10 Crack-opening profiles close to the tip versus $(r/\omega)^{1/2}$ for a crack of $a/\omega=100$.

The stress intensity factors from eq.(A2.2.1) are plotted in Fig. A2.11a as the solid circles together with the results from the J-Integral in Fig. A2.9a as the squares. In this representation no differences of the two K -values can be seen. Figure A2.11b shows the ratio of the two stress intensity factors. Note the significantly higher resolution of the ordinate. The mean value and the standard deviation SD (in brackets) are

$$\frac{K_{COD}}{K_J} = 0.999987 [0.001134]$$

Although in principle no theoretical facts can be proven by numerical calculations, this good agreement of the K factors speaks for the validity of K_J using different methods.

Conclusions: From the FE results and the theoretical solution by Merkle [A2.3] it was obtained

$$K = K_{appl} \sqrt{\frac{E}{E_0}}$$

When comparing the results for the extended areas of reduced module (here: length $L \approx a$) with the solution according to Merkle [A2.3], no agreement can be expected a priori. The zones on which the FE calculations are based do no longer meet the basic requirements of the analytical calculation, namely $(\omega, L) \ll (a, W, H)$.

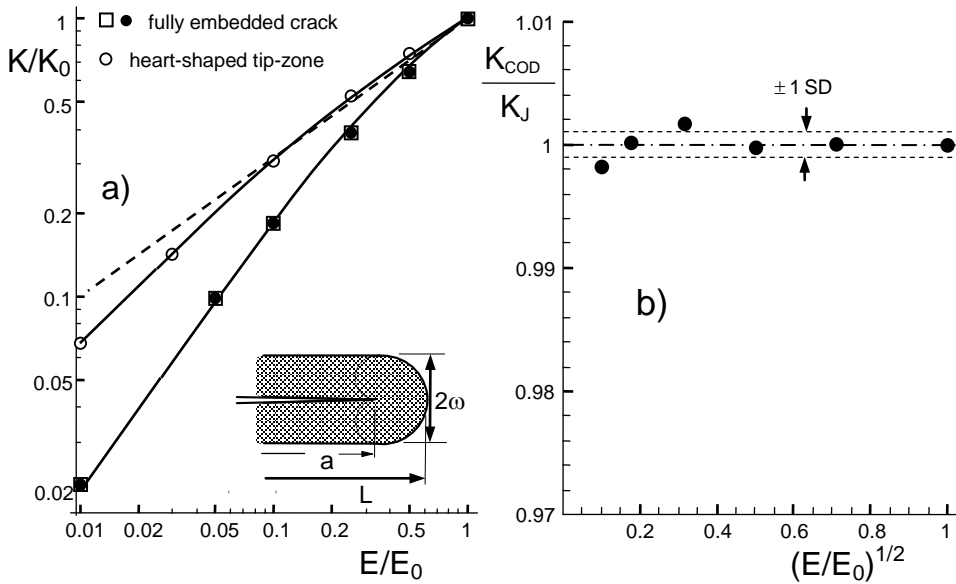


Fig. A2.11 a) K_I vs. E/E_0 as squares, results from Fig. A2.5 as open circles, K_{COD} from Fig. A2.10 via eq.(A2.2.1) as solid circles, b) ratio K_{COD}/K_I .

A2.5 Crack-Opening Displacements (COD)

We evaluated COD-results in Section A2.2 in order to compute the stress intensity factors for different Young's moduli and obtained the near-tip profiles. Stress intensity factors K_{COD} were computed from the Irwin-parabola, eq.(A2.4.2). Again v is the opening displacement in the distance r from the crack tip and $\nu=0.17$ is Poisson's ratio. Normalized displacements v' represented in Fig. A2.12 are defined by

$$v' = v \frac{E_0}{K(E_0)\sqrt{\omega(1-\nu^2)}} \tag{A2.5.1}$$

where $K(E_0)$ denotes the stress intensity factor for the case of homogeneous material. In the following COD in larger distance are considered.

A2.5.1 COD for heart-shaped zones

Crack-opening displacements for the crack with a heart-shaped zone ahead of the tip are shown in Fig. A2.12a in the form $v'=f(r/\omega)$ and in Fig. A2.12b in the form of $(v')^2=f(r/\omega)$. From the diagram of $(v')^2=f(r/\omega)$ it becomes obvious that the squares of CODs tend to straight lines for about $r/\omega > 1.5$. The straight lines for $E/E_0 < 1$ show fictive crack origins as indicated by the intersections of the dashed extensions of the crack profiles with the abscissa. In the case of very short crack-tip distance the COD is similar to crack-tip blunting in elastic-plastic fracture mechanics although the material behaviour is purely linear-elastic. In larger distances of about $r/\omega > 1.5$, the straight line for $E/E_0 = 0.01$ shows nearly the same slope as obtained for $E/E_0 = 1$ and seems to be shifted by the constant amount $(v'(0))^2$ (see the inset in Fig. A2.13).

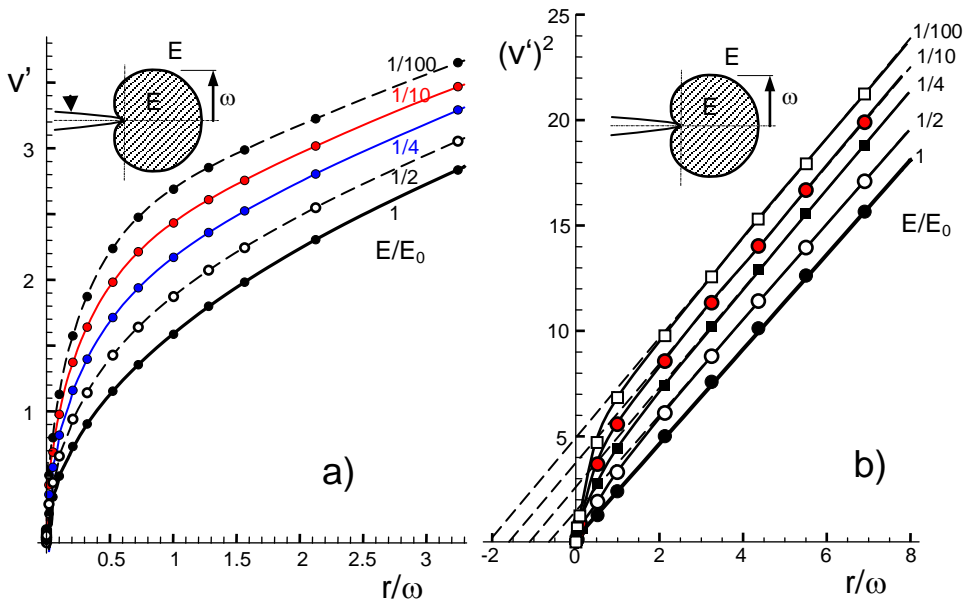


Fig. A2.12 Influence of reduced Young's modulus in the heart-shaped crack-tip zone, a) linear representation of the normalized COD according to eq.(A2.5.1), b) square of the COD as the ordinate.

The values of the straight lines v' at $r=0$ are called in elastic-ideal plastic fracture mechanics the “Crack-Tip-Opening Displacements (CTOD)” and used as material property for yielding. Figure A2.13 again shows the COD-profiles for the extremely different Young’s moduli ratios $E/E_0=1$ and $1/100$. The apparent crack-tip blunting is illustrated by the inset in Fig. A2.13, when the COD is simplified by the thick red contours, resulting in an apparent crack-tip opening and an apparent increase Δa of the fictive crack length.

E/E_0	$d(v')^2/d(r/\omega)$	$(v')^2(r=0)$	$\Delta a/\omega$
1	2.436	0	0
0.5	2.433	1.396	0.573
0.25	2.494	2.746	1.101
0.1	2.488	3.966	1.594
0.01	2.511	5.197	2.067

Table A2.3 Parameters of straight lines in Fig. A2.12b: Slopes of straight lines, opening displacements $(v'(r=0))^2$ at the crack tip, fictive crack-length increase Δa as a function of Young’s modulus ratio E/E_0 for $\nu=0.17$.

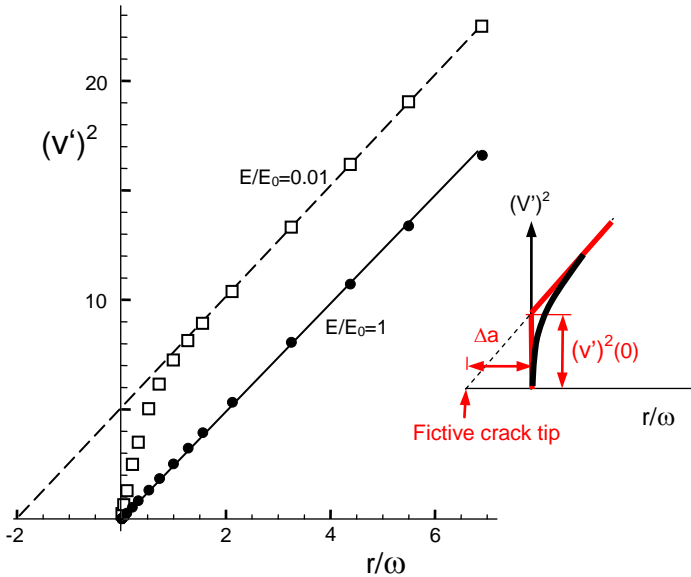


Fig. A2.13 Representation of near-tip COD by the crack-tip opening displacement.

A2.5.2 COD for zones extended in the crack wake

For the zone extending over the whole crack wake, we performed the same evaluations as done for the heart-shaped zone. Figure A2.14 and Table A2.4 show the results.

E/E_0	$d(v')^2/d(r/\omega)$	$(v')^2(r=0)$	$\Delta a/\omega$
1	2.58	0	0
0.5	2.69	0.47	0.17
0.25	2.76	1.32	0.48
0.1	2.81	2.25	0.80
0.05	2.83	2.74	0.97
0.01	2.86	3.19	1.12

Table A2.4 Parameters characterizing the dashed straight lines in Fig. A2.14.

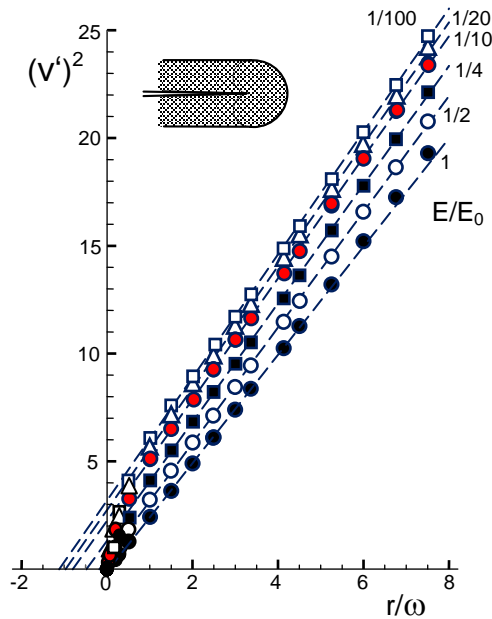


Fig. A2.14 Influence of reduced Young's modulus in the extended zone, square of the COD as the ordinate.

A2.6 Comparison of parameters for the two zone shapes

Figure A2.15 shows again the parameters from Tables A2.3 and A2.4. In Fig. A2.15a the slopes are given and in Fig. A2.15b the offsets of the straight line asymptotes at $r/\omega=0$. It is obvious that the slopes hardly vary noticeably with the modulus of elasticity. Only very slight changes with increasing modulus can be stated.

Summary on COD: We studied the COD-behaviour of cracks in a bi-material. The following points may be emphasized:

- From our FE-computations on crack-opening displacements it can be stated that the effect of a reduced Young's modulus is visible only in a crack-tip distance of $r/\omega < 1.5$.
- The slopes of the asymptotes, reached for distances $r/\omega > 1.5$, are within about $\pm 5\%$ independent of the modulus.
- The fictive crack lengths defined by the intersections of the straight asymptotes with the abscissa is in the order of $\Delta a/\omega \approx 0-2$.
- The steeply rising displacements at $r/\omega \approx 0$ may suggest to the observer an occurrence of "crack-tip blunting", although purely linear-elastic material behaviour is present.

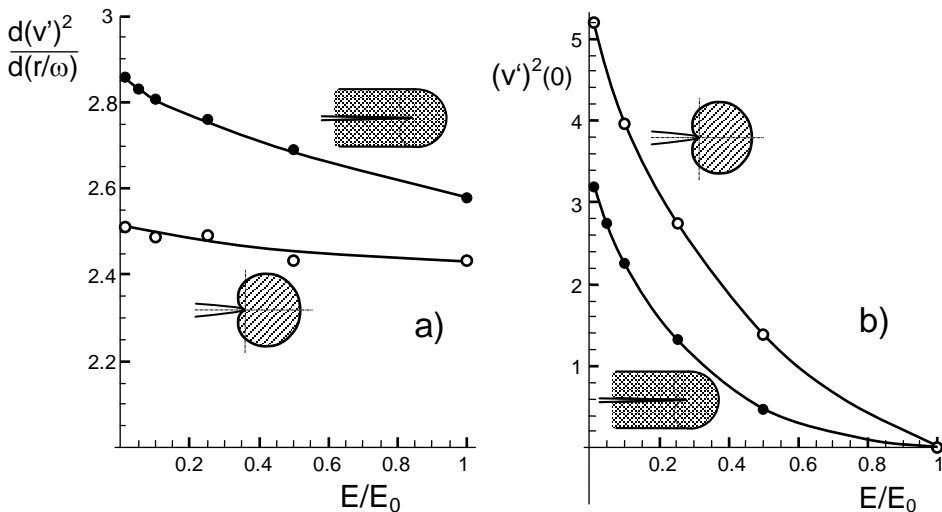


Fig. A2.15 a) Comparison of slopes and b) crack-tip displacements from Tables A2.3 and A2.4.

References

A2.1 Evans, A.G., Faber, K.T., Crack-growth resistance of microcracking brittle materials, *J. Am. Ceram. Soc.* **67**(1984), 255-260.

A2.2 Rice, J.R., A path independent integral and the approximate analysis of strain concentration by notches and cracks, *Trans. ASME, J. Appl. Mech.* (1986), 379-386.

A2.3 J. G. Merkle, An application of the J-integral to an incremental analysis of blunt crack behavior, *Mechanical Engineering Publications*, London, 1991, 319-332.

A3 Hydrostatic stress at crack tips

A3.1 Hydrostatic stress under hydroxyl damaging

The hydroxyl generation by the reaction eq.(1.1.1) causes damage since the originally intact silica ring structure is cracked by the water attack. One of the consequences of such damage is the reduction of Young's modulus E . In order to describe this E -decrease, we used in [A3.1] the rather simple damage model proposed by Phany and Niyogi [A3.2].

When E_D is the modulus in the damaged state and E_0 the value for undamaged silica, we could derive the relation (see Section 11 and [A3.1])

$$\frac{E_D}{E_0} = (1 - S / S_{\max})^2 \quad (\text{A3.1.1})$$

with $S_{\max}=0.188$. Under the condition that the damage is isotropic, the multiaxiality in damaged states remains unchanged. In a volume element that is hydrostatically loaded by tensile stresses $\sigma_x=\sigma_y=\sigma_z$, the externally applied hydrostatic stress is

$$\sigma_{h,appl} = \frac{1}{3}(\sigma_x + \sigma_y + \sigma_z) \quad (\text{A3.1.2})$$

The hydroxyl concentration as a function of stress, reads by using eq.(A3.1.1)

$$S = S_0 \exp\left[\sigma_{h,D} \frac{\Delta\bar{V}}{RT}\right] = S_0 \exp\left[\sigma_{h,appl} (1 - S / S_{\max})^2 \frac{\Delta\bar{V}}{RT}\right] \quad (\text{A3.1.3})$$

In Fig. A3.1a, the hydroxyl concentration is plotted vs. the applied hydrostatic stress for $S_0=0.1$ wt-%, and $\theta=90^\circ\text{C}$. The dash-dotted line indicates the maximum hydroxyl concentration of $S_{\max}=18.8$ wt-%. Figure A3.1b shows the related hydrostatic stress in the damaged state, $\mu\sigma_{h,D}$, vs. the applied hydrostatic stress $\mu\sigma_{h,appl}$. In the notation of the coordinate axis the abbreviation μ is defined as

$$\mu = \frac{\Delta\bar{V}}{RT} \quad (\text{A3.1.4})$$

The maximum hydrostatic stress, asymptotically reached for $\sigma_{h,appl} \rightarrow \infty$, is

$$\mu\sigma_{h,D,max} = -\text{Log} \left[\frac{S_0}{S_{max}} \right] \quad (\text{A3.1.5})$$

The curves $\sigma_{h,D}(\sigma_{h,appl})$ of Fig. A3.1b may be simplified by a bi-linear description as introduced by the dash-dotted lines in Fig. A3.1b.

In this case, the maximum possible stress in the damaged state is depending on the temperature. In the sense of an upper limit solution, the stresses can be approximated as

$$\sigma_{h,D} = \begin{cases} \sigma_{h,appl} & \text{for } \sigma_{h,appl} < \sigma_{D,h,max} \\ \sigma_{h,D,max} & \text{else} \end{cases} \quad (\text{A3.1.6})$$

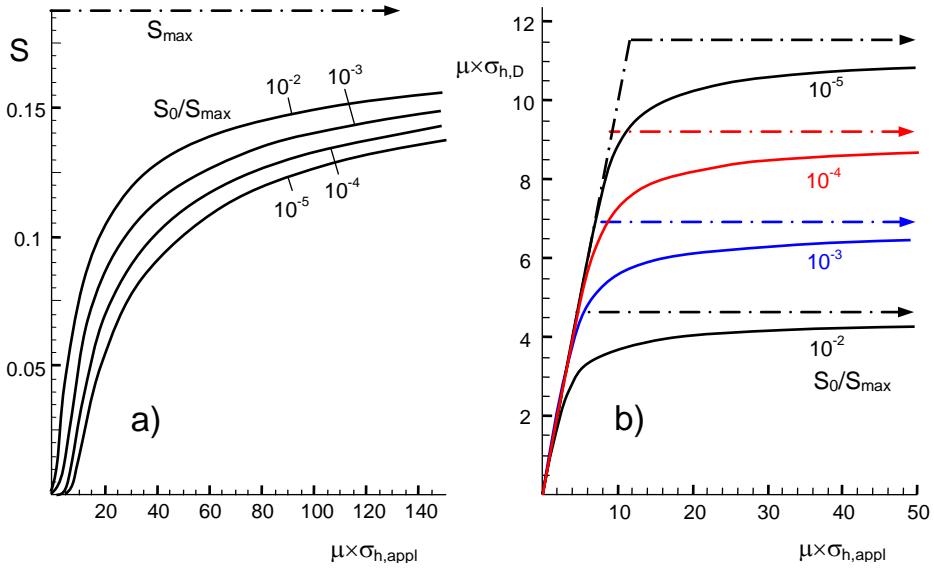


Fig. A3.1 a) Hydroxyl concentration vs. applied stress under condition of constant strains, b) hydrostatic stress in the damaged material $\sigma_{h,D}$ as a function of the applied hydrostatic stress $\sigma_{h,appl}$ and the initial hydroxyl concentration S_0 with the abbreviation μ defined by eq.(A3.1.4), limits of hydrostatic stress and approximation by an upper bound description (dash-dotted straight lines).

A3.2 Irwin and Dugdale model

Due to the damage via hydroxyl generation, the stress-strain behavior at a crack tip is no longer linear. By application of the bi-linearized dependency eq.(A3.1.6), fracture mechanics problems can approximately be solved applying for instance the well-known Irwin and Dugdale models, originally developed for elastic/plastic material behaviour.

The Irwin [A3.3] and the Dugdale model [A3.4] describe *plastic deformations* in a zone ahead of the crack. Whereas in the Irwin model the size of the “plastic zone” was computed from “yield”-condition $\sigma_{\text{appl,y}}=\sigma_Y$ and by force equilibrium along the prospective crack plane, the size of the Dugdale zone results from the condition that the stress intensity factor for the fictive crack in Fig. A3.2a disappears. So the shape of the zones is not fixed, especially not for the Dugdale zone. The latter is mostly concentrated along the x -axis.

According to these models the “length” L of the “plastic” zone, is under *plane stress* conditions

$$L_{\text{Irwin}} = \frac{1}{\pi} \left(\frac{K_{\text{appl}}}{\sigma_Y} \right)^2, \quad L_{\text{Dugdale}} = \frac{\pi}{8} \left(\frac{K_{\text{appl}}}{\sigma_Y} \right)^2 \quad (\text{A3.2.1})$$

where σ_Y is the “yield stress” for the case of a linear-elastic/ideal-plastic material. The opening at the tip of the physical crack, called *Crack Tip Opening Displacement* (CTOD), δ_t , results from [A3.3, A3.4] as

$$\delta_{t,\text{Irwin}} = \frac{4}{\pi} \frac{K_{\text{appl}}^2}{E \sigma_Y}, \quad \delta_{t,\text{Dugdale}} = \frac{K_{\text{appl}}^2}{E \sigma_Y} \quad (\text{A3.2.2})$$

The CTOD, δ_t , is illustrated in Figs. A3.2b and A3.2c. Whereas the Irwin model [A3.3] is preferred for circular “plastic zones”, the Dugdale model [A3.4] describes also plastic deformations in a narrow strip in front of the crack. In the derivation of the Dugdale formula, it was assumed that there exists an internal through-the-thickness crack in an infinite plate and that the yield stress is constant over the zone size L regardless of the locally varying strains. This provided the analytical solutions (A3.2.1) and (A3.2.2) for the zone size and the CTOD.

Remark: It should be emphasized here once again that it is not claimed that the glass behaves in an elastic/ideally plastic manner. This approach only leads to a simple fracture

mechanical treatment of the crack tip problem for the “deformation” curves represented by the limit case eq.(A3.1.6).

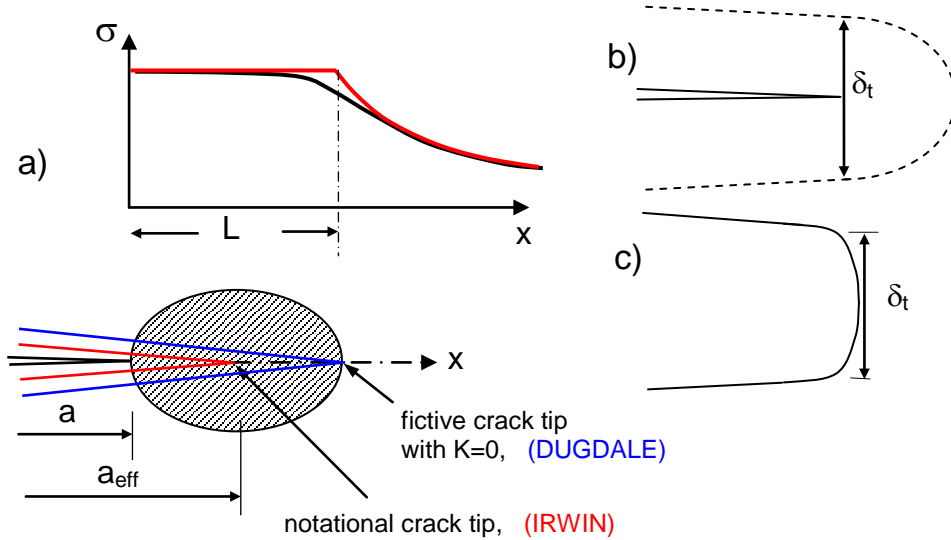


Fig. A3.2 a) Stress distribution curve near a crack tip (black curve) approximated by an elastic-“plastic” material behaviour (red curve) in the crack-tip region (zone shape is not necessarily a circle), b) crack tip opening displacement (CTOD) δ_t , c) observable crack profile.

References

A3.1 T. Fett, G. Schell, C. Bucharsky, Hydroxyl Damage in Silica: Full-range description including large damages **126**, 2019, ISSN: 2194-1629, Karlsruhe, KIT.

A3.2 Phani, K.H. Niyogi, K. De, Young's modulus of porous brittle solids, *J. Mater. Sci.* **22**(1987), 257–263.

A3.3 G. R. Irwin, Plastic zone near a crack and fracture toughness, *Proc. 7th Sagamore Conf.* 1960, p. IV-63 (1960).

A3.4 D.S. Dugdale, Yielding of steel sheets containing slits. *J. Mech. Phys. Solids* **8** (1960), 100-8.

A4 Swelling stresses from crack-terminating angles

A4.1 Estimation of the magnitude of residual stresses

A4.1.1 Shielding stress intensity factors and residual stresses

Volume expansions occur by swelling of the glass volume due to hydroxyl generation [A4.1, A4.2, A4.3]. The results from [A4.1] can be expressed by eq.(1.1.9) in terms of the hydroxyl concentration S in mass units.

Due to the mechanical boundary conditions, the swelling strains result in swelling stresses proportional to the amount of hydroxyl concentration as were described by eq.(1.1.11). A volume element in a thick plate that undergoes swelling cannot freely expand. If the diffusion zone is small compared to the component dimensions, expansion is completely prevented in the plane of the surface and can only take place normal to the surface plane.

In Section 2 we determined the shielding stress intensity factor from the externally applied stress intensity factor K_{appl} and the total stress intensity factor K_{tip} . In the case of silica, K_{tip} is for spontaneous and stable crack extension identical with the toughness K_{c} and was in our rather fast subcritical crack growth tests on silica about $K_{\text{tip}}=0.55-0.6$ MPa $\sqrt{\text{m}}$. Therefore, we used an average of $K_{\text{tip}}=0.575$ MPa $\sqrt{\text{m}}$.

The crack-shielding stress intensity factor must be proportional to the swelling stresses σ_{sw} acting normal on the crack plane and the square-root of the layer thickness

$$K_{sh} = F(\varphi, b) \sigma_{sw} \sqrt{\pi b} \quad (\text{A4.1.1})$$

The fracture mechanics geometric function for this loading over a small region, $F(\varphi, b)$, is so far unknown, but may be estimated by not too large effort. Very often the stresses caused by diffusion processes (here: water diffusion into silica) and the stress distribution can be described by

$$\sigma_{sw} = \sigma_{sw,0} \operatorname{erfc}\left[\frac{z}{2b}\right] \quad (\text{A4.1.2})$$

where $\sigma_{sw,0}$ is the surface value, $z=0$, of the stresses and b is the diffusion depth at which the water concentration and consequently the swelling stresses are reduced to $\cong 50\%$ of the surface value as is illustrated in Fig. A4.1a.

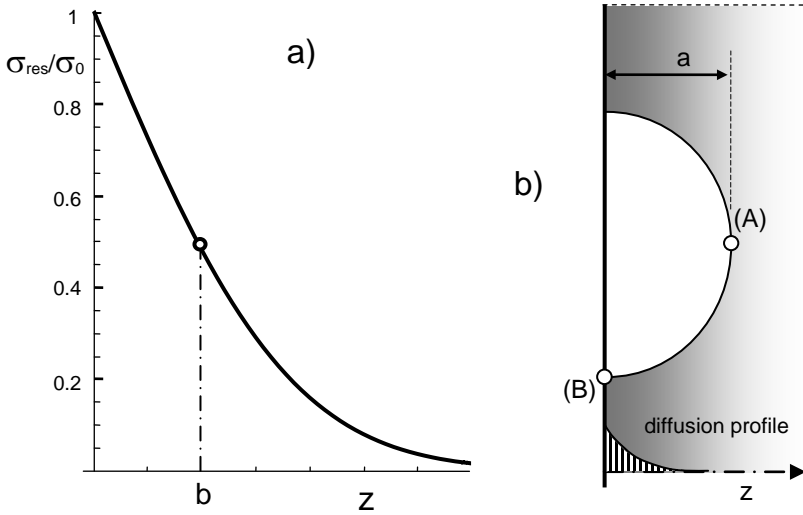


Fig. A4.1 a) Stresses in the surface region according to eq.(A4.1.2), b) semi-circular surface crack loaded by the erfc-shaped stresses.

A4.1.2 Stress intensity factor solutions for residual stresses

In order to give an estimation for the maximum swelling stresses in eq.(A4.1.2) on the basis of the experimentally obtained shielding stress intensity factor, the geometric function $F(\varphi, b)$ must be known. Following an approximate procedure proposed by Underwood [A4.4], the interrelation between shielding and applied stress intensity factors reads

$$K_{sh}(\varphi, b) = \lambda \frac{K_{appl}(\varphi)}{K_{appl}(90^\circ)} K_{sh}(90^\circ, b) \quad (\text{A4.1.3})$$

However, this procedure can yield larger errors if the shapes of the two cracks to be compared are significantly different. In the original paper by Underwood [A4.4] it was shown that the stress intensity factors for complicated cracks (semi-elliptical surface cracks in thick-walled tubes) under complicated stresses (tension and bending superimposed) were always smaller than those for the reference crack (continuous crack in a plate under pure tension), compare e.g. Fig. 6 in [A4.4]. This fact may be indicated by the parameter $\lambda \leq 1$ in the following eq.(A4.1.3). The equal sign, $\lambda=1$, trivially holds when the crack to be predicted is identical with the reference case. From the special result of [A4.4], we can conclude for the coefficient λ , introduced in eq.(A4.1.3), $\lambda \approx 2/3$.

The shielding stress intensity factor is available for the special case of a crack terminating with $\varphi=90^\circ$. For this purpose let us replace the straight crack by a semi-circular surface crack of depth a that might be large compared to the layer thickness, $a \gg b$. The stress intensity factor at the surface point (B), Fig. A4.1b, obtained from [A4.3], is

$$K_{sh,B} \cong 1.29 \sigma_{sw,0} \sqrt{a} \tanh \left[1.327 \sqrt{\frac{b}{a}} + 0.064 \frac{b}{a} \right] \quad (\text{A4.1.4})$$

A series expansion of the FE-results in [A4.3] for $b/a \rightarrow 0$ results in the simple expression

$$K_{sh,B} \cong 1.72 \sigma_{sw,0} \sqrt{b} \approx \sigma_{sw,0} \sqrt{\pi b} \quad (\text{A4.1.5})$$

When calculating K -factors, it does not matter whether the applied stresses are externally applied or internal ones. Therefore, both must show the same type of angle dependencies. In our first derivation in [A4.5] it was implicitly assumed that the coefficient λ can be regarded as a constant value. From the comparison with experimental results in Fig. 4 of [A4.5], however, a dependence on the terminating angle emerged, $\lambda = \lambda(\varphi)$. This finding should be taken into account in the current evaluation. The shielding stress intensity factor $K_{sh}(\varphi, b)$ can now be obtained as

$$K_{sh}(\varphi, b) = \lambda(\varphi) \frac{1}{0.00658 \varphi + 7.66 \times 10^{-13} \varphi^6} \sigma_{sw,0} \sqrt{\pi b} \quad (\text{A4.1.6})$$

from which the swelling stress $\sigma_{sw,0}$ can be estimated.

The results for K_{sh} in Table 2.1 shall be used here to estimate at least the order of magnitude of the residual stresses.

From the shielding stress intensity factors we estimated the residual stresses [A4.5]. For the tests by Schell et al. [A4.6] and Haranoh et al. [A4.7], crack extension is governed by $K_{ip}=K_{ic}$. Fracture toughness of soda-lime glass is according to Wiederhorn [A4.8]: $K_{ic}=0.75 \text{ MPa}\sqrt{\text{m}}$ and Poisson's ratio $\nu=0.225$.

From [A4.5] it follows for the applied stress intensity factor of the crack-terminating angle φ (soda-lime glass $\nu=0.225$)

$$K_{sh}(\varphi, b) = \lambda(\varphi) \frac{1}{0.00606 \varphi + 8.54 \times 10^{-13} \varphi^6} \sigma_{sw,0} \sqrt{\pi b} \quad (\text{A4.1.7})$$

A4.2 Discussion of stresses

All residual stresses in Table A4.1 were found to be negative indicating that the water/silica reaction, the ion exchange, and chemical toughening are accompanied by volume expansion. The absolute values of the compressive stresses resulting by the extension of the Underwood procedure depend on the coefficient λ that is not yet known. As can be concluded from Underwood [A4.4], the value of λ decreases with increasing deviation from the reference crack. A rough estimation of λ as a function of φ may be suggested based on soda-lime glass undergoing ion-exchange.

In [A4.6] the stresses by ion exchange were concluded from strength measurements as $\sigma_{res} = -2425 \text{ MPa}$. A theoretical value of -2300 MPa was determined in [A4.9, A4.10] for the volume change by the ion-exchange fully transformed in stresses. As an average value, $\sigma_{res} = -2.4 \text{ GPa}$ may be used to compute the value of λ . From the data of $-\lambda\sigma_{res}$ in Table A4.1 and the related terminating angles φ , φ_0 in Table 2.1, the red circles in Fig. A4.2a were obtained. In this plot, the terminating angles φ were normalized on $\varphi=90^\circ$ representing the reference case (black circle).

The solid curve represents a quadratic fit based on the results for the soda-lime glass with the "weight" for the 1-week result (in parentheses) described by

$$\lambda(\varphi) \cong \frac{1}{2} \frac{\varphi}{90^\circ} \left(1 + \frac{\varphi}{90^\circ} \right) \quad (\text{A4.2.1})$$

In the case of swelling stresses in silica, the surface stresses at $\theta=250^\circ\text{C}$ can be computed from the hydroxyl concentration at the free surface as shown in [A4.11]. The swelling stress components in the surface plane are

$$\sigma_{sw,x} = \sigma_{sw,y} = \frac{3}{2} \frac{13.75 \text{ MPa} \exp(0.00868 \theta)}{\frac{1}{2} + \frac{1}{A} \exp(Q/RT)} \quad (\text{A4.2.2})$$

with $A=32.3$ and $Q=10.75 \text{ kJ/mol}$, $T=\theta+273^\circ$.

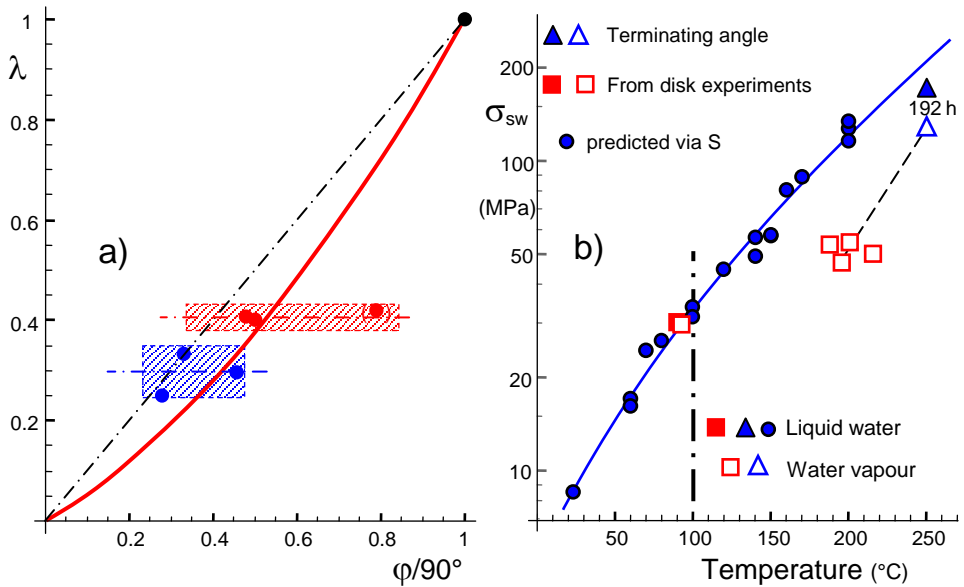


Fig. A4.2 Coefficient λ of eq.(A4.1.3) as a function of the crack-terminating angle ϕ ; red circles: results for soda-lime glass, red line: related fitting curve for reduced weight of the data point at $\phi=71^\circ$ (in parentheses); blue circles: results for silica, b) swelling stress under saturation pressure from crack-terminating angles compared with results from disk experiments, and water concentrations by Zouine et al [A4.12], full symbols: liquid water, open symbols: water vapour.

Equation (A4.2.2) yields for $\theta=250^\circ\text{C}$: $\sigma_{sw,x,y} = -209 \text{ MPa}$. The results for silica predicted with eq.(A4.2.1), are introduced in Fig. A4.2a by the blue circles, showing compressive stresses in the range of -130 MPa to -170 MPa .

Applying eq.(A4.2.1) on the chemically toughened soda-lime glass gives a residual stress of $\sigma_{\text{res}}=-1980$ MPa. This result is in agreement with a surface stress of “more than -1000 MPa” as had been reported by Haranoh et al. [A4.7].

Glass	Treatment	$\lambda\sigma_{\text{res}}$ (MPa)	σ_{res} (MPa)
Soda-lime	Chem. toughened	-174	-1980
	Ion exchange 1 week	-1009.	≈ 2400
	5 weeks	-976.	≈ 2400
	6 weeks	-968.	≈ 2400
Silica	192h H ₂ O-vapour	-52.4	-128
	48h H ₂ O-liquid	-62.1	-151
	192h H ₂ O-liquid	-69.7	-170

Table A4.1 Estimates of residual stresses, $\sigma_{\text{res}}=\sigma_{\text{sw}}$, in soda-lime glass and silica, predicted residual stresses for silica and chemically toughened soda-lime glass by use of eq.(A4.2.1).

Figure A4.2b gives a comparison between the swelling stresses from crack terminating angles with data from disk bending experiments, [A4.2], and hydroxyl concentrations via eqs.(1.1.11) and (3.1.4). The results for liquid water and 192 h soaking time are about 15% below the curve predicted by eq.(A4.2.2). For the shorter soaking time, the deviation is somewhat larger. Vapour soaking results in clearly deviations from the curve and show the same effect as found for the disk tests, in both cases an indication for the fact, that saturation was not reached.

The silica/water reaction at silica surfaces exposed to water causes volume expansion in the water diffusion layer and as the consequence of mechanical boundary conditions compressive stresses. Evaluation of crack-terminating angles resulted in strongly *negative* shielding stress intensity factors of about $K_{\text{sh}}=-2.5$ MPa $\sqrt{\text{m}}$ (see Table 2.1), a clear evidence for compressive stresses in the water-affected surface layer. Consequently, the existence of swelling stresses due to the silica/water reaction is proven. For silica, heat-treated in humid environments, compressive stresses in the order of about -130 MPa to -170 MPa are obtained for 250°C.

References

- A4.1 Shelby, J.E., Density of vitreous silica, *J. Non-Cryst.* **349** (2004), 331-336
- A4.2 S.M. Wiederhorn, T. Fett, G. Rizzi, S. Fünfschilling, M.J. Hoffmann and J.-P. Guin, Effect of Water Penetration on the Strength and Toughness of Silica Glass, *J. Am. Ceram. Soc.* **94** (2011) [S1] S196-S203.
- A4.3 T. Fett, G. Rizzi, M. Hoffmann, S. Wagner, and S.M. Wiederhorn, Effect of Water on the inert Strength of Silica Glass: Role of Water Penetration, *J. Am. Ceram. Soc.* **95** (2012) [12], 3847-3853.
- A4.4 H.J. Underwood, Stress intensity factors for internally pressurized thick-wall cylinders, *ASTM STP* **53**(1972), 59.
- A4.5 P. Hettich, K. G. Schell, G. Rizzi, S. Wagner, T. Fett, Estimation of swelling stresses from crack-terminating angles, *Scientific Working Papers, SWP* **119**, 2019, ISSN: 2194-1629, Karlsruhe, KIT.
- A4.6 K.G. Schell, S. Wagner, P. Hettich, T. Fett, G. Rizzi, M.J. Hoffmann, Identification of residual stress layers at glass surfaces via crack terminating angles, *J. Am. Ceram. Soc.* **100**(2017), 4173-4179.
- A4.7 T. Haranoh, H. Ishikawa, N. Shinkai, M. Mizuhashi, Crack evolution in Vickers indentation for soda-lime-silica glass, *J. of Mater. Science* **17**(1982) 1493-1500.
- A4.8 S.M. Wiederhorn, Fracture Surface Energy of Glass, *J. Am. Ceram. Soc.* **52** [2] 99-105 (1969).
- A4.9 T. Fett, J.P. Guin, S.M. Wiederhorn, Stresses in ion-exchange layers of soda-lime-silicate glass, *Fatigue Fract. Engng. Mater. Struct* **28**(2005), 507-514.
- A4.10 J.P. Guin, S.M. Wiederhorn, T. Fett, Crack-tip structure in soda-lime-silicate glass *J. Am. Ceram. Soc.* **88**(2005), 652-59.
- A4.11 T. Fett, K.G. Schell, Elimination of swelling stresses from measurements of the equilibrium constant in silica, *Scientific Working Papers, SWP* **117**, 2019, ISSN: 2194-1629, Karlsruhe, KIT.
- A4.12 A. Zouine, O. Dersch, G. Walter and F. Rauch, Diffusivity and solubility of water in silica glass in the temperature range 23-200°C, *Phys. Chem. Glass: Eur. J. Glass Sci and Tech. Pt. B*, **48** [2] (2007), 85-91.

Schriftenreihe des Instituts für Angewandte Materialien

ISSN 2192-9963

- Band 1 Prachai Norajitra
Divertor Development for a Future Fusion Power Plant.
ISBN 978-3-86644-738-7
- Band 2 Jürgen Prokop
Entwicklung von Spritzgießsondervverfahren zur Herstellung von Mikroteilen durch galvanische Replikation.
ISBN 978-3-86644-755-4
- Band 3 Theo Fett
New contributions to R-curves and bridging stresses – Applications of weight functions.
ISBN 978-3-86644-836-0
- Band 4 Jérôme Acker
Einfluss des Alkali/Niob-Verhältnisses und der Kupferdotierung auf das Sinterverhalten, die Strukturbildung und die Mikrostruktur von bleifreier Piezokeramik $(K_{0,5}Na_{0,5})NbO_3$.
ISBN 978-3-86644-867-4
- Band 5 Holger Schwaab
Nichtlineare Modellierung von Ferroelektrika unter Berücksichtigung der elektrischen Leitfähigkeit.
ISBN 978-3-86644-869-8
- Band 6 Christian Dethloff
Modeling of Helium Bubble Nucleation and Growth in Neutron Irradiated RAFM Steels.
ISBN 978-3-86644-901-5
- Band 7 Jens Reiser
Duktilisierung von Wolfram. Synthese, Analyse und Charakterisierung von Wolframlaminaten aus Wolframfolie.
ISBN 978-3-86644-902-2
- Band 8 Andreas Sedlmayr
Experimental Investigations of Deformation Pathways in Nanowires.
ISBN 978-3-86644-905-3

- Band 9 Matthias Friedrich Funk
Microstructural stability of nanostructured fcc metals during cyclic deformation and fatigue.
ISBN 978-3-86644-918-3
- Band 10 Maximilian Schwenk
Entwicklung und Validierung eines numerischen Simulationsmodells zur Beschreibung der induktiven Ein- und Zweifrequenzrandschichthärtung am Beispiel von vergütetem 42CrMo4.
ISBN 978-3-86644-929-9
- Band 11 Matthias Merzkirch
Verformungs- und Schädigungsverhalten der verbundstranggepressten, federstahldrahtverstärkten Aluminiumlegierung EN AW-6082.
ISBN 978-3-86644-933-6
- Band 12 Thilo Hammers
Wärmebehandlung und Recken von verbundstranggepressten Luftfahrtprofilen.
ISBN 978-3-86644-947-3
- Band 13 Jochen Lohmiller
Investigation of deformation mechanisms in nanocrystalline metals and alloys by in situ synchrotron X-ray diffraction.
ISBN 978-3-86644-962-6
- Band 14 Simone Schreijäg
Microstructure and Mechanical Behavior of Deep Drawing DC04 Steel at Different Length Scales.
ISBN 978-3-86644-967-1
- Band 15 Zhiming Chen
Modelling the plastic deformation of iron.
ISBN 978-3-86644-968-8
- Band 16 Abdullah Fatih Çetinel
Oberflächendefektausheilung und Festigkeitssteigerung von niederdruckspritzgegossenen Mikrobiegebalken aus Zirkoniumdioxid.
ISBN 978-3-86644-976-3
- Band 17 Thomas Weber
Entwicklung und Optimierung von gradierten Wolfram/EUROFER97-Verbindungen für Divertorkomponenten.
ISBN 978-3-86644-993-0

- Band 18 Melanie Senn
Optimale Prozessführung mit merkmalsbasierter Zustandsverfolgung.
ISBN 978-3-7315-0004-9
- Band 19 Christian Mennerich
Phase-field modeling of multi-domain evolution in ferromagnetic shape memory alloys and of polycrystalline thin film growth.
ISBN 978-3-7315-0009-4
- Band 20 Spyridon Korres
On-Line Topographic Measurements of Lubricated Metallic Sliding Surfaces.
ISBN 978-3-7315-0017-9
- Band 21 Abhik Narayan Choudhury
Quantitative phase-field model for phase transformations in multi-component alloys.
ISBN 978-3-7315-0020-9
- Band 22 Oliver Ulrich
Isothermes und thermisch-mechanisches Ermüdungsverhalten von Verbundwerkstoffen mit Durchdringungsgefüge (Preform-MMCs).
ISBN 978-3-7315-0024-7
- Band 23 Sofie Burger
High Cycle Fatigue of Al and Cu Thin Films by a Novel High-Throughput Method.
ISBN 978-3-7315-0025-4
- Band 24 Michael Teutsch
Entwicklung von elektrochemisch abgeschiedenem LIGA-Ni-Al für Hochtemperatur-MEMS-Anwendungen.
ISBN 978-3-7315-0026-1
- Band 25 Wolfgang Rheinheimer
Zur Grenzflächenanisotropie von SrTiO₃.
ISBN 978-3-7315-0027-8
- Band 26 Ying Chen
Deformation Behavior of Thin Metallic Wires under Tensile and Torsional Loadings.
ISBN 978-3-7315-0049-0

- Band 27 Sascha Haller
Gestaltfindung: Untersuchungen zur Kraftkegelmethode.
ISBN 978-3-7315-0050-6
- Band 28 Nicht erschienen
- Band 29 Gunnar Picht
Einfluss der Korngröße auf ferroelektrische Eigenschaften dotierter $\text{Pb}(\text{Zr}_{1-x}\text{Ti}_x)\text{O}_3$ Materialien.
ISBN 978-3-7315-0106-0
- Band 30 Esther Held
Eigenspannungsanalyse an Schichtverbunden mittels inkrementeller Bohrlochmethode.
ISBN 978-3-7315-0127-5
- Band 31 Pei He
On the structure-property correlation and the evolution of Nanofeatures in 12-13.5% Cr oxide dispersion strengthened ferritic steels.
ISBN 978-3-7315-0141-1
- Band 32 Jan Hoffmann
Ferritische ODS-Stähle – Herstellung, Umformung und Strukturanalyse.
ISBN 978-3-7315-0157-2
- Band 33 Wiebke Sittel
Entwicklung und Optimierung des Diffusionsschweißens von ODS Legierungen.
ISBN 978-3-7315-0182-4
- Band 34 Osama Khalil
Isothermes Kurzzeitermüdungsverhalten der hoch-warmfesten Aluminium-Knetlegierung 2618A (AlCu2Mg1,5Ni).
ISBN 978-3-7315-0208-1
- Band 35 Nicht erschienen
- Band 36 Christoph Hage
Grundlegende Aspekte des 2K-Metallpulverspritzgießens.
ISBN 978-3-7315-0217-3
- Band 37 Bartłomiej Albiński
Instrumentierte Eindringprüfung bei Hochtemperatur für die Charakterisierung bestrahlter Materialien.
ISBN 978-3-7315-0221-0

- Band 38 Tim Feser
Untersuchungen zum Einlaufverhalten binärer alpha-Messinglegierungen unter Ölschmierung in Abhängigkeit des Zinkgehaltes.
ISBN 978-3-7315-0224-1
- Band 39 Jörg Ettrich
Fluid Flow and Heat Transfer in Cellular Solids.
ISBN 978-3-7315-0241-8
- Band 40 Melanie Syha
Microstructure evolution in strontium titanate Investigated by means of grain growth simulations and x-ray diffraction contrast tomography experiments.
ISBN 978-3-7315-0242-5
- Band 41 Thomas Haas
Mechanische Zuverlässigkeit von gedruckten und gasförmig abgeschiedenen Schichten auf flexiblem Substrat.
ISBN 978-3-7315-0250-0
- Band 42 Aron Kneer
Numerische Untersuchung des Wärmeübertragungsverhaltens in unterschiedlichen porösen Medien.
ISBN 978-3-7315-0252-4
- Band 43 Manuel Feuchter
Investigations on Joule heating applications by multiphysical continuum simulations in nanoscale systems.
ISBN 978-3-7315-0261-6
- Band 44 Alexander Vondrous
Grain growth behavior and efficient large scale simulations of recrystallization with the phase-field method.
ISBN 978-3-7315-0280-7
- Band 45 Tobias Kennerknecht
Fatigue of Micro Molded Materials – Aluminum Bronze and Yttria Stabilized Zirconia.
ISBN 978-3-7315-0293-7
- Band 46 Christopher Scherr
Elektrochemisches Verhalten von Lithium-Schwefel-Zellen mit unterschiedlicher Kathodenstruktur.
ISBN 978-3-7315-0296-8

- Band 47 Konstantin Frölich
Der Decal-Prozess zur Herstellung katalysatorbeschichteter Membranen für PEM-Brennstoffzellen.
ISBN 978-3-7315-0334-7
- Band 48 Benedikt Haspel
Werkstoffanalytische Betrachtung der Eigenschaften von mittels neuartiger RTM-Fertigungsprozesse hergestellten glasfaserverstärkten Polymerverbunden.
ISBN 978-3-7315-0337-8
- Band 49 Marco Berghoff
Skalenübergreifende Modellierung und Optimierung vom atomistischen kristallinen Phasenfeldmodell bis zur mesoskopischen Phasenfeldmethode.
ISBN 978-3-7315-0416-0
- Band 50 Michael Selzer
Mechanische und Strömungsmechanische Topologieoptimierung mit der Phasenfeldmethode.
ISBN 978-3-7315-0431-3
- Band 51 Michael Mahler
Entwicklung einer Auswertemethode für bruchmechanische Versuche an kleinen Proben auf der Basis eines Kohäsivzonenmodells.
ISBN 978-3-7315-0441-2
- Band 52 Christoph Bohnert
Numerische Untersuchung des Verformungs- und Bruchverhaltens von einkristallinem Wolfram auf mikroskopischer Ebene.
ISBN 978-3-7315-0444-3
- Band 53 Stefan Guth
Schädigung und Lebensdauer von Nickelbasislegierungen unter thermisch-mechanischer Ermüdungsbeanspruchung bei verschiedenen Phasenlagen.
ISBN 978-3-7315-0445-0
- Band 54 Markus Klinsmann
The Effects of Internal Stress and Lithium Transport on Fracture in Storage Materials in Lithium-Ion Batteries.
ISBN 978-3-7315-0455-9

- Band 55 Thomas Straub
Experimental Investigation of Crack Initiation in Face-Centered Cubic Materials in the High and Very High Cycle Fatigue Regime.
ISBN 978-3-7315-0471-9
- Band 56 Maren Lepple
Kupfer- und Eisenoxide als Konversions-Elektrodenmaterialien für Lithium-Ionen-Batterien: Thermodynamische und Elektrochemische Untersuchungen.
ISBN 978-3-7315-0482-5
- Band 57 Stefan Andreas Slaby
Charakterisierung und Bewertung der Zug- und Ermüdungseigenschaften von Mikrobauteilen aus 17-4PH Edelstahl. Ein Vergleich von mikropulverspritzgegossenem und konventionell hergestelltem Material.
ISBN 978-3-7315-0484-9
- Band 58 Kumar Ankit
Phase-field modeling of microstructural pattern formation in alloys and geological veins.
ISBN 978-3-7315-0491-7
- Band 59 Kuo Zhang
Characterization and Modeling of the Ratcheting Behavior of the Ferritic-Martensitic Steel P91.
ISBN 978-3-7315-0503-7
- Band 60 Nicht erschienen
- Band 61 Fabian Lemke
Untersuchung des Sinterverhaltens von SrTiO₃ unter Berücksichtigung der Defektchemie.
ISBN 978-3-7315-0510-5
- Band 62 Johannes Kümmel
Detaillierte Analyse der Aufbauschneidenbildung bei der Trockenerspannung von Stahl C45E mit Berücksichtigung des Werkzeugverschleißes.
ISBN 978-3-7315-0518-1
- Band 63 László Hagymási
Modellierung der Stoffübertragung beim Niederdruckcarbonitrieren mit Ammoniak und Acetylen.
ISBN 978-3-7315-0568-6

- Band 64 Reza Eslami
A novel micro-mechanical model for prediction of multiaxial high cycle fatigue at small scales.
ISBN 978-3-7315-0583-9
- Band 65 Sebastian Schulz
Phase-field simulations of multi-component solidification and coarsening based on thermodynamic datasets.
ISBN 978-3-7315-0618-8
- Band 66 Markus Stricker
Die Übertragung von mikrostrukturellen Eigenschaften aus der diskreten Versetzungsdynamik in Kontinuumsbeschreibungen.
ISBN 978-3-7315-0658-4
- Band 67 Luis Straßberger
Untersuchung und Modellierung des viskoplastischen Verformungsverhaltens oxidpartikelverstärkter Stähle.
ISBN 978-3-7315-0674-4
- Band 68 Mark Wobrock
Microplasticity of idealized single crystalline Ag cantilevers characterized with methods of high resolution.
ISBN 978-3-7315-0682-9
- Band 69 Amritesh Kumar
Micromechanical study on the deformation behaviour of directionally solidified NiAl-Cr eutectic composites.
ISBN 978-3-7315-0694-2
- Band 70 Johannes Hötzer
Massiv-parallele und großskalige Phasenfeldsimulationen zur Untersuchung der Mikrostrukturentwicklung.
ISBN 978-3-7315-0693-5
- Band 71 Thomas Hupfer
Herstellung von LATP für den Einsatz als Festkörperelektrolyt und dessen Eigenschaften.
ISBN 978-3-7315-0702-4
- Band 72 Florentin Pottmeyer
Schädigungsverhalten von in CFK-Laminaten eingebetteten Inserts unter bauteilnahen Beanspruchungen.
ISBN 978-3-7315-0719-2

- Band 73 Andres Höweling
Untersuchung der Hochvoltstabilität und Tiefentladung von dotierten $\text{LiNi}_{0,5}\text{Mn}_{1,5}\text{O}_4$ -Hochvoltspinellen.
ISBN 978-3-7315-0728-4
- Band 74 Tabea Gisela Schwark
Deformation and Fracture Properties of the Soft Magnetic Composite Somaloy 700 3P on Different Length Scales.
ISBN 978-3-7315-0759-8
- Band 75 Klaudia Lichtenberg
Metallmatrixverbunde mit Verstärkungselementen aus metallischem Glas $\text{Ni}_{60}\text{Nb}_{20}\text{Ta}_{20}$ – Herstellung und Charakterisierung.
ISBN 978-3-7315-0782-6
- Band 76 Claudio Findeisen
Charakterisierung und Modellierung von instabilen Metamaterialien.
ISBN 978-3-7315-0869-4
- Band 77 Nilesa Mishra
Influence of strain on the functionality of ink-jet printed thin films and devices on flexible substrates.
ISBN 978-3-7315-0853-3
- Band 78 Simon Werner Bonk
Plastische Verformungsmechanismen in hochgradig kaltgewalzten, ultrafeinkörnigen Wolframblechen.
ISBN 978-3-7315-0878-6
- Band 79 Tim Gräning
Herstellung, Charakterisierung und Optimierung von austenitischen ODS Stählen.
ISBN 978-3-7315-0732-1
- Band 80 Peter Rupp
Herstellung, Prüfung und Modellierung neuartiger hybrider Aluminiumschaum-CFK-Sandwichverbunde.
ISBN 978-3-7315-0880-9
- Band 81 Benjamin Sebastian Ehreiser
Einfluss mechanischer Lasten auf die Herstellung von Stahl-Glaskeramik-Verbunden.
ISBN 978-3-7315-0954-7

- Band 82 Hans Giel
Weiterentwicklung experimenteller Methoden zur Ermittlung thermodynamischer Werkstoffdaten von Lithium-Ionen-Batterien.
ISBN 978-3-7315-0981-3
- Band 83 Anna Trauth
Characterisation and Modelling of Continuous-Discontinuous Sheet Moulding Compound Composites for Structural Applications.
ISBN 978-3-7315-0950-9
- Band 84 Jonas Johannes Hüther
The Impact of Recycling on the Fibre and the Composite Properties of Carbon Fibre Reinforced Plastics.
ISBN 978-3-7315-0983-7
- Band 85 Nicolas A. Mayer
Thermodynamik von Kobaltoxid Anodenmaterialien für Lithium-Ionen-Batterien und ihr elektrochemisches Verhalten.
ISBN 978-3-7315-0996-7
- Band 86 Ulrich Führer
Untersuchung und Modellierung des Haltezeiteinflusses auf die zyklische Entfestigung ferritisch-martensitischer Stähle.
ISBN 978-3-7315-0837-3
- Band 87 Ebru Cihan
Structure evolution in tribological interfaces studied by multilayer model alloys.
ISBN 978-3-7315-0999-8
- Band 88 Markus Sudmanns
Entwicklung einer Kontinuumsbeschreibung für die Versetzungsmobilität in Versetzungsnetzwerken.
ISBN 978-3-7315-1001-7
- Band 89 Tao Zhang
Phase-field Modeling of Phase Changes and Mechanical Stresses in Electrode Particles of Secondary Batteries.
ISBN 978-3-7315-1002-4

- Band 90 Markus Ganser
**On the Electro-Chemo-Mechanical Coupling
in Solid State Batteries and its Impact
on Morphological Interface Stability.**
ISBN 978-3-7315-1047-5
- Band 91 Michael Kellner
**Modellierung mehrkomponentiger Materialsysteme
für die Phasenfeldmethode und Analyse der simulierten
Mikrostrukturen.**
ISBN 978-3-7315-1044-4
- Band 92 Felix Schröckert
**Herstellung dünner Folien aus Lithium-Lanthan-Titanat
zur Anwendung als Festkörperelektrolyt.**
ISBN 978-3-7315-1008-6
- Band 93 Ephraim Schoof
**Chemomechanische Modellierung der Wärmebehandlung
von Stählen mit der Phasenfeldmethode.**
ISBN 978-3-7315-1050-5
- Band 94 Alexander Valentin Brabänder
**Registrierende Härtemessung an neutronenbestrahlten
Materialien bei hohen Temperaturen.**
ISBN 978-3-7315-1097-0
- Band 95 Denny Schmidt
**Einfluss der Kompaktierung auf die Elektrodenmikrostruktur
und elektrochemische Performance bei Lithium-Ionen-Zellen.**
ISBN 978-3-7315-1098-7
- Band 96 Svenja Dittrich
**Entwicklung von Siebdruckpasten zur Herstellung
von Glaslotfugungen für die Festoxidbrennstoffzelle.**
ISBN 978-3-7315-1085-7
- Band 97 Michael Dippon
**Bestimmung der Betriebsgrenzen für das Schnellladen
von Lithium-Ionen Batterien.**
ISBN 978-3-7315-1123-6
- Band 98 Patricia Haremski
**Diffusionseigenschaften von Nickel in einer Festoxid-
Brennstoffzelle.**
ISBN 978-3-7315-1124-3

- Band 99 Florian Wankmüller
**Mehrskalige Charakterisierung der Hochtemperatur-
Brennstoffzelle (SOFC).**
ISBN 978-3-7315-1142-7
- Band 100 Niklas Russner
Modellgestützte Analyse des Stackbetriebs von Festoxidzellen.
ISBN 978-3-7315-1144-1
- Band 101 Theo Fett, Karl Günter Schell, Ethel C. Bucharsky, Gabriele Rizzi,
Pascal Hettich, Susanne Wagner, Michael J. Hoffmann
**Consequences of hydroxyl generation by the silica/water reaction
Part I: Diffusion and Swelling.**
ISBN 978-3-7315-1148-9
- Band 102 Theo Fett, Karl Günter Schell, Ethel C. Bucharsky, Gabriele Rizzi,
Susanne Wagner, Michael J. Hoffmann
**Consequences of hydroxyl generation by the silica/water reaction
Part II: Global and local Swelling
Part III: Damage and Young's Modulus.**
ISBN 978-3-7315-1159-5

KARLSRUHER INSTITUT FÜR TECHNOLOGIE (KIT)
SCHRIFTENREIHE DES INSTITUTS FÜR ANGEWANDTE MATERIALIEN

Water diffusing into silica surfaces gives rise for several effects on diffusion behaviour and mechanical properties. In a preceding booklet, we focused on diffusion and fiber strengths and deformations which were obtained by water soaking under external loading. In the present booklet we deal with results and interpretations of strength increase in the absence of applied stresses. In detail the following topics are discussed:

- Estimation of swelling effects on crack-terminating angles.
- Strength in absence and presence of humid environments.
- Crack-tip shielding.
- Anomalous subcritical crack growth.

ISSN 2192-9963
ISBN 978-3-7315-1159-5

